In search of strong light-harvesting and long-lived Ru(II) and Ir(III) triplet photosensitisers

Junsi Wang

A thesis submitted to the University of Dublin for the degree of

Doctor of Philosophy

School of Chemistry

Trinity College Dublin

October 2017

Declaration

This thesis has not been submitted as an exercise for a degree at this or any other university. Except where acknowledgement is given, all work is original and was carried out by the author alone. I agree that the library may lend or copy this thesis upon request.

Junsi Wang

Summary

Chapter 1: This chapter begins with a general introduction of triplet photosensitisers and Triplet-Triplet Annihilation Upconversion process. It also contains a short literature review of the photophysical properties of different families of triplet photosensitisers, such as Ru(II), Ir(III), Pt(II) and Pd(II) transition metal complexes and organic compounds, followed by their Triplet-Triplet Annihilation upconversion quantum yields and singlet oxygen photosensitisation capabilities. The method of designing triplet photosensitisers is illustrated. Moreover, the applications of triplet photosensitisers are introduced.

Chapter 2: This chapter describes the synthesis of two polyimine complexes (Ru(II) and Ir(III)) with two homo-nuclear coordination centres tethered to a BODIPY chromophore *via* ethynyl linkers. In the comparison with their mononuclear analogues, the ISC effect was enhanced with the addition of second transition metal centre, the absorption profiles of the complexes were extended, and the triplet excited state lifetime of the materials were lengthened. These complexes are explored as triplet photosensitisers for applications of Triplet-Triplet Annihilation upconversion, singlet oxygen photosensitisation and photodynamic therapy.

Chapter 3: This chapter contains a series of carbazole-based transition metal complexes (mono- and di- nuclear N-substituted carbazole-bridged Ru(II) and Ir(III) complexes). This molecule design approach was based on Chapter 2. The dinuclear complexes resulted in a desirably high absorption intensity as expected. The characters of their triplet excited states were analysed *via* photophysical properties and computational results. Finally, the complexes are also examined for their potential applications in Triplet-Triplet Annihilation upconversion and singlet oxygen sensitisation.

Chapter 4: This chapter's work is to synthesise novel Ir(III) triplet photosensitisers bearing ligands of multiple chromophores to broaden the absorption wavelength. The cyclometalated iridium complexes generated contain BODIPY and pyrene as the light-harvesting groups. Compared to mono-chromophore complexes, these complexes show desirably enhanced photophysical properties. The upconversion and singlet oxygen quantum yields are measured and compared.

Chapter 5: This chapter contains novel Ir(III) triplet photosensitisers bearing ligands of multiple chromophores (triphenylamine and pyrene) based on the work in Chapter 4.

Analysis of their photophysical processes were presented. The high light of this work is the novel link position on 2-phenylpridine prolongs cyclometalated Ir(III) complexes's triplet excited state lifetime. The investigations of upconversion and singlet oxygen photosensitisation abilities were discussed at the end.

Chapter 6: This chapter introduces a novel application of Triplet-Triplet Annihilation upconversion towards photoinitiated polymerisation. This work demonstrates the use of a transition metal-based photosensitiser, which absorbs efficiently in the visible region, and shows a high Triplet-Triplet Annihilation upconversion quantum yield. The upconverted emission which is higher energy light acts as a secondary photon source to initiate the photo-polymerisation process.

Chapter 7: This chapter gives a full account of the experimental work carried out in this research, and includes a useful summary of many of the NMR techniques used.

Acknowledgements

I would firstly express my sincere thanks to my supervisor Sylvia. M. Draper for providing me the opportunity to study in Trinity College and for all her advice, encouragement and guidance. I really appreciate her understanding and support throughout my time here in Trinity College. I would also like to express my gratitude to Dr. John O'Brien and Dr. Manuel Rüther for both expertise and time for NMR analysis, to Dr. Martin Feeney and Dr. Gary Hessman for mass spectrometry and to Dr. Brendan Twamley for crystallographic support.

I also wish to express thanks to Prof. Jianzhang Zhao and his group, especially his students Dr. Xiaoneng Cui and Ms. Wenbo Yang for collaborative work in this project in Dalian, teaching me new techniques and giving me advice.

My sincere thanks also go to all the past and current Draper group members – Gearóid, Niamh, Lankani, Colm, Nitheen, Yue, Robert, Bryan, Eugene, Colin, Marta and Claire. Thank those who were there from the very beginning for helping me adapt to the very different culture and new lab life very quickly. I particularly wish to thank Gearóid, Niamh, Robert and Eugene for all their support and proof reading efforts. I wish to express my heartfelt thanks to my colleagues, Byran and Robert. Thank you very much for your company, useful suggestions and endless help in the last four years.

My heartiest gratitude to my parents, my cousins, my uncles and aunts. Thank you for your understanding, support and unconditional love. To my friends Dian, Yan, Yong and Dan, thank you for your constant motivation, encouragement and for always being there. Last but not least, thanks to myself.

Table of Contents

Table of Figures

Table of Schemes

Table of tables

Abbreviations

1D	one-dimensional
2D	two-dimensional
A	acceptor
Å	angstrom
abs	absorption
BODIPY	1,3,5,7-tetramethyl-8-phenyl-4,4-difluoroboradiazaindacene
bpy	2,2-bipyridine
C	Celsius
CH_2Cl_2	methylene chloride
CH_3CN	acetonitrile
CH_3OH	methanol
$(CH_3CH_2)_3N$	triethylamine
CH_3CH_2OH	ethanol
$(CH_3)_2SO$	dimetyl sulfoxide
$CHCl_3$	chloroform
cm	centimeter
COSY	correlated spectroscopy
D	donor
δ	chemical shift
d	doublet
DE	rigidochromic shift
DFT	density functional theory
DMF	dimethylformamide
DPA	9,10-diphenylanthracene
DPBF	1,3-diphenylisobenzofuran
ε	molar absorption coefficient
em	emission
ESI-MS	electro-spray mass
eV	electronvolt
ex	excitation
Φ	quantum yield
GS	ground state
h	hour
H_2O	water
HMBC	heteronuclear multiple bond correlation
HOMO	highest occupied molecular orbital
HSQC	heteronuclear single quantum correlation
DSSC	dye-sensitised solar cell
Hz	Hertz

IC	internal conversion
$(i\text{-}Pr)_2NH$	N, N-diisopropylamine
IL	intraligand
ILCT	intraligand charge transfer
ISC	intersystem crossing
J	coupling constant
K	Kelvin
λ	wavelength
LC	ligand centred
LMCT	ligand-to-metal charge transfer
LUMO	lowest unoccupied molecular orbital
M	molarity
m	multiplet
m/z	mass to charge ratio
MALDI-TOF	matrix assisted laser desorption ionisation-time of flight
mg	milligram
min	minute
mL	millitre
MLCT	metal-to-ligand charge transfer
mmol	millimole
ms	millisecond
μs	microsecond
NIR	near infrared
nm	nanometer
NMR	nuclear magnetic resonance
ns	nanosecond
NO_x	nitrogen oxides
OLEDs	organic light emitting diodes
O/PLEDs	organic/polymer light emitting diodes
PDT	photodynamic therapy
ppm	parts per million
ppy	2-phenylpyridine
PS	photosensitiser
RT	room temperature
s	singlet
t	triplet
τ	lifetime
TBAF	tetra-n-butylammonium fluoride
TDDFT	Time-dependent density functional theory
THF	tetrahydrofuran
TMAS	trimethylacetylene
TPA	triphenylamine

TTET	Triplet-triplet energy transfer
TTA	Triplet-triplet annihilation
UC	upconversion
VOCs	volatile organic compounds
^{13}C NMR	carbon nuclear magnetic resonance
^{1}H NMR	proton nuclear magnetic resonance
UV-vis	ultraviolet-visible
º	degree
%	percentage

New compounds and main references structures

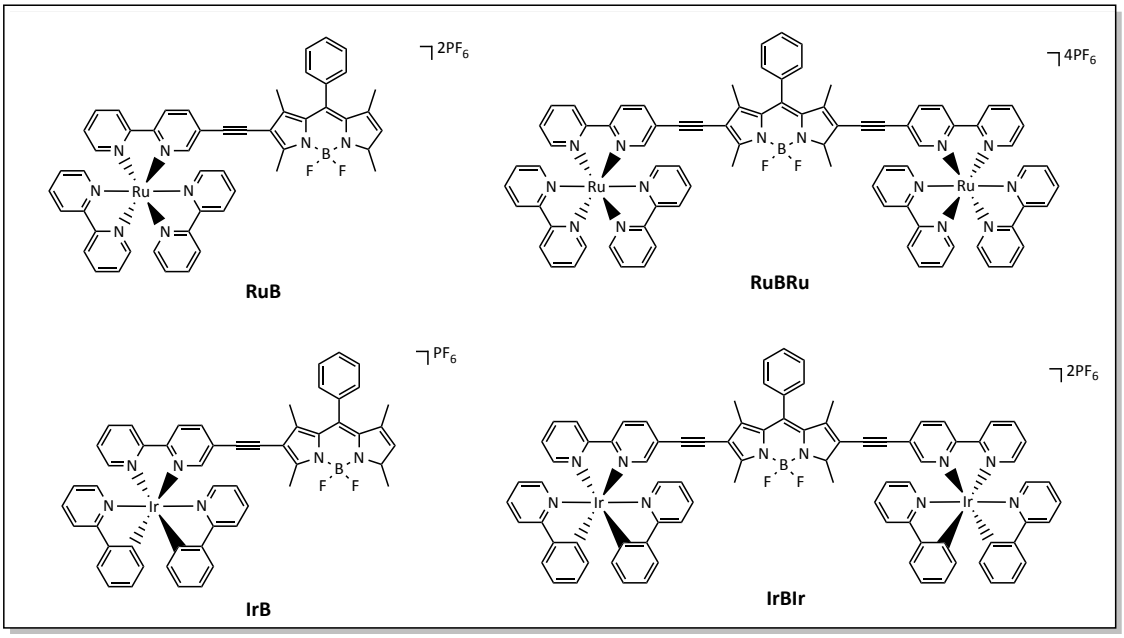

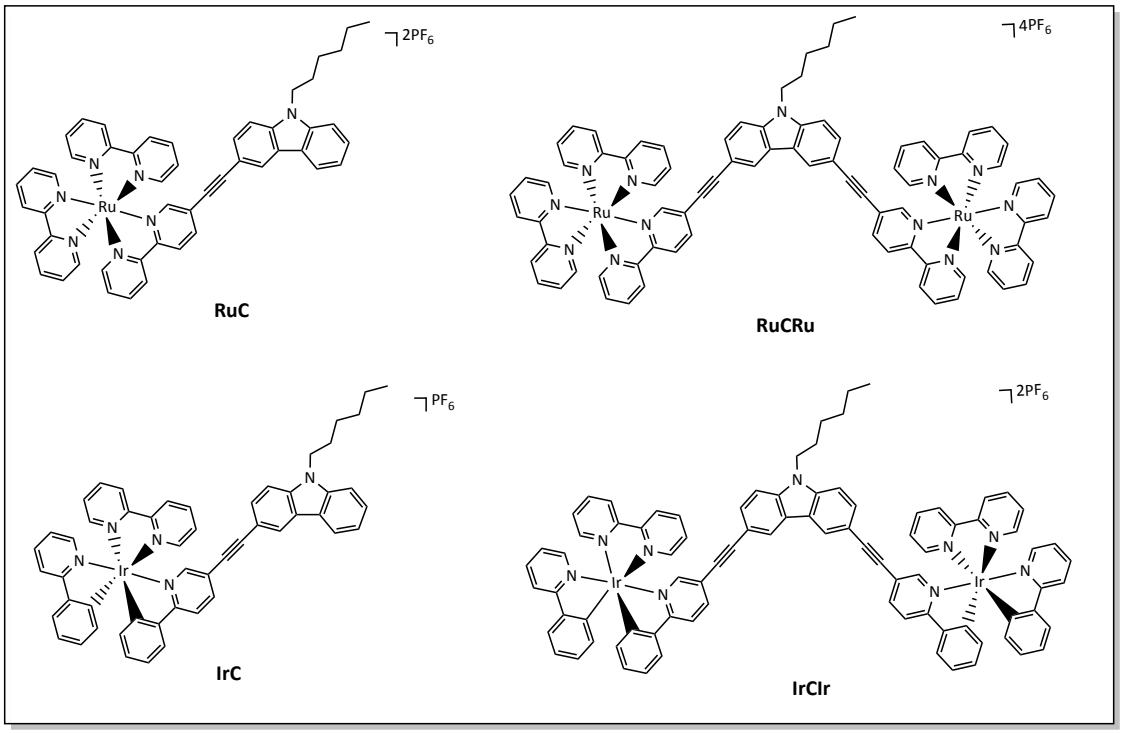

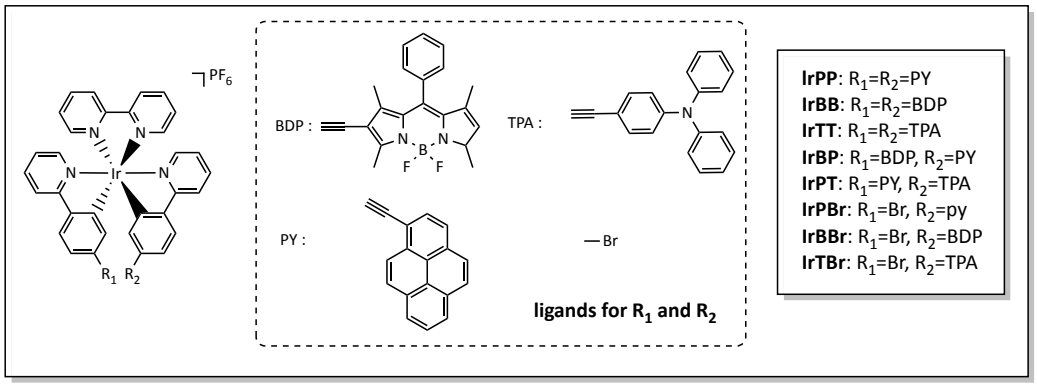

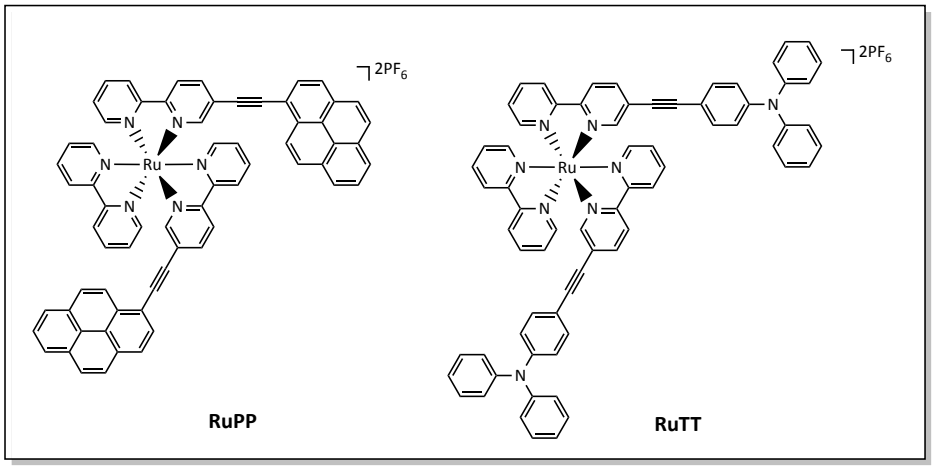
2PF6
Ru
N
RuPP
RuTT

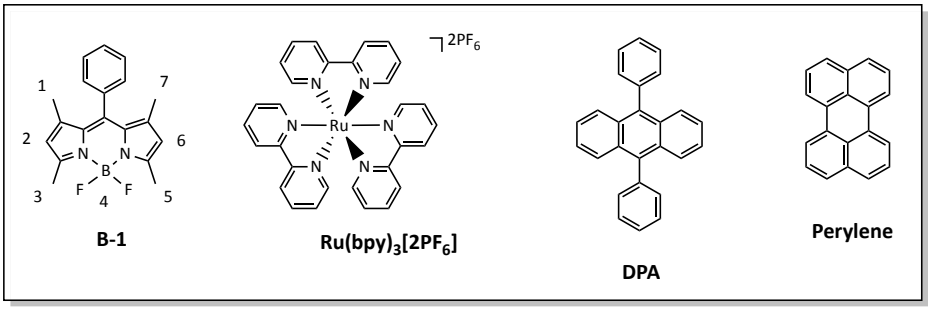
1
2
3
4
5
6
7
B
F
F
B-1
2PF6
Ru
Ru(bpy)3[2PF6]
DPA
Perylene

1 Introduction

1.1 General

In recent decades the demand for energy, especially from fossil fuels, and limits on the rate of fuel production have resulted in a bottleneck. Currently, the world's growing thirst for crude oil amounts to almost a thousand barrels per second, which corresponds to about 2 litres per day per person living on Earth.[1] Facing into this serious problem, a number of renewable energies have been proposed as solutions, such as wind, solar, and biomass. Each one has its own advantages, but also challenges. For example, wind is dependent on weather and climate and thus may be unreliable, and biomass may actually exacerbate the problem of global warming. Biomass is a biological material derived from living, or recently living organisms.[2] Using biomass as a fuel produces air pollution in the form of carbon monoxide, carbon dioxide, NOx (nitrogen oxides), VOCs (volatile organic compounds), particulates, and other pollutants at potentially higher levels than those generated from traditional fuel sources such as coal or natural gas (e.g. indoor heating and cooking).[3]

As more sunlight falls on the earth in one hour than is required by its inhabitants in one year, solar energy appears to be an excellent potential source of energy. Photovoltaic devices provide a possible solution to the energy crisis as they utilise and harvest solar energy. Photovoltaic or solar cells convert solar light directly into electricity using semiconducting materials.

The traditional and prototypical solar cell is the semiconductor solar cell. When photons hit the solar cell, excited and thus freed electrons (-) attempt to unite with holes in the p-type layer. The p-n junction (a p-n junction is a boundary or interface between two types of semiconductor material, p-type and n-type, inside a single crystal of semiconductor.), acts as a one-way pathway, restricting the electrons to movement in only one direction. The electron flow provides the current (I), and the cell's electric field generates a voltage (V).[4] The biggest problem with this conventional approach is the cost of manufacturing these solar cells. A semiconductor solar cell requires a relatively thick layer of doped silicon in order to have reasonable photon capture rates, and this silicon processing is expensive. Thus, in the early 1970s, experiments of electric power generation *via* the dye-sensitised solar cell (DSSC) principle were demonstrated, and discussed extensively in the literature.[5]

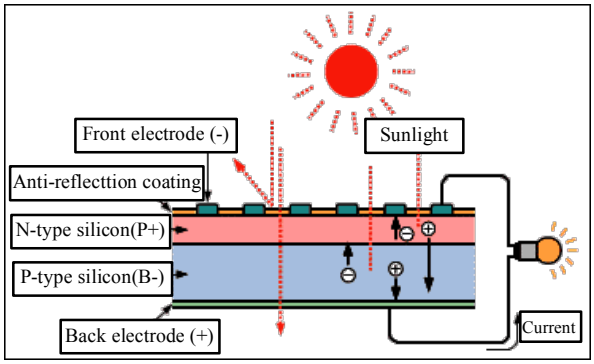

Scheme 1.1 *A model of traditional semiconductor solar cell with p-n junction. When light strikes a solar cell, part of it is absorbed. The absorbed light excites the bound electrons into a higher energy state, making them free electrons. These free electrons move about in all directions within the crystal, leaving holes where the electrons used to be, and the holes also shift around the crystal. The electrons (-) collect in the N-layer, the holes (+) in the P-layer. When the outside circuit is closed, electricity flows.* [6]

A modern DSSC is composed of a porous layer of titanium dioxide nanoparticles, covered with a molecular dye capable of absorbing photons of sunlight; a role similar to that of chlorophyll in green leaves. The general structure of a DSSC is shown in Figure 1.1. In the majority of these DSSC systems, the dye molecules generally suffer poor absorption in the red region of the visible spectrum which comprises photons which are lower in energy, compared to their silicon-based counterparts due to the nature of dye. This results in fewer sunlight photons being used for the generation of current. Therefore, in order to make them more efficiently, the photophysical phenomenon of upconversion may be utilised to help to convert some of these lower energy photons to higher energy photons. As an energy transfer process, upconversion has drawn much attention not just in photovoltaics, but also due to its potential application in a number of research areas including photodynamic therapy, artificial photosynthesis, photocatalysis, photovoltaics and luminescent oxygen sensing.[7]

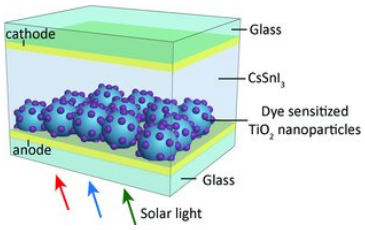

Figure 1.1 *The structure of a dye-sensitised solar cell (DSSC).*[8]

If current DSSCs are modified with upconverting materials, to convert lower energy wavelength photons to higher energy wavelength photons, the efficiency of the solar cell can be improved significantly.[9] There are four families of compounds that have been used in upconversion processes. The first example is known as two-photon absorption dyes (TPA) upconversion. This method utilises a non-linear optical process, and the atomic transition rate depends on the square of the light intensity. The drawback of these TPA compounds is that they need to be excited by a laser source, of a high-power density. The second family of compounds are inorganic crystals. These have the stability of an inorganic crystalline structure, but are poor absorbers. The third family of compounds are the rare-earth materials, including lanthanide-ion (Yb^{3+}, Er^{3+}, *etc*.) doped $NaYF_4$. These are also weakly absorbing due to the spectrally narrow absorption band of the respective rare earth metal used.[10] The fourth and most promising method is based on triplet photosensitisers, and includes Ru(II), Ir(III), Pt(II), Pd(II) and Re(I) complexes which work *via* the process of triplet-triplet annihilation (TTA) upconversion (Section 1.1.2; Scheme 1.3).

TTA was first explored by Parker and Hatchard more than fifty years ago,[11, 12] and has recently begun to draw considerable and focused research interest. Other techniques suffer through the requirement of high excitation power sources, and problems arising from weak absorption of visible and near infrared light (solar light). These systems therefore also suffer low upconversion quantum yields (Φ_{UC}). The excitation power density source when using the TTA upconversion method can be as low as a few $mW \cdot cm^{-2}$.[13] According to the standardised solar spectrum, the solar irradiation energy at sea level is $1kW \cdot m^{-2}$ ($0.1\ W \cdot cm^{-2}$, AM1.5G). Therefore, it is possible for the TTA upconversion process to utilise terrestrial solar light.

A solar energy device using a p-n junction to generate power suffers a maximum threshold, referred as to the Shockley-Queisser limit. The theoretical efficiency of a semiconductor solar cell, such as one derived from the most popular material silicon is no more than 30 %, as first calculated by Shockley and Queisser.[14] Triplet-Triplet Annihilation upconversion offers a novel approach to overcome this threshold. It relies on an ability to transfer energy from a low energy donor to a high energy acceptor. The limitation on the efficiency of the cell would therefore be broken as a consequence. The seminal paper by Baluschev *et al.*[15] in 2006 was the first TTA upconversion method reported to be achieved by using ultra low intensity non-coherent sunlight (Figure 1.2(a)).

In this process, DPA (9,10-diphenylanthracene) was used as the annihilator molecule, and was populated with 2 *wt* % PdOEP ((2,7,8,12,13,17,18-octaethyl-porphyrinato)Pd(II)). The excitation light source used was in the green region of the terrestrial solar spectrum (λ 550 nm). The paper represented a breakthrough for solar cell technique design through the inclusion of an upconversion component, and by demonstrating that it is possible to utilise terrestrial solar light directly.

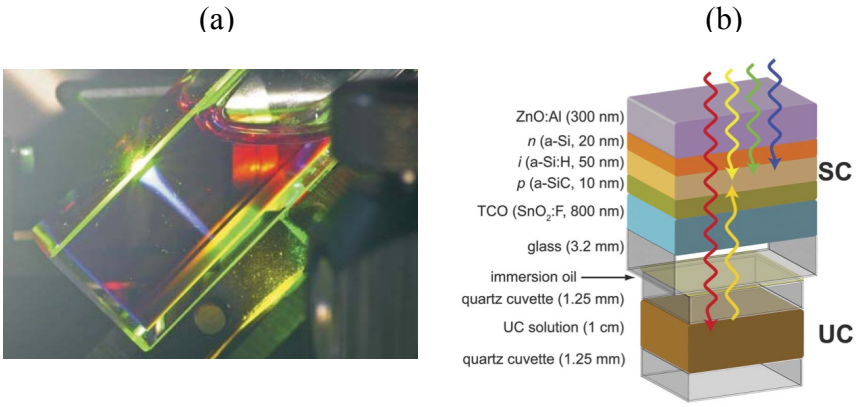

Figure 1.2 *(a) A CCD-camera image of the up-converted fluorescence inside a 1 cm*^{3} *cuvette, excited with the green region of the solar spectrum (no filters were used).* [15] *(b) An illustration of the integrated a-Si:H p-i-n/UC device. Low energy (shown in red) photons pass though the p-i-n structure (there is an intrinsic or undoped layer sandwiched between a p- and an n-doped region) and excite dye molecules in the upconversion unit, which subsequently returns photons of a shorter wavelength (yellow) to be used by the cell.* [16]

In 2012, Schmidt *et al.*[16] applied this technique to hydrogenated amorphous silicon thin-film solar cells to improve their light-harvesting ability (Figure 1.2(b)). After the low energy light passes through the silicon solar cell, it reaches an upconversion solution layer, from which the upconverted light then goes back to the silicon solar cell unit. The combination of the silicon solar cell, and the upconversion solution device, contributed to an improved photovoltaic efficiency of 1.0 ± 0.2 % at 720 nm (rubrene was used as the acceptor molecule).[16] This improvement represented a breakthrough in the threshold of solar energy devices.

In conclusion, when compared to other upconversion approaches, the TTA method allows for strong absorption in the visible or NIR wavelength region, tuneable absorbance

wavelength through molecular design, and high chemical stability. It represents an exciting viable addition to future solar cell design.

To date, the majority of TTA UC studies have been carried out in deoxygenated solution at room temperature, yet it remains highly desirable that appropriate sensitiser/acceptor molecules are embedded in suitable solid materials for potential device integration. Prof. Jea-Hong Kim and his co-worker reported polymer based upconverting material which is easily molded into a variety of forms. With PdOEP as photosensitiser and DPA as acceptor/annihilator molecules, the solid-state upconversion system's efficiency is up to 22 %.[17] It convinced that the TTA UC is able to be applied in devices.

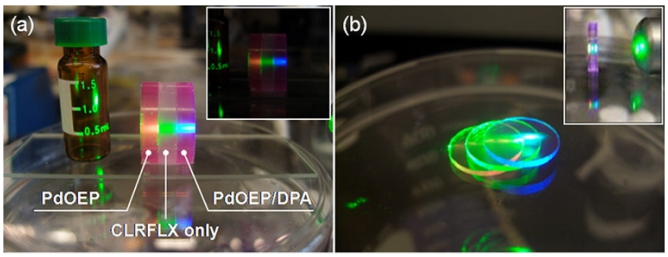

Figure 1.3 *Photographs of the prepared polymer samples irradiated by a green laser pointer, λ_{ex} = 532 nm (<10 mW incident power). RGB light emission from the (a) polymer disk and (b) the polymer film (thickness: ca. 100 mm).*[17]

1.1.1 Triplet Excited States and Triplet Photosensitisers

In order to establish how the triplet state is accessed, a modified Jablonski diagram is presented in Scheme 1.2. Use of the diagram clearly illustrates the energy states and energy transfer processes. The diagram also shows two types of energy states, singlet (S) and triplet (T).

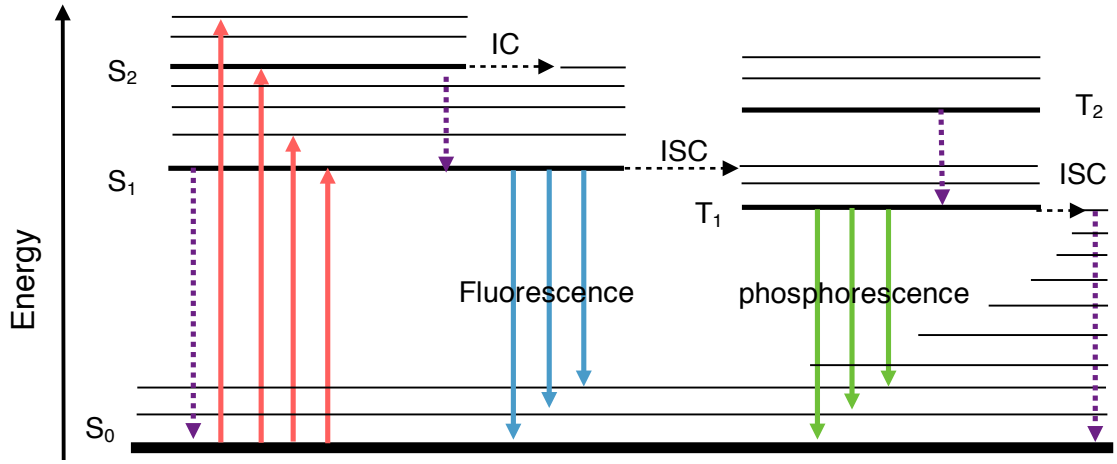

Scheme 1.2 *Modified Jablonski diagram for photoexcitation and luminescence events. Red arrows indicate steady-state absorption, blue arrows indicate fluorescence, and green arrows indicate phosphorescence. Purple dotted lines show non-radiative processes (the transformation of electronic excitation energy into vibrational/rotational energy, instead of the emission or the absorption arising through the transformation of photons). IC - Internal conversion. ISC - intersystem crossing. S - singlet state. T - triplet state.*

For a system that exists as a singlet, all electron spins are paired, and the total spin for the system is 0. In a triplet system, with two unpaired electrons for example, the total spin for the system is 1. According to the Spin-Angular Momentum vector L (L = 2S + 1, S-total spin), the spin multiplicity of a singlet is 1 and a triplet is 3. In addition, according to the Frank-Condon principle, transitions only happen between different electronic states. For example, a molecule can only be excited from the ground state (S_0) to a higher electronic state (S_1, S_2, *etc*.). The process of internal conversion (IC) is a relaxation from an upper excited electronic state, such as S_2, S_3, *etc*., to a lower electronic state, such as S_1, with the same multiplicity (or from T_2, T_3, *etc*. to T_1). Since the energy gap between upper excited electronic states is smaller than the energy gap between S_0 and S_1, the highest vibrational level of S_1 is very close in energy to S_2. The transition process between higher electronic states is rapid and this means that the excited-state molecule quickly relaxes to the S_1 (v = n, vibrational levels). This also demonstrates the basis of Kasha's rule that luminescence emission and significant chemical reaction by excited molecules will always originate from the lowest vibrational level of S_1 or T_1.

The transition from the singlet state to the triplet state, which is referred to as intersystem crossing (ISC), is a spin-forbidden process due to the different multiplicities of the two states. The electron in the molecule experiences a magnetic field as a result of the relative motion of the positive nucleus with respect to it. During this process, the field promotes mixing of the singlet and the triplet states and provides a means of conserving spin states between the orbitals of a similar energy, so called Spin-Orbit Coupling (SOC).[18] This means, that the excited molecule will be transferred from S_1 to T_1 (v = n) or T_n (v = n) when these states are similar in energy. It should be noted that since SOC depends on interaction with the nucleus, its magnitude increases with increasing nuclear charge. Therefore, the spin-forbidden transitions are stronger when heavy nuclei are involved. Elements with a large atomic number, such as Ir, Ru, Pt, Re, I and Br, *etc.* can induce

strong SOC, and can result in an efficient ISC process. This phenomenon is known as the heavy atom effect, and thus compounds which can easily generate a triplet excited state using ISC, are called triplet photosensitisers. Due to its spin-forbidden nature, the typical lifetime of a phosphorescent process (photon emission from T_1) is in the microsecond to second scale, which is much longer than typical fluorescence lifetimes (spin-allowed photon emission from S_1).

1.1.2 Triplet-Triplet Annihilation Upconversion

The constituents of a TTA Upconversion system play two important roles, as triplet sensitisers and also as triplet acceptors (Scheme 1.3). The triplet sensitiser is excited by photo-irradiation and the energy is then transferred to the triplet acceptor, which emits photons at a shorter wavelength (higher energy) than the excitation wavelength.

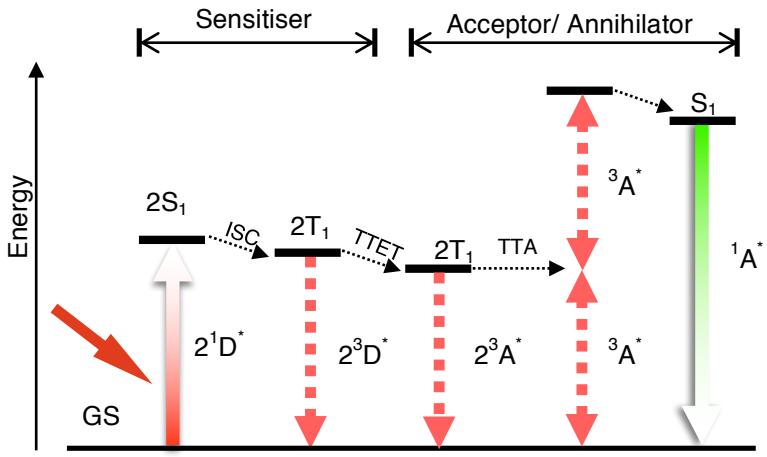

Scheme 1.3 *Generalised energy level diagram of the TTA upconversion processes between the triplet states of the sensitiser and the triplet acceptor leading to a delayed fluorescence. TTET is Triplet-Triplet Energy Transfer. D is the sensitiser. A is the acceptor/annihilator. * is excited state and GS is ground state.*

To look at the process in more detail, the singlet excited state of the sensitiser is populated, which means the energy is transferred from the ground state (S_0) of the molecule to the first singlet excited state (S_1). Then, the triplet excited state of the sensitiser is populated *via* ISC which is usually facilitated by the heavy atom effect. The harvested triplet excited state energy of the sensitiser is transferred to the triplet acceptor *via* Triplet-Triplet Energy Transfer (TTET). The lifetime of the triplet excited state is much longer than that of the singlet excited state. This facilitates the energy transfer from the triplet excited states,

through contact between the two molecules. This is a Dexter process. Dexter energy transfer is a process by which two molecules (or two parts of a molecule) bilaterally exchange their electrons in a non-radiative process (Scheme 1.4).

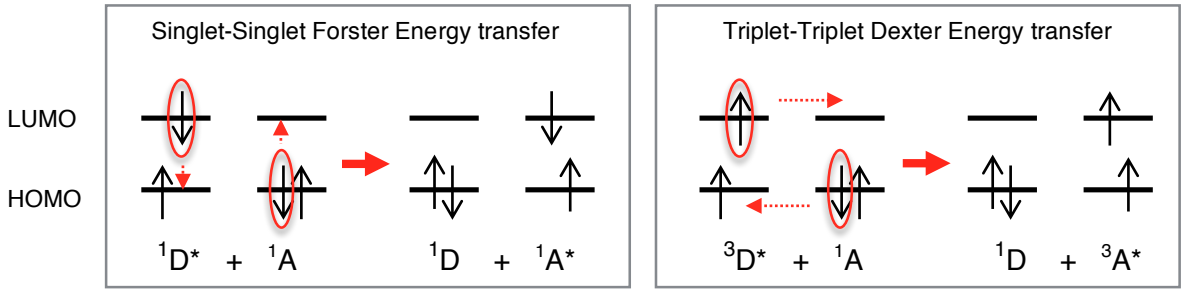

Scheme 1.4 *Illustration of Singlet-Singlet Forster Energy Transfer and Triplet-Triplet Dexter Energy Transfer. D denotes donor; A denotes acceptor; * represents excited state.*

During the TTET process, the donors in their triplet excited states and the acceptors in their singlet ground states collide with each other, producing the triplet acceptors. The Triplet-Triplet Annihilation (TTA) process then occurs usually between two triplet acceptors resulting in one acceptor with a singlet excited state, and the other returns to its ground state (Scheme 1.5). The singlet excited state then decays *via* a radiative transition and generates upconverted fluorescence, referred to as P-type delayed fluorescence. The other possible type of delay fluorescence is E-type. It occurs when there is a small energy gap between singlet and triplet states. It results in reverse intersystem crossing from a triplet excited state to a singlet excited state due to thermal activation. The singlet excited state decays *via* a radiative transition which is E-type fluorescence.

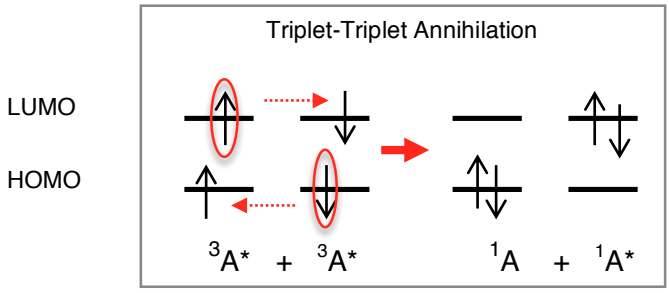

Scheme 1.5 *Illustration of Triplet-Triplet Annihilation process. A is acceptor in the TTA UC process; * is excited state.*

It should be noted that the TTA process does not have to be between two triplet excited state acceptors. There is another potential mechanism between a $^3D^*$ (donor) and a $^3A^*$ (Acceptor), especially when the $^3A^*$ energy is less than half of $^1A^*$ ((Equation 1.1e); Scheme 1.3). When a triplet excited state donor is involved in a TTA collision, the

collision efficiency is improved. This illustrates why triplet acceptors like perylene and 9,10-bis(phenylethynyl)-anthracene (whose excited state energy levels do not meet $2E_T>E_S$) can be used for TTA upconversion. However, it is difficult to distinguish energy-pooling between the two different species ($^3A^* + {}^3A^*$ and $^3D^* + {}^3A^*$). The TTA process can be summarised in the following series of equations:

$$D(S_0) + h\nu \rightarrow D(S_1) \quad (1.1a)$$

$$D(S_1) \rightsquigarrow D(T_1) \quad \text{ISC} \quad (1.1b)$$

$$D(T_1) + A(S_0) \rightarrow D(S_0) + A(T_1) \quad \text{energy transfer} \quad (1.1c)$$

$$A(T_1) + A(T_1) \rightarrow A(S_1) + A(S_0) \quad \text{energy-pooling} \quad (1.1d)$$

$$D(T_1) + A(T_1) \rightarrow A(S_1) + D(S_0) \quad \text{energy-pooling} \quad (1.1e)$$

$$A(S_1) \rightarrow A(S_0) + h\nu \quad \text{delayed fluorescence} \quad (1.1f)$$

Equation 1.1 *The TTA UC process illustration via equations 1.1a-f.*

1.1.3 The Efficiency Limit of TTA Upconversion

In the process of TTA upconversion, it is clear that the upconversion quantum yield depends on the efficiency of ISC, TTET, TTA and the fluorescence of the emitter (Equation 1.2). In addition to the efficiency of these processes, according to the spin-statistic law, the efficiency limit of the TTA process is 11.1 %. In this theory, when two triplet molecules collide with each other, nine encounter pairs are generated with the same probability. Three types of spin multiplicity of the encounters would be formed: singlet, triplet, and quintet. Finally, the $^1A_0^*$ is formed with 11.1 % (1/9) possibility. Therefore, according to this theory, the maximum Φ_{TTA} cannot be over 11.1 %. However, a number of triplet photosensitisers have been reported with TTA upconversion quantum yields above this value.[19, 20] This means that the limitation of 11.1 % can be overcome and is not fixed. Schmidt *et al.* write that it is unlikely that the triplet and quintet encounter complexes quench directly to singlet ground states.[21] Quintet encounters could dissociate back to triplets, and the triplet encounter could convert to isoenergetic triplet states. This assumption is also supported by the conclusion of Charlton *et al.* that the quintet encounter has a 92 % chance to decay into two triplet excited state molecules ($^3A_1^*$).[22] Therefore, the TTA process efficiency can be improved up to values of at least 40 %.

Moreover, 100 % Φ_{TTA} could be imagined through the following process: i) the T_2 states can undergo decay back to S_1 *via* ISC and generate more fluorescence ii) where the T_2

state is double the energy of the T_1 state, then the triplet states will act as the quintet states. To summarise, the unit Φ_{TTA} is can considered theoretically possible.

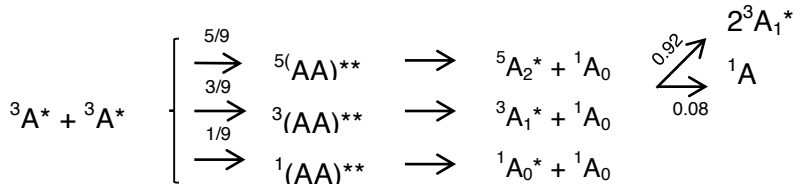

$$\Phi_{UC} = \Phi_{ISC} \times \Phi_{TTET} \times \Phi_{TTA} \times \Phi_{Fl}$$

Equation 1.2 *The equation of upconversion yield. Φ_{uc} is the upconversion yield; Φ_{ISC} is the intersystem crossing yield, Φ_{TTET} is the triplet-triplet energy transfer yield; Φ_{TTA} is the triplet-triplet annihilation yield; Φ_{Fl} is the fluorescence quantum yield.*

The TTET efficiency is dependent on the interaction between the triplet energy donor and acceptor. Φ_{Fl} is the fluorescence quantum yield depending on the triplet emitter (acceptor) only. Φ_{ISC} is related to the properties of the triplet photosensitiser.

1.1.4 Design of Triplet Photosensitisers

To achieve a high TTA upconversion yield, the design of triplet photosensitisers still presents a significant challenge.[23] In 2011, Zhao *et al.* reported some general rules about the design of triplet photosensitisers, of which several factors were considered.[9] Firstly, the triplet photosensitisers should have a high molar absorbance coefficient at the excitation wavelength, especially in the visible and near-infrared region. This improves the utilisation yield of solar light and at the same time, improves the yield of TTA upconversion. Secondly, a long triplet excited lifetime can promote the triplet-triplet energy transfer, which is based on diffusional collision. For example, microsecond scale is usually favoured. Thirdly, high ISC yield is necessary. This is the reason why heavy metal atoms, such as Ru(II), Pt (II), Pd (II), and Ir (III) are utilised in triplet photosensitisers, all of which display high ISC efficiencies.

In addition, the triplet excited state energy of the sensitiser should be higher than the triplet excited state energy of the acceptor, or the TTET process cannot occur. Also, the sensitiser's singlet excited state must lie below that of the acceptor's, while its triplet excited state must lie above that of the acceptor. The combination energy of two triplet excited state acceptor molecules or the total energy of one triplet excited state acceptor

and donor must be higher than or equal to the singlet excited state energy of the acceptor. Otherwise, the TTA process cannot happen. Furthermore, acceptor molecules which have a high fluorescence quantum yield (Φ_{Fl}) need to be carefully chosen. For example, 9,10-diphenylanthracene (DPA), perylene, anthracene and boron-dipyrromethene (BODIPY) *etc.* display good quantum yields.[9] Finally, good photochemical stability is required.

In addition, the power density of the external light source will also have an effect on the TTA upconversion yield. This suggests that it has a non-linear profile and presents as a quartic incident light power dependence.[23, 24] Due to this, this thesis is only concerned with the TTA upconversion yield under solar power-like excitation conditions.

1.2 Families of Photosensitisers

1.2.1 Ruthenium(II) and Iridium(III) Complexes

As discussed in the earlier section, heavy metal complexes are usually chosen as triplet photosensitisers due to their efficient ISC ability. However, not all transition metal complexes have the ability to be an effective triplet photosensitiser. This is due to the difference in Δ of the d orbitals in the octahedral field of the different metal centres. The size of Δ depends on different electron occupations in t_{2g} and e_g, the type of orbitals in the different spatial extension, e.g. 3*d*(Fe), 4*d*(Ru), 5*d*(Os, Ir)), and the field strength exerted by the ligand.

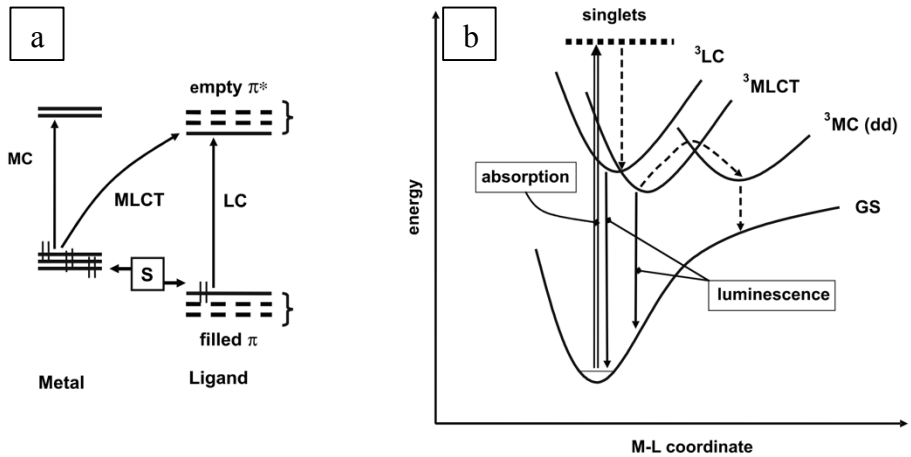

Scheme 1.6 *(a) Orbital description of MC, MLCT and LC transitions. S is substitution group capable of exerting electron withdrawing or releasing effects. (b) Electron*

transitions involving MC, MLCT and LC excited states for polyimine complex of d^6 metal centres. [25]

As shown in Scheme 1.6(a), there are three possible transition types that can occur in a polyimine d^6 metal complex. MC is a metal centred transition (dd); MLCT is a metal to ligand charge transfer; LC is a ligand centred transition. Despite population of the upper states based on the Boltzmann distribution theory, according to Kasha's rule, only the lowest excited state will be involved in the photochemical and photophysical properties. When a MC transition is the lowest excited state in a complex, emission from the MLCT and LC states may not occur. If this lowest excited state (MC) contains a cross point (the point where two energy levels are very close to each other and at which the radiation-less transition would like to occur) with the ground-state, the MC excited state may deactivate to the ground state *via* an ultrafast radiation-less transition (surface crossing). Therefore, the triplet energy transfer rarely happens in these cases. For example, for an Fe(II) centre in an octahedral field, due to Δ_{oct} being small, its polyimine complexes usually have a MC lowest excited state. This is the reason Fe(II) complexes are not typically seen as triplet photosensitisers. When the lowest excited state is MLCT or LC, both are deactivated *via* a radiative transition and luminescence is usually observed. The luminescence is long-lived, and the lifetime is often in the microsecond region. According to earlier studies, if heavy atoms are involved in the transition, the ISC rate constant will be high. Therefore, in these cases, the radiative deactivation rate constant is higher in ^{3}MLCT than in ^{3}LC. This results in the luminescence lifetime of ^{3}LC being longer than of ^{3}MLCT. However, if the lowest excited state is MLCT and it is very low-lying, a radiative transition may not be observed. This is due to the energy gap law. This law states that the non-radiative decay rate increases as the energy gap decreases.[7] For instance, in Os(II)-polyimine complexes, the MLCT is around 1.6 eV and no luminescence is observed.[25] Taking these issues into account, Ru(II) and Ir(III) polyimine complexes prove to be the metal centres of choice for effective metal complex triplet photosensitisers.

1.2.1.1 Ruthenium polyimine complexes as triplet photosensitiser

Ruthenium polyimine complexes have been widely used from the 1970s onwards in photovoltaics, and molecular arrays. More recently, ruthenium complexes have been used as triplet photosensitisers due to their good photophysical properties, absorption in the visible region, long lived triplet excited states, and efficient ISC ability.

In 2004, Castellano *et al.* reported a ruthenium polyimine complex **P-1** (Figure 1.3).[12] The anthracene moiety, the triplet energy acceptor, was linked to the metal complex *via* a covalent bond to form a compound containing a triplet energy donor and acceptor. Upon excitation at λ_{ex} = 450 nm, delayed fluorescence of the anthracene was generated, and the lifetime was determined as 9 μs. It indicates that the bimolecular intramolecular triplet-triplet annihilation process occurs. In a comparison experiment, the parent ruthenium complex, $Ru(dmb)_3^{2+}$, **P-2** (Figure 1.3), was chosen as the triplet photosensitiser, and a separate anthracene **A-1** was selected as the triplet acceptor. Under identical experimental conditions, the delayed fluorescence was found to be 2.9-fold higher than that of **P-1**. This led the authors to conclude that the intramolecular TTA upconversion process exhibits a lower efficiency than intermolecular TTA upconversion.

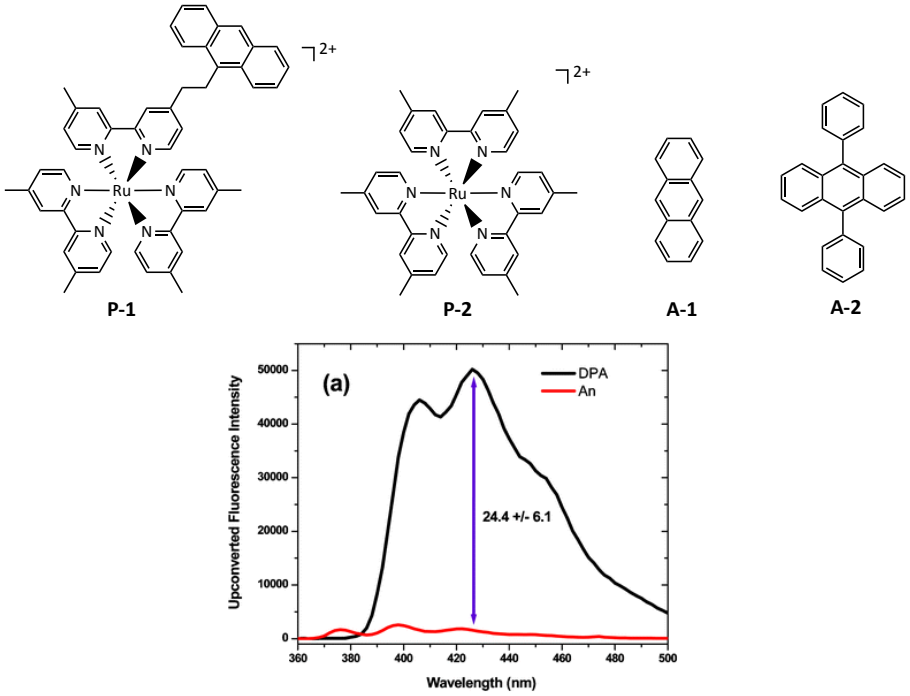

Figure 1.4 *Ruthenium photosensitisers* ***P-1***[12]*,* ***P-2*** *and triplet acceptor* ***A-1***, ***A-2***; ***P-1*** *is a combination of a traditional ruthenium photosensitiser and anthracene as a triplet acceptor tethered to it.* ***P-2*** *is for comparison. (a) the upconverted luminescence of* ***A-1*** *and* ***A-2*** *with* ***P-2*** *as the triplet photosensitser.*[26]

One year later, they used **P-2** to sensitise the TTA upconversion with 9,10-diphenylanthracene (DPA, **A-2**). Compared to anthracene as the triplet energy acceptor, the upconverted luminescence of DPA was significantly enhanced, and approximately 24-fold higher when excited with a green light (λ_{ex} = 514.5 nm). This is mainly due to the high fluorescence quantum yield of DPA (Φ_F(DPA, **A-2**) = 0.95, Φ_F(**A-1**) = 0.27). The

key outcome of this work was that the system can be excited using a low power external laser light source, such as a laser pointer (λ_{ex} = 532 nm, <5 mW), suggesting that the TTA upconversion method could be applied to utilise solar-type light in future designs.

In common with most of the traditional ruthenium complexes, however, the absorption of **P-2** in the visible region is weak, and the triplet excited lifetime is short. A solution to this problem has been achieved through attachment of novel strong light-harvesting chromophores to the ligand architecture to enhance the absorption. Concurrently, if the ligand's triplet excited state energy is equal to or lower than the MLCT excited state energy, the triplet excited state lifetime can be prolonged by the ^{3}LC* excited state.

Wilson *et al.* have studied a series of ruthenium complexes **P-3**–**P-5** (Figure 1.4).[27, 28] These structures contain naphthalene, pyrene and anthracene as the respective functional group(s).

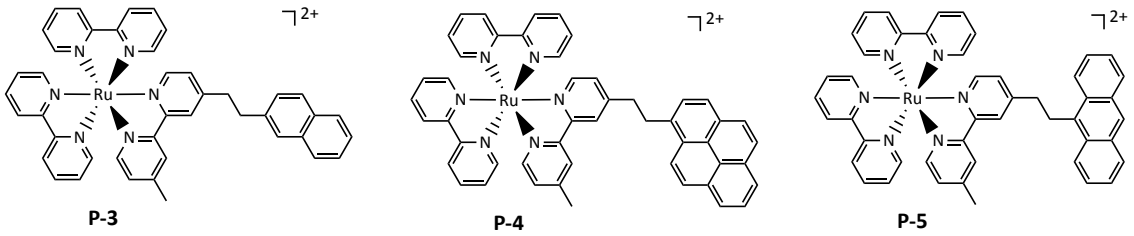

Figure 1.5 *Structures of ruthenium polyimine complexes* ***P-3*** *–* ***P-5****, with different tethered triplet acceptors (naphthalene, pyrene and anthracene).*[27, 28] *Due to different* ^{3}*LC*, they showed different triplet excited state properties.*

They found that the triplet excited state of **P-3** is ^{3}MLCT* in nature, and its emissive band lifetime is 0.81 μs. This is due to the triplet state of the naphthalene being higher than that of the MLCT state. The triplet excited state of **P-4** is of mixed character combining MLCT and pyrene LC. Its triplet energy is mainly localised on the pyrene moiety (85 %), and a ruthenium centred MLCT (15 %). The equilibrium between the LC and MLCT states contributes to a longer triplet excited state lifetime (5.23 μs). (Scheme 1.7 illustrates the relation between the emissive triplet excited state and their energy levels) The triplet excited state lifetime of **P-5** is up to 350 μs, which is much longer than that of **P-3** or **P-4**. This is due to the presence of a low-lying triplet state on the anthracene. As illustrated at the beginning of this section, in general, ^{3}LC* states have longer lifetimes than ^{3}MLCT* states. In **P-5**, the energy gap between the MLCT and LC states is quite big (1,900 cm^{-1}). Therefore, in this case, the pure ligand centred triplet character is generated.

It should be noted that the phosphorescence is quenched in this case and results in a non-luminescent process. This is due to its very efficient triplet-triplet quenching (anthracene moiety).

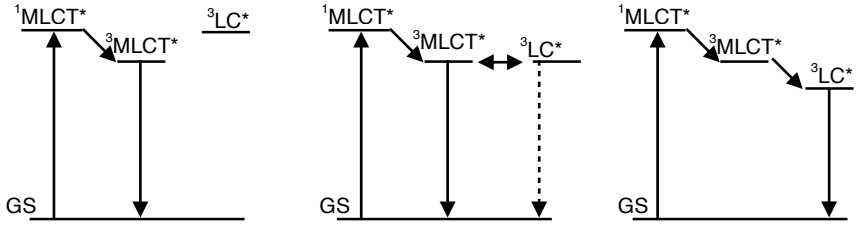

Scheme 1.7 *Simplified energy level diagram and the emission states.*

P-7 (Figure 1.5) displays more favourable photophysical properties than **P-4**.[29] The absorption is enhanced and the phosphorescence quantum yield (assigned as MLCT) is increased (Φ_P(**P-4**) = 4.4 %, Φ_P(**P-7**) = 7.1 %). Moreover, the triplet excited state lifetime is greatly extended to 148 μs. In the model complex **P-6**, where the ligand is 5-phenyl-1,10-phenanthroline, the lifetime under similar conditions is 1.15 μs. However, even though the triplet excited state MLCT/LC equilibrium is established, the emission spectrum shows that the lowest triplet excited state is still ^{3}MLCT* at room temperature.

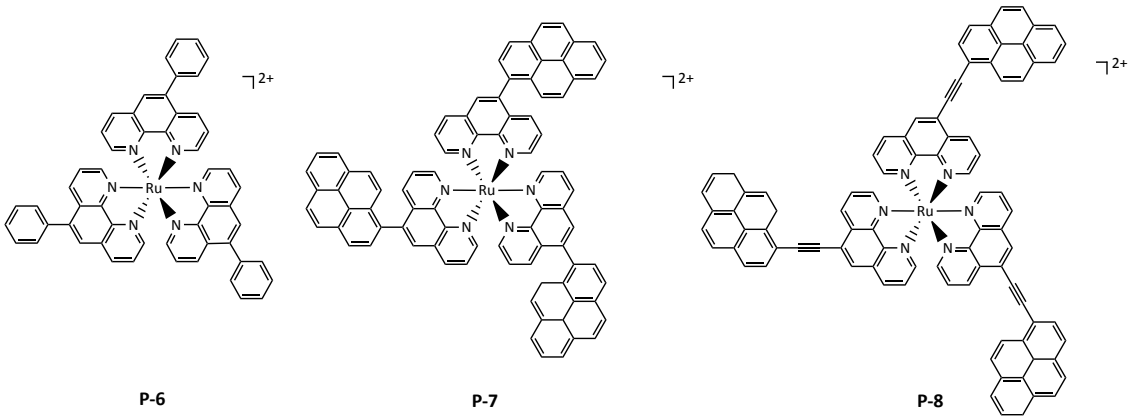

P-6 **P-7** **P-8**

Figure 1.6 *Structures of ruthenium polyimine complexes,* ***P-6***, ***P-7***[29], ***P-8***[30]*. This series of complexes show the effect of multi-chromophore and acetylene linker on the triplet excited state.*

Zhao *et al.* studied a series of ruthenium complexes **P-9**–**P-11** (Figure 1.6).[31] For **P-10**, the ^{3}MLCT emission band was observed with a lifetime of 9.22 μs due to the MLCT/LC equilibrium. For **P-11**, the ^{3}LC emission band was observed with a lifetime of 58.4 μs. The enlarged π-conjugation framework of **P-11** contributed to the ligand centred triplet excited state which is lower than its corresponding ^{3}MLCT* state. At the same time, the

absorption of **P-11** (ε 38,800 M^{-1} cm^{-1}) is also enhanced when compared to **P-10** (ε 14,100 M^{-1} cm^{-1}). This indicates that an ethynyl linker is more efficient than a C-C single bond connection.[32] In 2013, **P-8** was reported as having the longest lifetime of a Ru(II)-based dyad.[30] Its ^{3}LC* emission lifetime was determined as 270 μs.

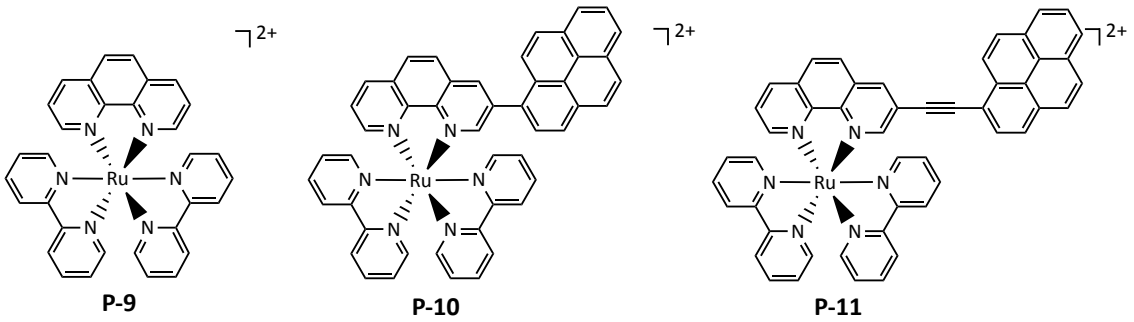

Figure 1.7 *Structures of ruthenium polyimine complexes* ***P-9*****–*****P-11***[31].

However, even though the triplet lifetime can be prolonged in this way, the absorption in the visible region is still weak. To enhance the absorption, strong light-harvesting chromophores can be linked to the Ru(II) polypyridine subunit. Boron-dipyrromethene (BODIPY) is a class of fluorescent dyes with strong absorption in the visible region. In 2005, Ziessel *et al.* reported two novel multichromophoric compounds, **P-12** and **P-13** (Figure 1.7).[33] They display intense absorption in the visible region in acetonitrile ($\varepsilon_{\mathbf{P\text{-}12}}$ 66,100 M^{-1} cm^{-1}; $\varepsilon_{\mathbf{P\text{-}13}}$ 89,600 M^{-1} cm^{-1}). The lowest triplet excited state is localised on the BODIPY unit. At 77 K, the phosphorescence of BODIPY was observed for the first time. However, at room temperature, only the intense fluorescence of the BODIPY unit was observed. This indicates that the absorption of the BODIPY moiety cannot be efficiently utilised to generate triplet excited states in these compounds. Moreover, the non-emissive triplet excited state lifetimes are short (8 μs and 30 μs, respectively).

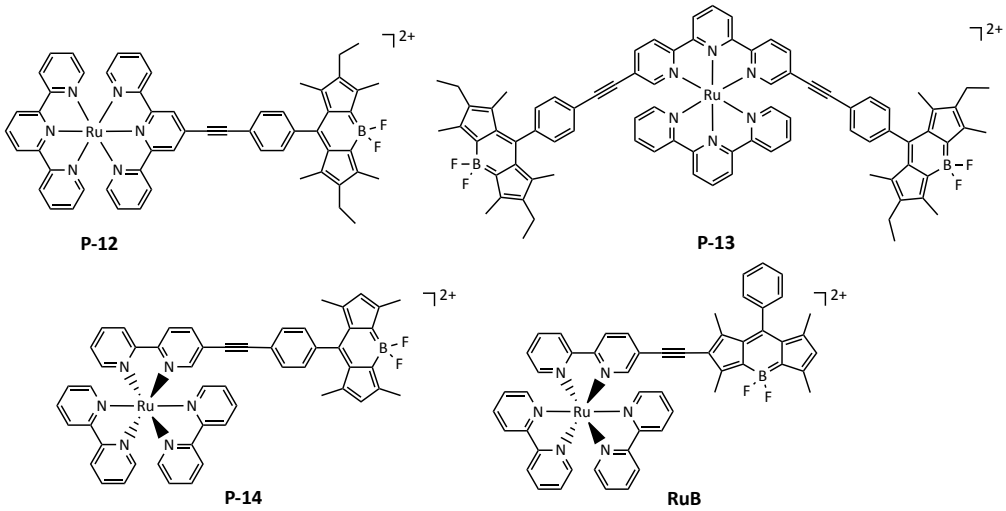

Figure 1.8 *Structures of ruthenium polypyridine complexes* ***P-12–P-14*** *and* ***RuB****.* [33, 34] *This series of complexes shows the effect of different link positions between BODIPY and polypyridine complexes on triplet excited states.*

Zhao *et al.* further published compounds **P-14** and **RuB** (Figure 1.7).[34] Both show strong absorption in the visible region (λ_{abs} 499 nm, ε 76,700 M^{-1} cm^{-1}; λ_{abs} 528 nm, ε 65,200 M^{-1} cm^{-1}). For **RuB**, the fluorescence of BODIPY was quenched, and the complex demonstrates the phosphorescence of BODIPY at room temperature. On the other hand, **P-14** shows some residual fluorescence of the BODIPY subunit, and no phosphorescence. The triplet excited lifetime from ^{3}BODIPY* is prolonged to 279.7 μs in **RuB**. **RuB** also shows a high singlet oxygen quantum yield of 0.93, whereas it is only 0.64 in **P-14**. The TTA-UC experiments were carried out with pyrene as triplet acceptor, and the quantum yield was determined as Φ_{UC}(**RuB**) = 1.2 %; Φ_{UC}(**P-14**) = 0.7 %. This indicates that the π-conjugated structure of the BODIPY core, and the coordination centre combine to produce more efficient visible light absorption than those without the π-conjugated link.

1.2.1.2 Cyclometalated Iridium Complexes as Triplet Photosensitisers

2-phenylpyridine (ppy) is a cyclometalating ligand with the ability to generate a strong field strength in coordinated metal complexes of Ir(III). Anionic ligands (chloride, cyclometalating ligand) make the emitting excited states have MLCT character and there is sufficient charge compensation for the metal-centred oxidation to proceed, whereas neutral ligands donate less charge density to the metal and only ligand centred emission can be observed.[35] At the same time, the reduction potentials in Scheme 1.8 demonstrate

that $Ir(ppy)_3$ is a better photoreductant than $[Ir(bpy)_3]^{3+}$. Furthermore, $[Ir(bpy)_3]^{3+}$ is proven to be more difficult to synthesise in the earlier studies.[25]

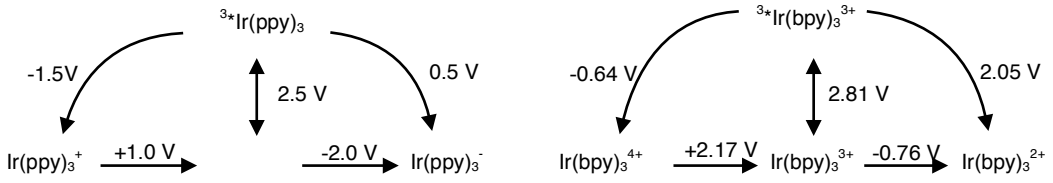

Scheme 1.8 *Reduction potentials (vs. SHE) of ground and excited states of fac-$Ir(ppy)_3$ and $[Ir(bpy)_3]^{3+}$.*[35]

In 2006, Castellano *et al.* reported $Ir(ppy)_3$ **P-15** as a triplet photosensitiser, with pyrene as the triplet acceptor for TTA upconversion (Figure 1.8).[36] Upon excitation at λ 450 nm, pyrene excimers were produced following the triplet energy quenching and TTA process. Interestingly, the total system gives a white emission centred at λ 470 nm due to the pyrene excimers. In the control experiment, to circumvent the energy-wasting excimer production, ***tert*-Butylpyrene** was used as the triplet emitter. The upconverted blue fluorescence at λ 400 nm (assigned to pyrene) was generated. Of note here however, is the fact that the UV-vis absorption of **P-15** is moderate in the visible region, and mainly located in the UV and blue region.

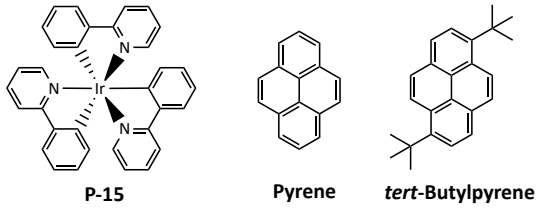

Figure 1.9 *Structures of **P-15**, Pyrene, tert-Butylpyrene.* [36]

For $[Ir(ppy)_2(bpy)]^{+1}$, there are three possible isomers (Figure 1.9). However, the cyclometalating carbons of the $[(C^N)_2Ir(N^N)]^+$ centre occupy mutually *cis* positions, which are in turn *trans* to the nitrogen atoms of the N^N coordinating ligand configuration ***a***. Therefore, isomers **b** and **c** are typically not generated during the coordination reaction of $(Ir(C^N)_2)_2Cl_2$, and the bipyridine based ligand. This results in a more facile synthesis, and enhances the reaction yield of the single isomer.

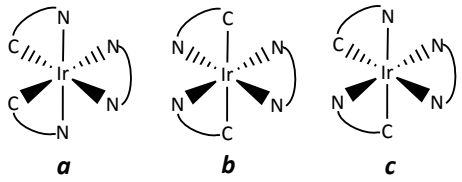

Figure 1.10 *Geometrical isomers:* ***a, b, c*** *of* $[Ir(ppy)_2(bpy)]^+$.

In 2001, Thompson *et al.* found that a combination of 2,4-diphenyloxazole and coumarin 6 as the cyclometalating ligand, in comparison with **P-16** and **P-17**, had interesting photophysical properties.[37] Two intense absorption bands were observed in **P-17** at λ 444 nm and 482 nm. Compared to the traditional iridium photosensitiser, $[Ir(ppy)(bpy)]^+$, the absorption was enhanced and bathochromically shifted. This is due to the strong light-harvesting effect of the coumarin 6 ligand. The luminescence quantum yield of **P-17** was determined as 0.6, and its lifetime was recorded as 14 μs. The quantum yield efficiency and lifetime for **P-16** were found to be only 0.3 and 3 μs respectively, whereas the triplet excited state lifetime of $[Ir(ppy)(bpy)]^+$ is only 0.35 μs. Subsequently, Thompson and co-workers coordinated coumarin 6 to a platinum metal centre, **P-18**.[38] This gives a triplet emission band at λ = 590 nm, with a lifetime of 28 μs. Unfortunately, no further detailed application as triplet photosensitisers was included in their work.

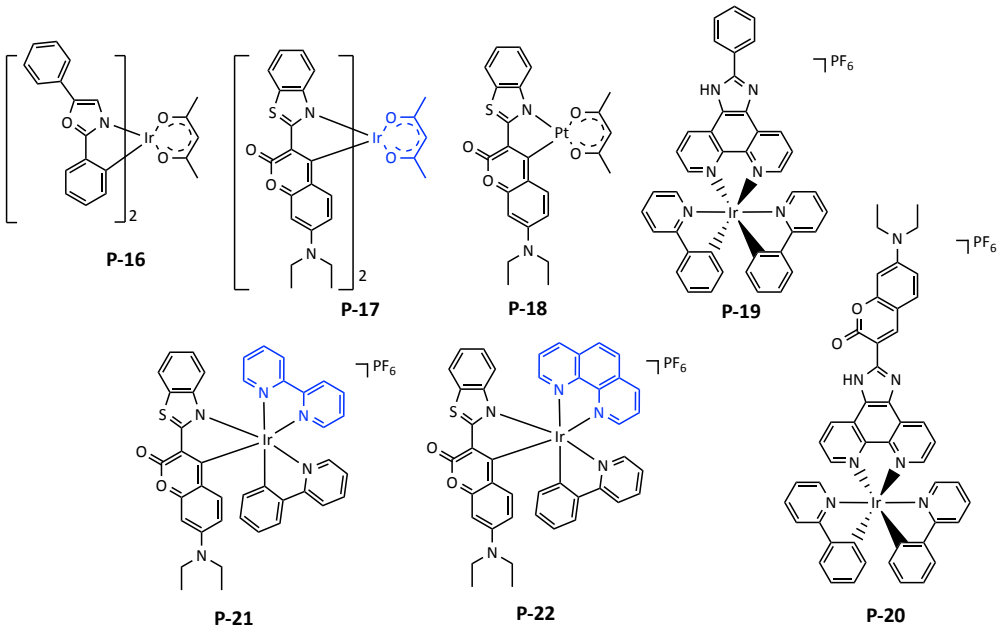

Figure 1.11 *Structures of cyclometalated iridium complexes with coumarin derivatives as light-harvesting chromophores,* ***P-16–P-22****.* [37, 38-40]

In 2012, **P-21** and **P-22** were prepared by Murata *et al.* (Figure 1.10).[39] Both show a stronger absorption (λ_{abs} 483 nm, ε 129,000 M^{-1} cm^{-1}; λ_{abs} 485 nm, ε 126,000 M^{-1} cm^{-1}, respectively) in the visible region than $[Ir(C6)(ppy)(acac)]^{-}(PF_6)^{+}$, the electroneutral complex with acetylacetonate (λ_{abs} 480 nm, ε 90,000 M^{-1} cm^{-1}). However, these complexes were only applied to hydrogen generation. Coumarin is not limited to acting as a cyclometalating ligand, but also can be modified *via* grafting to 1,10-phenanthroline. In 2011, Zhao *et al.* modified 1,10-phenanthroline with a coumarin moiety extending from its 5- and 6-positions. It was further coordinated to an Ir(III) centre from the precursor, the $(Ir(ppy)_2)_2Cl_2$ dimer, to give complexes **P-20** (Figure 1.10). Compared to the model complex **P-19** (λ_{abs} 466 nm, ε 1,353 M^{-1} cm^{-1}), **P-20** gives intense absorption at λ 466 nm (ε 70,920 M^{-1} cm^{-1}).[40] The triplet excited state lifetime was measured as 75.5 μs. Interestingly, even though the phosphorescence emission of **P-20** (Φ_P = 0.6 %) is much weaker than that of **P-19** (Φ_P = 55.6 %), the TTA-UC quantum yield is much higher (Φ_{UC} = 21.3 % for **P-20**). TTA-UC is not applicable for **P-19** with an external laser light source at λ 445 nm due to its poor absorption at the excited wavelength. A further example of a Ru(II) polyimine-coumarin dyad complex (a similar structure to **P-20**) shows a phosphorescence quantum yield of 0.2 %, and shows efficient TTA-UC with DPA.[41] This illustrated that the triplet excited state is localised on the coumarin moiety (LC), which is a non-emissive ^{3}IL* state.

1.2.2 Pt(II) and Pd(II) Complexes

Platinum and palladium porphyrin complexes are commonly used in luminescent oxygen sensing and photodynamic therapy applications. In contrast to Ru(II) and Ir(III) model polyimine complexes, they display intense absorption in the visible region, and have relatively long triplet excited lifetimes.

As previously mentioned (Section 1.1), Baluschev *et al.* reported **P-23** (Figure 1.11) as a triplet photosensitiser, with DPA as an acceptor, utilising solar light as the external light source in 2006.[15] Although the TTA-UC quantum yield is low (1 %), it confirms that non-coherent solar light can be used to excite the TTA-UC process. One year later, Castellano *et al.* applied the same system to solid polymer films.[42] This evidence is quite compelling that sequential triplet excited-state bimolecular processes are operative under ambient, air-saturated conditions.

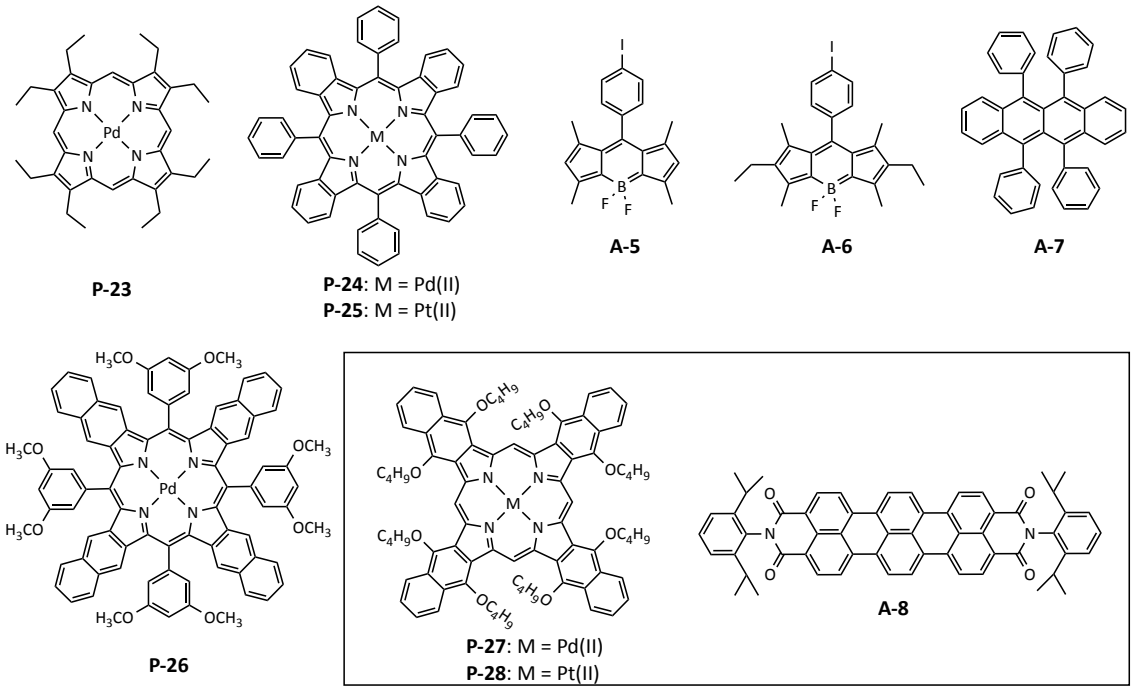

Figure 1.12 *Structures of Pt(II)/Pd(II) porphyrin complexes* ***P-23–P-27*** *and triplet energy acceptors* ***A-5–A-7****.* [15, 43-46]

To broaden the visible light absorption, simultaneous use of **P-24** and **P-26** (Figure 1.11) with rubrene (**A-7**) as the acceptor for TTA-UC was studied.[43] This system demonstrated absorption at λ 630 nm and λ 700 nm. These bands were assigned to the Q band absorption of **P-24** and **P-26** respectively. The yellow upconverted fluorescence of rubrene was stronger after excitation by the combined light source (λ_{ex} 635 nm and 695 nm) than with any single one. To allow more choice of acceptor, the Pt(II) porphyrin complex **P-25** was reported with two different novel BODIPY-based acceptors (**A-5**, **A-6**) by Castellano in 2008.[44] On excitation at λ 635 nm, the mixture of **P-25** and **A-5** produces stable green upconverted fluorescence in benzene (Φ_{UC} = 3.1 %). At the same time, the mixture of **P-25** and **A-6** produces stable yellow upconverted fluorescence (Φ_{UC} = 7.5 %). In a further study, **P-25** was found to show strong absorption at λ 430 nm (Soret band) and at λ 611 nm (Q-band).[45] The complex phosphoresces at λ 700 nm, with a lifetime of 41.5 μs. Perylene was used as the acceptor for TTA-UC to achieve a red-to-blue light conversion process. The anti-Stokes shift is up to 0.8 eV, which is much higher than that of the earlier studies. However, the upconversion quantum yield was low and determined as Φ_{UC} = 0.6 %. In 2005, Nobuo *et al.* reported a near infrared photon upconversion system.[46] TDI (**A-8**) was used as the triplet acceptor for the first time. Upon

excitation at λ_{ex} 856 nm, the mixture of TDI and **P-27**/**P-28** generated an upconverted luminescence of TDI at λ 690 nm. This is a considerable breakthrough in near-infrared region upconversion. Nevertheless, the upconversion quantum yields of both are very low, 0.067 % for **P-27** and 0.0089 % for **P-28**.

Although Pt(II) and Pd(II) porphyrin complexes have been successfully used for TTA-UC, the absorption and emission profiles of these structures is difficult to modify chemically. For this reason, use of a family of Pt(II) acetylide complexes offers more readily tuneable photophysical properties.[9] For example, the prominent photophysical properties can be easily changed *via* a change in the structure of the acetylide ligand.

In 2010, Eisenberg and Du used a Pt(II) terpyridine acetylide complex (**P-29**) to sensitise upconverted blue fluorescence from DPA (**A-2**) (Figure 1.12).[47]

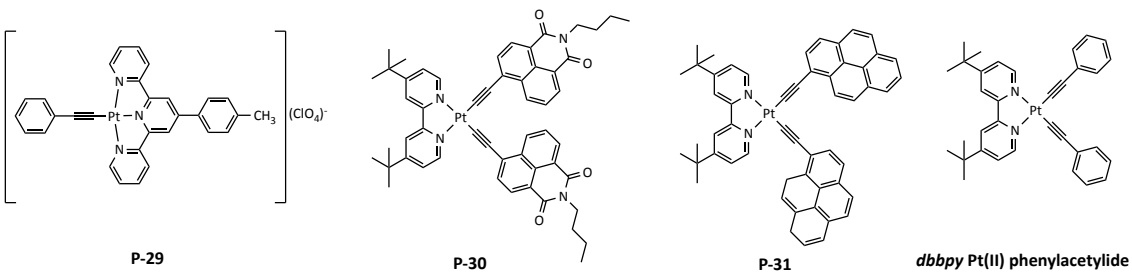

Figure 1.13 *Structures of Pt(II) acetylide complexes* ***P-29–P-31*** *and dbbpy Pt(II) phenylacetylide is presented here for comparison.* [47-50]

This was the first time that the ^{3}MLCT excited state had been used to promote photon upconversion. However, due to the weak absorption at λ 400-500 nm and the short lifetime of the triplet excited state (4.8 μs), its TTA-UC quantum yield was relatively low at 1.1 %. Zhao *et al.* later reported a novel naphthalimide (NI) acetylide-containing Pt(II) complex (**P-30**) (Figure 1.12),[48] as a comparison to the known complex, **P-31**.[49, 50] Both show an intense absorption when compared to the model complex ***dbbpy*** **Pt(II) phenylacetylide**.[50] **P-31** shows a long triplet excited lifetime of 73.7 μs, based on ^{3}IL. Similarly, **P-30** phosphoresces from a ^{3}IL excited state, and shows a prolonged triplet excited lifetime of 118 μs. Significantly high TTA-UC quantum yields were obtained (Φ_{UC}(**P-31**) = 28.8 %; Φ_{UC}(**P-30**) = 39.9 %). Based on this work, Zhao reported numbers of N^N Pt(II) acetylide complexes with different light-harvesting chromophores, such as coumarin, BODIPY, naphthalenediimide (NDI) *etc.*[51-53]

1.2.3 Organic Heavy Atom-based Photosensitisers

In addition to transition metals, bromine and iodine can also be used to tap into or access the heavy atom effect. Organic chromophores substituted with bromine and iodine can therefore be used as triplet photosensitisers. **P-32** was reported by Sun *et al.* as a triplet photosensitiser for TTA-UC in 2009 (Figure 1.13).[54] In the experiment, DPA was used as the triplet acceptor. Due to the upconverted blue fluorescence from DPA (Φ_{UC} = 0.6 %), and the residual green fluorescence (Φ_F = 13 %) from **P-32**, a white emission from the mixture was observed. The long triplet excited lifetime of **P-32** was 25 μs.

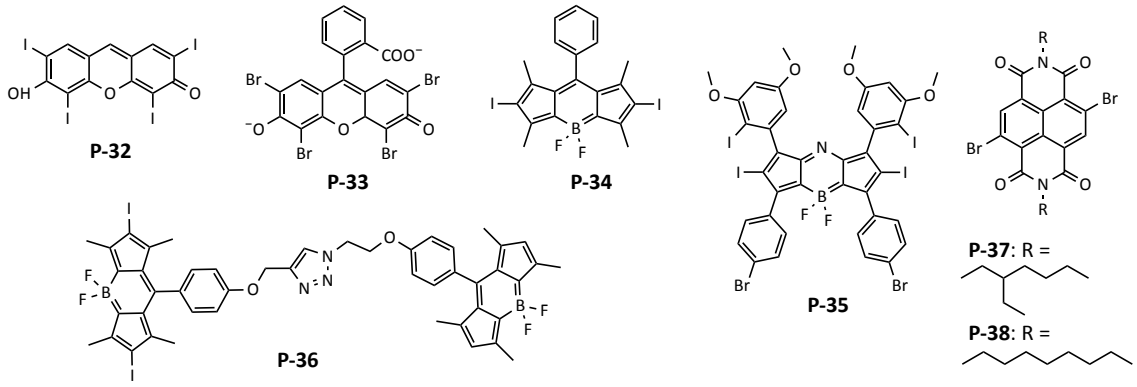

Figure 1.14 *Structures of non-metal organic heavy atom based photosensitisers* ***P-32–P-38****.* [54-59]

Eosin Blue has been explored for a long time, and is mainly used for staining proteins in biochemical applications. Recently, the brominated Eosin Blue, **P-33**, was reported as a triplet photosensitiser for photocatalytic aerobic cross-dehydrogenative coupling reactions.[55] BODIPY is also a strong light-harvesting chromophore, and its iodinated derivatives have been reported. **P-34** shows strong absorption in the visible region (λ_{abs} 529 nm, ε 89,000 M^{-1} cm^{-1}), and a long triplet lifetime with 57 μs. Upon excitation at λ 532 nm, the Φ_{UC} is 5.7 % with perylene as the acceptor.[56] Aza-BODIPY shows a longer absorption wavelength than the model BODIPY system (**P-34**). **P-35** shows near infrared absorption at λ 666 nm with ε 69,900 M^{-1} cm^{-1} (Figure 1.13).[57] Its singlet oxygen generation quantum yield has been determined as 70 %. However, its triplet excited lifetime is only 1.6 μs. To enhance the light-harvesting ability of BODIPY derivatives, Zhao *et al.* reported **P-36** containing intramolecular RET pheromone.[58] The absorption shows two main bands which are from the model BODIPY and iodo-BODIPY respectively. In the experiment, two triplet excited states were observed to exist at the

same time, which have been assigned to the model BODIPY and iodo-BODIPY respectively. In conclusion, a forward singlet energy transfer from the model BODIPY energy donor to the iodo-BODIPY (energy acceptor), followed by ISC of the iodo-BODIPY moiety, and a backward triplet energy transfer to the model BODIPY system occurs. Due to this process, the triplet excited lifetime is prolonged to 286 μs. The Φ_{UC} is 8.1 % with perylene as the acceptor. Other brominated or iodinated organic chromophores have also been studied for triplet photosensitisers, such as NDI (**P-37**, **38**) (Figure 1.13).[59]

1.2.4 Heavy Atom Free Photosensitisers

In organic molecules, some "mixing" of singlet and triplet states takes place as a result of a small amount of spin-orbit interaction. Based on the selection rules, El-Sayled *et al.* has suggested the rules for spin-forbidden intermolecular energy transfer. [18] He suggested that the energy could transfer from $^{1 \text{ or } 3}(n, \pi^*) \rightarrow {}^{3 \text{ or } 1}(\pi, \pi^*)$, instead of $^{1 \text{ or } 3}(n, \pi^*) \rightarrow {}^{3 \text{ or } 1}(n, \pi^*)$ or $^{1 \text{ or } 3}(\pi, \pi^*) \rightarrow {}^{3 \text{ or } 1}(\pi, \pi^*)$. Since the transition from the $^1(\pi, \pi^*)$ state to the ground state is fully allowed, and from the $^1(n, \pi^*)$ state is somewhat forbidden, in general, it follows that the $^3(n, \pi^*) \rightarrow S_0$ transition is more favourable than the $^3(\pi, \pi^*) \rightarrow S_0$ transition. Thus, the relative probability of triplet-singlet transitions from (n, π^*) or (π, π^*) states is the opposite of that observed for singlet-singlet transitions. On the other hand, due to the transition from $^1(n, \pi^*)$ being somewhat forbidden, and the energy gap from it often being small when compared to the gap from $^1(\pi, \pi^*)$, the transition $^1(n, \pi^*) \rightarrow {}^3(\pi, \pi^*)$ could have a higher probability of occurring. Therefore, the compound with $^1(n, \pi^*)$ as the singlet excited state is more likely to produce a triplet excited state.

However, considering the absorption ability in the visible region, an organic aromatic compound is preferable (show intensity absorption when compared to metal-based compound). Unfortunately, most of organic aromatic compounds' low lying transitions are $^1(\pi, \pi^*)$ in origin. Such molecules are rarely used as triplet photosensitisers due to their weak ISC. In some special cases, including carbonyl-containing compounds, phosphorescence may be strong, with weak fluorescence or non-emissive due to efficient ISC. Both S_1 and T_1 are assigned to (n, π^*), and T_1 may be populated by $^3(\pi, \pi^*)$ (Scheme 1.9). Above all, the design of pure organic triplet photosensitisers with strong absorption in the visible region is a difficult endeavour.

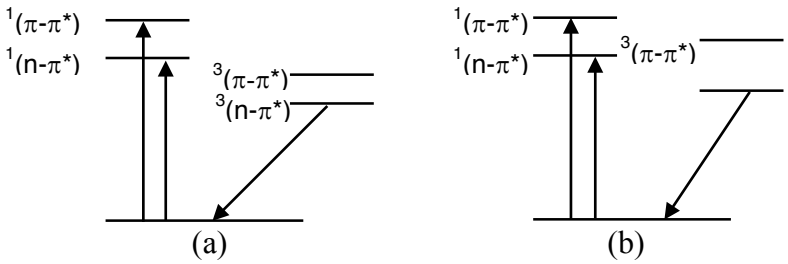

Scheme 1.9 *The possible arrangement of singlet and triplet excited states in carbonyl compounds.*[18]

Castellano *et al.* has published 2,3-butanedione (**P-39**) as a triplet photosensitiser, with 2,5-diphenyloxazole (**A-9**) as the triplet acceptor in a TTA upconversion system (Figure 1.14.[60] The mixture was selectively excited at λ 442 nm, and the upconverted emission was centred at λ 360 nm. The anti-Stokes shift was determined as 0.64 eV. Ketocoumarin derivatives have efficient ISC ($S_1 \rightarrow T_1$), some of which approach unity. They have been used as triplet photosensitisers for photocatalytic reactions.[61] **P-40** has been reported to be a triplet photosensitiser for TTA-UC.[62] The triplet excited lifetime was determined as 30.4 μs. Upon excitation at λ 445 nm, the upconverted luminescence of DPA was generated with Φ_{UC} = 11.3 %.

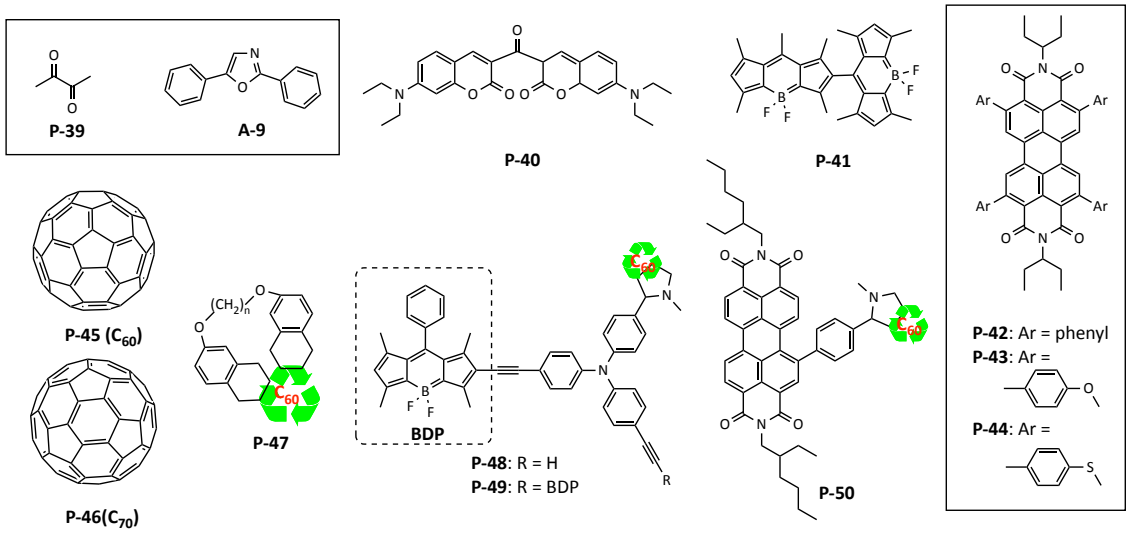

Figure 1.15 *Structures of heavy atom free triplet photosensitisers* ***P-39–P-50*** *and* ***A-9****.* [60, 62, 63, 64-69]

In 2011, due to its ISC ability, a BODIPY dimer was reported to generate singlet oxygen for potential application in PDT (Φ_Δ = 51 %).[63] This work was based on the theory that among multiple excited configurations, doubly substituted systems are particularly important in enhancing S_1–T_1 coupling as shown by the seminal work of Salem and

Rowland.[70] Later, a similar novel dimer, **P-41** was synthesised for TTA-UC applications (Figure 1.14).[64] It shows a strong absorption in the visible region with ε 136,000 M^{-1} cm^{-1}(λ_{abs} 506 nm). The triplet excited lifetime was determined as 115.4 μs, with perylene as the triplet acceptor upon the excitation at λ = 532 nm, and the TTA-UC quantum yield was calculated as 3.7 %.

In 2016, Fu *et al.* developed a heavy atom free strategy to promote ISC ($S_1 \rightarrow T_1$) in perylenediimides (PDIs) by introducing electron-donating aryl groups.[65] The ISC efficiency is increased from 8 % (**P-42**) to 54 % (**P-43**), and then to 86 % (**P-44**) with the increasing electron-donating ability of the substituted aryl groups (Figure 1.14). The triplet excited state lifetimes are 30.6 μs, 59.7 μs and 61.4 μs, respectively. These were used for singlet oxygen generation. Values of Φ_Δ = 0.05, 0.50, and 0.80 were obtained for **P-42**, **P-43** and **P-44**, respectively. Currently, no exploration towards TTA-UC applications has been made.

As explained in the earlier section, purely organic triplet photosensitisers are difficult to design with predictable triplet characters. One solution to this problem is to attach a spin-transfer centre to the organic chromophores. C_{60} (**P-45**) has near unity ISC efficiency due to its highly-curved surface.[66] Therefore, C_{60} derivatives have been used as triplet photosensitisers. In 1999, a series of fullereneo-quinodimethane bisadducts (**P-47**) were synthesised and tested for singlet oxygen production.[67] In 2012, Zhao *et al.* reported C_{60}-boron dipyrromethene dyads (**P-48**,**49**)[68], C_{60}-naphthalenediimide dyads[71], and C_{60}-perylenebisimide dyad (**P-50**)[72] (Figure 1.14). The attached chromophore enhances the absorption of C_{60} in the visible region, which is then followed by the enhancement of the photosensitisation ability. However, for TTA-UC applications, perylene was used as the acceptor. The Φ_{UC} is still low, such as Φ_{UC}(**P-48**/perylene) = 0.36 %. In 2013, P. Steer *et al.* reported fullerene C_{60} as an absorber-sensitiser system, with anthanthrene (An) as emitter in the system.[73] In comparison with the C_{60}/perylene pair, C_{60}/An shows a higher TTET rate due to the An's lower triplet energy.

Compared with C_{60}, C_{70} (**P-46**) shows better properties for TTA-UC. Kim *et al.* reported C_{70} as a triplet photosensitiser for TTA-UC in 2013.[69] C_{70} has a stronger absorption at λ 480 nm. This is due to relaxation in the symmetry from a I_h to D_{5h} point group symmetries in C_{70}. The low energy transitions that are symmetry-forbidden in C_{60}, resulting in its weak visible light absorption, are allowed in C_{70}, yet ISC quantum yields remain near

unity. In their study, the Φ_{UC} achieved was 8 % for green-to-blue UC (C_{70}/perylene), and 0.8 % for red-to-green UC (C_{70}/9,10-bis(phenylethynyl)anthracene).

In 2017, Hariharan *et al.* found that the highly core-twisted aromatic structure facilitates the ISC process in a molecule.[74] In traditional work, planar nanostructures of carbon display a low singlet–triplet energy gap and weak SOC diminishing their ISC in graphene.[75] However, Hariharan's work reported the first systematic investigation on "twist-only" induced intersystem crossing in imide functionalised core-twisted aromatics (Figure 1.15). This result provides a new route in the design of heavy atom free organic triplet photosensitisers.

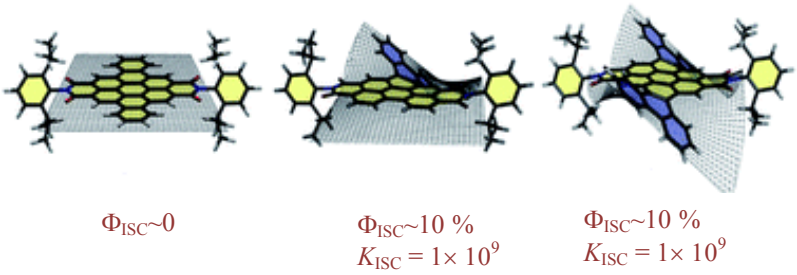

Figure 1.16 *The imide functionalised core-twisted aromatics.*[74]

1.3 Other Applications of Triplet Photosensitisers

1.3.1 Photodynamic Therapy

Photodynamic therapy (PDT) is a form of phototherapy using non-toxic light-sensitive compounds that when exposed to excitation from light, become toxic or generate other toxic compounds that target diseased cells. PDT was first mentioned by Tappeiner in 1903, and he used topical eosin and sunlight to treat skin tumours.[76] The field has developed slowly during the last century.

In photodynamic therapy processes with triplet photosensitisers, there are two competing pathways; type-I and type-II (Scheme 1.10). For type I, the electron or photon transfers from the photosensitiser (PS) to cellular organic substrates (lipids, proteins, nucleic acids, *etc.*), yielding free radicals or radical ions that interact with molecular oxygen (O_2) to produce reactive oxygen species (ROS), such as hydrogen peroxide (H_2O_2), the superoxide anion ($O_2^{\cdot-}$), and the hydroxyl radical ($OH^{\cdot}$). In type-II, the key mechanism is the generation of singlet oxygen ($^1O_2^*$). Most molecular species exist in a singlet ground

state, with a common exception being O_2. The ground state of O_2 is a triplet state ($^3O_2$) and the lowest excited state is a singlet state ($^1O_2^*$). The singlet state oxygen ($^1O_2^*$) cannot be obtained directly from irradiative excitation from the photosensitisers. In type-II, the triplet photosensitisers are populated to the first singlet state through excitation, with its triplet excited state being populated *via* ISC. Later, TTET can occur between the triplet photosensitiser and triplet oxygen. Thus, an energy transfer occurs from the sensitiser to $^3O_2$, resulting in the subsequent and rapid generation of $^1O_2^*$. Both reactions can result in tumour cell death. In particular, the singlet oxygen generated *via* the type-II reaction is thought to be responsible for the cell death induced by PDT.[77]

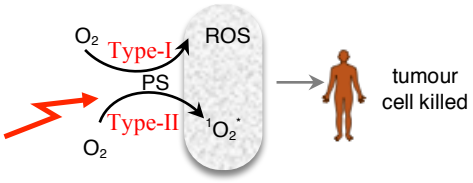

Scheme 1.10 *The simplified process of PDT.*

Until recently, the majority of photodynamic therapy reagents displayed absorption in the UV or visible region. However, this short wavelength light is harmful to human tissues, with only longer wavelengths actually capable of penetrating deeply into biological tissues. Therefore, reagents that exhibit a near-IR absorption have become widely investigated as suitable materials for medical applications. For example, BODIPY (boron-dipyrromethene) derivatives have proven to be excellent reagents due to their tuneable absorption. C_{60} is also a good organic chromophore with visible light harvesting ability, triplet state population, and low toxicity in most cases.[78] Moreover, good photosensitisers should also show low "dark toxicity" to normal cells, and high singlet oxygen generated quantum yields.

For clinical applications, targeting is also of significant importance for PDT photosensitisers.[79] The targeting strategy for drug delivery in PDT aims to increase the accumulation of the photosensitiser at the malignant tissue during the treatment. This is mainly driven by the tumour microenvironment, including pH, or tumour-associated enzymes.

1.3.2 Luminescence Bioimaging

Triplet photosensitisers have many potential applications due to their phosphorescent emission, which can be quenched by oxygen and used to generate TTA upconversion with a fluorescence acceptor. For example, triplet photosensitisers are used to be applied to monitor blood oxygenation during intensive care, and to analyse tissue oxygenation based on phosphorescent lifetimes.[80] Another activity for these systems in this area is ratiometric sensing. This has developed with dual emission organic complexes in recent years. They display both phosphorescence emission, and fluorescence emission. Phosphorescence is quenched by oxygen while fluorescence is not, and the change of colour of the emission indicates oxygenation. In most cases, ratiometric oxygen sensors are a combination of a fluorescent dye and a phosphorescent material. It remains a challenge however to design a dual emission compound with a mono-chromophore.[19]

1.3.3 Photoinduced Catalytic H_2 Production

As a more environmentally friendly energy source and energy storage method, hydrogen production has drawn a great deal of attention. Since the early 1970s, papers have emerged in which hydrogen is reduced *via* heterogeneous cycles under light irradiation.[81] Triplet photosensitisers play an important role in this area due to their long-lived excited states. For example, a novel iridium(III) complex has been reported for catalytic hydrogen generation from water (Scheme 1.11) in 2012.[82]

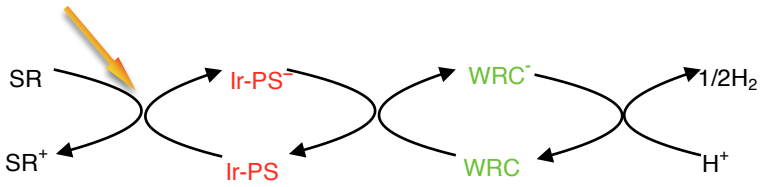

Scheme 1.11 *Typical processes in H_2 production with a triplet photosensitiser. SR- sacrificial reductant; PS- photosensitiser; WRC- water-reduction catalyst.* [82]

Firstly, the Ir-PS (Ir(phenylazole)$_2$(bpy)[PF_6]) is photoexcited (Ir-PS*) with a Xe light source (300 W), resulting in energy transfer along with electron transfer between Ir-PS* and a so-called sacrificial reductant (SR). During that process, Ir-PS* generates Ir-PS$^-$ *via* a reductive quenching mechanism, and SR is oxidised to SR$^+$. The electron of Ir-PS$^-$ can transfer onto a water-reduction catalyst (WRC, such as Pt, Rh, *etc*.), while the sensitiser is then regenerated in its ground state. Finally, WRC$^-$ transfers electrons to aqueous protons to generate molecular hydrogen. The key characteristics of triplet photosensitisers

are their long-lived excited states, and a decent visible-light harvesting ability. However, in this case, even though the triplet excited lifetime was prolonged, it was still less than 6 μs and thus progress still needs be made in this field.

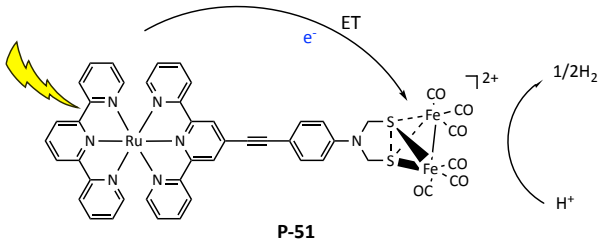

Scheme 1.12 *Structure of* ***P-51*** *and the process of photoinduced reduction of a proton.* [83]

Sun *et al.* reported a 2-aza-1,3-dithiol-bridged dinuclear iron complex covalently linked to a ruthenium terpyridine complex for the photoinduced reduction of protons (Scheme 1.12).[83] The acetylenic linker between the redox-active termini was selected not only to gain precise control over their spatial separation, but also to prolong the lifetime of the excited state. This facilitates the electron transfer from the ruthenium moiety to the iron centre. It was proved in later work that this intramolecular electron transfer is more efficient than the intermolecular electron transfer.[84]

1.3.4 TTA-UC Applied Water Splitting

As discussed at the beginning of this chapter, the utilisation of the TTA-UC process could enhance and broaden the absorption wavelength in DSSCs. A similar function could be applied with photoinitiated water splitting. In 2012, Castellano *et al.* reported an example of the employment of TTA-UC in water splitting (Scheme 1.13a).[85]

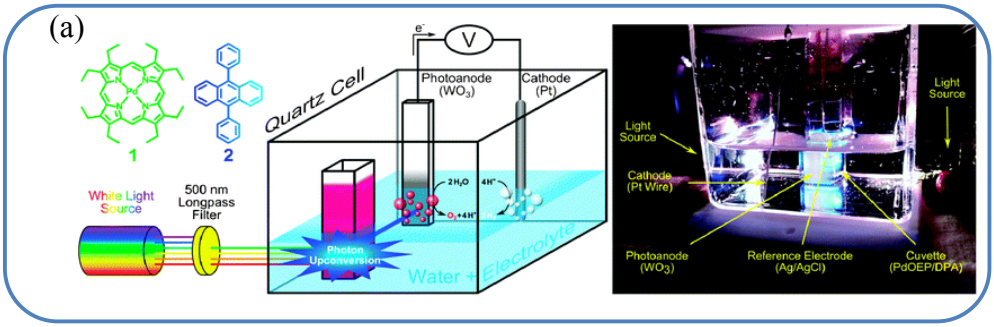

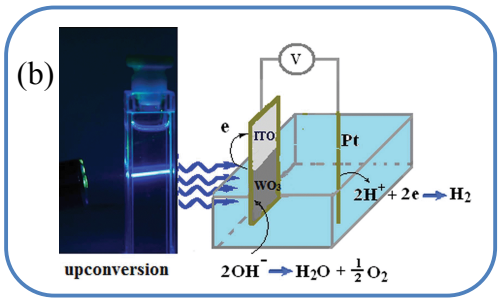

Scheme 1.13 *(a) Chemical structures of* ***PdOEP*** *(1) and* ***DPA*** *(2) along with a schematic representation of an upconversion-powered photoelectrochemical cell relying on stochastic collection of photons (left). Photograph of the upconversion-driven photoelectrochemical cell (right). (b) Photographs of the upconversion-driven photoelectrochemical cell biased to +0.33 V vs. Ag/AgCl.*

A sub-bandgap photoaction from a prototypically wide bandgap semiconductor in a photoelectrochemical cell was demonstrated for the first time using the concept of photon upconversion. The upconverted photons were stochastically collected at the WO_3 photoanode. Through this inclusion, the photon to current efficiency was improved. The system was sensitive to air due to the existence of triplet oxygen. In 2014, Wang *et al.* reported an alternative solvent for this process, through the use of an oil-in-water (o/w) microemulsion to reduce the effect of the oxygen.[86] They suggested that the upconverted o/w microemulsion provides a simple approach to obtain high TTA-UC efficiency without the requirement of degassing (Scheme 1.13b.) This upconverted o/w microemulsion can maintain a high efficiency (Φ_{UC} = 33.12 %), without degassing, for several days.

1.4 Aim of the Project

This project aims to synthesise heavy metal containing systems, such as polyamine Ru(II) and cyclometalated Ir(III) complexes with nearly unit ISC efficiency, that show strong absorption in the visible region, and possess long triplet excited state lifetimes for TTA upconversion applications towards future solar cells, and singlet oxygen generation for photodynamic therapy.

The molecular design of these systems is based on the attachment of light-absorbing organic antenna chromophores to a coordination centre *via* an acetylene linker. The π-conjugation is expected to facilitate ^{1}IL transfer to ^{3}IL directly, such that there is no need to make the ^{1}IL significantly higher than the ^{1}MLCT (to allow energy transfer from ligand

to metal). Furthermore, the ^{3}IL state will have a longer lifetime than the ^{3}MLCT state, which can be of values of several hundreds of microsecond. It was felt that these designs would help to contribute to the improvement of TTA upconversion efficiency over other reported systems. Two main series of complexes are studied in this work to achieve these targets. The first was use of dinuclear metal complexes with different rigid organic chromophore bridges; the second will be mononuclear and will incorporate multiple light-harvesting groups. (Figure 1.16)

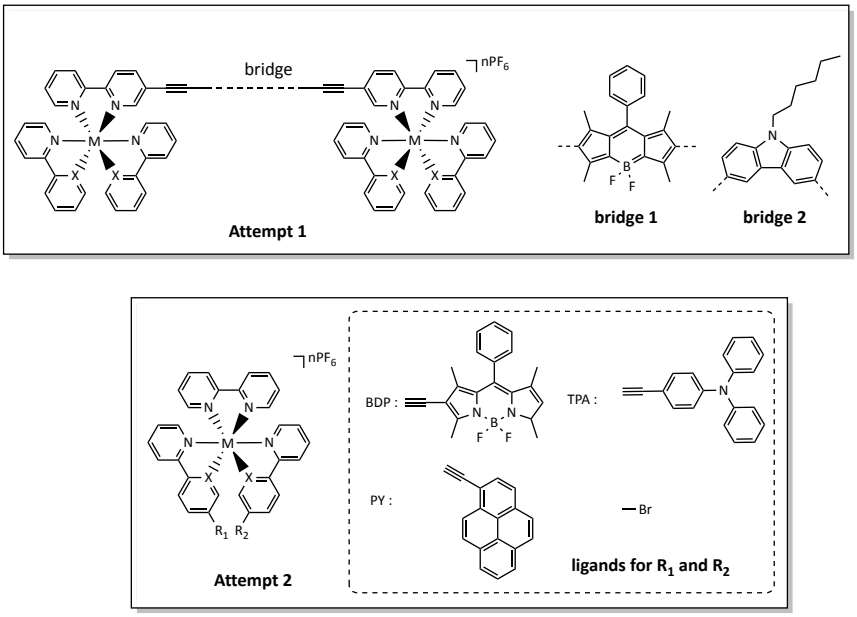

Figure 1.17 *Designed molecules.*

Combined with a detailed report of the synthesis of all the novel complexes, each compound will be fully characterised by nuclear magnetic resonance techniques (^{1}H NMR, ^{13}C NMR, ^{11}B NMR, ^{19}F NMR, 2D-NMR), and high resolution mass spectroscopy (MALDI, ESI). The measurement of their photophysical properties will be carried out *via* static and transient spectroscopy, luminescence at low temperature (77 K) measurements, and luminescent quantum yields. Further detailed methods will also be used in some cases. In addition, Time-Dependent Density Functional Theory (TD-DFT) calculations will be undertaken for the complexes to corroborate the location and nature of the studied excited states in the molecular systems. The TTA-UC quantum yields and singlet oxygen generation ability of most of the complexes will be measured, and used to comment on the molecules' suitability as a photosensitiser in potential applications. The evaluation of the properties of the generated complexes will allow for further improvements in the design of photosensitisers and their applications moving forward.

2 BODIPY Bridged Dinuclear Ruthenium(II) and Iridium(III) Complexes for Triplet Photosensitisation

2.1 Introduction

As discussed in the Chapter 1, to date, conventional PSs based on transition metal complexes have suffered from weak absorption in the visible region and short-lived triplet excited states. Zhao and his co-workers have succeeded in bathochromically shifting the wavelength of absorption without restricting the ligand-centred excited state energy levels. This was achieved by increasing the conjugation between the metal coordination site and ligand chromophore. Their complexes utilise an ethynyl linker to tether a mononuclear Ru(II) centre to a BODIPY or naphthalenediimide chromophore. In this approach, the steric bulk of the substituents can typically decrease the intersystem crossing (ISC) efficiency of the complex.[19] However, Ziessel and his co-workers illustrates significant increases in the triplet excited state lifetimes of their dinuclear metal complexes when compared to their mononuclear analogues.[87, 88] In this project, by incorporating a second metal centre into the compound design the effect on ISC efficiency of steric bulk ligands should be minimised.

This chapter describes the synthesis of two polyimine complexes with two homo-nuclear coordination centres tethered to a BODIPY chromophore *via* ethynyl linkers. It was hoped that by taking a modular design approach inspired by the earlier work of the contributors to the field, ISC could potentially be enhanced, the absorption profile of the complexes extended, and the triplet excited state lifetime of the materials could be lengthened. This would make these compounds eliglible for photosensitisation applications such as Triplet-Triplet Annihilation Upconversion (TTA UC) and Photodynamic therapy (PDT). Their mononuclear analogues are also presented here for comparison. The work of this study was published in "*Journal of Material C*", 2016, **4**, 6131-6139.[89]

2.2 Synthesis of BODIPY Bridged Ruthenium (II) and Iridium (III) Dinuclear Complexes

2.2.1 Synthesis of 2,6-diethynyl-1,3,5,7-tetramethyl-8-phenyl-4,4'-difluoroboradiazaindacene, B-3

Boron-dipyrromethene (BODIPY) was prepared by reacting a dimethylpyrrole precursor with boron trifluoride etherate in the presence of a tertiary amine, usually

trimethylamine.[90] Based on the synthesis of boron-dipyrromethane 1,3,5,7-tetramethyl-8-phenyl-4,4'-difluoroboradiazaindacene derivatives reported by Zhao *et al.*, the synthesis of **B-1** was developed from benzoyl chloride and 2,4-dimethylpyrrole. (Scheme 2.1) 2- and 6- positions were easily iodised in the presence of excess N-iodosuccinimide in dry methylene dichloride (CH_2Cl_2) at room temperature.[58] The acetylene was added to BODIPY moiety *via* a Sonogashira coupling reaction with trimethylsilylacetylene (TMSA). The silyl-protection group was removed at low temperature (–78 °C) in the presence of mild base tetra-n-butylammonium fluoride (TBAF) in tetrahydrofuran (THF) under an argon atmosphere.

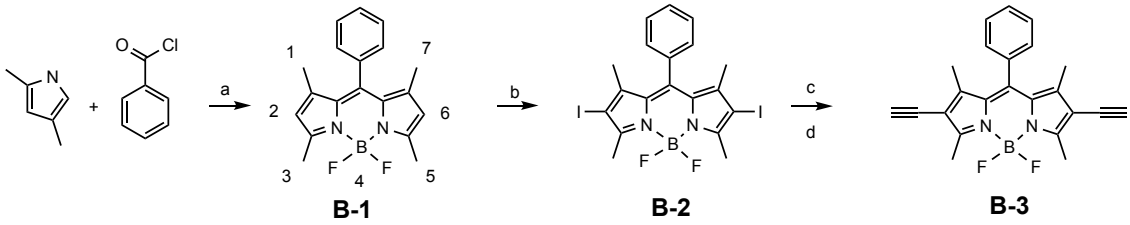

Scheme 2.1 *Synthesis of **B-3**. (a) Dry CH_2Cl_2, $(CH_3CH_2)_3N$, $BF_3{\cdot}O(CH_3CH_2)_2$, yield: 24.8 %. (b) N-Iodosuccinimide, CH_2Cl_2, RT, 1 h (in air), yield: 85.3 %. (c) TMSA, $(CH_3CH_2)_3N$, $Pd(PPh_3)_2Cl_2$, PPh_3, CuI, 8 h, 80 °C, yield: 77.5 % (d) THF, Bu_4NF, –78 °C, 1 h, yield: 91.4 %. All steps were carried out under argon except where indicated.*

2.2.2 Synthesis of 4-bromo-2,2'-bipyridine, L-1

L-1 was prepared in two steps by stannylation of 2-bromopyridine, followed by a tetrakis(triphenylphosphine)palladium(0) ($Pd(PPh_3)_4$) catalysed Stille coupling with 2,5-dibromopyridine according to the accepted literature procedure.[91] The synthetic route is given in Scheme 2.2.

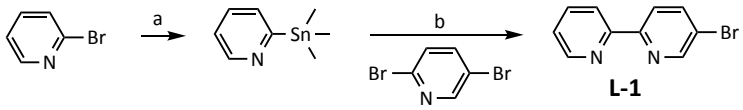

Scheme 2.2 *Synthesis of **L-1**. (a) n-BuLi, $(CH_3CH_2)_2O$, –78 °C, $(CH_3)_3SnCl$ 2.5 M in hexane, 53.5 %. (b) 2,5-dibromopyridine, $[Pd(PPh_3)_4]$, m-xylene, reflux, 35.7 %.*

2.2.3 Synthesis of BODIPY Bridged Dinuclear Ruthenium (II) Complex, RuBRu

Cis-$Ru(bpy)_2Cl_2$ was synthesised from commercially available Ruthenium(III) chloride and 2,2'-bipyridine. (Scheme 2.3) The mixture was refluxing in dimethyl sulfoxide

(DMSO) for 8 h. **Ru-1** was generated by a traditional coordination with refluxing *cis*-$Ru(bpy)_2Cl_2$ and **L1** in a mixture of methanol (CH_3OH) and water. The addition of a saturated solution of KPF_6 precipitated a crude sample of **Ru-1** from the cooled reaction mixture. The final compound **RuBRu** was synthesised *via* a Sonogashira cross-coupling reaction in a dry mixture solvent of diisopropylamine and acetonitrile (CH_3CN) under an argon atmosphere with an excess **Ru-1**. After the purification, the compound was treated with saturated solution of KPF_6 to precipitate the target complex.

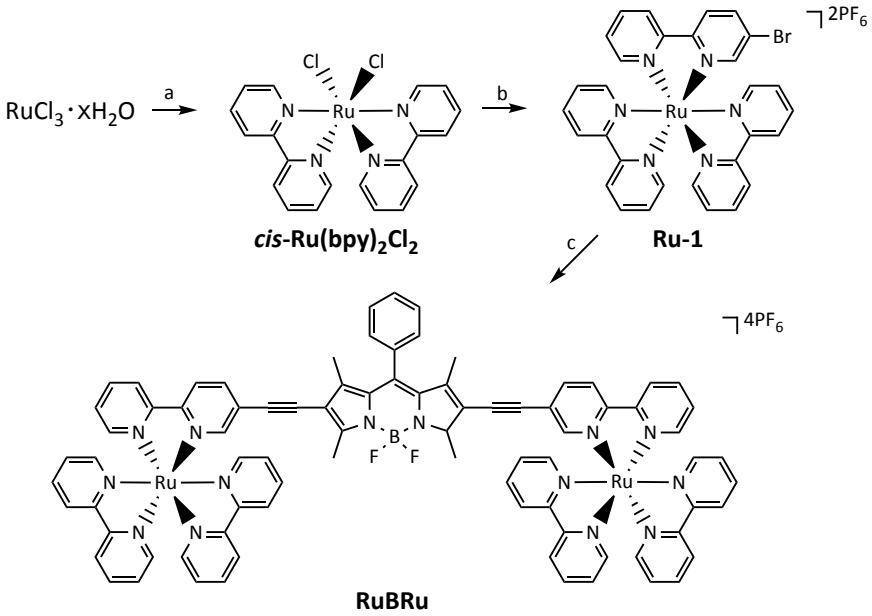

Scheme 2.3 *Synthesis of* ***RuBRu****. (a) 2,2'-bipyridine, LiCl, DMSO, reflux, 8 h. (b)* $CH_3OH:H_2O$ *(3:1, v/v), overnight, yield: 66.7 % (c)* $(i\text{-}Pr)_2NH:CH_3CN$ *:benzene (1:2:2, v/v/v),* $Pd(PPh_3)_2Cl_2$*,* PPh_3*, CuI, 8 h, 60 ℃, Ar, yield: 27.9 %.*

2.2.4 Synthesis of BODIPY Bridged Dinuclear Iridium(III) Complex, IrBIr

The commonly used Iridium(III) dichloro-bridged dimer, $[Ir(ppy)_2Cl]_2$, was prepared using the commercially available iridium trichloride hydrate and 2-phenylpyridine, according to the accepted literature procedure.[92] Refluxing this dimer in a mixture solution of methanol and dichloromethane with **L1** gave the compound **Ir-1**. The final compound **IrBIr** was synthesised *via* the similar Sonogashira cross-coupling reaction of **RuBRu**. (Scheme 2.4) After the purification, the compound was also treated with a saturated solution of KPF_6 to give the target product. It was observed that, the purification of the dinuclear complexes was difficult and this explained the low yield of the final complexes.

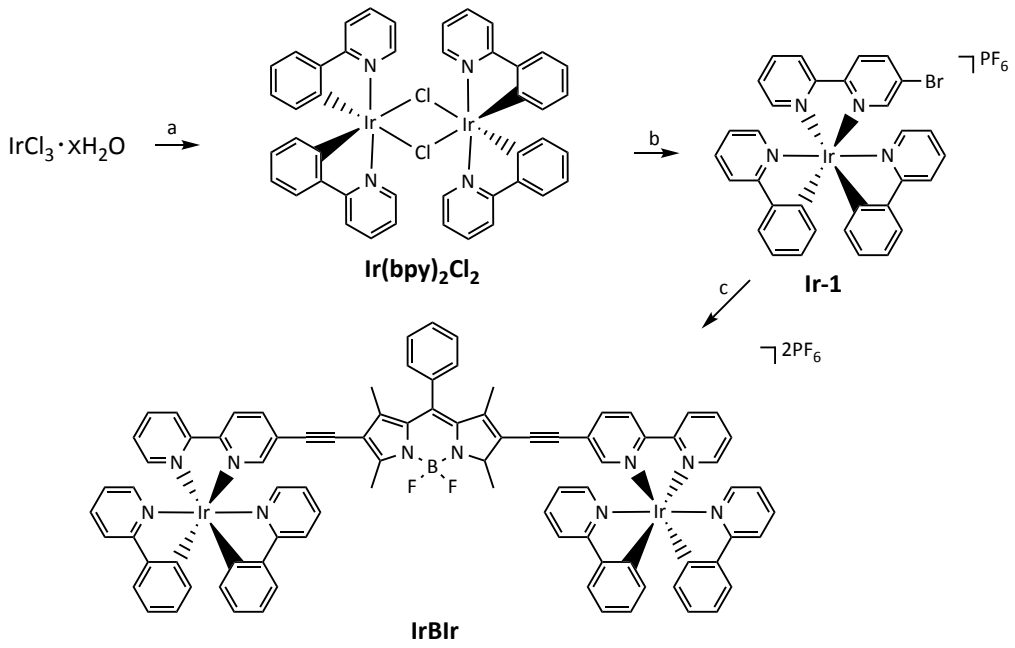

Scheme 2.4 *Synthesis of* ***IrBIr****. (a) 2-phenylpyridine, 2-ethoxyethanol:H_2O (3:1, v/v), Ar, reflux 130 °C, overnight, yield: 60.0 %. (b) CH_3OH:CH_2Cl_2 (3:1, v/v), reflux, 60 °C, 4 h, yield: 98.4 %. (c) (i-Pr)$_2$NH:CH_3CN (1:1, v/v), $Pd(PPh_3)_2Cl_2$, PPh_3, CuI, 8 h, 60 °C, Ar, yield: 12.9 %.*

2.3 Structural Characterisation of RuBRu and IrBIr

The isolated **RuBRu** and **IrBIr** complexes were characterised by a range of NMR techniques (^{1}H NMR, ^{13}C NMR, 2D-NMR, ^{19}F NMR and ^{11}B NMR). The symmetrical structures of these two complexes simplified the work of assigning proton and carbon signals. To be concise, only the characterisation of **IrBIr** will be elucidated in this section.

Figure 2.1 shows the ^{1}H proton spectrum of **IrBIr**. As it is well resolved, the proton signals can be clearly integrated to 63. Two single proton signals due to methyl groups were found at δ 1.42 ppm and δ 2.56 ppm respectively and the deshielding effect of heterocyclic in the structure is attributed to the larger deshielding of the methyl group. The other protons are located at the phenyl and pyridyl rings, and all of them are identified in the downfield region (δ 6.00–8.60 ppm) of the spectrum.

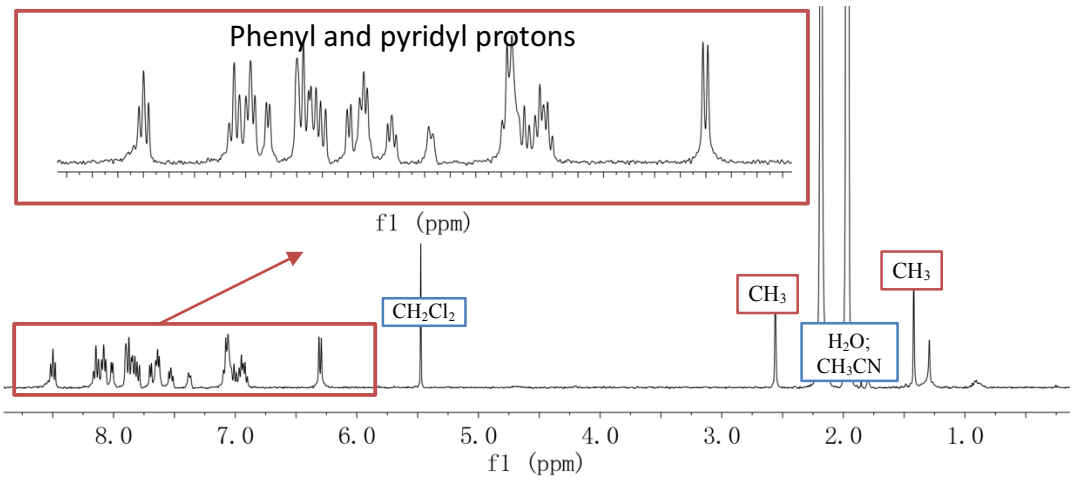

Figure 2.1 *^{1}H NMR spectrum of* ***IrBIr*** *(400 MHz, CD_3CN, 20 ℃).*

The ^{1}H spectrum of **IrBIr** contains seven spin systems. This is due to its symmetrical structure: one three-spin and three four-spin pyridyl systems, two four-spin systems corresponding to the phenyl on the 2-phenylpyridine moiety, one three-spin system of benzene on the BODIPY moiety. The identity of these spin systems can be established according to the ^{1}H-^{1}H COSY (COrrelation SpectroscopY) which shows all coupled spins within the same spin system. The shielded doublet at δ 6.30 ppm is assigned as the proton adjacent to the carbon *trans* to the metal centre and the protons in the four-spin system of benzene on 2-phenylpyridine are grouped in the ^{1}H-^{1}H COSY spectrum (the blue box in Figure 2.2). In order to analyse the pyridyl spin systems, HSQC (Heteronuclear Single Quantum Coherence) spectrum was used to distinguish the pyridyl carbons.

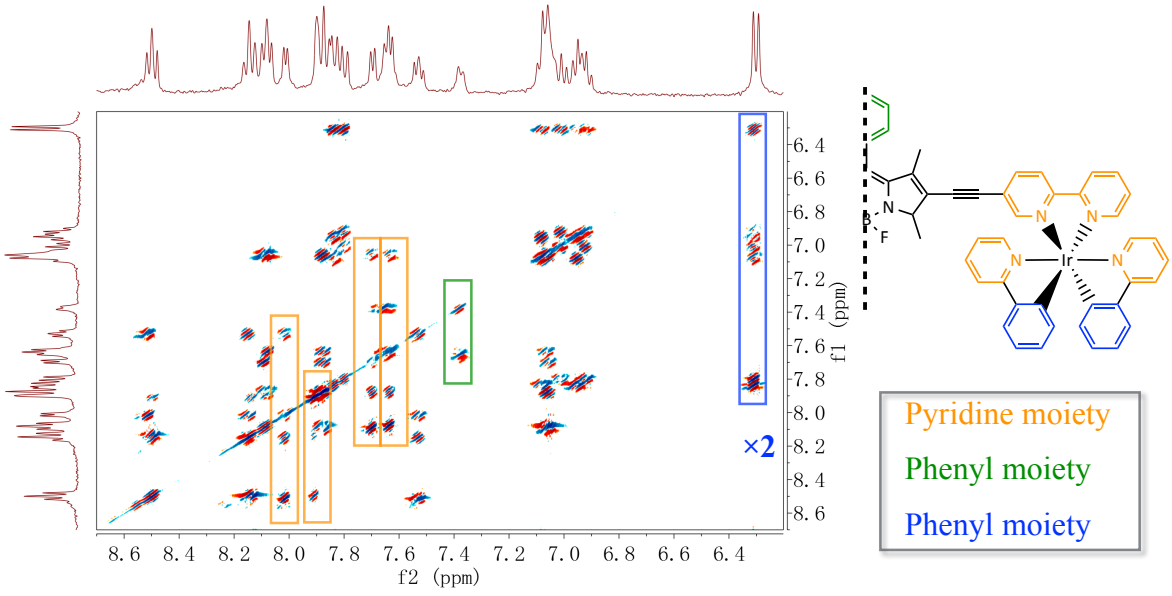

Figure 2.2 *The ^{1}H-^{1}H COSY analysis of* ***IrBIr*** *(600 MHz, CD_3CN, 20 ℃).*

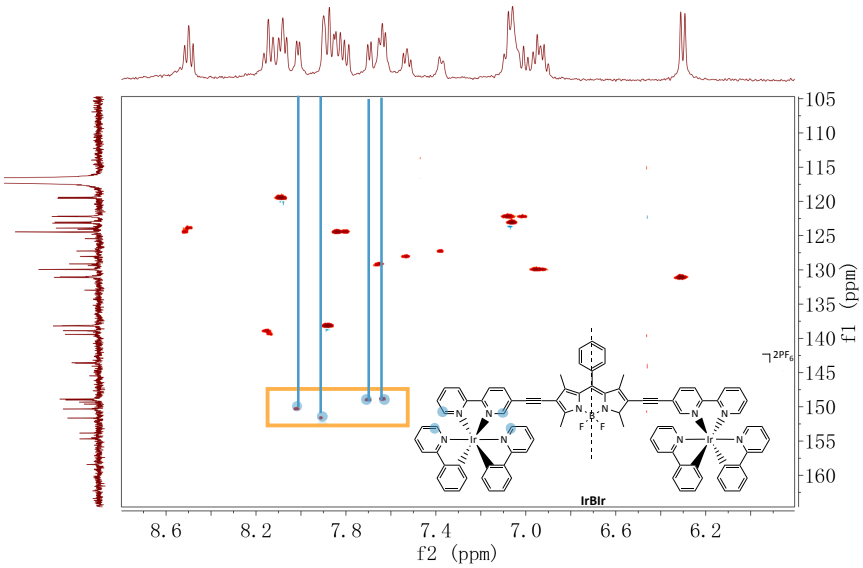

Figure 2.3 *The HSQC analysis of* ***IrBIr*** *(600 MHz, CD_3CN, 20 ℃).*

According to Figure 2.3, four ^{1}H signals are visible at δ 145 ppm -160 ppm respectively (f1). These are the pyridyl carbons adjacent to N-atoms (labelled ● in Figure 2.3). Four pyridyl spin systems are then directly identifiable in the ^{1}H-^{1}H TOCSY spectrum (the orange boxes in Figure 2.2). Based on the remaining unaccounted signals, the benzene three-spin system was assigned using a combination of the ^{1}H NMR and the ^{1}H-^{1}H TOCSY spectrum in Figure 2.2 (green box). The C-H representing the methyl groups was shown in HSQC spectrum ((2.56 ppm, 12.58 ppm); (1.42 ppm, 12.83 ppm)).

In ^{13}C NMR spectrum (Figure 2.4), two carbon signals attributed to the acetylene bond were found at δ 88.68 ppm and δ 91.33 ppm respectively and the carbon's from the methyl groups were identified at δ 12.30 ppm and δ 12.47 ppm. The ^{11}B NMR spectrum of **IrBIr** shows a triple peak at δ 0.45 ppm (split by two fluorine, I(^{19}F) = 1/2) and ^{19}F NMR shows a quartet peak at around δ -145 ppm (split by boron, I(^{11}B) = 3/2), both of which have been attributed to the B-F group.

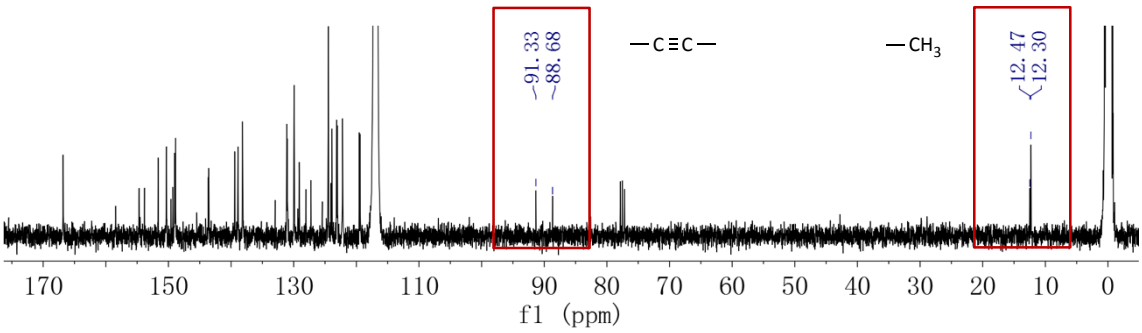

Figure 2.4 *^{13}C NMR spectrum of* ***IrBIr*** *(150 MHz, CD_3CN, 20 ℃).*

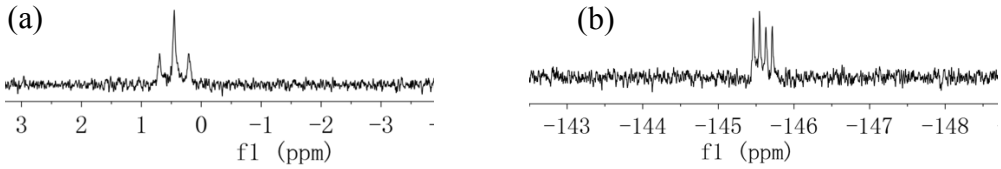

Figure 2.5 *(a) ^{11}B NMR spectrum of **IrBIr** (128 MHz, CD_3CN, 20 °C). (b) ^{19}F NMR spectrum of **IrBIr** (376 MHz, CD_3CN, 20 °C).*

A similar strategy was employed in the assignment of **RuBRu** structure.

In order to fully compare the effect of introducing a second metal centre into this family of complexes, the mononuclear complexes, **RuB** and **IrB** are presented in this section. (Figure 2.6) The synthesis , characterisation and the photophysical data of these structures are available in the literature. [34, 93] They are provided here for comparison only.

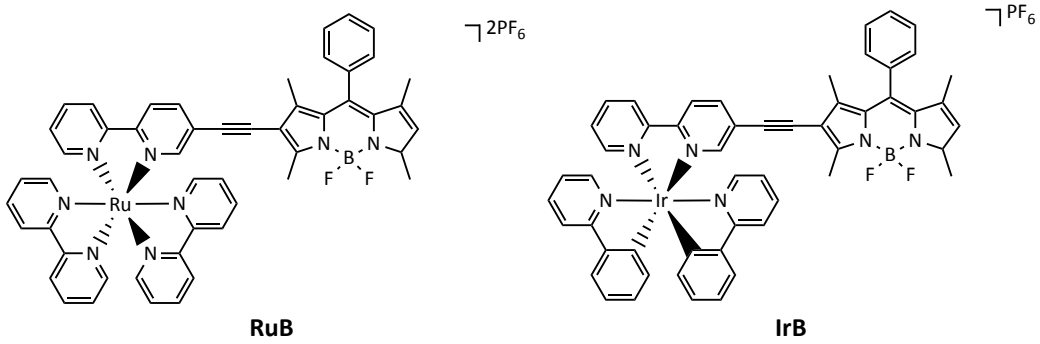

Figure 2.6 *Structures of reference compounds **RuB** and **IrB**.*[34, 93]

2.4 Photophysical Studies

2.4.1 Steady State Properties of RuBRu and IrBIr

The overlaid UV-Vis absorption spectra of **RuBRu** and **IrBIr** are presented in Figure 2.7. **RuBRu** shows a maximum absorption at λ 570 nm, which is bathochromically-shifted with respect to the reference complex **RuB**[34]. This is due to its larger π-conjugated framework. The molar absorption coefficient of **RuBRu** (ε 113,317 dm^3 mol^{-1} cm^{-1}, see Table 2.1), is approximately twice that of its mononuclear analogue, **RuB**.

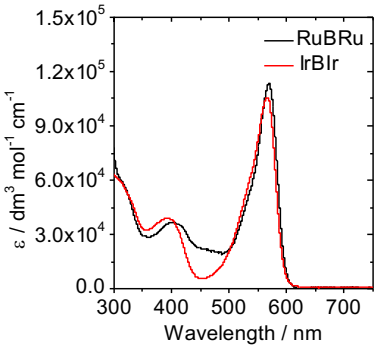

Figure 2.7 *Absorption spectra of* ***RuBRu*** *and* ***IrBIr****. C = 1 × 10^{-5} mol/L in CH_3CN, 298 K.*

For **IrBIr**, a similar strongly absorbing and bathochromically shifted profile is observed (ε = 105 713 dm^3 mol^{-1} cm^{-1}, see Table 2.1) relative to its reference complex **IrB**.[93] Ru(II) and Ir(III) complexes with such large absorption coefficients in the visible range are unusual in the literature.

Table 2.1 *Photophysical properties of mono- and di- nuclear BODIPY based complexes.*[a]

	λ_{abs} (nm)	ε[b] (10^5 dm^3 mol^{-1} cm^{-1})	λ_{em} (nm)	Φ_F[c]/Φ_P[c] (%)	τ_F[d] (ns)	τ_P[e] (μs)(298 K)	τ_P[f] (ms)(77 K)	τ_T[g] (μs)
RuB[34]	528	0.65	748	-----[h]/-----	----	----	----	279.7
RuBRu	398/570	0.38/1.13	595/739	---- /0.28	0.13	574.7/611.2	15.8	1316.0
IrB[93]	527	0.83	533/742	0.30/0.03	2.6	----	----	87.2
IrBIr	394/567	0.37/1.06	591/740	0.24/0.04	0.63	457.9/552.0	9.40	630.7

[a] Results of complexes in acetonitrile solution (1 × 10^{-5} mol/L), 298 K. [b] Molar absorption coefficient at the absorption maxima. [c] Quantum yield of fluorescence and phosphorescence, with 2,6-diiodo-BODIPY as a standard (Φ_f = 2.7 % in CH_3CN)[23]. [d] Fluorescence lifetime. [e] Phosphorescence lifetime at λ 570 nm and 740 nm, λ_{ex} = 570 nm. [f] Phosphorescence lifetime at λ 740 nm, 77 K, λ_{ex} = 570 nm. [g] Triplet-state lifetime, λ_{ex} = 530 nm.[h] Not determined.

The luminescence properties of **RuBRu** and **IrBIr** were studied under different atmospheres (Figure 2.8) and temperatures (Figure 2.10). The phosphorescence excited state lifetimes of both bands in **RuBRu** at λ 595 nm and 739 nm are long lived, (τ_P at 298 K, 574.7 μs and 611.2 μs respectively) supporting their probable triplet-excited state origin. The emission profiles under both oxygen and air atmosphere indicate that the triplet-triplet energy transfer (TTET) between **RuBRu** and molecular oxygen is efficient

(Figure 2.8a) because the phosphorescence was significantly quenched in aerated solution.

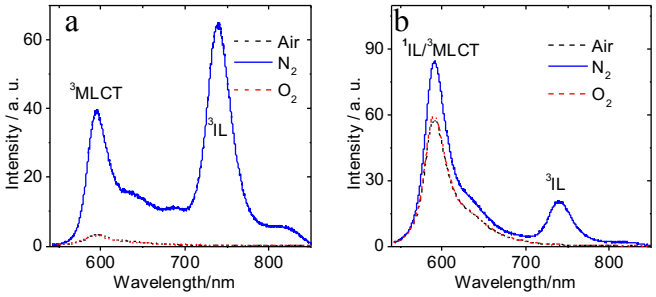

Figure 2.8 *Emission spectra of (a)**RuBRu** and (b)**IrBIr** in CH_3CN under N_2, air and O_2 -saturated atmosphere. λ_{ex} = 530 nm, C = 1 × 10^{-5} mol/L, 298 K.*

IrBIr also shows two emissions in deaerated solution (at λ 591 nm and 740 nm) (Figure 1.7b). Their respective lifetimes are 457.9 μs and 552.0 μs. Compared to **RuBRu**, the luminescence at λ 591 nm is only partially quenched by molecular oxygen in aerated solutions. The lifetime of this **IrBIr** emissive band decreases to 0.63 ns in aerated solution, as is expected when fluorescence occurs. In this case, the intersystem crossing (ISC) is not as efficient as in **RuBRu**, and the emission at λ 591 nm has considerably more ^{1}BODIPY* character (as well as a small ^{3}MLCT* contribution in deaerated solution, it is concludes from the comparison between aerated and deaerated emission profiles of **IrBIr**).

2.4.2 Transient State Studies

In order to examine the triplet excited states of the complexes, the nanosecond time-resolved transient difference absorption spectra were studied (Figure 2.9).

Upon pulsed laser excitation (λ_{ex} = 570 nm) of **RuBRu** significant bleaching peak of the BODIPY moiety was observed at λ 566 nm (Figure 2.9a), as is characteristic of the depletion of the ground state of the BODIPY ligand. The transient difference absorption spectrum agrees with the steady-state absorption spectrum (Figure 2.7) and indicates that the triplet excited state of **RuBRu** is mainly localised on the BODIPY moiety, rather than the metal centre. The triplet excited state lifetime of **RuBRu** was measured to be τ_T = 1316.0 μs. To the best of our knowledge, this is the longest observed triplet-state lifetime of any BODIPY complex.[94, 95] By comparison the triplet excited state (^{3}IL*) lifetime of **RuB** is 279.7 μs.[30] The data supports the conclusion that the binuclear **RuBRu** has a

prolonged triplet excited lifetime which is likely to suggest more significant ^{3}IL transfer is a feature of its T_1 excited state.

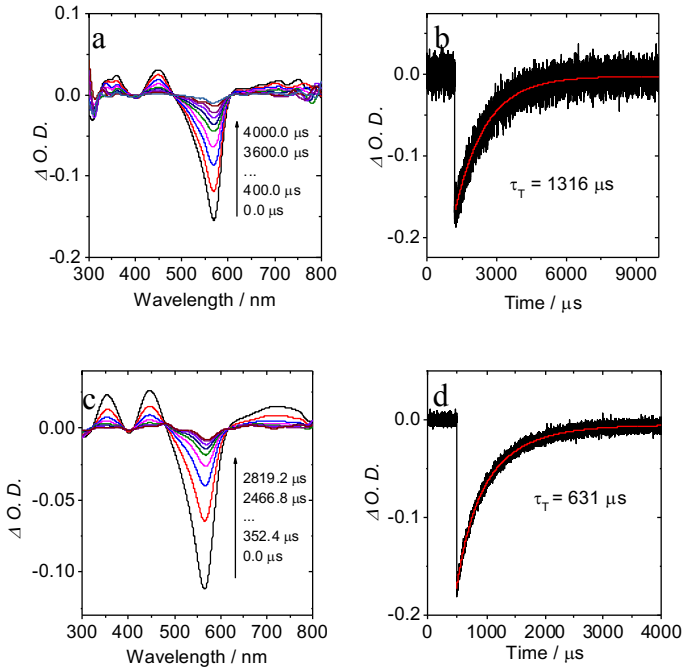

Figure 2.9 *Nanosecond time-scaled transient difference absorption spectra of (a)**RuBRu** and (c)**IrBIr** after plus an excitation at λ_{ex} = 570 nm and their decay traces: (b) **RuBRu** at λ 585 nm and (d)**IrBIr** at λ 575 nm. C = 1 × 10^{-5} mol/L, in CH_3CN, 298 K.*

Broadly similar results were obtained for **IrBIr**. (Figure 2.9c) The bleaching peak was observed at λ 565 nm and the triplet excited state lifetime of **IrBIr** was measured and found to be τ_T = 630.7 μs. This value is much longer than the triplet excited state lifetime of the mononuclear complex **IrB** (τ_T = 87.2 μs), which again can be attributed to the presence of the additional metal centre and the corresponding increases in the organic framework.[93]

2.4.3 Low Temperature Emission (77 K)

The luminescence spectra of both complexes were studied at 77 K (Figure 2.10). When the emission spectra of the room and low temperature spectra of **RuBRu**, are compared (Figure 2.10a), the luminescence previously at λ 595 nm diminishes, while the intensity of the emission at λ 739 nm remains static although slightly bathochromically-shifted (Figure 2.8a). Such a small thermally induced Stokes shift for the band at λ 739 nm further supports its assignment as arising from the ^{3}IL excited state as does the lifetime of this emission at λ 739 nm which was determined as 9.4 ms.

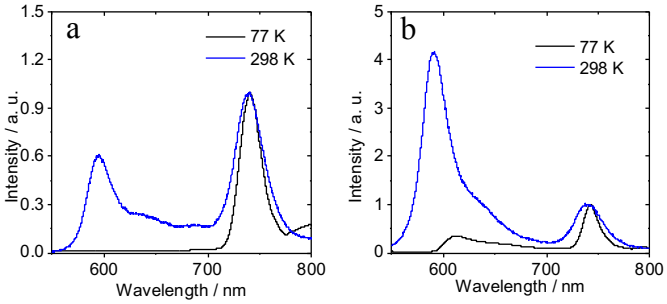

Figure 2.10 *Normalised emission spectra of (a)**RuBRu** and (b)**IrBIr** at 298 K and at 77 K in CH_3CN. $C = 1 \times 10^{-5}$ mol/L.*

The intensity of the emissive band previously apparent at λ 595 nm (room temperature), is quenched at 77 K. We propose that the ^{3}MLCT excited state phosphorescence is quenched due to ^{3}MLCT* → ^{3}IL* energy transfer. The energy equilibrium between the ^{3}MLCT and ^{3}IL excited states is temperature dependent.[81] As the temperature drops, and the higher vibrational levels cannot be thermally depopulated, the high lying ^{3}MLCT state cannot be populated by thermal activation of the ^{3}IL excited state. The rationale put forward is that only the lower energy ^{3}IL* emission, is observed at 77 K, as a result.

For **IrBIr**, changes similar to those of **RuBRu** are seen in the low temperature spectrum (Figure 2.10b). The emission at λ 591 nm becomes much weaker *versus* that of the emission band at λ 740 nm due to what is believed to be ^{3}MLCT* → ^{3}IL* energy transfer. However, this process is not as efficient as in **RuBRu** (as the band at λ 740 nm displays considerable ^{1}IL* character). The lifetime of the emission at λ 740 nm was determined as 15.8 ms.

2.5 Density Functional Theoretical (DFT) Calculation

To further corroborate the findings of the photophysical studies, Density Functional Theoretical (DFT) calculations were carried out for each complex.

The ground state geometry of the complexes was first optimised. For **RuBRu**, the BODIPY chromophore takes a coplanar orientation with respect to the attached bipyridine on the Ru(II) coordinated centre, further enhancing the π-conjugation of the complex. Spin density surfaces were computed for the complexes (Figure 2.11). In **RuBRu**, the lowest triplet state is mainly located on the BODIPY moiety, which is in an agreement with the experimental results of the nanosecond time-resolved transient

absorption spectroscopic study (Figure 2.9a). The contribution of the Ru(II) centres to the T_1 state is small, which is in an agreement with the long lifetime of **RuBRu**.

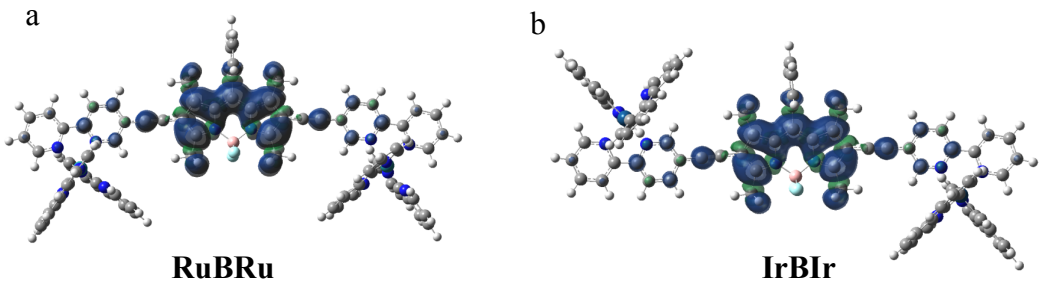

Figure 2.11 *Isosurface of spin density of* ***RuBRu*** *and* ***IrBIr*** *at the optimised triplet-state geometries. Acetonitrile was used as the solvent in the calculations. Calculations were proformed at TDDFT/B3LYP/GENECP/LANL2DZ with Gaussian 09.*

The absorption properties of **RuBRu** were calculated using the time-dependent DFT (TDDFT) method. Time-dependent density-functional theory (TDDFT) extends the basic ideas of ground-state density-functional theory (DFT) to the treatment of excitations or more general time-dependent phenomena.[96] The calculated absorption wavelengths of **RuBRu** are λ 543 nm and 406 nm (Table 2.2). These are found to be close to the experimental results (λ_{abs} = 570 nm and 398 nm). The energy gap between S_0/T_1 was calculated to be 1.55 eV (800 nm) and is very similar to the experimental value for the phosphorescence of **RuBRu** at 739 nm (1.68 eV), it has been assigned as ^{3}IL*. The energy gap between S_0/T_2 was calculated as 2.12 eV and appears to have both a IL and a small MLCT contribution. The energy gap between S_0/T_3 was calculated as 2.16 eV (575 nm) and appears to have MLCT character, supporting the previous assignment that the phosphorescence at λ 595 nm of **RuBRu** is attributed to ^{3}MLCT*. In summary, the calculations closely support the conclusions drawn from the experimental data including the existence of a triplet state equilibrium between ^{3}MLCT and ^{3}IL excited states.

Table 2.2 *Electronic Excitation Energies (eV) and corresponding Oscillator Strength (f), main configurations and CI coefficients of the Low-lying Electronic Excited States of the complex* ***RuBRu*** *calculated by TDDDFT/B3LYP/GENECP/LANL2DZ, CH_3CN as the solvent (PCM model) based on the optimised Ground State Geometries.*

	Electronic transition	TD-SCF/B3LYP/GEN				
		Energy [a]	*f* [b]	Composition [c]	CI [d]	Character [e]
Singlet	$S_0 \rightarrow S_1$	2.2832 eV 543 nm	1.9522	H→L	0.6870	IL
	$S_0 \rightarrow S_{13}$	2.8414 eV 436 nm	0.1570	H-2→L	0.3727	MLCT
				H→L+2	0.3765	LL'CT
	$S_0 \rightarrow S_{23}$	3.0333 eV 409 nm	0.1767	H-3→L+1	0.2336	L'LCT
				H-3→L+3	0.2442	LL'CT
				H→L+6	0.2810	L'LCT
Triplet	$S_0 \rightarrow T_1$	1.5504 eV 800 nm	0.0000[f]	H-8→L	0.2329	IL
				H→L	0.6212	IL
				H→L+2	0.1924	IL/MLCT
	$S_0 \rightarrow T_2$	2.1295 eV 585 nm	0.0000[f]	H-8→L	0.4356	IL
				H→L	0.2738	IL
				H-1→L+1	0.1729	MLCT
				H→L+2	0.2715	IL/MLCT
	$S_0 \rightarrow T_3$	2.1570 eV 575 nm	0.0000[f]	H-7→L	0.3821	MLCT
				H-1→L	0.2574	MLCT
				H→L+1	0.3444	IL/MLCT

[a] Only the selected low-lying excited states are presented. [b] Oscillator strengths. [c] Only the main configurations are presented. [d] The CI coefficients are in absolute values. [e] L stands for BODIPY localized ligand and L' stands for bipyridine localized ligand. [f] No spin-orbital coupling effect was considered, thus the *f* values are zero.

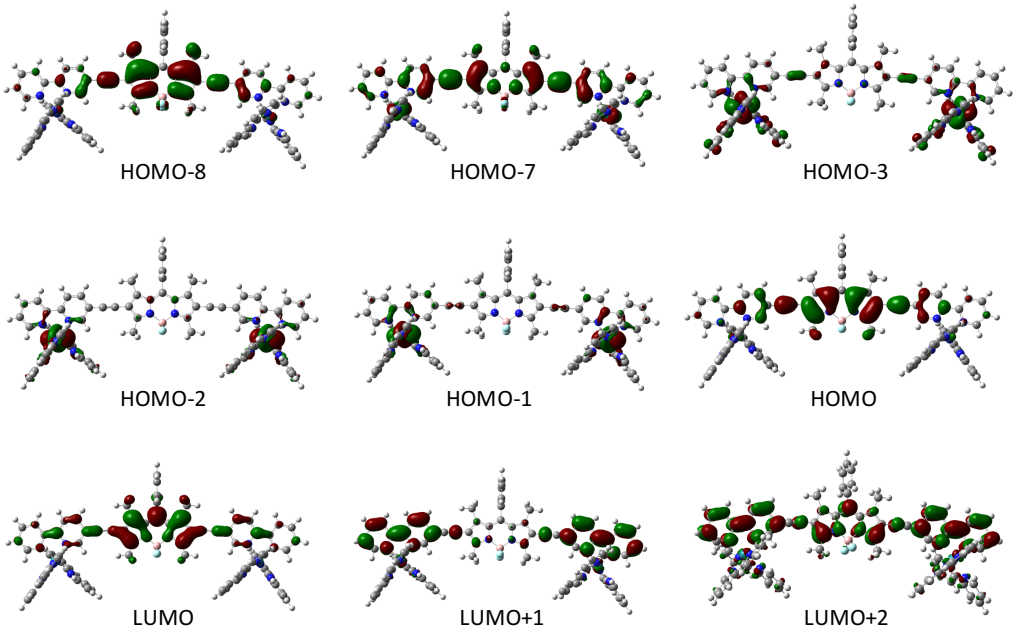

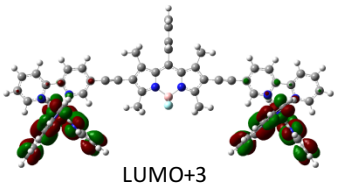

Figure 2.12 *Electron density maps of the frontier molecular orbital of the complex* ***RuBRu****, based on ground state optimised geometry by the TDDFT calculations at the TDDFT/B3LYP/GENECP/LANL2DZ level with Gaussian 09W.*

The computational results of the **IrBIr** calculations are presented in Table 2.3.

Table 2.3 *Electronic Excitation Energies (eV) and corresponding Oscillator Strength (f), main configurations and CI coefficients of the Low-lying Electronic Excited States of the complex* ***IrBIr*** *calculated by TDDDFT/B3LYP/GENECP/LANL2DZ, CH_3CN as the solvent (PCM model) based on the optimised Ground State Geometries.*

	Electronic transition	**TD-SCF/B3LYP/GEN**				
		Energy [a]	***f*** [b]	**Composition** [c]	**CI** [d]	**Character** [e]
Singlet	$S_0 \rightarrow S_1$	2.2837 eV 543 nm	1.9723	H-2 –L	0.11933	MLCT
				H–L	0.67951	IL
	$S_0 \rightarrow S_{11}$	2.8767 eV 431 nm	0.2980	H-8–L	0.23264	MLCT
				H–L+2	0.58867	IL
	$S_0 \rightarrow S_{19}$	3.1523 eV 393 nm	0.2372	H-10–L	0.33818	L'LCT
				H-8–L	0.23258	MLCT
				H-5–L+1	0.24395	IL
Triplet	$S_0 \rightarrow T_1$	1.5467 eV 802 nm	0.0000 [f]	H-8–L	0.21184	MLCT
				H-2–L	0.19874	MLCT
				H–L	0.59488	IL
	$S_0 \rightarrow T_2$	2.1266 eV 583 nm	0.0000 [f]	H-12–L	0.15212	L'LCT
				H-8–L	0.39479	MLCT
				H-5–L+2	0.23322	IL
				H–L	0.29387	IL
				H–L+2	0.28617	IL
	$S_0 \rightarrow T_3$	2.1648 eV 573 nm	0.0000 [f]	H-8–L	0.22045	MLCT
				H-2–L	0.50778	MLCT
				H-1–L+1	0.29611	L'LCT; MLCT

[a] Only the selected low-lying excited states are presented. [b] Oscillator strengths. [c] Only the main configurations are presented. [d] The CI coefficients are in absolute values. [e] L stands for BODIPY localised ligand and L' stands for bipyridine localised ligand. [f] No spin-orbital coupling effect was considered, thus the *f* values are zero.

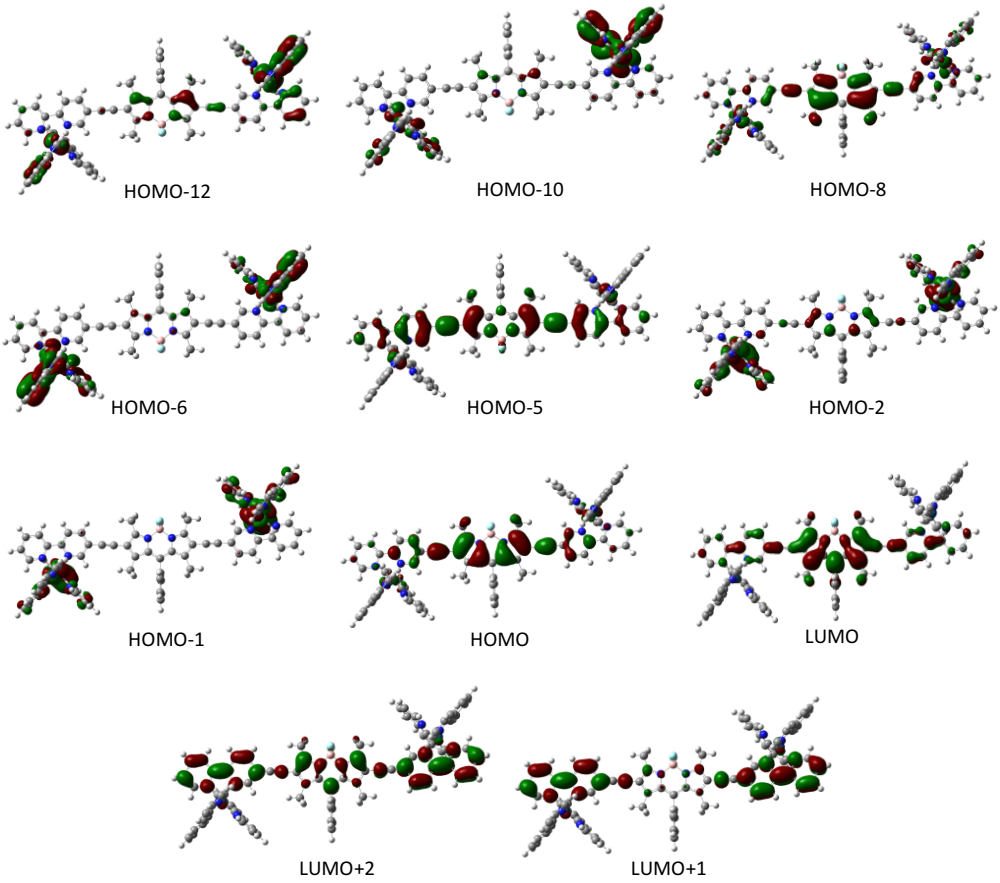

Figure 2.13 *Electron density maps of the frontier molecular orbital of the complex* ***IrBIr****, based on ground state optimised geometry by the TDDFT calculations at the TDDFT/B3LYP/GENECP/LANL2DZ level with Gaussian 09W.*

2.6 Triplet Photosensitisation Studies for TTA Upconversion and Photodynamic Therapy

2.6.1 TTA Upconversion of RuBRu and IrBIr as Triplet Photosensitiser

As discussed in the Chapter 1, TTA upconversion has already shown excellent potential in photovoltaic applications, with particular promise in dye-sensitised solar cells, due to its inherent low excitation energy, and tunable absorption wavelength.[9] **RuBRu** and **IrBIr** both show strong absorption in the visible region, and each complex has a long-lived triplet state lifetime. Therefore, both complexes are suitable as triplet

photosensitisers for TTA upconversion. In a standard TTA upconversion process, the triplet photosensitisers are excited by an external light source (approximate power output of 70.8 $mW \cdot cm^{-2}$). Energy transfer occurs from the photosensitiser to the acceptor molecule *via* intermolecular triplet-triplet energy transfer (TTET). The singlet excited state of the acceptor is accessed *via* TTA between the collision of two triplet excited state acceptors to generate fluorescence from the acceptor molecule. (Scheme 1.3, Chapter 1)

The luminescence of **RuBRu** was observed under a nitrogen atmosphere when the complex was excited at λ 589 nm (Figure 2.14a, c; Figure 2.15b). After the addition of 9,10–diphenylanthracene (**DPA**) as an acceptor to the solution, a strong blue emission at λ 428 nm was observed, confirming that TTA upconversion is occurring. Excitation of the triplet photosensitiser or DPA alone at λ 589 nm does not give rise to this blue emission. The upconversion yield of **RuBRu** in the presence of DPA as acceptor was calculated to be 19.1 % (Figure 2.14a), and 4.5 % (Figure 2.14c) respectively when using perylene as the acceptor molecule.

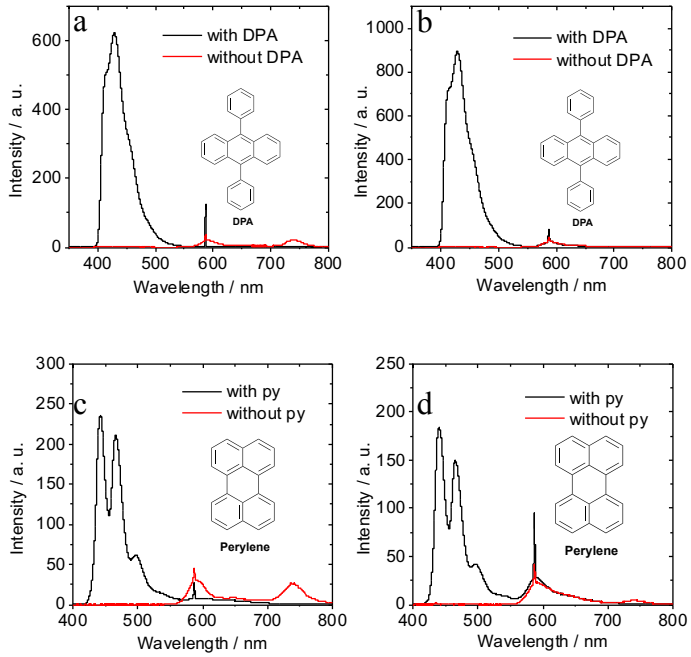

Figure 2.14 *Upconversion with* ***RuBRu*** *and* ***IrBIr*** *as triplet photosensitisers in CH_3CN ($C = 1.0 \times 10^{-5}$ mol/L), 25 ^{o}C. (a)* ***RuBRu*** *emission spectra with DPA added ($C = 1.67 \times 10^{-3}$ mol/L) (b)* ***IrBIr*** *emission spectra with DPA added ($C = 1.25 \times 10^{-3}$ mol/L) (c)* ***RuBRu*** *emission spectra with perylene added ($C = 4.0 \times 10^{-5}$ mol/L) (d)* ***IrBIr*** *emission*

spectra with perylene added (C = 1.5 × 10^{-5} mol/L). Excited with yellow laser, λ_{ex} = 589 nm, 5.0 mW.

According to the literature, the triplet excited state is found to be at 1.77 eV for **DPA**, and at 1.53 eV for perylene. For effective TTET, the energy of the acceptor's triplet excited state should be less than or equal to that of the donor. However, in this case, the lowest triplet excited state of **RuBRu** is found at 1.68 eV (739 nm). Therefore, when using **DPA** as an acceptor molecule, we assume that the existence of vibrational energy levels of triplet excited states contributes to the upconverted fluorescence. Moreover, the anti-Stokes shift in this process is 161 nm (589 nm–428 nm; 6.39 × 10^3 cm^{-1}). This is an unusually large anti-Stokes shift for TTA upconversion. The mononuclear metal complex **RuB** has a lower reported literature upconversion yield, of 1.2 % with perylene as acceptor.[34]

For **IrBIr**, the upconverted emission is clearly visible to the naked eye (Figure 2.15b). The upconversion yield with DPA as the triplet acceptor is calculated to be 25.5 % (Figure 1.14c); and is higher than that of **RuBRu**. The upconversion yield with perylene is considerably lower at 5.9 % (Figure 2.14d). Using **IrB**, the reported literature upconversion yield with perylene is only 2.8 %. [93]

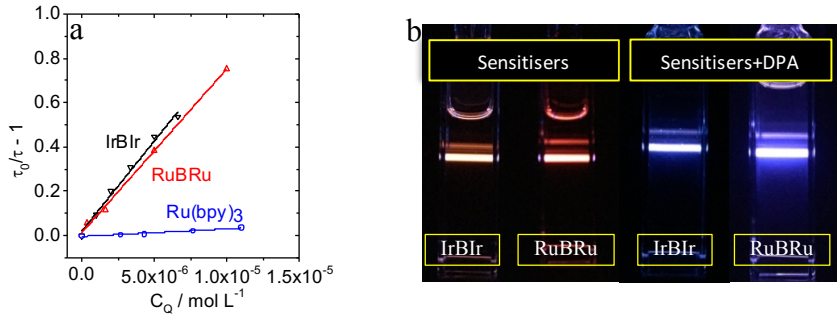

Figure 2.15 *(a)Stern–Volmer plots generated from triplet excited state lifetime (τ_T) quenching of complexes* ***RuBRu***, ***IrBIr*** *and* ***Ru(bpy)$_3$*** *measured with the increasing* ***DPA*** *concentration in CH_3CN. The lifetimes were measured with the nanosecond time-resolved transient absorption. C [Sensitisers] = 1.0 × 10^{-5} mol/L, 25 ^oC. (b) TTA UC photos.*

In order to study the efficiency of the TTET process, the triplet lifetime quenching Stern-Volmer graphs of **RuBRu** and **IrBIr** were plotted with **DPA** as the triplet acceptor. $[Ru(bpy)_3]^{2+}$ was used as the reference complex for each system (Figure 2.15). The results showed that the triplet lifetime quenching efficiency of **IrBIr** is only slightly higher than

that of **RuBRu,** and both complexes are approximately 22-fold higher than that of the reference compounds.

To further confirm that TTA upconversion is occurring, the lifetimes of the upconverted emissions at λ 428 nm (Figure 2.14a and b) were studied. Upon excitation, the prompt fluorescence lifetime of **DPA** alone at λ 428 nm was determined as 7.7 ns on laser excitation. For **RuBRu** and **IrBIr**, the delayed fluorescence lifetimes were (with an optical parametric oscillator laser light source) recorded to be τ_{DF} = 154.7 μs and 101.0 μs respectively (Figure 2.16). These long lifetimes cannot be generated by any singlet excited state alone and therefore we can confidently attribute them to the upconverted luminescence between the dinuclear ruthenium/iridium complex and **DPA**.

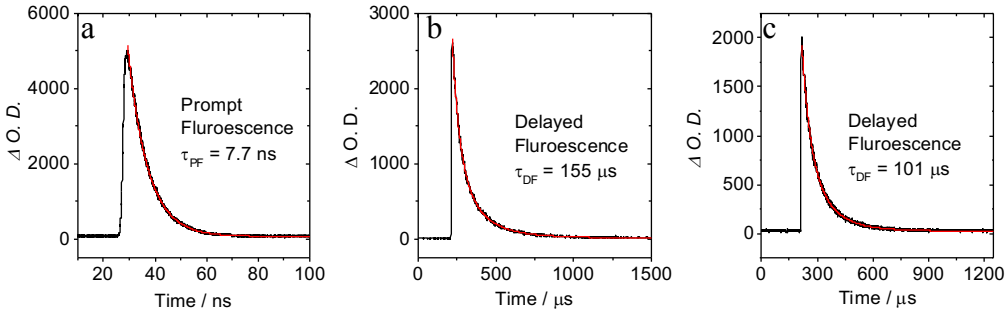

Figure 2.16 *The delayed fluorescence decay of* ***DPA*** *observed in the TTA upconversion with* ***RuBRu*** *and* ***IrBIr*** *complexes as triplet photosensitizer and* ***DPA*** *as the triplet acceptor, the complexes were excited at λ 589 nm (nanosecond pulsed OPO laser synchronized with spectrofluorometer) and the emission was due to the upconverted emission of* ***DPA*** *monitored at 428 nm. (a) The prompt fluorescence decay of* ***DPA*** *determined in a different experiment (excited with picosecond 405 nm laser, the decay of the emission was monitored at 428 nm). (b)* ***RuBRu*** *as triplet photosensitiser. (c)* ***IrBIr*** *as triplet photosensitiser. In deaerated CH_3CN, 25 ^oC. C [Sensitisers] = 1.0 × 10^{-5} M, C [**DPA**] = 2 × 10^{-3} mol/L.*

The photophysical processes involved in the TTA upconversion with **RuBRu** as photosensitiser are summarised in Scheme 2.6. Upon excitation of **RuBRu**, both ^{3}MLCT* and ^{3}IL* states are generated, and the triplet excited state equilibrium is created. The triplet-triplet energy transfer from triplet energy donor to triplet acceptor produces the triplet excited states of **DPA**. Promptly, the TTA process between two triplet excited states then produces the singlet excited state of **DPA**, and its radiative decay results in the upconverted luminescence.

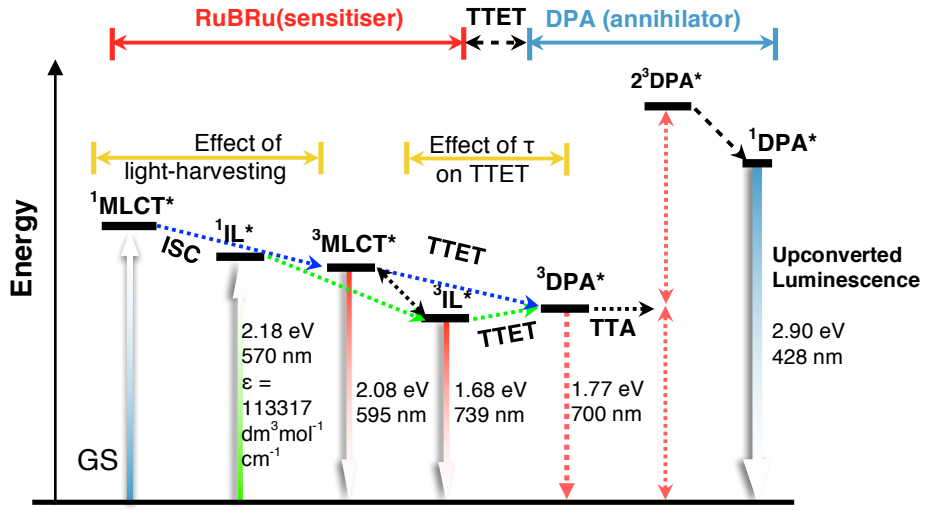

Scheme 2.5 *Jablonski diagram of TTA upconversion with* ***RuBRu*** *as a triplet photosensitiser and* ***DPA*** *as a triplet acceptor. The effect of the light-harvesting ability and the triplet lifetimes of the Ru(II) sensitisers on the efficiency of the TTA upconversion are also shown. E is the energy. GS is the ground state (S_0). ^{1}MLCT* is the Ru(II) based metal-to-ligand charge transfer singlet excited state, ^{1}IL* is the Bodipy localised intraligand singlet excited state. ^{3}MLCT* is the Ru(II) based metal-to-ligand charge transfer triplet excited state. ^{3}IL* is the BODIPY based intraligand triplet excited state. TTET is the triplet-triplet energy transfer.* ^{3}***DPA**** *is the triplet excited state of* ***DPA****.* ^{1}***DPA**** *is the singlet excited state of* ***DPA****.*

Table 2.4 *Triplet excited state properties of* ***RuBRu*** *and* ***IrBIr****.*

	τ_{DF}[a] (μs)	K_{sv}[b] (10^4 M^{-1})	K_q[c] ($M^{-1}s^{-1}$)	Φ_{UC}[d] (%)	Φ_{Δ}[e] (%)
RuBRu	154.7	8.4	63.9	19.1[d1]/4.5[d2]	79.4
IrBIr	101.0	8.5	135.3	25.5[d1]/5.9[d2]	74.9

[a] Delayed fluorescence. [b] Quenching constant. [c] Bimolecular quenching constants in 10^6. [d] TTA upconversion yield in deaerated CH_3CN with triplet acceptor **DPA**[d1] and perylene[d2], excited with a λ 589 nm laser, with the prompt fluorescence of iodo-BDP as the standard (Φ_f = 2.7 % in CH_3CN)[56]. [e] Quantum yield of singlet oxygen in CH_3CN, excited at λ 540 nm and 2,6-diiodo-BODIPY (Φ_Δ = 0.83 in CH_2Cl_2) as standard.[97]

2.6.2 Intermolecular Triplet Energy Transfer

Intermolecular triplet energy transfer is meaningful for a myriad of research areas, including photosynthesis, photoredox catalytic organic reactions and photodynamic therapeutic reagents. For this reason, the intermolecular triplet energy transfer between the complex and added aliquots of **B-1** (Scheme2.1, P36) were studied.

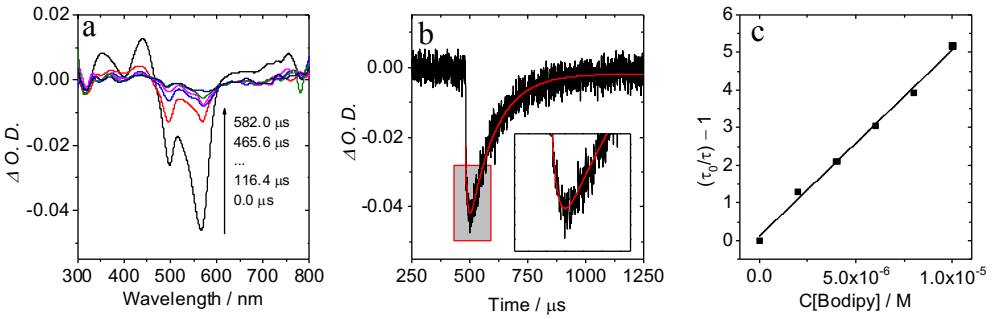

Figure 2.17 *Nanosecond time-resolved transient absorption spectra and decay traces of the mixture of* ***IrBIr*** *and* ***B-1****. (a) the molar ratio is 1 : 1 (****IrBIr*** *:* ***B-1****). The decay traces of* ***B-1*** *(b) at λ 500 nm; (c) triplet lifetime quenching Stern-Volmer plot of* ***IrBIr*** *with the increasing concentration of* ***B-1****, λ_{ex} = 570 nm, C[****IrBIr****] = 1.0 × 10^{-5} mol/L, in deaerated CH_3CN at 25 °C.*

A solution containing just the iridium complex, **IrBIr**, shows a strong bleaching peak at λ 565 nm during nanosecond time-resolved transient different absorption spectroscopy (Figure 2.9c). Upon the addition of increasing concentrations of **B-1**, it acts as a triplet state quencher and so, the bleaching peak of **IrBIr** decreases and a new bleaching peak at λ 500 nm develops. This new peak is typical of BODIPY ground state bleaching (Figure 2.17a). These two changes are indicative of triplet state energy transfer from **IrBIr** to **B-1**, and the bleaching band lifetime of **IrBIr** was measured (Figure 2.18a). The excited state lifetime is seen to decrease from 630.7 μs (**Ir-2**) to 89.0 μs (**IrBIr**: **B-1** = 1: 1.5). The similar phenomenon was observed in the mixture of **RuBRu** and **B-1**. For **RuBRu**, the triplet excited state lifetime was seen to quench from 1316.0 μs (**RuBRu**) to 72.2 μs (**RuBRu** : **B-1** = 1 : 0.6) (Figure 2.18b).

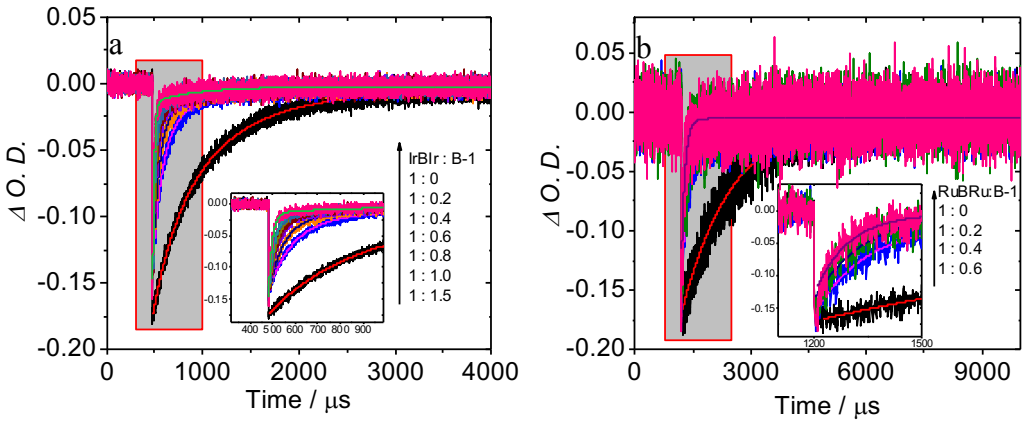

Figure 2.18 *Nanosecond time-resolved transient absorption decay traces of (a)**IrBIr**/(b)**RuBRu** at λ 575 nm with the increasing concentration of **B-1**, λ_{ex} = 570 nm, C[Sensitiser] = 1.0 × 10^{-5} mol/L, in deaerated CH_3CN at 25 °C.*

Interestingly, the decay trace that appears at λ 500 nm has biphasal character for both of **RuBRu** and **IrBIr** (Figure 2.17b and 2.19b). It has a sharp increase at the beginning, and then decreases by a slow decay process. The first stage can be attributed to the production of the triplet state of **B-1** *via* intermolecular triplet energy transfer. The second stage is due to the decay of this same triplet state. The triplet energy transfer rate constant (k_{ET}) and triplet energy transfer efficiency (Φ_{ET}) were calculated using Equations (2.1) and (2.2), respectively.

$$k_{ET} = \frac{1}{\tau_1} - \frac{1}{\tau_2} \qquad (2.1)$$

$$\Phi_{ET} = 1 - \frac{\tau_2}{\tau_1} \qquad (2.2)$$

where τ_1 is the original lifetime of triplet donor without acceptor and τ_2 is the triplet lifetime of donor with addition of acceptor. Table 2.5 shows the values uptained for **IrBIr**.

Table 2.5 *The triplet energy transfers rate constant (k_{ET}) and triplet energy transfer efficiency (Φ_{ET}) for TTET in the mixture of **IrBIr** : **B-1**.*[a]

IrBIr:**B-1**	k_{ET} (s^{-1})	Φ_{ET} (%)
1.0:0.2	2.05 × 10^3	56.3
1.0:0.4	3.34 × 10^3	67.8
1.0:0.6	4.82 × 10^3	75.2
1.0:0.8	6.23 × 10^3	79.7
1.0:1.0	8.22 × 10^3	83.8
1.0:1.5	9.65 × 10^3	85.9

[a]In deaerated CH_3CN at 25 °C.

For **IrBIr**, the calculated K_{ET} was in the 10^3 s^{-1} range. The Φ_{ET} increases with the addition of acceptor because this increases the chance of a collision occurring between the two molecules (Table 2.5). When the **IrBIr**: **B-1** ratio is 1: 1, the Φ_{ET} is 83.8 %, meaning that the intermolecular triplet energy transfer between **IrBIr** and **B-1** is very efficient. For **RuBRu**, the highest calculated value of K_{ET} was 1.26 × 10^5 s^{-1} and the highest Φ_{ET} was determined as 94.3 % (**RuBRu** : **B-1** = 1 : 0.6).

The triplet state lifetime quenching of **IrBIr** was also used to generate the Stern-Volmer plot (Figure 2.17c). From this, the Stern-Volmer quenching constant was determined as

$K_{SV} = 5.1 \times 10^5$ M^{-1} (for **RuBRu**, $K_{SV} = 2.76 \times 10^6$ M^{-1}, Figure 1.19c). The bimolecular quenching constant k_q, was calculated (Equation 2.3) and found to be 8.11×10^8 M^{-1} s^{-1} for **IrBIr**. Finally, the quenching efficiency (f_Q) was calculated as 3.6 % (in CH_3CN at 25 ^oC) (Equation 2.4).

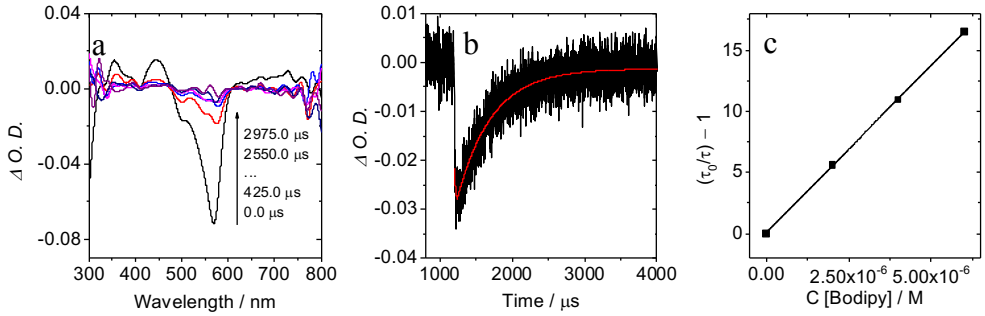

Figure 2.19 *Nanosecond time-resolved transient absorption spectra and decay traces of the mixture of* ***RuBRu*** *and* ***B-1****. (a) the molar ratio is 1: 0.2 (****RuBRu****: ****B-1****). The decay traces of* ***B-1*** *(b) at λ 500 nm; (c) triplet lifetime quenching Stern-Volmer plot of* ***RuBRu*** *with the increasing concentration of* ***B-1****, λ_{ex} = 570 nm, C[****RuBRu****] = 1.0 × 10^{-5} mol/L, in deaerated CH_3CN at 25 ^oC.*

Bimolecular quenching constant (k_q):

$$k_q = K_{sv}/\tau_0 \qquad (2.3)$$

K_{sv} Stern-Volmer quenching constant; τ_0 is the triplet state lifetime of the triplet energy donor.

Quenching efficiency (f_Q):

$$f_Q = k_q/k_0 \qquad (2.4)$$

$$k_0 = \frac{4\pi N}{1000}(R_f + R_q)(D_f + D_q) \qquad (2.5)$$

where k_0 is the diffusion-controlled bimolecular quenching rate constant; N is Avogadro's number; R is the collision radius, the sum of the molecule radii of the energy donor (R_f) and the energy quencher (R_q); D is the diffusion coefficients, the sum of the energy donor(D_f) and energy quencher (D_q). Diffusion coefficients can be obtained by the Stokes-Einstein equation. (Equation 2.6).

$$D = kT/6\pi\eta R \qquad (2.6)$$

where k is Boltzmann's constant, η is the solvent viscosity, R is the molecule radius. The radius of **IrBIr** or **RuBIr** is 15.6 Å and the radius of **B-1** is 5.7 Å (from optimised structure in Gaussian view). According to equation (6), the diffusion coefficients of donor and acceptor were 3.8×10^{-6} cm^{-2} s^{-1} and 1.0×10^{-5} cm^{-2} s^{-1}.

For **RuBRu**, the bimolecular triplet energy transfer value in the presence of **B-1** was also studied. The bimolecular quenching constant was calculated as $k_q = 2.09 \times 10^9$ M^{-1} s^{-1} and the quenching efficiency as 9.2 %. **RuBRu** is therefore found to undergo much more efficient bimolecular triplet energy transfer with **B-1,** than **IrBIr**.

2.6.3 Singlet Oxygen Sensing of RuBRu and IrBIr as Triplet Photosensitiser

The singlet oxygen quantum yield (Φ_Δ) can indicate the photosensitising ability of potential compounds which can be used as photosensitisers. The mechanism of this singlet oxygen sensing process is illustrated in Scheme 2.7. This work utilises 1,3-diphenylisobenzofuran (DPBF) as the scavenger. The triplet photosensitiser is excited by an external light source and undergoes ISC to its triplet excited state. The triplet energy transfers from photosensitiser to the acceptor, triplet state oxygen, $^3O_2$. It then produces singlet oxygen, $^1O_2$. In accordance with the mechanism below, the scavenger, DPBF, can then be oxidised by the singlet oxygen and the absorption of the scavenger is changed as result.

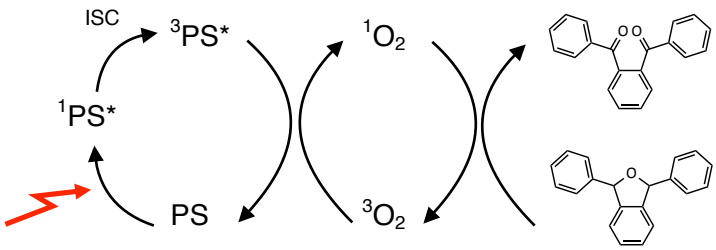

Scheme 2.6 *Mechanism of singlet oxygen photosensing process and the transformation undergone by the scavenger DPBF.*

In the experiment, the absorbance of DPBF was adjusted to around 1.0 in air-saturated solution. The photosensitiser was added to cuvette, and the absorbance of it was adjusted to around 0.2 - 0.3. The cuvette was irradiated with monochromatic light. The absorbance was measured every 15 seconds after each irradiation, at intervals for 90 seconds. The slope of absorbance maximum of DPBF at λ 410 nm versus the time graph was calculated. The singlet oxygen quantum yield was then calculated according to Equation (2.7):

$$\Phi_{\Delta unk} = \Phi_{\Delta ref} \times \frac{k_{unk}}{k_{ref}} \times \frac{F_{ref}}{F_{unk}} \times \left(\frac{\eta_{unk}}{\eta_{ref}}\right)^2 \qquad (2.7)$$

Φ_Δ is the singlet oxygen quantum yield; Unk refers to the unknown sample, ref refers to the reference sample. *K* is the slope of difference in change in absorbance of DPBF at λ 410 nm with the irradiation time and *F* is the absorption correction factor, which is given by $F = 1 - 10^{-\text{O.D.}}$ (O.D. is the optical density of the solution at the irradiation wavelength). Here, 2,6-diiodo-BODIPY, **B-2** ($\Phi_\Delta = 0.82$ in CH_2Cl_2) was chosen as the standard.

For both **RuBRu** and **IrBIr**, significant changes in the absorption at λ 410 nm were observed. (Figure 2.20) The singlet oxygen quantum yields were calculated as 79.4 % and 74.9 % respectively. Compared to their mononuclear analogues, the yields are lower.

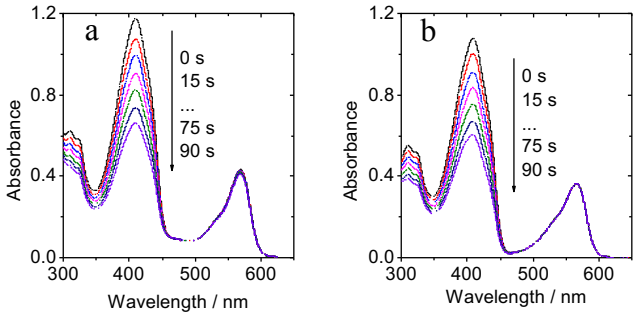

Figure 2.20 *Photosensitising of $^1O_2$. Irradiation time-dependent decrease of absorption at λ 410 nm of DPBF with (a)* ***RuBRu*** *and (b)* ***IrBIr*** *as the photosensitiser. λ_{ex} = 540 nm at 25 ^oC.*

2.6.4 Intracellular Photodynamic Studies for Potential Application of PDT

As both dinuclear complexes in this study have high singlet oxygen quantum yields, long-lived triplet excited state lifetimes, and strong broad absorbance in the visible range, features which make them suitable for their application in luminescence bioimaging and photodynamic therapy. HeLa cell, from a cervical tumour were used for this experiment. Being a cancer cell, unlike normal somatic cells, HeLa cells thrive indefinitely in laboratory tissue cultures, a trait that has allowed them to assume tremendous importance in biomedical research. Since the mid-twentieth century, the cells have been distributed around the world and used in innumerable medical testing, including investigations into the nature of cancer, the development of vaccines, the mapping of genes, the treatment of diseases, and the mechanisms involved with programmed cell death.[98, 99]

Our cell test of PDT was carried out by collaborator, Dr. Ping Hu, at the Shanghai Institute of Ceramics. In this experiment, HeLa cells were treated with 100 μM **RuBRu** and kept in the dark for 12 hours. On incubation of the cells with **RuBRu**, fluorescence microscopy shows a strong red fluorescence on excitation (Figure 2.21). The confocal images reveal that the photosensitiser, **RuBRu**, can easily penetrate into the cytosol. Since the long excitation wavelength can deep penetrate biological tissue the complex has a potential application in luminescence bioimaging and photodynamic therapy.

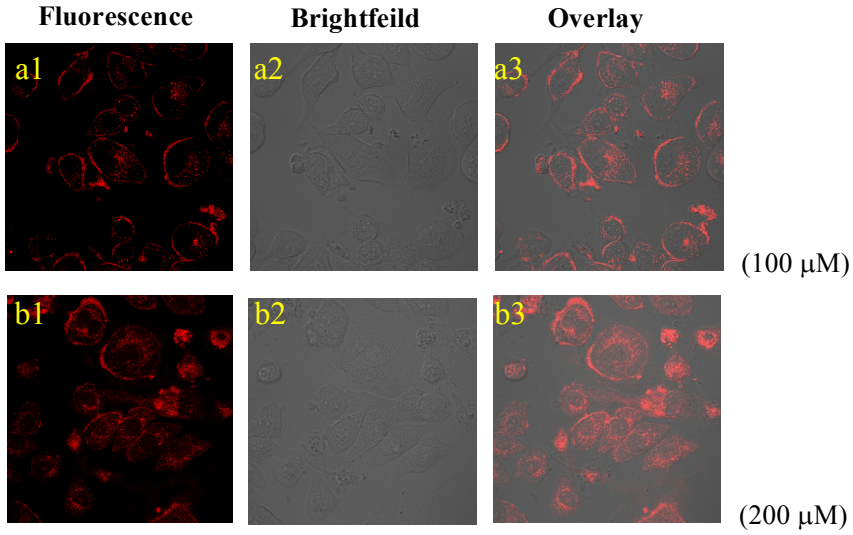

Figure 2.21 *Confocal fluorescence images in HeLa cells (λ_{ex} = 600 nm). The cells were incubated with photosensitiser* ***RuBRu*** *(a) (1.0 × 10^{-4} mol/L) and (b) 2.0 × 10^{-4} mol/L at 37 ^{o}C in the dark for 12 h.*

The photocytotoxic activity results of the complexes are shown in Figure 2.22. The HeLa cells were treated with **RuBRu** for 12 hours and irradiated with a λ 600 nm laser for 30 minutes. Trypan blue-stained cells indicated that a large proportion of the cancer cells were killed (Figure 2.22b). In the control experiment, the cancer cells survived in the absence of the triplet photosensitiser (Figure 2.22a).

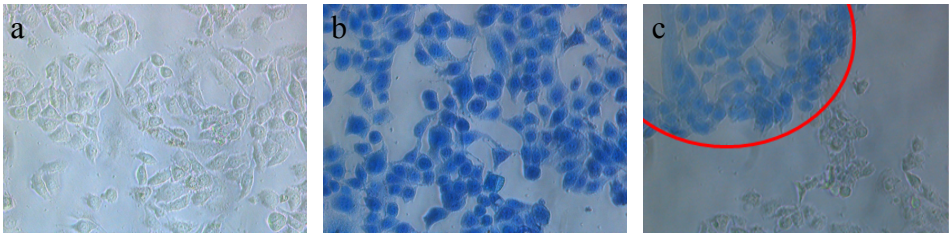

Figure 2.22 *Photocytotoxic activity of the sensitisers with Trypan blue-stained images of HeLa cells. (a) Cells incubated in the dark in the absence of triplet photosensitiser for 12*

h and illuminated with laser (600 nm, 0.2 W·cm^{-2}) for 30 min. (b) Cells incubated with ***RuBRu*** *(1.0 × 10^{-4} mol/L) and kept in dark for 12 h and illuminated with laser (600 nm, 0.2 W·cm^{-2}) for 30 min. (c) Cells incubated with* ***RuBRu*** *(1.0 × 10^{-4} mol/L) and kept in dark for 12 h and illuminated with spot laser light source (600 nm, 0.2 W·cm^{-2}). The cells marked in the red circle were under the illumination with laser.*

In a dark cytotoxicity experiment, the viable cells were treated with increasing concentrations of each photosensitiser. As shown in Figure 2.23, in the absence of light exposure, both **RuBRu** and **IrBIr** exhibit negligible dark toxicity to HeLa cells. The cellular viability was estimated to be greater than 90 % even at high concentration (300 μM). This is especially evident in the images obtained for **RuBRu**, where the cellular viability was estimated to be over 95 % at the concentration of 200 μM. Compared to a standard dinuclear cyclometalated iridium complex,[100] each complex showed low dark toxicity and long wavelength absorption. These positive results support the postulate that triplet photosensitisers **RuBRu** and **IrBIr** could be useful in the future as theranostic agents.

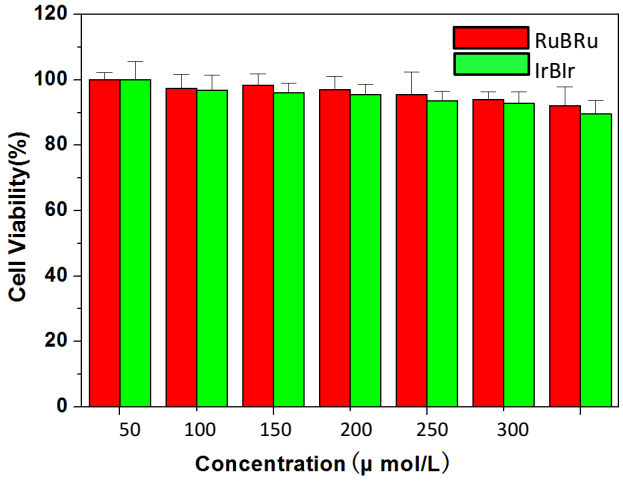

Figure 2.23 *In vitro cytotoxicity of* ***RuBRu*** *or* ***IrBIr*** *complex against HeLa cells at different concentrations after 24 h incubation in the dark by CCK-8 assay.*

Flow cytometric analyses of cell apoptosis experiment were carried out. In biotechnology, flow cytometry is a laser- or impedance-based, biophysical technology employed in cell counting, cell sorting, biomarker detection and protein engineering, by suspending cells in a stream of fluid and passing them by an electronic detection apparatus. It allows simultaneous multiparametric analysis of the physical and chemical characteristics of up to thousands of particles per second. There are two kinds of indicator, annexin V and

propidium iodide (PI). Annexin V is a Ca^{2+}-dependent phospholipid-binding protein that has a high affinity for phosphatidylserine. Phosphatidylserine is located inner of the cell membrane while would be transferred to outer of apoptotic cells. PI has an ability to bind to nucleic acid of dead cells.[101] Therefore, live cells show negative results for both annexin V and PI (B2); At the early stage of apoptosis, cells bind annexin V while still excluding PI (B4); The late apoptotic cells or dead cells are marked in B2 area, showing positive results of annexin V and PI.

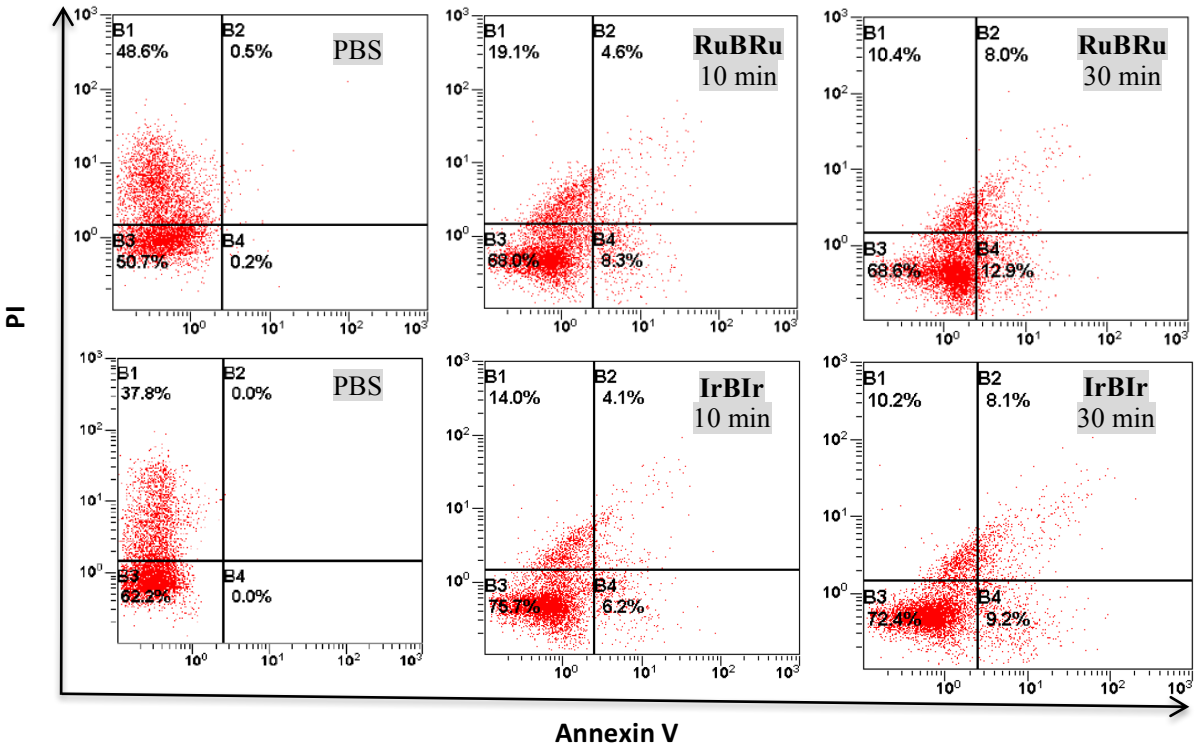

Figure 2.24 *Flow cytometric analyses of cell apoptosis treated with PBS (Phosphate-buffered Saline),* ***RuBRu*** *(100 μM) or* ***IrBIr*** *(100 μM) and then irradiated with 600 nm laser light (1 W·cm^{-2}) for 10 min and 30 min.*

According to our results in Figure 2.24, both of **RuBRu** and **IrBIr** showed positive results of PDT. With the increasing of exposure time, the number of cells in the early and late stage of apoptosis are increasing. **RuBRu** showed a marginally better result than **IrBIr**. Overall, this study shows that the lower toxicity, cost and higher efficiency of the BODIPY bridged dinuclear ruthenium complex is more suitable for photodynamic therapy than its iridium derivative.

2.7 Conclusion

Two BODIPY bridged binuclear transition metal complexes **RuBRu** and **IrBIr** were prepared. Their strong visible light-harvesting ability is due to the presence of a second metal centre, with both **RuBRu** and **IrBIr** performing better than their mononuclear transition metal analogues. The fluorescence of their BODIPY moieties was substantially quenched by efficient intersystem crossing. Dual phosphorescence was observed from both **RuBRu** and **IrBIr**. The strong intraligand (^{3}IL*) character of the T_1 state, is likely to be responsible for the long-lived triplet excited states of each complex. For **RuBRu**, τ_T is observed as 1316.0 μs. To the best of our knowledge, this is the longest triplet excited state lifetime resulting from a BODIPY based chromophore.

The complexes were used as triplet photosensitizers for two triplet-triplet energy transfer related processes, TTA upconversion and singlet oxygen quenching. In both applications, **RuBRu** and **IrBIr** demonstrate improved a performance *versus* current reports in the literature. With DPA as a triplet acceptor, **IrBIr** shows a high upconversion quantum yield (Φ_{UC} = 25.5 %) while the singlet oxygen quantum yield of **RuBRu** and **IrBIr** are 79.4 % and 74.9 % respectively.

Both complexes proved to be excellent candidates for photodynamic therapy with initial cell experiments showing minimal dark toxicity to HeLa cells, and promising uptake into the cytosol. Their unusual low energy and intense absorption makes them particularly effective photosensitisers for PDT. This study adopts a systematic approach to enhancing the molecular design of each photosensitisers, and reveals the fundamental improvements and novel opportunities that be created from the application of bimetallic complexes.

3 Novel Ruthenium and Iridium Complexes of N-substituted Carbazole as Triplet Photosensitisers

3.1 Introduction

As we discussed in Chapter 2, Ziessel and co-workers reported a series of dinuclear Ru-terpy derivatives with aromatic bridging ligands including benzene, naphthalene, anthracene, and pyrene; and unsaturated simple hydrocarbon chains, including phenylene, and acetylenic groups.[88, 102] They concluded that the dinuclear complexes often have longer triplet excited state lifetimes compared to their mononuclear analogues, especially when the ligand is highly conjugated.[103, 104] Further to the discussion in Chapter 2,[89] the introduction of a second transition metal centre to generate a bridged symmetric dinuclear transition metal complex can result in significantly enhanced absorbance, with prolonged triplet lifetimes. In this chapter, a series of carbazole-based transition metal complexes (mono- and di-nuclear N-substituted carbazole-bridged ruthenium and iridium complexes) were introduced. The dinuclear complexes resulted in a desirably high absorption.

3.2 Synthesis of Mono- and Di-nuclear N-substituted carbazole-bridged Ruthenium and Iridium Complexes

3-Bromo-9H-carbazole (**L0**) is a common and commercially available compound. 3-Bromo-9-hexyl-carbazole (**L1**) was synthesised *via* an amino-alkylation reaction between 1-bromohexane and **L0**. The mixture was refluxed in THF for 2 h and generated the product with a high yield (98.6 %). (Scheme 3.1)

The carbazole ring system of **L1** is essentially planar and the n-hexyl chain is in the fully extended conformation. The acetylene of **L2** was attached *via* a Sonogashira coupling reaction with TMSA. Unlike in the BODIPY-bridged dinuclear complexes where the silyl-protecting group was removed at low temperature with a mild base, the silyl-protecting group in **L2** was removed by a strong base system (a mixture of potassium fluoride and potassium hydroxide) in methanol at room temperature. It should be noted that **L2** is a viscous colourless liquid.

The final compounds, **RuC** and **IrC**, were synthesised *via* a Sonogashira coupling reaction with **Ru-1** and **Ir-1**, respectively. The detailed syntheses of **Ru-1** and **Ir-1** were mentioned in the previous chapter.

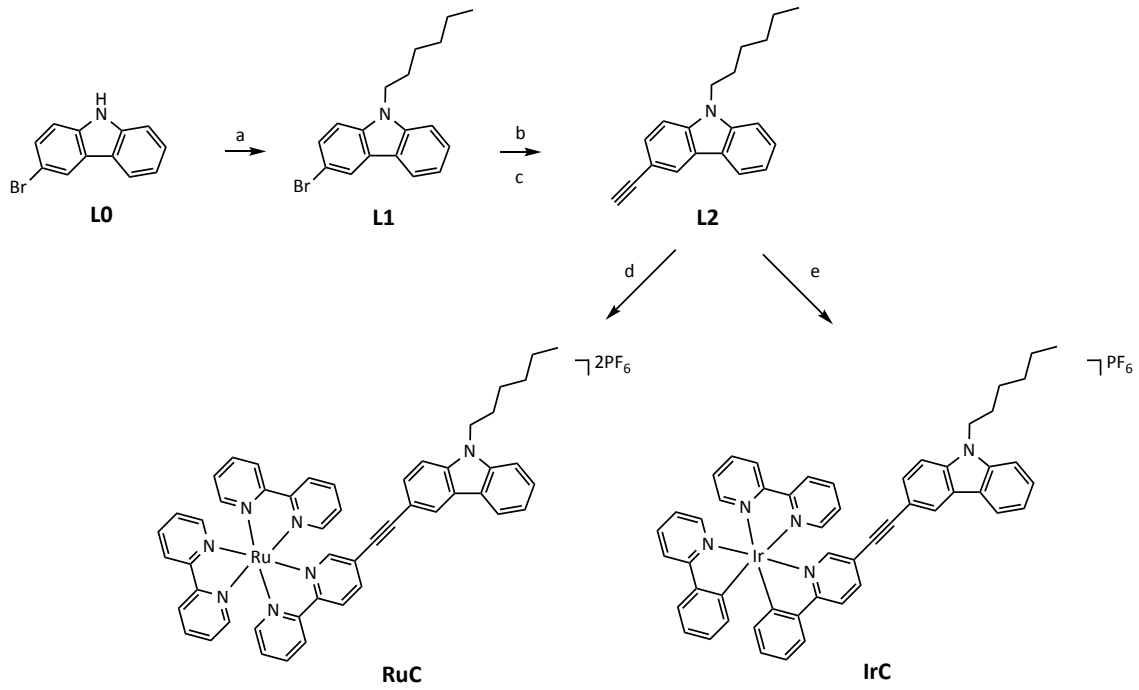

Scheme 3.1 *Synthesis of mononuclear N-substituted carbazole ruthenium complex (**RuC**) and iridium complex (**IrC**). (a) 1-bromohexane, THF, reflux, 2 h, yield: 99 %. (b) TMSA, dry $(CH_3CH_2)_3N$, $Pd(PPh_3)_2Cl_2$, PPh_3, CuI, Ar, overnight, 90 ℃, yield: 59 %. (c) CH_3OH, KF, KOH, Ar, 3 h, yield: 89 %. (d) $Pd(PPh_3)_2Cl_2$, PPh_3, CuI, dry $(CH_3CH_2)_3N$:CH_3CN (1:1, v/v), Ar, 90 ℃, overnight, yield: 24 %. (e) $Pd(PPh_3)_2Cl_2$, PPh_3, CuI, dry $(CH_3CH_2)_3N$:CH_3CN (1:1, v/v), Ar, 90 ℃, overnight, yield: 52 %.*

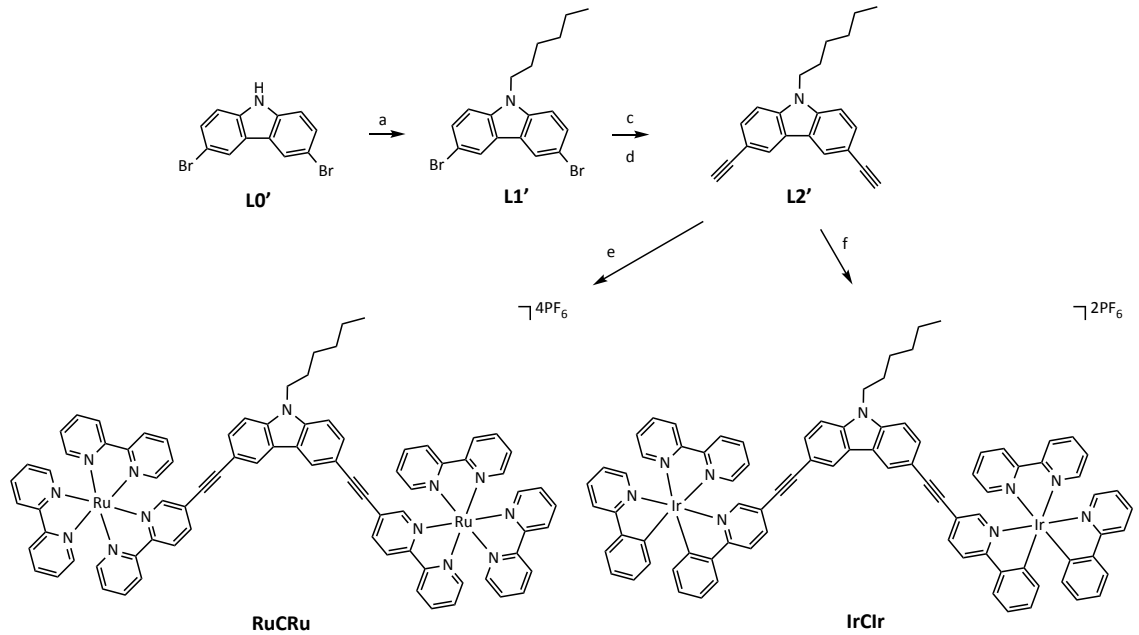

Scheme 3.2 *Synthesis of dinuclear N-substituted carbazole-bridged ruthenium complex (**RuCRu**) and iridium complex (**IrCIr**). (a) 1-bromohexane, THF, reflux, 2 h, yield: 70 %. (b) TMSA, dry $(CH_3CH_2)_3N$, $Pd(PPh_3)_2Cl_2$, PPh_3, CuI, Ar, overnight, 80 °C, yield: 56 %. (c) CH_3OH, KOH, N_2, 3 h, yield: 96 %. (d) $Pd(PPh_3)_2Cl_2$, PPh_3, CuI, dry $(CH_3CH_2)_3N$:CH_3CN (1:1, v/v), Ar, 60 °C, overnight, yield: 13.3 %. (e) $Pd(PPh_3)_2Cl_2$, PPh_3, CuI, dry $(CH_3CH_2)_3N$:CH_3CN (1:1, v/v), Ar, 60 °C, 10 h, yield: 46.3 %.*

The synthesis of dinuclear complexes based on N-substituted carbazoles was similar to their mononuclear analogues. The main difference is that the addition of **Ru-1** and **Ir-1** in steps (e) and (f) in Scheme 3.2 is carried out in excess, in order to promote complete coupling of the acetylenes to the metal centres, in order to avoid the formation of mono-substituted derivatives, and also to make following purification easier.

3.3 Structural Characterisation

3.3.1 Crystallographic Analysis of RuC

The crystals of **RuC** suitable for single crystal X-ray diffraction were obtained by the slow evaporation from a solvent mixture of acetone and hexane. Data for **RuC** were collected on a Bruker APEX DUO using Cu Kα radiation (λ = 1.54184 Å) by Dr. Brendan Twamley in Trinity College Dublin. The sample was mounted on a Mitegen cryoloop and data collected at 100(2) K (Oxford Cobra cryosystem). Bruker APEX[105] software was used to collect and reduce data, determine the space group, solve and refine the structures. Absorption corrections were applied using SADABS 2014[106]. All non-hydrogen atoms were refined anisotropically. Hydrogen atoms were assigned to calculated positions using a riding model with appropriately fixed isotropic thermal parameters. $C_{50}H_{43}F_{12}N_7P_2Ru$ (M =1132.92 g/mol): triclinic, space group P-1 (no. 2), a = 9.9192(3) Å, b = 12.7350(4) Å, c = 19.0381(6) Å, α = 86.0585(19)°, β = 80.675(2)°, γ = 83.0251(18)°, V = 2352.61(13) Å^3, Z = 2, T = 100(2) K, μ(CuKα) = 4.163 mm^{-1}, $Dcalc$ = 1.599 g/cm^3, 38148 reflections measured (4.71° ≤ 2Θ ≤ 136.894°), 8598 unique (R_{int} = 0.0686, R_{sigma} = 0.0548) which were used in all calculations. The final R_1 was 0.0494 (I > 2σ(I)) and wR_2 was 0.1380. **CCDC no. 1566335**.

The complex displays a distorted octahedrally coordinated Ru centre (Σ = 72.9(6) °)[107] surrounded by two bipys and the bipycarbazole ligand, with Ru-N bonds lengths of 2.054(4)-2.086(3) Å, see Figure 3.1. The ligand is not planar with a significant twist of

48.46(9)° between the bipy and the carbazole moieties. There is also an angle of 113.99(10) ° between the carbazole and the hexyl arm. The extended structure does not show the expected Ru bipy packing motifs observed in the literature.[108] In the structure of **RuC**, there are no strong intermolecular interactions or H-bonding. Weaker interactions are present and a Hirshfeld surface analysis[109] shows the majority of these are CH…F and CH…π interactions (Figure 3.2 and 3.3).

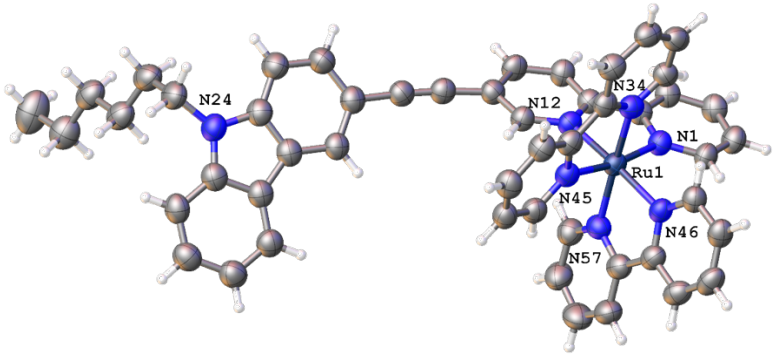

Figure 3.1 *Partially labelled atomic displacement (50% probability) image of* ***RuC*** *with both PF_6 counter ions removed for clarity.*

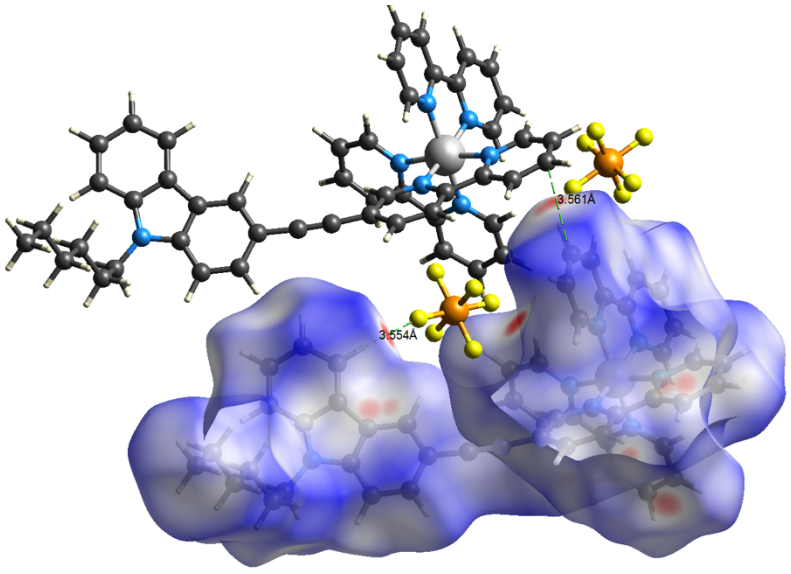

Figure 3.2 *Hirschfeld surface mapped with d_{norm} for* ***RuC*** *over the range -0.29 to 1.37. PF_6 anions and a neighbouring cation with close contacts are shown with some of the distances involved. The CH…π of C54...C4i is ca. 3.56Å.*

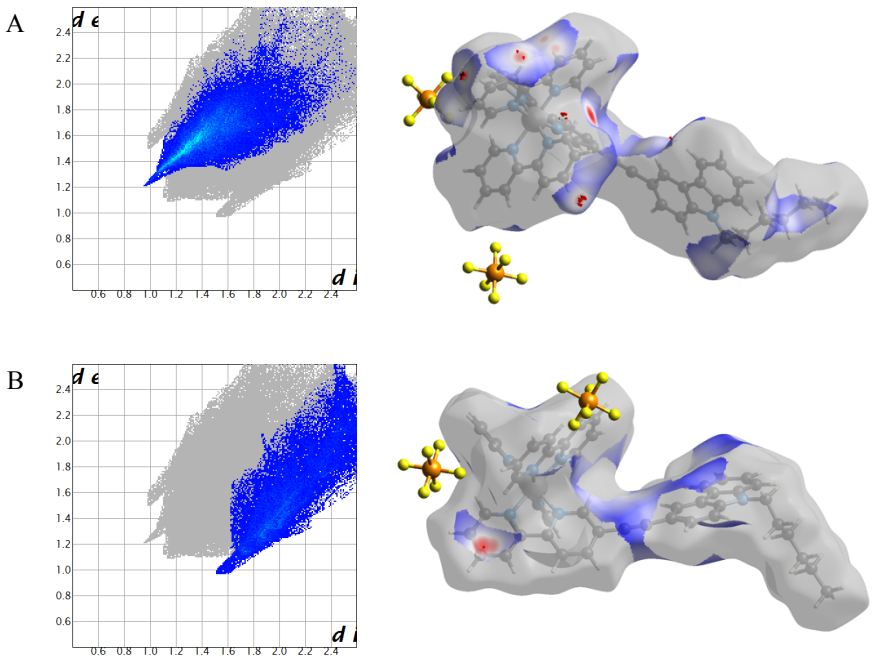

Figure 3.3 *Fingerprint plots of* ***RuC*** *broken down into contributions from specific pairs of atom types. The blue highlighted section of the plot is (A) internal H to external F (CH..F interactions and (B) internal C to external H contributions which includes the CH…π interactions. The corresponding highlighted Hirshfeld plot is on the right.*

3.3.2 Structural Characterisation of RuC and IrC *via* NMR Studies

The isolated **RuC** and **IrC** complexes were characterised by a range of NMR techniques, including 1-D and 2-D NMR spectroscopy. Due to their similar structure, only **IrC**'s structural characterisation was discussed here.

As the proton spectrum is well resolved, the proton signals can clearly be integrated. (Figure 3.4) The triplet signal due to the methyl group on the hexyl chain was found at δ 0.83 ppm (●). The deshielding effect of the nitrogen atoms in the structure on the chemical shift of the -CH_2- groups in the hexyl chain results in an increase in the chemical shift with increasing proximity to N. Therefore, the ethyl groups were found at δ 1.28 ppm, δ 1.82 ppm and δ 4.36 ppm (● ● ●). The other protons in the region of low-field chemical shift are assigned to the phenyl and pyridyl rings, and the carbazole moiety (δ 6.00–8.60 ppm). This was further confirmed by 2-D and carbon NMR spectroscopy.

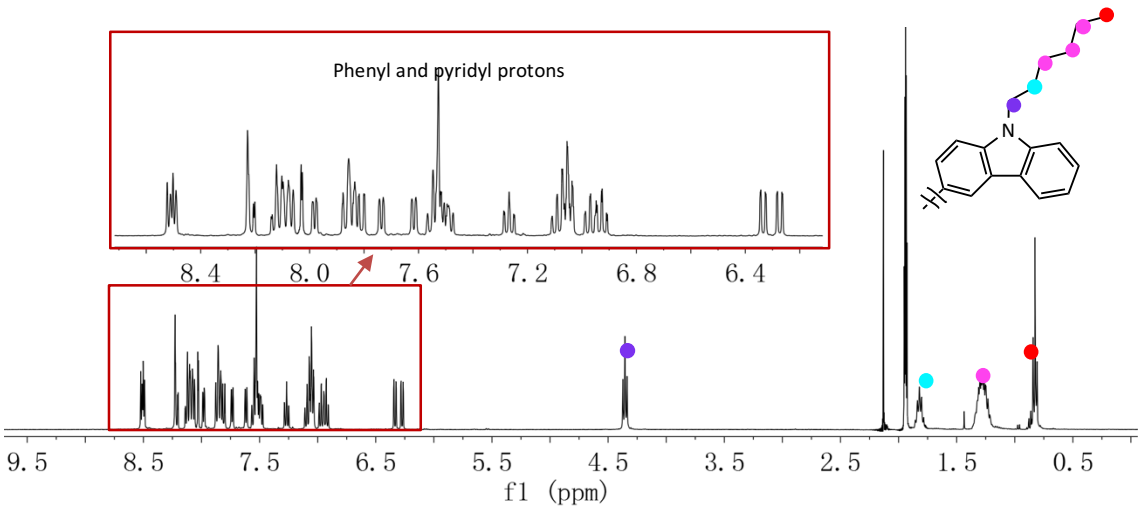

Figure 3.4 *^{1}H NMR spectrum of* ***IrC*** *(400 MHz, CD_3CN), 20 ^{o}C.*

As we can see from the structure of **IrC** (Figure 3.5), it consists of eight spin systems: one three-spin and one four-spin system corresponding to the carbazole moiety (in green), three pyridyl four-spin and one pyridyl three-spin system (in orange), two phenyl four-spin system of 2-phenylpyridine (in blue). Since the proton spectrum was well resolved, the proton signals can be grouped into their own spin system by examining the cross peaks in the ^{1}H-^{1}H COSY (Figure 3.5). HSQC is useful in assigning pyridyl C-H due to pyridyl carbon signals usually have a larger chemical shift. In Figure 3.6, four proton signals were observed in the N-atom adjacent to the ^{13}C typical region (δ 145-160 ppm, in which pyridyl carbons attached to N-atoms are usually found). Then the pyridyl spin systems were facilely assigned in ^{1}H-^{1}H COSY (orange boxes).

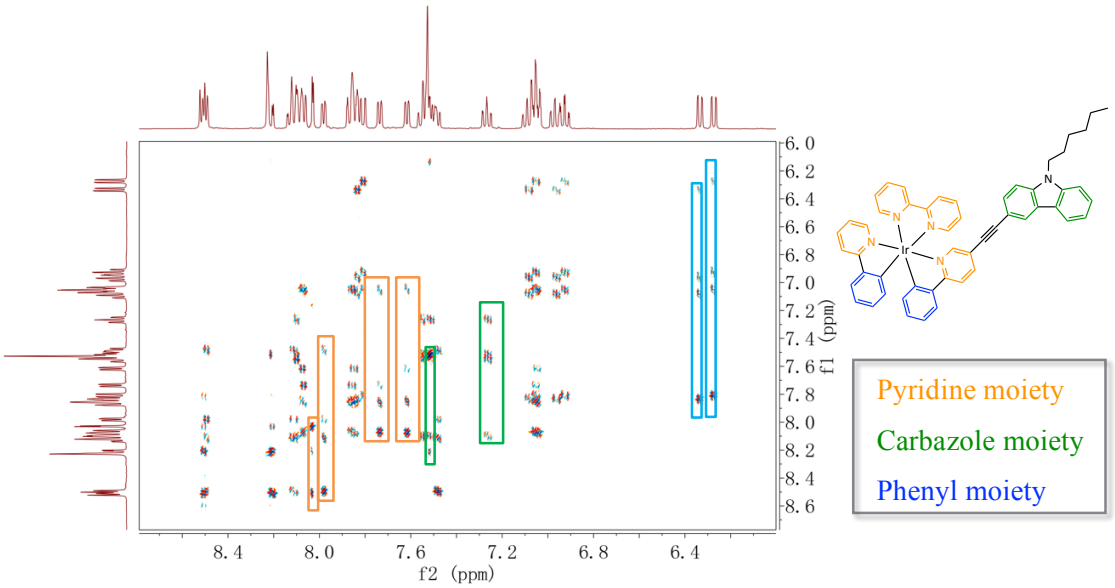

Figure 3.5 *The ^{1}H-^{1}H COSY analysis of* ***IrC*** *(400 MHz, CD_3CN, 20 ℃).*

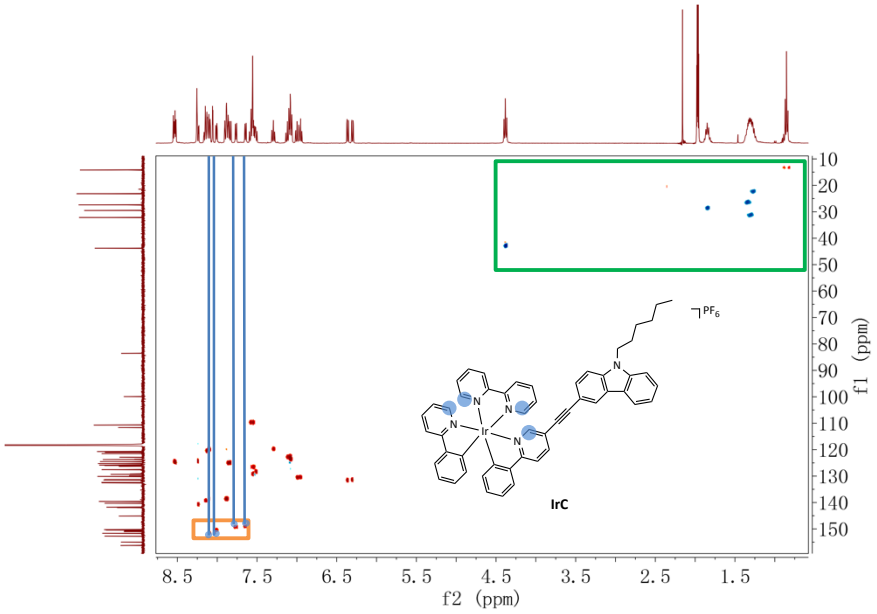

Figure 3.6 *The HSQC analysis of* ***IrC*** *(400 MHz, CD_3CN, 20 ^oC).*

In the ^{13}C NMR spectrum (Figure 3.7), two typical signals of acetylene carbons were found in the upfield region which were deshield by the carbazole moiety (δ 99.82 and 83.50 ppm). The hexyl carbons were found in the downfield region δ 14-44 ppm. It should be noted here, the carbon at δ 30.82 ppm and δ 207.43 ppm were assigned to the solvent acetone.

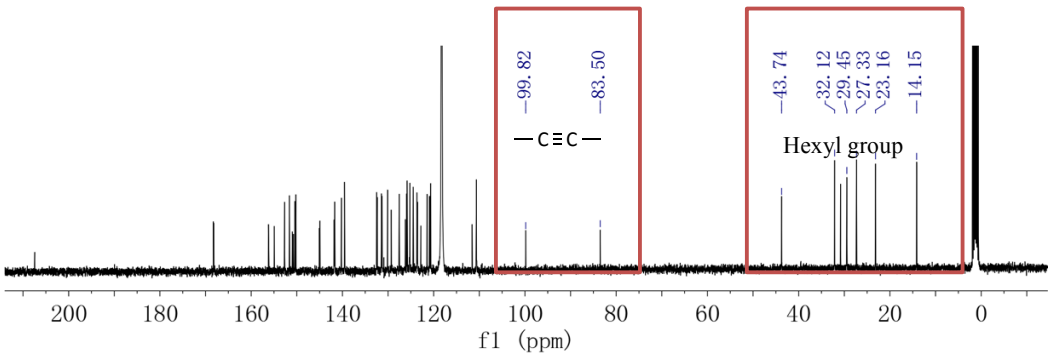

Figure 3.7 *^{13}C NMR spectrum of* ***IrC*** *(100 MHz, CD_3CN, 20 ℃).*

The mass spectroscopy analysis further confirmed the presence of **IrC** using MALDI-TOF mass spectrometry. The results showed the value of the $[C_{52}H_{43}N_5Ir]^+$ ion was *m/z* 930.3156, which correlates to the calculated value ($[C_{52}H_{43}N_5Ir]^+$) *m/z* = 930.3148 well.

3.3.3 Structural characterisation of RuCRu and IrCIr

Due to the symmetric structures of **RuCRu** and **IrCIr**, their characterisation was accordingly quite straightforward . Since the structural analysis is similar to their mononuclear analogues, their further detailed NMR data and mass spectra are presented in the experimental chapter.

3.4 Photophysical Studies

3.4.1 Steady State Studies

The absorption spectra of the mono- and di- nuclear N-substituted carbazole bridged complexes are shown in Figure 3.8.

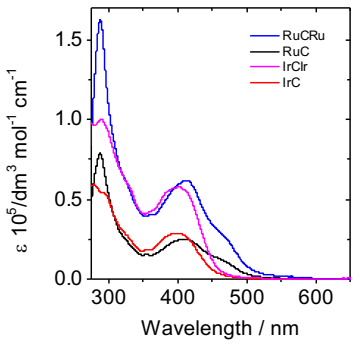

Figure 3.8 *Absorption spectra of* ***RuCRu***, ***IrCIr***, ***RuC*** *and* ***IrC****. C = 1.0 × 10^{-5} mol/L in CH_3CN, 298 K.*

For **RuCRu**, the intense absorption at λ 288 nm was assigned to the π → π* transition of the parent 2,2'-bipyridine ligand. The band at 412 nm was assigned to an intraligand π →π* transition of the ancillary carbazole-substituted bipyridine ligand.[110] The shoulder band at approximately 470 nm is dominated by a metal to ligand charge transfer (^{1}MLCT). The low-energy ^{1}MLCT absorption band of **RuCRu** is bathochromically shifted by 20 nm when compared to that of [Ru(bpy)$_3^{2+}$].[34] This can be attributed to the extended π-conjugation of the **RuCRu** bridging ligand, and the strong electron donating N-substituted carbazole component of that same ligand structure. It results in a decrease in the HOMO and LUMO gap.[111, 112] This explanation was further confirmed through cyclic voltammetry measurements (see Table 3.2). The enhanced absorbance intensities of the dinuclear structures are immediately apparent in Figure 3.8. The molar absorption

coefficient of **RuCRu** (λ_{abs} 412 nm, ε 62, 000 dm^3 mol^{-1} cm^{-1}) is approximately twice that of its mononuclear analogue, **RuC** (λ_{abs} 411 nm, ε 25 000 dm^3 mol^{-1} cm^{-1}). Comparable results are also observed with **IrCIr** and **IrC**. Therefore, the introduction of the second metal centre could increase the absorption of complexes.

The absorption of all four complexes were measured in four solvents of different polartiy, namely toluene, dichloromethane, methanol and acetonitrile. As can be observed from Figure 3.9, all of them show a blue shifted absorption with increasing polarity. This indicates that the ground state will be affected by the polarity of the solvent.

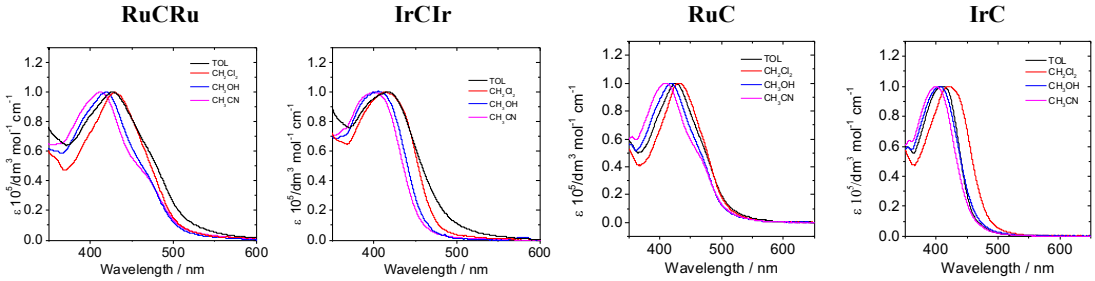

Figure 3.9 *Normalised absorption spectra of compounds in different solvents. C = 1.0 × 10^{-5} mol/L in CH_3CN, 298 K.*

The emission properties of the generated complexes were also studied under various different atmospheres and temperatures. For **RuCRu,** the emission band at λ 642 nm measured under N_2 was quenched in an aerated solution, with the luminescence measurement possessing a microsecond scale lifetime (1.2 μs). (Figure 3.10) This result implies that the luminance of **RuCRu** has a strong phosphorescent character. Compared to **[Ru(bpy)$_3^{2+}$]**,[34] the phosphorescence emission is bathochromically shifted by 37 nm, with the lifetime being prolonged from 0.8 μs to 1.2 μs. Similar results were found for **RuC**, **IrCIr** and **IrC**.

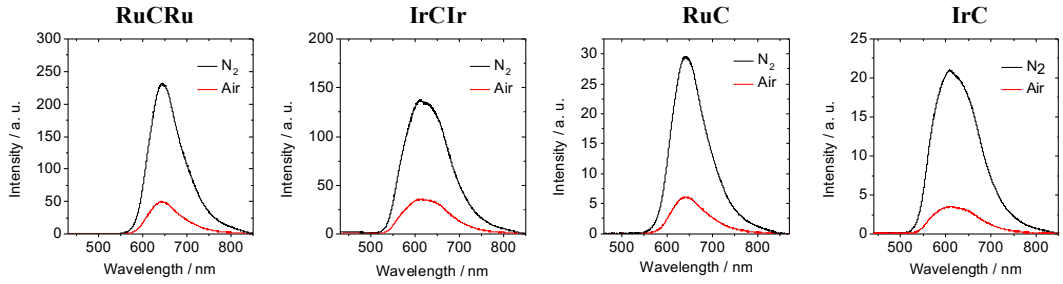

Figure 3.10 *Emission spectra of **RuCRu**, **IrCIr**, **RuC** and **IrC**. C = 1.0 × 10^{-5} mol/L in CH_3CN, 298 K.*

Both the mononuclear and dinuclear complexes showed a large thermal anti-Stokes shift between the room and low temperature (77 K) emission measurements (Figure 3.11). The anti-Stokes shift indicates the presence of these expected charge separated states (charge transfer (CT) processes).[81] Moreover, for example, the emission bands from the triplet metal-to-ligand charge transfer (^{3}MLCT) states are generally broad and featureless, while ligand-based ($^3\pi-\pi^*$) states typically give highly structured emission profiles at room temperature (IL-intraligand). Considering the relatively short lifetimes, these emissions were assigned as mainly a mixture of ^{3}MLCT* and ^{3}ILCT*.

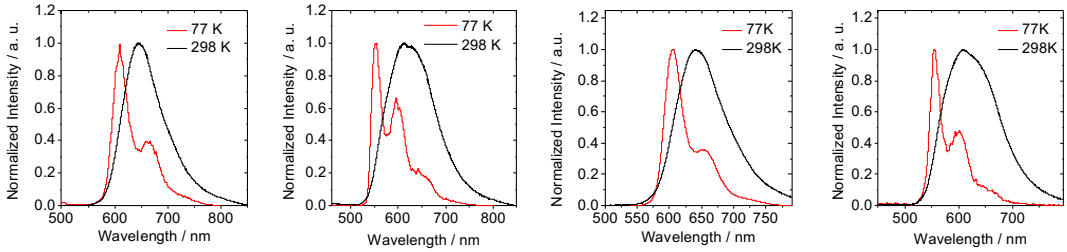

Figure 3.11 *Normalised emission spectra of low temperature (in red) and room temperature (in black). C = 1.0 × 10^{-5} mol/L in CH$_3$CN, 298 K.*

Table 3.1 *Photophysical properties of* ***RuCRu***, ***RuC***, ***IrCIr*** *and* ***IrC***.

	λ_{abs} (nm)	ε [b]	λ_{em} [c] (nm)	Φ_P [d] (%)	τ_P [e] (μs)
RuCRu	288/ 412	1.63/ 0.62	644	6.7	1.2 [e1]/4.7 [e2]
RuC	288/ 411	0.79/ 0.25	642	6.9	1.3 [e1]/3.9 [e2]
IrCIr	288/ 400	1.00/ 0.58	614	5.0	0.4 [e1]/2.7 [e2]
IrC	279/ 399	0.59/ 0.29	613	8.3	0.9 [e1]/5.0 [e2]

[a] Results of complexes in CH$_3$CN solution (1 × 10^{-5} M), 298 K. [b] Molar absorption coefficient, ε 10^5 dm^{-3} mol cm^{-1}. [c] Emission peak at 298 K in N^2. [d] Quantum yield of phosphorescence, in N_2, with 2,6-diiodo-BODIPY as a standard (Φ_F = 2.7% in CH$_3$CN).[56] [e] Phosphorescence lifetime, λ_{ex} = 403 nm, at 298 K (e1) and 77 K (e2) in N_2.

3.4.2 Transient State Studies

In order to study the triplet excited states of these complexes, the nanosecond time-resolved transient difference absorption spectra were studied. Upon excitation, a significant bleaching peak at λ 400 nm was observed in **RuCRu** (Figure 3.12a) due to depletion of the ground state. This corresponds to π → π* transitions within the ancillary carbazole-substituted bipyridine ligand (LC), indicating that the triplet excited state of

RuCRu is localised on the large bridging ligand. However, the phosphorescence emission of **RuCRu** was assigned to the ^{3}MLCT state, as previously discussed. It was therefore proposed that the triplet excited states of **RuCRu** contain mixed characters of both ^{3}LC and ^{3}MLCT. By comparison with the transient absorption spectrum of $[Ru(bpy)_3^{2+}]$ (Figure 3.12c), the ^{3}MLCT bleaching peak of **RuCRu** (expected at approx. λ 450 nm) would be overlapped by the strong positive signal at λ 425-750 nm from the ancillary carbazole-substituted bipyridine ligand (LC). Similar results were also obtained for **RuC** (Figure 3.12b), **IrCIr** and **IrC** (Annex, Figure A1 a,b). The triplet lifetimes of the complexes were also determined and displayed in Table 3.4. The triplet lifetimes were observed to correspond to their phosphorescence lifetimes.

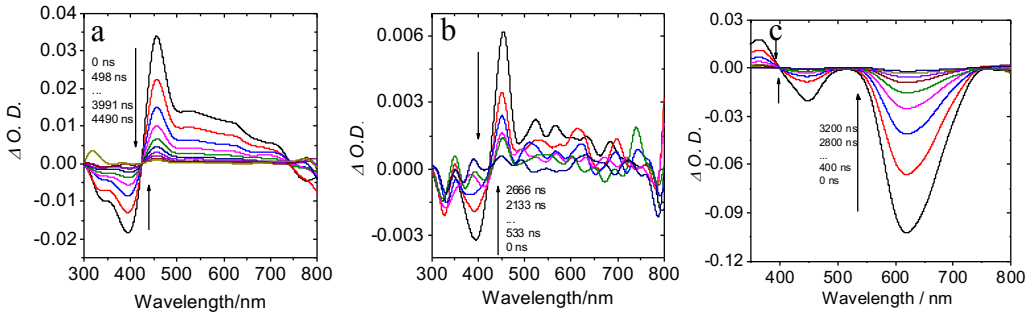

Figure 3.12 *Nanosecond time-scaled transient difference absorption spectra of (a)**RuCRu**, (b)**RuC** and (c)$Ru(bpy)_3^{2+}$ in CH_3CN at 298 K. C = 1.0 × 10^{-5} mol/L.*

3.5 Electrochemical Studies

The electrochemical properties of the generated complexes were studied *via* cyclic voltammetry measurements. (Table 3.2). The oxidation potentials (E_{ox}) of **RuCRu** and **RuC** are compared to the reported oxidation potential data of the parent $[Ru(bpy)_3]^{2+}$ [113]. Both the potentials are close to the parent tribipyridine ruthenium complex. For **RuCRu**, the oxidation process is reversible, and MLCT dominates this process. For **RuC**, the oxidation process is also irreversible, and so it can be concluded that there is not only MLCT involved in this oxidation process, but the N-carbazole based ligand is also involved. Otherwise, the oxidation potential will be nice reversible with a small value of ΔE_p. Therefore, the HOMO is not only located on the metal centre, it is also delocalised all the way through the ligand. In other words, it confirms that there is mixing of MLCT and ILCT. Similar results were also obtained from **IrCIr** and **IrC**. (Of note here however,

is that even though **RuCRu** is a symmetric bimetallic structure, the oxidation and reduction processes are assumed to be one electron processes. Similar results were seen by Salpage *et al.*, where the observed redox couples in the bimetallic complexes are confirmed as one electron processes.[114] Also, it can be confirmed with the same ΔI between the reversible oxidation and reduction peaks.) The first oxidation event is a single electron process from one of the metal centres, despite there being two metal centres. This first oxidation occurs within the solvent window of acetonitrile, with the second oxidation likely occurring at a higher potential, and outside of the solvent window. As reported by Salpage, this is likely due to electrostatic interactions, with the second oxidation resulting in a large solvent reorganisation energy. For the reduction potentials (E_{red}) of **RuCRu**, the first reduction is found at −1.58 V, and lower than the first reduction potential of the parent $[Ru(bpy)_3]^{2+}$. This is likely to be the reduction of the largely conjugated carbazole-substituted bipyridine ligand. A similar result can be observed for **IrCIr**. The CV plots of **RuCRu** and **IrCIr** (Figure 3.13), show a sharp wave shape, indicating that electroprecipitation is occurring at this redox process.[115, 116]

Table 3.2 *Electrochemical Potentials vs. Fc (+/0)* [a]

Compound	Oxidation $E_{1/2}$(V)[ΔE_p(mV)]	Reduction $E_{1/2}$[ΔE_p(mV)]
RuCRu	+0.93[74]	−1.58[62]; −1.82[92][c1]
RuC	+0.94[E_{pa}]	−1.58[55]; −1.88[76]
IrCIr	+0.99 [E_{pa}]	−1.56[88][c2]
IrC	+0.95 [E_{pa}]	−1.59[56]
$[Ru(bpy)_3]^{2+}$ [b]	+0.90	−1.77; −1.97; −2.21
$[Ir(ppy)_2(bpy)]^+$ [117]	+0.87	−1.78

[a] Cyclic voltammetry in deaerated CH_3CN containing a 0.10 M Bu_4NPF_6 supporting electrolyte; the counter electrode is a Pt electrode; the working electrode is a glassy carbon electrode; the $Ag/AgNO_3$ couple is the reference electrode. Ferrocene (Fc) was used as an internal reference. C[Ag^+] = 0.1 mol/L; 0.5 mM photosensitiser in deaerated CH_3CN at 298 K. [b] These values were calculated from a literature source.[113] c Electroprecipitation effect on reduction. [c1] E_{pc} = −1.86 V; E_{pa} = −1.77 V. [c2] E_{pc} = −1.60 V; E_{pa} = −1.52 V.

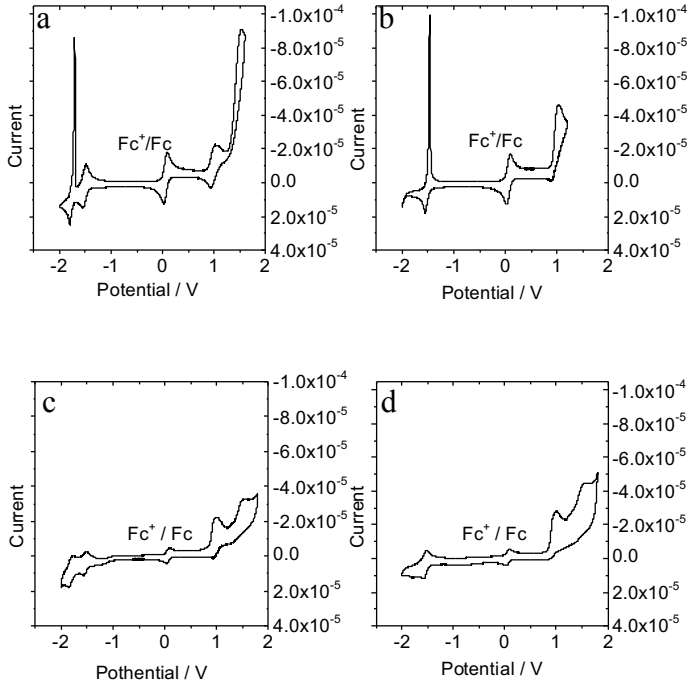

Figure 3.13 *Cyclic Voltammetry plots of a)* ***RuCRu****, b)* ***IrCIr****, c)* ***RuC*** *and d)* ***IrC*** *in CH_3CN under a nitrogen atmosphere at room temperature.*

3.6 Density Functional Theoretical (DFT) Calculation

In order to confirm the mixture of ^{3}ILCT and ^{3}MLCT states of **RuCRu**, density functional theory (DFT) calculations were carried out. The isosurface of spin density of the triplet state was computed using the optimised geometry. Shown in Figure 3.14, the triplet spin density is located on both the large ancillary carbazole-substituted bipyridine ligands and their coordinated metal centre. These computational measurements are in full agreement with the transient absorption experimental data.

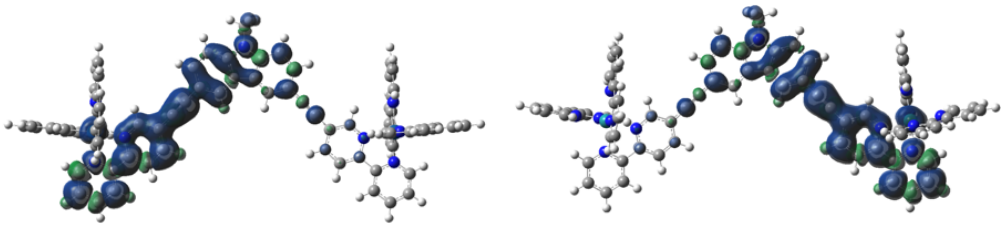

RuCRu **IrCIr**

RuC **IrC**

Figure 3.14 *Isosurfaces of spin density of* ***RuCRu***, ***RuC***, ***IrCIr*** *and* ***IrC*** *at the optimised triplet-state geometries. CH_3CN was used as the solvent in the calculations. Calculation was performed at TDDFT/B3LYP/GENECP/LANL2DZ with Gaussian 09.*

The absorption and triplet state energy levels of those complexes were also calculated with time-dependent DFT (TDDFT). The results correspond highly to the experimental data. **RuCRu** was chosen as an example to be analysed here. In Table 3.3, the calculated absorption wavelengths of **RuCRu** are λ 493 nm and λ 400 nm. They are found to be close to the experimental results (λ_{abs} = 470 nm and 412 nm). Their characters are mainly MLCT and ILCT respectively. For its triplet energy results, there are two triplet excited states found at λ 594 (2.08 eV) and 578 nm (2.14 eV). It means that T_1 and T_2 are close to each other. Moreover, they correspond to MLCT and ILCT. In summary, this supports the conclusion of the transient absorption results (Figure 3.12). For **RuC**, the energy of T_2 is much higher than T_1. Therefore, it is more difficult for it to be emissive. The tables of calculation results of **IrCIr** and **IrC** are presented in the Annex (Table A1,A2).

Table 3.3 *Electronic Excitation Energies (eV) and corresponding Oscillator Strength (f), main configurations and CI coefficients of the Low-lying Electronic Excited States of the complex* ***RuCRu*** *calculated by TDDDFT/B3LYP/GENECP/LANL2DZ, CH_3CN as the solvent (PCM model) based on the optimised Ground State Geometries.*

	Electronic transition	**TDDFT//B3LYP/GEN**				
		Energy [a]	***f*** [b]	**Composition** [c]	**CI** [d]	**Character**
Singlet	$S_0 \rightarrow S_1$	492.66 nm 2.5166 eV	1.1777	H-2-L	0.1557	MLCT
				H-1-L+1	0.1914	MLCT/ILCT
				H-L	0.6474	ILCT
	$S_0 \rightarrow S_2$	474.02 nm 2.5921 eV	0.2084	H-2-L+1	0.4251	MLCT
				H-1-L	0.4117	MLCT/ILCT
	$S_0 \rightarrow S_{23}$	399.57 nm 3.1029 eV	0.3474	H-3-L	0.4656	MLCT/ILCT
				H-1-L	0.4435	MLCT/ILCT
Triplet	$S_0 \rightarrow T_1$	594.44 nm	0.0000[f]	H-1-L+1	0.2552	MLCT/ILCT

	2.0857 eV		H-L	0.5639	ILCT
$S_0 \rightarrow T_2$	577.98 nm 2.1451 eV	0.0000[f]	H-1-L	0.3403	MLCT/ILCT
			H-L+1	0.4962	ILCT

[a] Only the selected low-lying excited states are presented. [b] Oscillator strengths. [c] Only the main configurations are presented. [d] The CI coefficients are in absolute values. [e] L stands for carbazole localized ligand. [f] No spin-orbital coupling effect was considered, thus the *f* values are zero.

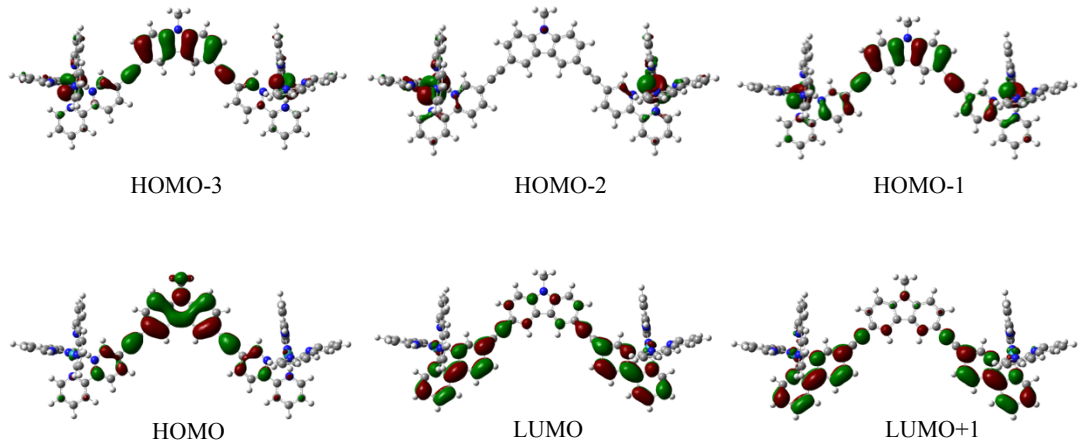

Figure 3.15 *Electron density maps of the frontier molecular orbitals of the complex* ***RuCRu****, based on ground state optimised geometry by the TDDFT calculations at the TDDFT/B3LYP/GENECP/LANL2DZ level with Gaussian 09W.*

Table 3.4 Oscillator Strength (f), main configurations and CI coefficients of the Low-Electronic Excitation Energies (eV) and corresponding lying Electronic Excited States of the complex **RuC** calculated by TDDDFT/B3LYP/GENECP/LANL2DZ, CH3CN as the solvent (PCM model) based on the optimised Ground State Geometries.

	Electronic transition	**TDDFT//B3LYP/GEN**				
		Energy [a]	***f* [b]**	**Composition [c]**	**CI [d]**	**character**
Singlet	$S_0 \rightarrow S_1$	486.29 nm 2.5496 eV	0.6782	H-L	0.6476	ILCT
				H-2-L	0.2098	ILCT/MLCT
				H-1-L	0.1500	ILCT/MLCT
	$S_0 \rightarrow S_{11}$	408.46 nm 3.0354 eV	0.1395	H-3-L+1	0.4902	ML'CT/MC
				H-4-L+2	0.4053	ML'CT
				H-4-L+1	0.2029	ML'CT
Triplet	$S_0 \rightarrow T_1$	602.13 nm 2.0591 eV	0.0000	H-L	0.5967	ILCT
				H-5-L	0.2013	ILCT

			H-1-L	01718	ILCT/MLCT
			H-2-L	0.4105	ILCT/MLCT
$S_0 \rightarrow T_2$	498 nm 2.5309 eV	0.0000	H-2-L+1	0.3370	ML'CT/LL'CT
			H-1-L	0.2759	ILCT/MLCT

[a] Only the selected low-lying excited states are presented. [b] Oscillator strengths. [c] Only the main configurations are presented. [d] The CI coefficients are in absolute values. [e] L stands for carbazole localized ligand; L' stands for the other two bipyridine. [f] No spin-orbital coupling effect was considered, thus the *f* values are zero.

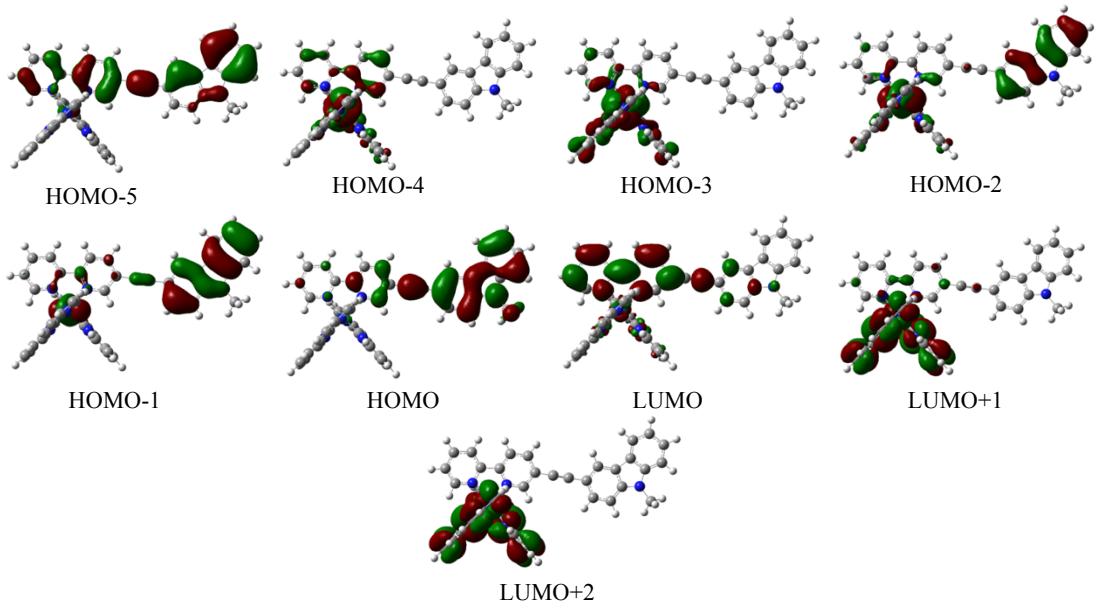

Figure 3.16 *Electron density maps of the frontier molecular orbital of the complex* ***RuC****, based on ground state optimised geometry by the TDDFT calculations at the TDDFT/B3LYP/GENECP/LANL2DZ level with Gaussian 09W.*

3.7 Triplet Photosensitisation Studies for TTA Upconversion and Photodynamic Therapy

3.7.1 TTA Upconversion Studies of RuCRu, IrCIr, RuC and IrC as triplet photosensitisers

Since they display the properties of triplet photosensitisers, each complex was studied for its use towards triplet-triplet annihilation (TTA) upconversion (UC). 9,10-Diphenylanthracene (**DPA**) was used as an optimum triplet acceptor according to the absorption of the generated photosensitisers, and their triplet excited state energy levels. Upon excitation at λ 473 nm, the phosphorescence of **RuCRu** was observed in the deaerated solution (Figure 3.17). On addition of **DPA**, the phosphorescence of **RuCRu**

decreased significantly, with a new luminescence λ 410 nm being concurrently generated. This new emission band is assigned as the upconverted fluorescence of **DPA**, which cannot be excited at λ 473 nm alone. This new luminescence confirms that the TTA UC between **RuCRu** and **DPA** has occurred. The upconversion quantum yield for **RuCRu** was determined as 21.6 %. For **IrCIr**, in the presence of **DPA**, the upconversion quantum yield was calculated as 15.3 %. Compared to their mononuclear analogues, **RuC** and **IrC** (Φ_{UC} = 19.1 % for **RuC**, and Φ_{UC} = 19.0 % for **IrC**), the upconversion quantum yields were not significantly increased.

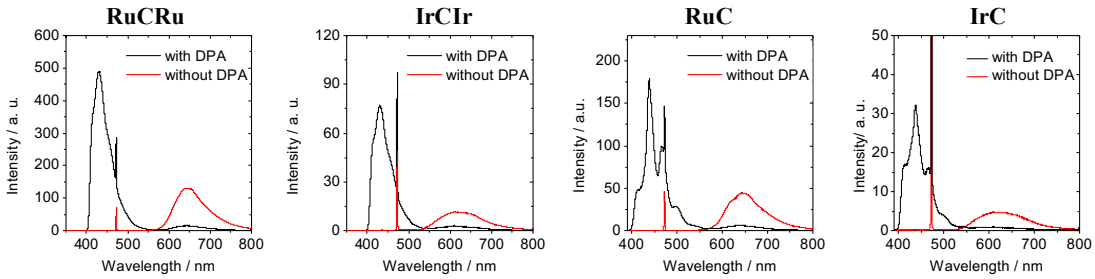

Figure 3.17 *Upconversion with **RuCRu**, **IrCIr**, **RuC** and **IrC** as triplet photosensitisers in CH_3CN ($C = 1.0 \times 10^{-5}$ mol/L), 25 °C. (a)(b) with **DPA** added, $C = 2.0 \times 10^{-3}$ mol/L) (c)(d) with **DPA** added, $C = 1.67 \times 10^{-3}$ mol/L. Excited with blue laser, λ_{ex} = 473 nm, 5.0 mW.*

In order to study the TTET efficiency of the different complexes, triplet state lifetime quenching studies (with the presence of the triplet acceptor, DPA) were carried out. The resulting Stern-Volmer quenching curves were then plotted (Figure 3.18). The quenching of the triplet state of **IrCIr** was found to be less efficient than the other three generated complexes, and this may be due to its short-lived triplet excited state lifetime. A comparison of the overall upconversion capacity is listed in Table 3.4.

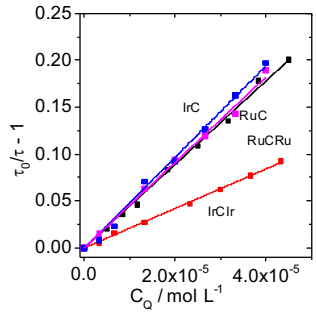

Figure 3.18 *Stern–Volmer plots generated from triplet excited state lifetime (τ_T) quenching of complexes **RuBRu**, **IrBIr**, **RuC** and **IrC** measured with increasing **DPA***

concentration in CH_3CN. The lifetimes were measured with nanosecond time-resolved transient absorption. C [Sensitisers] = 1.0 × 10^{-5} mol/L, 25 °C.

***Table 3.5** Triplet excited state properties of **RuCRu**, **IrCIr**, **RuC** and **IrC**.*

	τ_T [b] (μs)	τ_{DF} [c] (μs)	K_{SV} [d] (M^{-1})	k_q [e] (10^6 M^{-1} s^{-1})	Φ_{UC} [f] (%)	Φ_Δ [g] (%)
RuCRu	1.2	252	4448	3706	21.6	83.3
RuC	1.4	284	4477	3197	19.1	56.3
IrCIr	0.4	386	2102	5255	15.3	67.2
IrC	0.9	301	4809	5343	19.0	54.1

[a] Results of complexes in CH_3CN solution (1 × 10^{-5} mol/L), 298 K. [b] Triplet-state lifetime under N_2. [c] Upconverted luminance lifetime, called delayed fluorescence. [d] Quenching constant. [e] Bimolecular quenching constant. [f] TTA UC quantum yield under N_2, with BODIPY as a standard (Φ_F = 71.2 % in CH_3CN).[56] [g] Singlet oxygen quenching quantum yield with $Ru(bpy)_3[2PF_6]$ as a standard (Φ_Δ = 57.1 % in CH_3CN),[118] at 298 K.

To unambiguously confirm the blue luminance at λ 410 nm is that of upconverted fluorescence, time-resolved emission spectra were collected (Figure 3.19). The lifetime of the blue emission was measured in the TTA UC experiments (Table 3.4), with the long-lived and microsecond scaled lifetimes indicating that the blue emission was generated from a TTA UC process. It was also found that the upconverted fluorescence lifetime of **IrCIr** was 386 μs, which is much longer than that of the other three complexes. The delayed fluorescence lifetime mainly describes the duration of the TTET and TTA processes (since the fluorescence lifetime of **DPA** itself is very short, only lasting several nanoseconds). Concurrently the TTA process is occurring between two **DPA** molecules. Therefore, for different triplet photosensitisers, the only process which can cause this difference in the delayed lifetime is the TTET process. The longer the delayed fluorescence lifetime, the less efficient the TTET process will be. It is related to the short triplet excited lifetime of **IrCIr**. This is also in agreement with the discussion in the earlier section (triplet excited state lifetime quenching measurement).

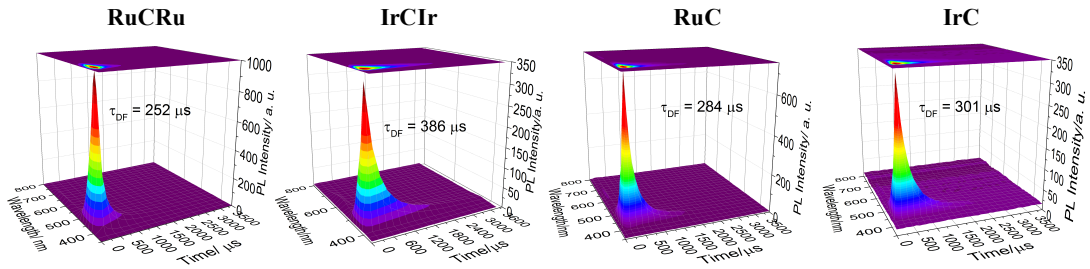

***Figure 3.19** Delayed fluorescence of **DPA** with **RuCRu**, **RuC**, **IrCIr** and **IrC** as the triplet photosensitisers for TTA UC, which were selectively excited at 473 nm (nanosecond pulsed OPO laser synchronised with spectrofluorometer) in deaerated CH_3CN at 298 K.*

*C[Sensitisers] = 1.0 × 10^{-5} mol/L and the concentration of **DPA** was corresponding to their TTA-UC.*

3.7.2 Singlet Oxygen Sensitisation of RuCRu, IrCIr, RuC and IrC as Triplet Photosensitisers

Mono- and di- nuclear N-substituted carbazole complexes were also investigated as triplet photosensitisers for singlet oxygen sensitisation. $[Ru(bpy)_3]Cl_2$ was used as the reference standard (Φ_Δ = 57.1 % in CH_3CN) and DPBF (1,3-diphenylisobenzofuran) was used as the singlet oxygen scavenger. All the measurements were carried in CH_3CN. They were excited at λ 436 nm and 421 nm selectively, with a monochromator. The absorption spectra were recorded at 15 second intervals, for a total of 90 s. Compared to the mononuclear complexes, the carbazole-bridged dinuclear complexes, **RuCRu** and **IrCIr**, showed higher singlet oxygen quantum yields (Φ_Δ = 83.3 % for **RuCRu**; Φ_Δ = 67.2 % for **IrCIr**). (Figure 3.20) The singlet oxygen quantum yields of **RuC** and **IrC** were determined as 56.3 % and 54.1 %, respectively.

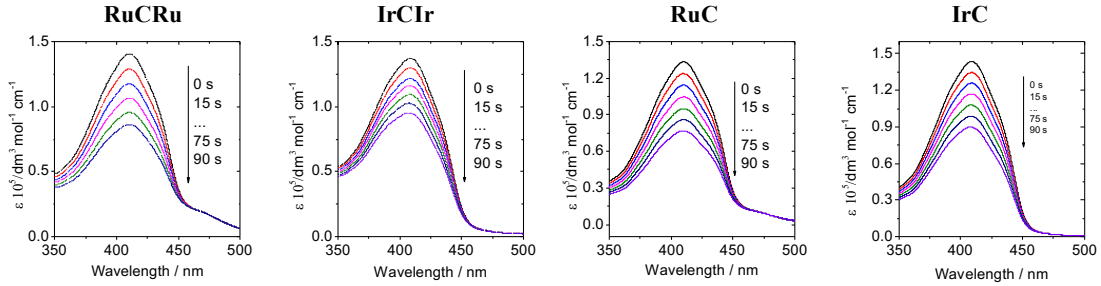

***Figure 3.20** Photosensitisation of $^1O_2$. Irradiation time-dependent decrease of absorption at λ 410 nm of DPBF with **RuBRu** and **IrBIr** (λ_{ex} = 436 nm); **RuC** and **IrC** ((λ_{ex} = 421 nm) as the photosensitisers at 25 ^oC.*

3.8 Conclusion

In conclusion, substituted carbazole-bridged dinuclear ruthenium and iridium complexes and their mononuclear analogues have been synthesised. The dinuclear complexes showed enhanced absorption in the visible region when compared to their mononuclear analogues. The triplet excited state lifetimes of these complexes were slightly prolonged by the attached carbazole moiety, with the triplet excited state being of mixed ^{3}MLCT and ^{3}ILCT character. The TTA UC quantum yields of the dinuclear ruthenium and iridium complexes were not increased significantly from those of the mononuclear complexes.

However, an enhancement was observed in singlet oxygen quenching quantum yield experiments. These results offer new insights into the use of dinuclear complexes towards the practical and industrial application of triplet photosensitisers for TTA-requiring technologies and operations.

4 Towards Multi-Chromophore Heteroleptic Ir(III) Complexes for TTA Upconversion (I)

4.1 Introduction

The aims of designing novel triplet photosensitisers are: (1) the enhancement of absorption in the visible region; (2) prolonging the triplet excited state lifetime. For the majority of recently developed triplet photosensitisers, these systems utilise only one major chromophore, corresponding to only one major absorption band. This is a striking drawback in their potential towards application in solar cells, which requires that the light-harvesting band should be broad across the visible region. The aim of this chapter's work is to synthesise novel triplet photosensitisers bearing ligands of multiple chromophores. The cyclometalated iridium complexes generated contain BODIPY and pyrene as the light-harvesting groups. Compared to mono-chromophore complexes, these moieties show desirable enhanced photophysical properties.

4.2 Synthesis of Cyclometalated Ir(III) Complexes Bearing BODIPY- and Pyrene-Moieties

L-2 (2-(4'-bromophenyl)pyridine) was prepared using 2-bromopyridine and 4-bromophenylboronic acid *via* a Suzuki cross-coupling reaction catalysed using palladium. This procedure is well established in the literature. [119] The addition of base activates the boronic acid, generating the product in a high yield (99 %). A detailed synthetic route is presented in Scheme 4.1.

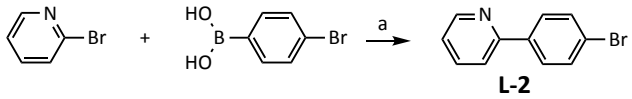

Scheme 4.1 *Synthesis of* ***L-2*** *(2-(4'-bromophenyl)pyridine). (a)Pd(PPh$_3$)$_4$, Na$_2$CO$_3$, toluene, CH$_3$CH$_2$OH, Ar, 17 h, yield: 99 %.*[119]

The synthetic preparation of **Ir(ppyBr)$_2$Cl$_2$** is similar to the preparation of the established Ir(III) dichloro-bridged dimer, **[Ir(ppy)$_2$Cl]$_2$**. Modification of the organic ligand precursor is the only necessary substitution to successfully generate the desired dimer. Following the successful generation of the required dichloro-bridged dimer, reaction with 2,2'-bipyridine facilitates the generation of **IrBrBr** (Scheme 4.2). After purification with chromatography, the compound is precipitated *via* anion metathesis with a saturated solution of KPF_6. As with other complexes of this kind, **IrBrBr** is exclusively formed as a symmetric complex. This was unambiguously confirmed by multinuclear NMR studies

(Chapter 7, synthesis of **IrBrBr**), combined with single crystal X-ray diffraction data (ANNEX). This character contributes to a more facile purification step in proceeding synthetic steps.

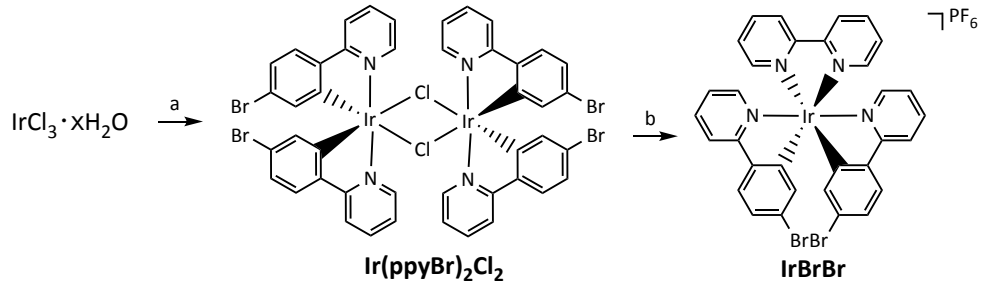

Scheme 4.2 *Synthesis of* ***IrBrBr****. (a) 2-ethoxyethanol : H_2O (3:1, v/v), 130 °C, overnight, yield: 82 %. (b) CH_3OH : CH_2Cl_2 (1:1, v/v), 60 °C, 4 h, Ar, yield: 97 %.*

The synthesis of boron-dipyrromethene (BODIPY) was previously discussed in Chapter 2, and was prepared according to the same procedure. Through strict control of the ratio of starting materials, selective substitution of the 2-position of BODIPY with iodine can be achieved *via* the use of N-iodosuccinimide (NIS) in pre-dried methylene chloride (CH_2Cl_2) at room temperature. Addition of the acetylene group was achieved through a Sonogashira cross-coupling reaction with TMSA. The silyl-protecting group of the TMSA was removed at low temperature (–78 °C), with the mild base TBAF in THF under an argon atmosphere. 1-ethynylpyrene was synthesised using similar synthetic preparations, using 1-bromopyrene. 1-Bromopyrene was obtained from the bromination of pyrene according to literature procedure.[120]

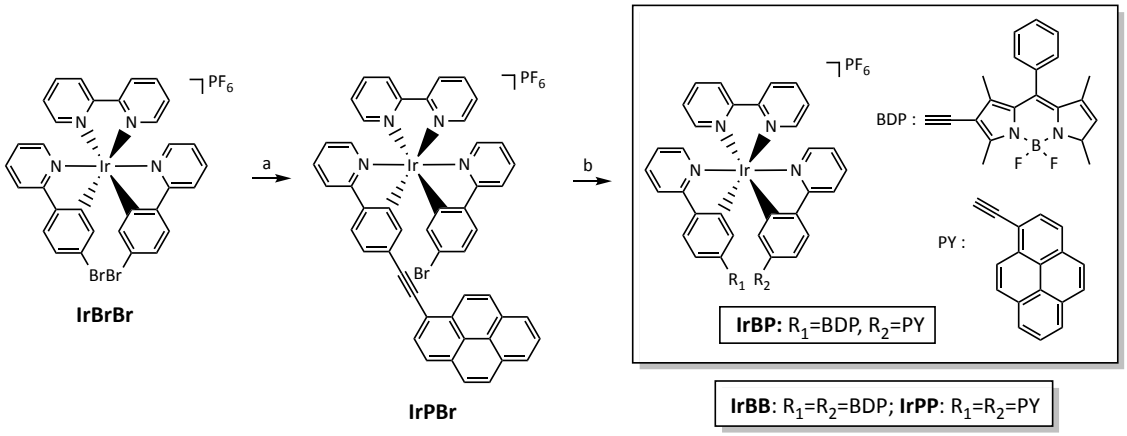

Scheme 4.3 *Synthesis of* ***IrBP****. (a) $(CH_3CH_2)_3N$: CH_3CN (1:1, v/v), $Pd(PPh_3)_2Cl_2$, PPh_3, CuI, 8 h, 60 °C, Ar, yield:* ***IrPBr****, 32 %;* ***IrPP****, 63 %. (b) $(CH_3CH_2)_3N$: CH_3CN (1:1, v/v), $Pd(PPh_3)_2Cl_2$, PPh_3, CuI, overnight, 60 °C, Ar, yield: 17.4 %.*

IrPBr was generated *via* a second Sonogashira cross-coupling reaction with **IrBrBr** and 1-ethynylpyrene, in a mixed solvent system of trimethylamine and CH_3CN (Scheme 4.3). **IrPP** is found as the generated side product. The solubility's of **IrPBr** and **IrPP** are found to be quite different in CH_3CN. This fortunately aids the purification of the two complexes, with **IrPP** easily precipitated in CH_3CN, and collected *via* subsequent filtration. The supernatant therefore containing the desired **IrPBr** complex. The final product **IrBP,** was isolated *via* a third Sonogashira cross-coupling reaction with **IrPBr**, and excess ethynyl-BODIPY ligand under an argon atmosphere. The purification of the final compound was extremely difficult, and contributes to a relatively low yield. **IrBB** was synthesised separately with **IrBrBr** in a similar fashion, with the ethynyl-BODIPY ligand in excess for the necessary Sonogashira cross-coupling step.

4.3 Structural Characterisation of IrPP and IrBP

4.3.1 Crystallographic Analysis of IrPP

Crystals suitable for single crystal X-ray diffraction studies of **IrPP** were collected *via* the slow evaporation of a mixed solvent system of CH_2Cl_2/CH_3OH. The structure was solved and refined using the Bruker SHELXTL Software Package and further refined with XL in Olex2 by Dr. Brendan Twamley in Trinity College Dublin. The compound was found to recrystallise in the space group C2/c, with Z = 8 for the formula unit, $C_{68}H_{40}F_6IrN_4P$. The final anisotropic full-matrix least-squares refinement on F^2 with 732 variables converged at R1 = 6.10 %, for the observed data and wR2 = 19.97 % for all data. The goodness-of-fit was 1.053. The largest peak in the final difference electron density synthesis was 1.779 $e^-/Å^3$ and the largest hole was -6.982 $e^-/Å^3$ with an RMS deviation of 0.150 $e^-/Å^3$. On the basis of the final model, the calculated density was 1.587 g/cm^3 and F (000), 4976 e^-. The asymmetric unit is presented in Figure 4.1. The bipyridine moiety is modelled in two positions with ca. 66:35 % occupancy with restraints. An unidentified solvent molecule was removed from the diffraction data using SQUEEZE.

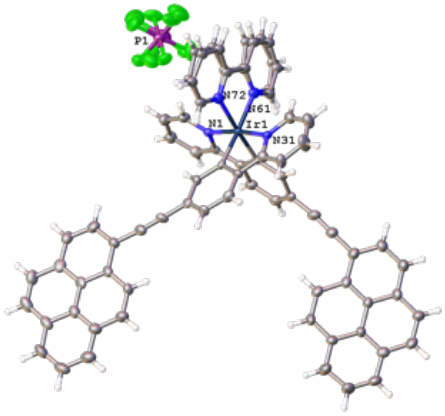

Figure 4.1 *Asymmetric unit of* ***IrPP*** *with atomic displacement shown at 50 % probability. Only selected heteroatoms labelled for clarity.*

The packing structure diagram as viewed down the b-axis is presented in Figure 4.2. There is approximately a 20^{o} angle between the two pyrene planes. Therefore, no π-π stacking is found to exist. This is due to the fixed geometry of the complex in its octahedral orientation. In the middle of the unit, the pyrenes are observed in a "zip-like" arrangement. The interaction between different molecules is found to be weak in the crystal structure.

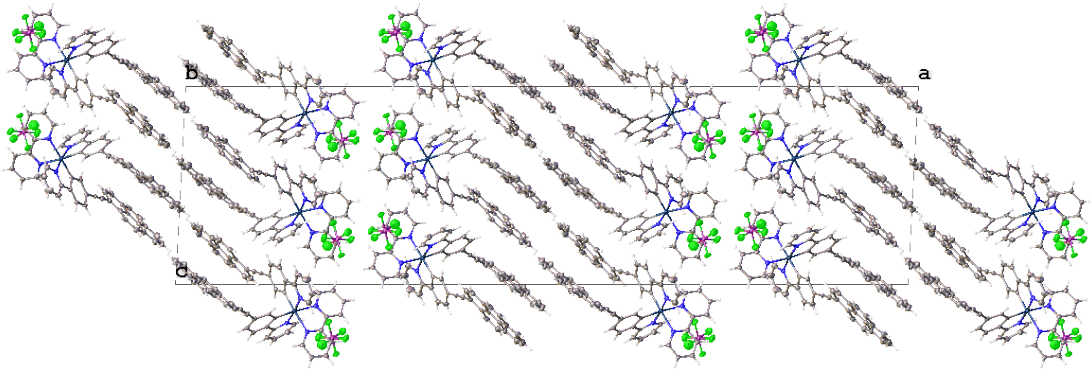

Figure 4.2 *Packing diagram of* ***IrPP*** *viewed down to the b-axis.*

4.3.2 Structural Characterisation of IrPP and IrBP *via* NMR Studies

The isolated **IrBB**, **IrPP**, and **IrBP** complexes were characterised by a range of multinuclear NMR techniques (^{1}H NMR, ^{13}C NMR, 2D-NMR, ^{19}F NMR and ^{11}B NMR).

IrPP is a symmetric structure, containing two pyrene ligands in its structure which aids its characterisation. The spin systems are grouped and presented in Figure 4.3 after analysis of the ^{1}H-^{1}H COSY, and HSQC spectra.

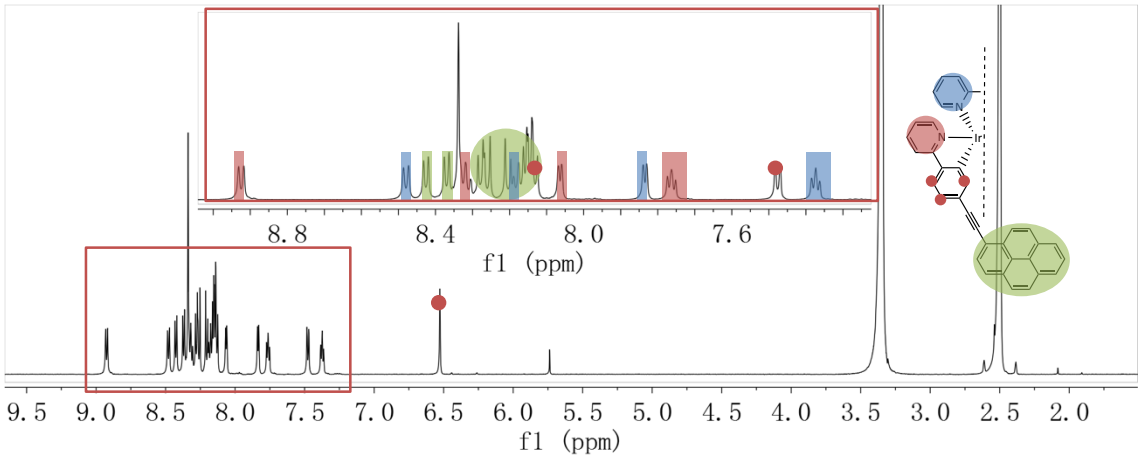

Figure 4.3 *^{1}H NMR spectrum of* ***IrPP*** *(400 MHz, $(CD_3)_2SO$, 20 °C).*

Unlike **IrPP**, **IrBP** is an asymmetric compound due to its multiple ligand character. Characterisation analysis of **IrBP** is presented. It consists of twelve spin systems: one three-spin and three two-spin systems of the pyrene moiety, one one-spin and one five-spin systems generated by the BODIPY moiety, and four pyridyl four-spin systems and two phenyl three-spin systems assigned to the 2-phenylpyridine moiety. Through comparison of the ^{1}H NMR data of **BDP**, the singlet proton peak appearing at δ 6.18 in Figure 4.4 is attributed to peak of the pyrrole proton from the BODIPY moiety. The five-spin system is found at δ 7.54-7.52 ppm (3H-BDP) and 7.32-7.29 ppm (2H-BDP) respectively (highlighted with green boxes ▫ in Figure 1.4). Moreover, the four methyl group protons are shown in the ^{1}H NMR spectrum at δ 2.52, 2.49, 1.39, 1.36 ppm as singlet peaks.

The protons of the 2-phenylpyridine ligand appear as four spin systems as expected. The two three-spin systems in the shielded region (blue boxes ▫) belong to the phenyl of 2-phenylpyridine (Figure 4.4). Analysis of HSQC (Figure 4.5), reveals those carbon atoms adjacent to the N-atom of the pyridyl ring of the ppy ligand usually show a large shift in the ^{13}C NMR; the corresponding protons are marked in purple box (▫). The four pyridyl four-spin systems were found in ^{1}H-^{1}H COSY spectrum are easily assigned (orange boxes ▫). All of the pyrene protons appear at the region δ 8.36-8.07 ppm. They are grouped into four groups as expected (▫).

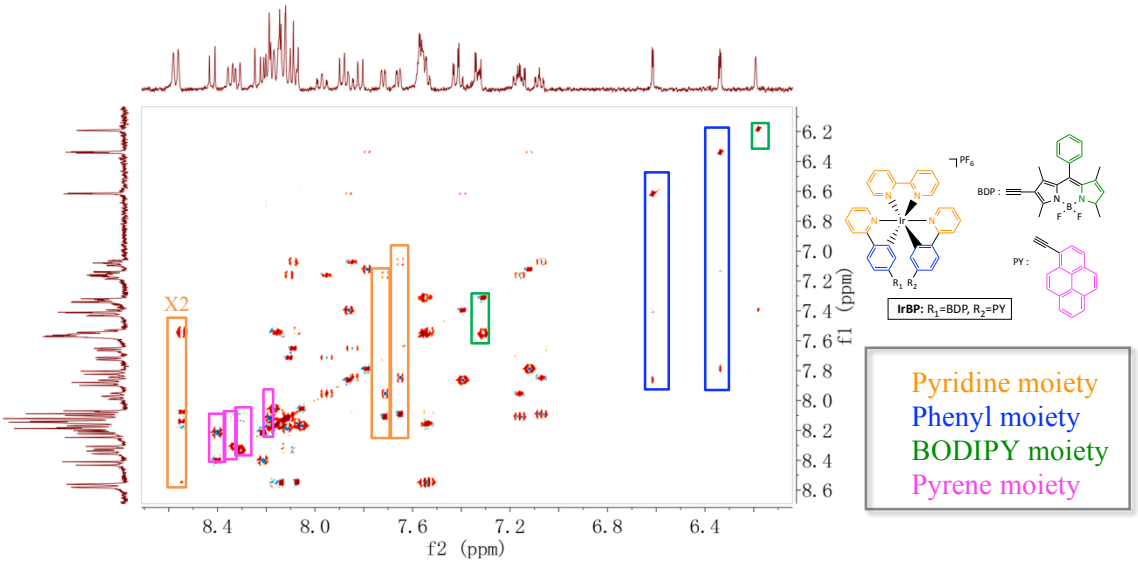

Figure 4.4 *The ^{1}H-^{1}H COSY analysis of* ***IrBP*** *(400 MHz, CD_3CN, 20 ℃).*

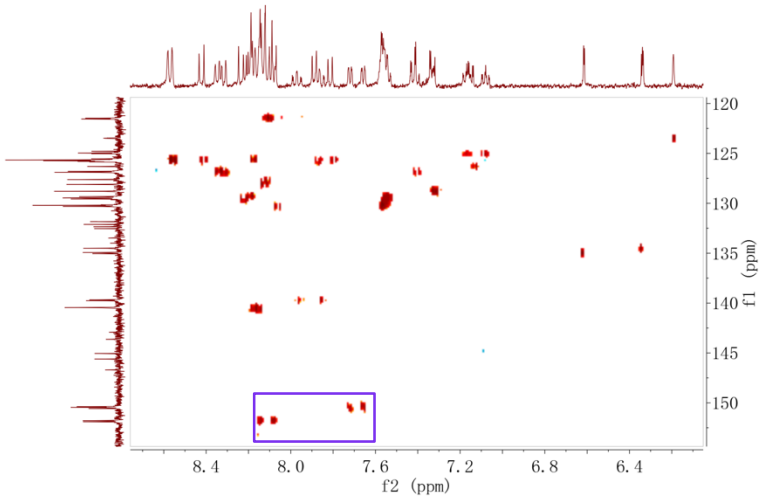

Figure 4.5 *The HSQC spectrum of* ***IrBP*** *(400 MHz, CD_3CN, 20 ℃).*

The ^{11}B NMR spectrum of **IrBP** shows a triple peak at δ 0.58 ppm and the ^{19}F NMR spectrum shows a quarter peak at δ -145.77. ppm (Figure 4.6)

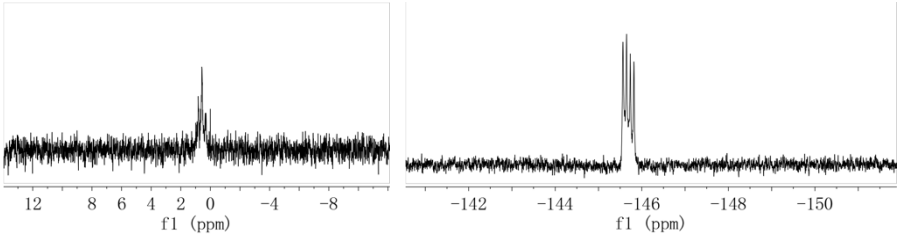

Figure 4.6 *(a) ^{11}B NMR spectrum of* ***IrBP*** *(128 MHz, CD_3CN, 20 ℃). (b) ^{19}F NMR spectrum of* ***IrBP*** *(376 MHz, CD_3CN, 20 ℃).*

4.4 Photophysical Studies

4.4.1 Steady State Studies

The UV-vis spectra of **IrPP**, **IrBB** and **IrBP** are presented in Figure 4.7. **IrPP** shows a maximum absorption at λ 399 nm, while the maximum peak of the UV-vis absorption of **IrBB** is at λ 543 nm.

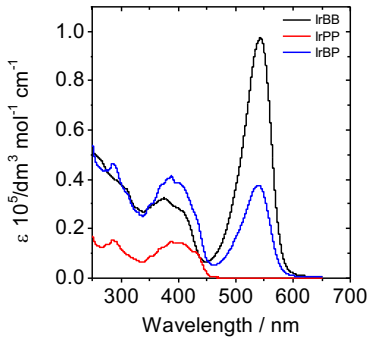

Figure 4.7 *Absorption spectra of* ***IrBB***, ***IrPP*** *and* ***IrBP***. *C = 1 × 10^{-5} mol/L in CH_2Cl_2, 298 K.*

IrBP presents two similar absorption bands at λ 389 nm and 539 nm, which are assigned to the absorption of the pyrene moiety and BODIPY moiety respectively. Moreover, the absorption profile of **IrBP** is superimposable to the sum of the absorption of **IrPP** and **IrBB**. This implies that there is no electronic interaction between the two different ligands at the ground state. However, the intensity of these two bands is approximately half of that of the absorption bands of **IrPP** and **IrBB** respectively. This is attributed to two of the same ligand in both **IrPP** and **IrBB** being present therefore they hand bands that are double the intensity of **IrB**. The molar absorption coefficients of each ligand are given in Table 4.1.

The absorption profiles of each complex were also collected in solvents of different polarities. The chosen solvents were toluene, methylene chloride, methanol and acetonitrile. As shown in Figure 4.8, the polarity of the respective solvent does not appear to have any profound effect on the absorption wavelengths. This indicates that the polarity of the solvent does not affect the ground state of those compounds.

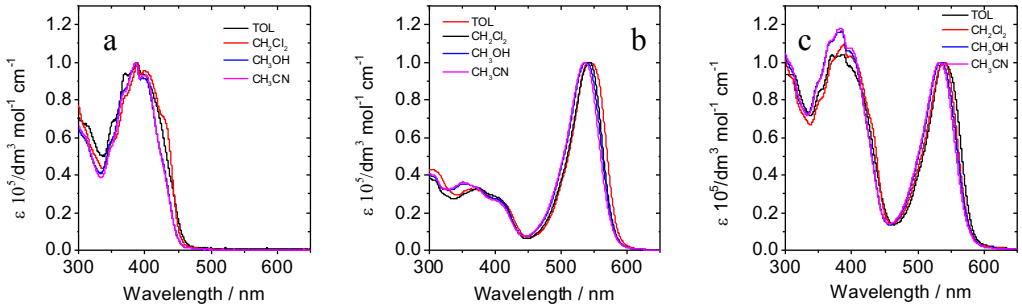

Figure 4.8 *Normalised absorption spectra of (a)**IrPP**, (b)**IrBB** and (c)**IrBP** in solvents of different polarity, TOL = toluene. C = 1.0 × 10^{-5} mol/L, 298 K.*

Table 4.1 *Photophysical properties of **IrPP**, **IrBB** and **IrBP**.*

	λ^a_{abs} (nm)	ε^b (10^5 dm^3 mol^{-1} cm^{-1})	$\lambda_{em}{}^c$ (nm)	$\Phi_P{}^d/\Phi_f{}^e$ (%)	$\tau_P{}^f$ (298 K/77 K) (μs)	$\tau_f{}^g$ (ns)	$\tau_T{}^h$ (μs)(N_2/Air)
IrPP	399	0.143	667/727	0.22/--	96/105	--	90/0.4
IrBB	543	0.973	581	--/12.8	--/--	0.95	121/0.6
IrBP	388/540	0.412/0.377	580	--/4.4	--/--	0.53	274/0.7

[a] Results of complexes in methylene chloride solution (1 × 10^{-5} mol/L), 298 K. [b] Molar absorption coefficient at the absorption maxima. [c] Main emission peak at 298 K in N_2. [d/e] Quantum yield phosphorescence/fluorescence, in N_2, with 2,6-diiodo-BODIPY as a standard (Φ_f = 2.7 % in CH_3CN). [f] Phosphorescence lifetime, at 298 K and 77 K in N_2. [g] Fluorescence lifetime, at 298 K. [h] Triplet-state lifetime, λ_{ex} = 355 nm, in N_2.

The emission properties of **IrPP**, **IrBB** and **IrBP** were studied under different atmospheres and temperatures. For **IrPP**, phosphorescence was observed under a nitrogen atmosphere (Figure 4.9a). Both of the observed peaks at λ 667 nm and 727 nm, were found to be quenched in the corresponding air saturated solvent. This supports its classification at phosphorescence originating from a triplet excited state. The lifetime of the emission was determined as 96 μs, which is a significantly longer excited state lifetime for comparable Ir(III) complexes.[19, 25] It is proposed therefore that the triplet excited state of **IrPP** mainly resides on the pyrene moiety of the ligand, as is denominated as a ligand-localised ^{3}IL* excited state. For **IrBB**, only one emissive band at λ 581 nm was observed (Figure 4.9b). The lifetime was determined as 0.95 ns, which is a typical excited state lifetime value for fluorescence. This implies that the emission band at λ 581 nm originates from a singlet excited state. Comparison of the emission profiles collected in nitrogen or air atmospheres, reveals only small differences in the emission profile. This fluorescence-type emission is stronger under an atmosphere of air, than under the nitrogen

atmosphere. The attenuation of the fluorescence intensity indicates that a decrease of radiative transitions, and an increase of non-radiative transitions is occurring from ^{1}BODIPY* under N_2. Similar results were obtained for **IrBP** (Figure 4.9c). Despite no observation of phosphorescence-type emission in **IrBB** and **IrBP**, the existence of the ^{3}BODIPY* excited state cannot be firmly ruled out. This state may exist as a non-radiative triplet excited state. Moreover, the fluorescence-type emission does not necessarily indicate a non-efficient ISC, as the calculated residual fluorescence quantum yields were low (Φ(**IrBB**) = 12.8 %; Φ(**IrBP**) = 4.4 %). It is also worth noting that the literature value for the fluorescence quantum yield of **B-1** is 72 % in THF.[56]

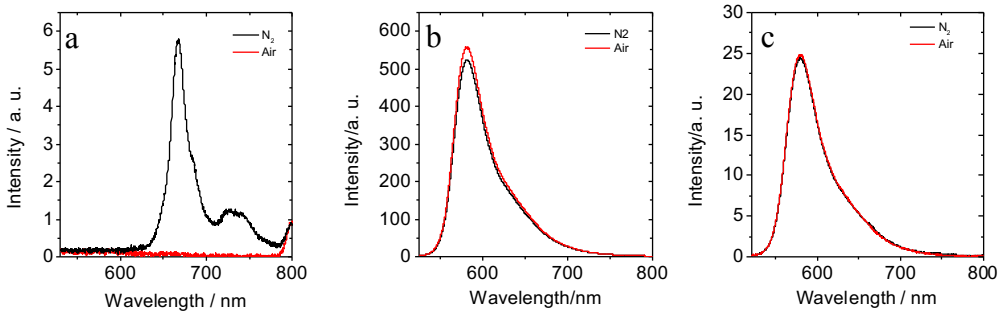

Figure 4.9 *Emission spectra of (a)* ***IrPP****, (b)* ***IrBB*** *and (c)* ***IrBP*** *in CH_2Cl_2 under nitrogen and air atmospheres. λ_{ex} = 400 nm, C = 1 × 10^{-5} mol/L, 298 K.*

To assist in the assignment of the respective photophysical processes, low temperature emission measurements were carried out. The low temperature emission measurements were collected at 77 K. The normalised emission at 77 K, and at room temperature, are compared in Figure 4.10.

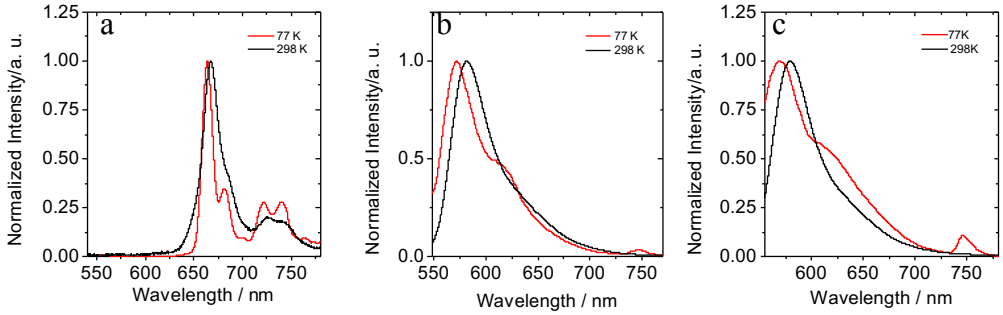

Figure 4.10 *Normalised emission spectra of (a)****IrPP****, (b)****IrBB*** *and (c)****IrBP*** *in a mixed solvent system of CH_3CH_2OH:CH_3OH (4:1, v/v) under nitrogen at 77 K (red line), and room temperature (black line). (a)λ_{ex} = 400 nm, (b)(c) λ_{ex} = 520 nm, C = 1 × 10^{-5} mol/L.*

For **IrPP**, the emission at 77 K has a similar profile to that at 298 K, however fine structure is now visible in both bands. A very small thermal anti-Stokes shift is seen for the peak at λ 668 nm, and is calculated as $\Delta E_s = 90$ cm^{-1}. This allows confirmation of the ^{3}IL nature of phosphorescence, as large anti-Stokes shifts are seen only for charge transfer processes. This shows minor metal perturbation through a lack of MLCT-type emission. For **IrBB**, a new peak at λ 747 nm was generated at 77 K. As discussed earlier, this was assigned to the phosphorescence-type emission band of the BODIPY triplet excited state. (Chapter 2) In the rigid solvent at 77 K, photoactive species are unable to diffuse towards each other, and biomolecular deactivation is slow. This contributes to an enhancement of the internal heavy atom effect, and results in an intensified phosphorescence emission from the complex. A similar process was observed for **IrBP**. When excited at λ_{ex} 400 nm, the same emission profile is generated as Figure 4.10c. It should be noted that the phosphorescence originating from the ^{3}IL* excited state of the pyrene moiety was quenched in **IrBP** at low temperature. As shown by previously discussed results, the triplet excited state of BODIPY is lower than the triplet excited state of pyrene. It is therefore proposed that the ^{3}pyrene* → S_0 transition is quenched by the ^{3}BODIPY* → S_0 transition *via* internal triplet triple energy transfer.

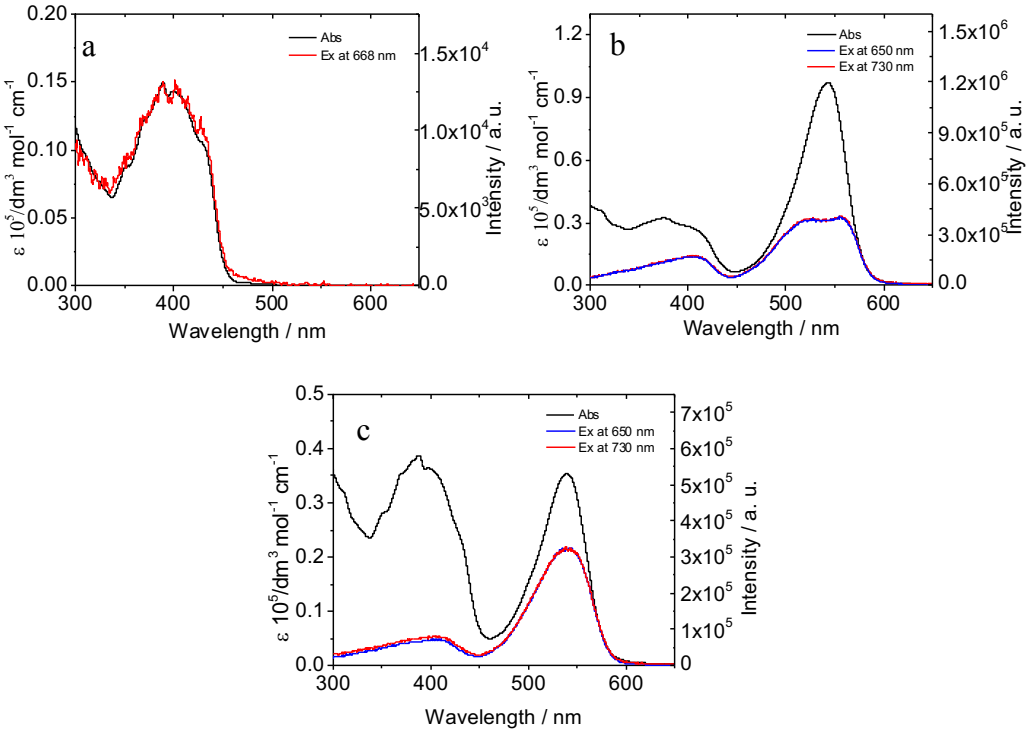

Figure 4.11 *Excitation spectra of **IrPP**, **IrBB** and **IrBP**. Determined at (a) 668 nm, (b)(c) 650 nm (blue line) and 730 nm (red line) in CH_2Cl_2, C = 1 × 10^{-5} mol/L, 298 K.*

In order to detect the presence of Förster resonance energy transfer (FRET), the excitation spectra of each complex were collected and studied. For **IrPP**, the excitation spectrum, when monitored at λ 668 nm, compares well to its steady state absorption spectrum (Figure 4.11a). For **IrBB**, the emission band of BODIPY was used as the monitored wavelength, and two excitation bands were observed at λ 400 nm and 450-600 nm. Both of the observed bands correspond to the BODIPY-chromophore absorption (Figure 4.11b). A similar excitation profile was obtained from **IrBP** (Figure 4.11c). The spectrum shows that the absorption at λ 388 nm does not contribute to the emission at either λ 650 nm or 730 nm. For these reasons, it is assumed that no FRET processes are occurring in the generated complexes.

4.4.2 Transient State Studies

4.4.2.1 Nanosecond Time-resolved Transient Difference Absorption of IrPP, IrBB and IrBP

Nanosecond time-resolved transient difference absorption spectra were collected and studied (Figure 4.12). Upon excitation at λ_{ex} 355 nm, a significant bleaching peak at λ 390 nm was observed in **IrPP**, as the depletion of the ground state of pyrene moiety. The transient difference absorption spectrum of **IrPP** corresponds well to its steady state absorption spectrum, and indicates that the triplet excited state is mainly localised on the ligand moiety, and without major contribution from the Ir(III) centre. The triplet excited state lifetime was determined as 90 μs for **IrPP**, which is close to its phosphorescence lifetime.

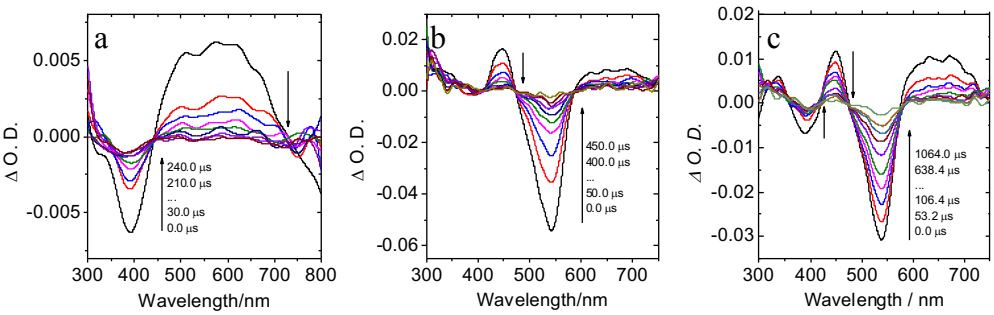

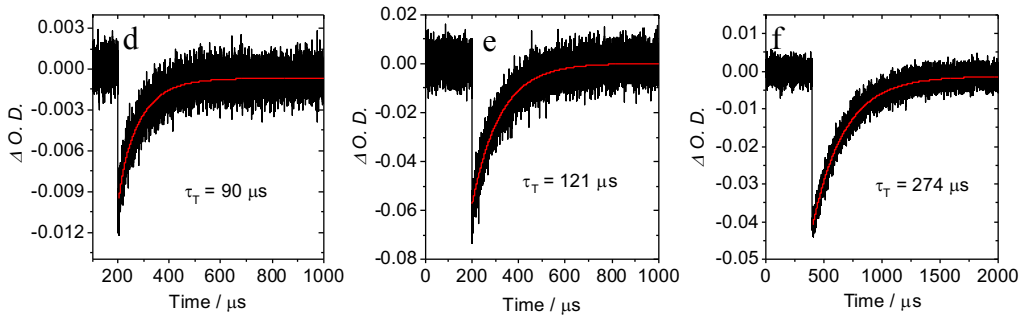

Figure 4.12 *Nanosecond time-scaled transient difference absorption spectra of (a)**IrPP**, (b)**IrBB** and (c)**IrBP** plus an excitation at λ_{ex} = 355 nm and their decay trace. C = 1 × 10^{-5} mol/L, in CH_2Cl_2, 298 K.*

For **IrBB**, there is only one bleaching peak at λ 542 nm (Figure 4.12b), which is attributed to the depletion of the ground state of the BODIPY moiety. The lifetime of the decay trace at λ 540 nm was determined as 121 μs. From this extended lifetime value, we can say that the triplet excited state is mainly a ligand-localised ^{3}IL*. However, when compared to the reference complex **IrB** (τ_T = 87 μs) in Chapter 2, the triplet excited state lifetime of **IrBB** is prolonged due to the addition of the acetylene linker to the phenyl ring of the ppy ring-system, *versus* that of the pyridyl ring. In the transient absorption spectrum of **IrBP**, two bleaching peaks at λ 390 nm and 540 nm were observed simultaneously (Figure 4.12c). The two bands correspond to the two absorption peaks of the pyrene and BODIPY ligands in the UV-vis absorption spectrum (Figure 4.7). This implies that the triplet excited state of **IrBP** is localised on both the pyrene moiety, and the BODIPY moiety, at the same time. The triplet excited state lifetime was measured as τ = 274 μs; twice that of **IrBB**.

4.4.2.2 Femtosecond Time-resolved Transient Difference Absorption of B-1 and IrBP

In order to explain where the triplet excited state originally comes from, the femtosecond time-resolved transient absorption spectra at different time delays were carried out by Prof. Gagik G. Gurzadyan at the Dalian University of Technology. **B-1** was measured as a reference compound in this experiment. As can be seen in Figure 4.14, with the exception of the excitation wavelength, only one bleaching peak is observed at λ 504 nm. It is very clear that the decay only has one component, which is generated by the depletion of its singlet excited state.

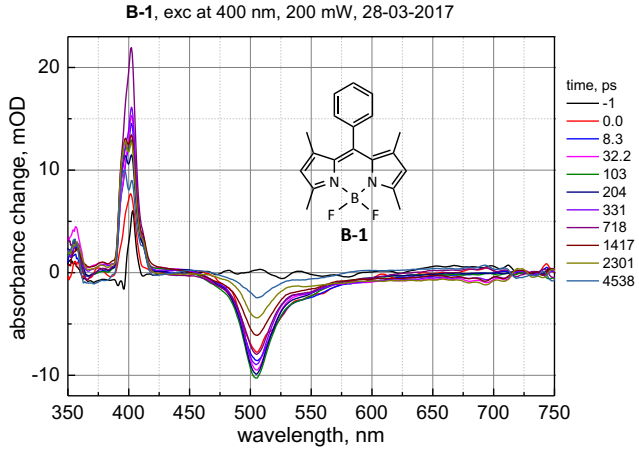

Figure 4.13 *Femtosecond time-scaled transient difference absorption spectrum of* ***B-1****.* λ_{ex} *= 400 nm with 200 mW, in* CH_2Cl_2*, at 298 K.*

The lifetime of **B-1** is approximately 3 ns. This is a typical length for a singlet excited state lifetime for BODIPY derivatives. There is no triplet component observed in the femtosecond time-resolved transient absorption spectrum of **B-1**.

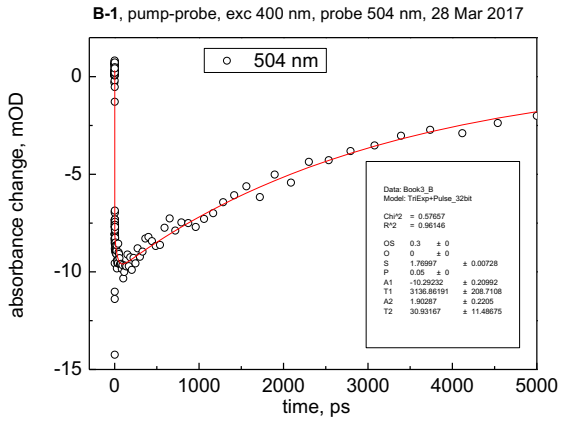

Figure 4.14 *Decay curve of* ***B-1*** *at λ 504 nm.* λ_{ex} *= 400 nm with 200 mW, in* CH_2Cl_2*, at 298 K.* $R^2 = 0.961$*.*

Upon excitation at λ 400 nm of **IrBP**, one bleaching band at λ 544 nm, and two excited state absorption (ESA) band at λ 451 nm and 625 nm were observed (Figure 4.15). The bleaching band corresponds to the steady state absorption of the BODIPY moiety of **IrBP**. The two ESA bands are attributed to the T_1-T_n transitions according to the previous nanosecond studies, and the fitted results of their kinetic data in femtosecond studies.

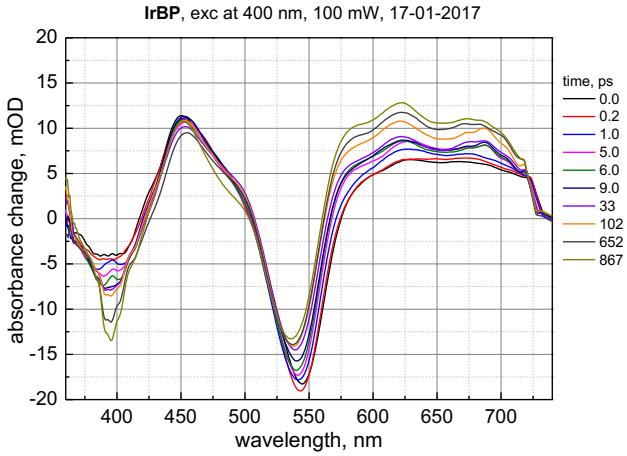

Figure 4.15 *Femtosecond time-scaled transient difference absorption spectrum of* ***IrBP****.* λ_{ex} *= 400 nm with 100 mW, in* CH_2Cl_2*, at 298 K.*

As shown in Figure 4.16a, the triplet excited state is generated in an ultrafast process. It could be considered that the triplet excited state is based on pyrene moiety of **IrBP**. However, the triplet excited state at λ 625 nm was generated at 124 ps (Figure 4.16d). This therefore could be assigned to the ^{3}BODIPY* excited state, with ISC needing 124 ps in duration. Previously, it has been reported that the ISC of 2,6-diiodobodipy takes 200 ps.[121] Therefore, these two different triplet excited state components confirm the previous assumption; that two triplet excited states are generated at the same time. The fitted results of the decay of **IrBP** are shown in Table 4.2.

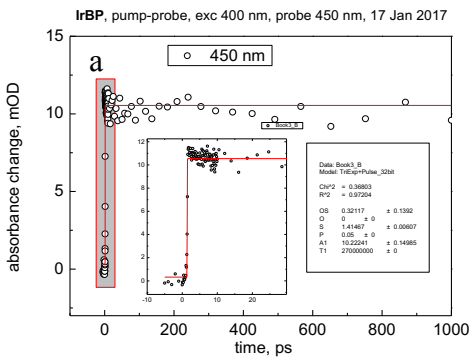

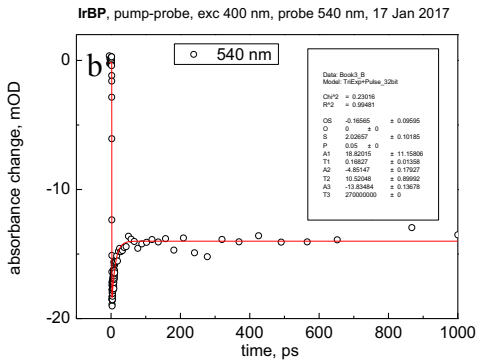

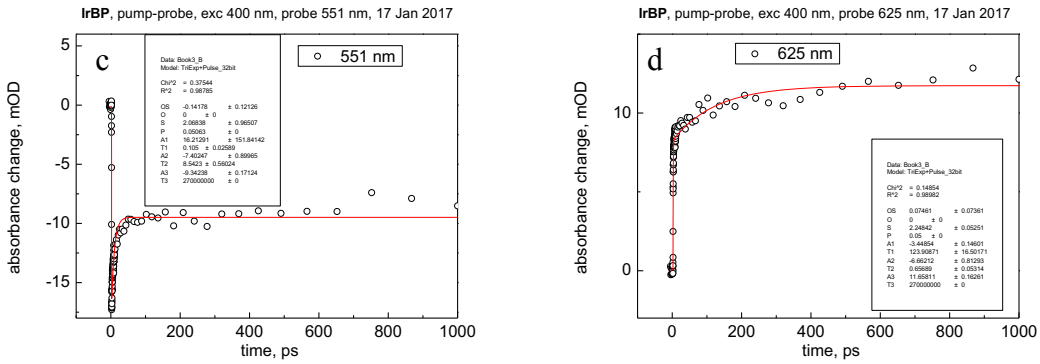

Figure 4.16 *Decay curves of* ***IrBP*** *at (a) 450 nm, (b) 540 nm, (c) 551 nm and (d) 625 nm. λ_{ex} = 400 nm with 100 mW, in CH_2Cl_2, at 298 K.*

Table 4.2 *The fitted results of the* ***IrBP*** *femtosecond decay.*

Probe	Band	τ_1, ps	$\mathbf{A_1}$	τ_2, ps	$\mathbf{A_2}$	τ_3, ps	$\mathbf{A_3}$	P	χ^2
450 nm	Positive	--	--	--	--	270,000,000	1.0	0.05	0.972
540 nm	Negative	0.168	1.0	11	-0.26	270,000,000	-0.74	0.05	0.995
551 nm	Negative	0.11	0.97	8.5	-0.43	270,000,000	-0.57	0.05	0.986
625 nm	Positive	124	-0.30	0.66	-0.57	270,000,000	1.0	0.05	0.990

4.4.3 Density Functional Theory (DFT) Calculations

To further corroborate the assignment of photophysical processes, DFT calculations were carried out for each complex. At the beginning of each experiment, the ground state geometry was optimised with Gaussian 09, and the spin density surfaces were computed.

In **IrPP**, the lowest triplet excited state is mainly located on the ligand's pyrene moiety. (Figure 4.17) This concurs with the previously discussed experimental photophysical results. The small contribution from the Ir(III) metal centre, elongates the lifetime of the triplet excited state. In **IrBB**, the lowest triplet excited state is mainly located on the BODIPY moiety (Ligand). This is also in agreement with the nanosecond time-resolved transient difference absorption spectrum. In **IrBP**, as we can see from Figure 4.17c, the spin density surface is mainly located on the BODIPY moiety, with the pyrene-containing ligand providing a minimal contribution to the lowest triplet excited state. This convincingly illustrates why only phosphorescence from the ^{3}BODIPY* excited state is observed in the low temperature emission spectrum (Figure 4.10c).

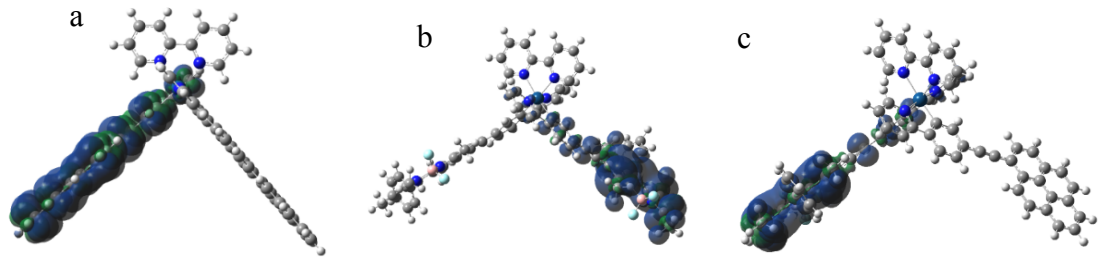

Figure 4.17 *Isosurface of spin density of* ***IrPP***, ***IrBB*** *and* ***IrBP*** *at the optimised triplet-state geometries. Methylene chloride was used as the solvent in the calculations. Calculations were performed at TDDFT/B3LYP/GENECP/LANL2DZ with Gaussian 09.*

The absorption properties of **IrBP** were also calculated with a time-dependent DFT method. The calculation wavelengths were λ 518 nm, 462 nm and 410 nm respectively. Moreover, as shown in Table 4.3, the characters of absorptions are assigned to BODIPY moiety, pyrene moiety and the metal centre respectively. These are found to be close to the experimental results. The first two triplet excited states energy were calculated as 1.52 eV (λ 814 nm, S_0/T_1) and 1.79 eV (λ 692 nm, S_0/T_2). They are attributed to the ^{3}IL'* (BODIPY-localised), and ^{3}IL* (pyrene-localised) respectively. The calculated energy gap S_0/T_1 is close to the experimental phosphorescence emission at λ 746 nm (1.66 eV) for **IrBP**. The calculated energy gap S_0/T_2 is also close to the experimental phosphorescence emission at λ 668 nm (1.85 eV) for **IrPP**, which is assigned as ^{3}IL*. In the photophysical measurements, no phosphorescence was observed for **IrBP**, even during low temperature measurements. This indicates S_0/T_2 is quenched by the lower triplet excited state S_0/T_1. The calculated results closely support the conclusions drawn from the experimentally collected data.

Table 4.3 *Electronic Excitation Energies (eV) and corresponding Oscillator Strength (f), main configurations and CI coefficients of the Low-lying Electronic Excited States of the complex* ***IrBP*** *calculated by TDDDFT/B3LYP/GENECP/LANL2DZ, CH_2Cl_2 as the solvent (PCM model) based on the optimised Ground State Geometries.*

	Electronic Transition	TD-DFT/B3LYP/GEN				
		Energy [a]	*f* [b]	Composition [c]	CI [d]	Character
Singlet	$S_0 \rightarrow S_1$	2.3930 eV 518 nm	0.7878	H-3–L	0.1021	ML'CT/LL'CT
				H-1–L	0.6100	IL'
				H–L	0.3231	LL'CT

Triplet	$S_0 \rightarrow S_5$	2.6862 eV 462 nm	1.2883	H-2–L+1 H–L+2	0.1354 0.6708	ML’’CT IL
	$S_0 \rightarrow S_{10}$	3.0227 eV 410 nm	0.5179	H-3–L H-1–L+3 H–L+3	0.3833 0.4457 0.3498	ML’CT/LL’CT L’C LL’CT
	$S_0 \rightarrow T_1$	1.5224 eV 814 nm	0.0000[f]	H-3–L H-2–L H-1–L	0.2707 0.2294 0.6052	ML’CT/LL’CT ML’CT/LL’CT IL’
	$S_0 \rightarrow T_2$	1.7915 eV 692 nm	0.0000[f]	H–L+2	0.6103	IL

[a] Only the selected low-lying excited states are presented. [b] Oscillator strengths. [c] Only the main configurations are presented. [d] The CI coefficients are in absolute values. [e] L stands for pyrene localised ligand, L’ stands for BODIPY localised ligand and L’’ stands for bipyridine localised ligand. [f] No spin-orbital coupling effect was considered, thus the *f* values are zero.

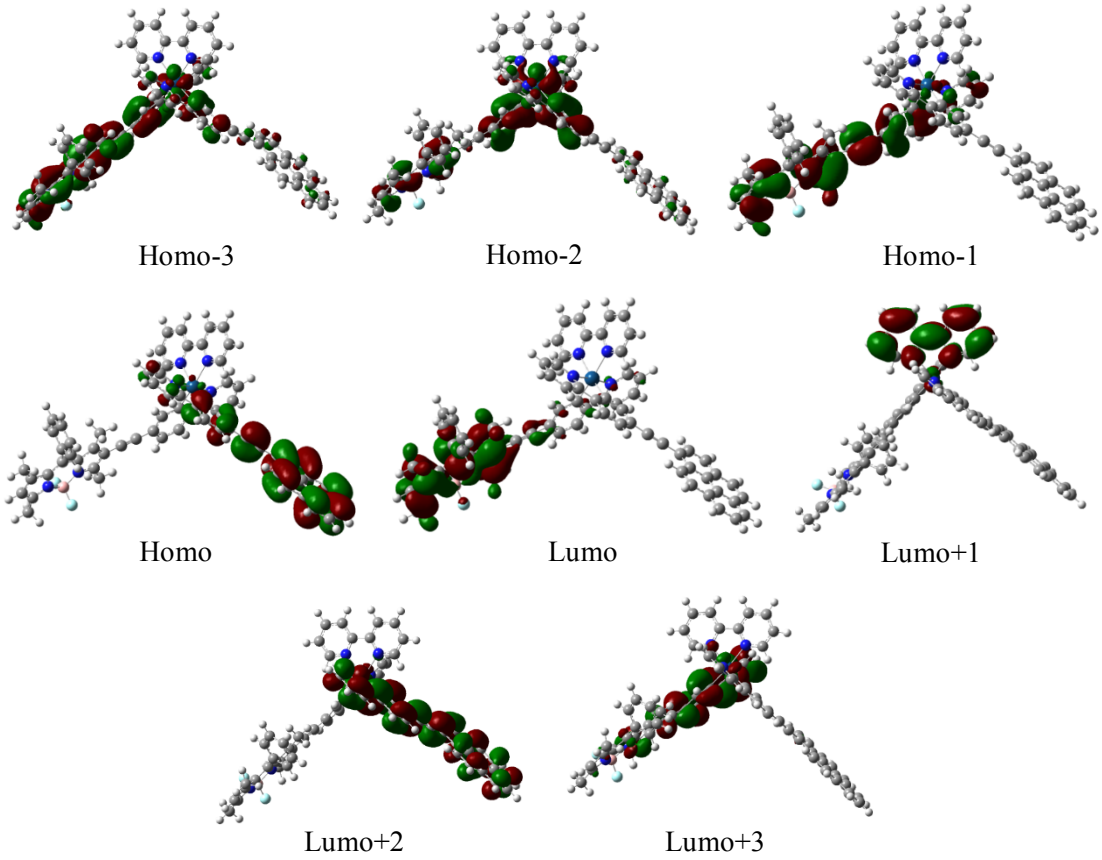

Figure 4.18 *Electron density maps of the frontier molecular orbital of the complex* ***IrBP****, based on ground state optimised geometry from the TDDFT calculations at the TDDFT/B3LYP/GENECP/LANL2DZ level with Gaussian 09W.*

In summary, as shown in Scheme 4.4, upon excitation, two triplet excited states are populated *via* ISC for **IrBP**. One is localised on the pyrene moiety, the other one localised

on the BODIPY moiety. Both are intraligand triplet excited states. According to femtosecond time-resolved transient difference absorption results, the ^{3}Pyrene* excited state is formed via a superfast process. At the same time, the ^{3}BDP* excited state is generated through a slower process which was measured to be within 200 ps. It is believed that the triplet energy could transfer from the ^{3}pyrene* state to the ^{3}BDP* state. Finally, only the ^{3}BDP*→S_0 transition would be observed.

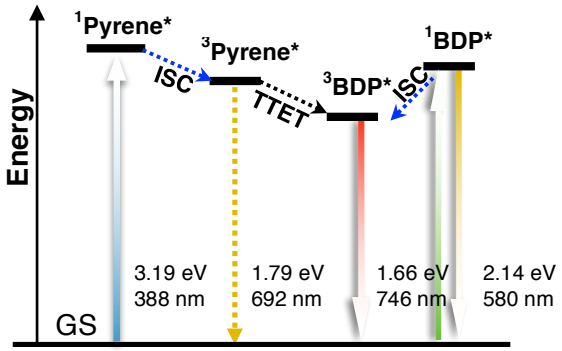

Scheme 4.4 *Simplified Jablonski diagram of light harvesting with* ***IrBP****. GS is the ground state (S_0). ^{1}Pyrene* is the pyrene-localised intraligand singlet excited state. ^{3}Pyrene* is the pyrene based intraligand triplet excited state. ^{1}BDP* is the BODIPY-localised intraligand singlet excited state. ^{3}BDP* is the BODIPY-based intraligand triplet excited state. TTET is the triplet-triplet energy transfer. The dashed line is non-radiative transition. The solid line is radiative transition.*

4.5 Triplet Photosensitisation Studies for TTA Upconversion and Photodynamic Therapy

4.5.1 TTA Upconversion Studies of IrPP, IrBB and IrBP as Triplet Photosensitisers

To explore each of the complex's triplet photosensitisation ability, TTA upconversion studies were carried out. On consideration of the absorption profile of **IrPP**, and its triplet excited state, an external laser light source was chosen at λ 473 nm, with **DPA** chosen as the selected triplet energy acceptor.

Upon excitation at λ 473 nm, luminescence of **IrPP** was observed at λ 668 nm under a nitrogen atmosphere (Figure 4.19a black line, with amplified spectrum in the middle). Upon the addition of the triplet energy acceptor **DPA** to the solution, a new emission band

is observed at λ 434 nm. Simultanous quenching of **IrPP** the luminescence is observed in the mixed solution. Therefore, TTA upconversion is believed to be occurring in the mixed solution. Through the use of BODIPY as a standard reference (Φ_F = 71.2 %, in CH_3CN), the TTA upconversion quantum yield was determined to be 8.6 %. It should also be noted that the absorption band of **IrPP** at λ 473 nm is very weak. This required four times the concentration of the triplet photosensitiser than that used in corresponding measurements of the other complexes. This increased concentration is used to assist in the accurate determination of the quantum yield measurement.

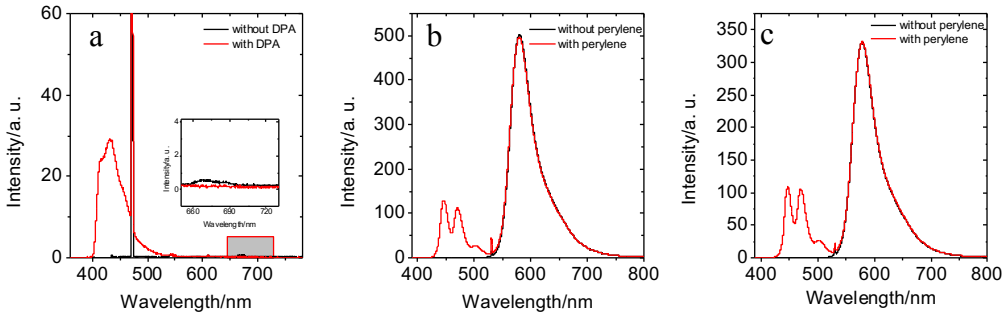

Figure 4.19 *Upconversion studies with **IrPP**, **IrBB** and **IrBP** as triplet photosensitisers in CH_2Cl_2, 298 K. (a) **IrPP** emission spectra with **DPA** added (C[**IrPP**] = 4.0 × 10^{-5} mol/L , C[**DPA**] = 2.0 × 10^{-3} mol/L) (b) **IrBB** emission spectra with perylene added ((C[**IrBB**] = 1.0 × 10^{-5} mol/L , C[**PY**] = 4.0 × 10^{-5} mol/L)) (c) **IrBP** emission spectra with perylene added (C[**IrBP**] = 1.0 × 10^{-5} mol/L , C[**PY**] = 5.0 × 10^{-5} mol/L). Excited with yellow laser, λ_{ex} = 589 nm, 5.0 mW.*

For **IrBB**, an external laser light source wavelength of λ 532 nm was used, with perylene (**PY**) chosen as the triplet energy acceptor. Upon the addition of perylene, a new emission band was observed at λ 446 nm, corresponding to the fluorescence of perylene. Perylene itself cannot be excited by the λ 532 nm wavelength, and thus, a TTA upconversion process must be occurring. The TTA upconversion quantum yield was determined to be 4.6 %.

A similar phenomenon was observed for **IrBP**. The TTA upconversion quantum yield with perylene as triplet energy acceptor, and *via* the use of a λ 532 nm laser as external laser light source, was obtained as 5.8 %. It is worth noting that **DPA** was also used as a triplet acceptor in a similar measurement. However, the upconverted luminescence was found to be insufficient to accurately calculate the TTA upconversion quantum yield. This

indicates that the triplet excited state of **DPA** and **IrBP** are not well matched and are not suitable in the TTA upconversion process. Moreover, it implies that the excitation of the BODIPY chromophore cannot efficiently generate the triplet excited state of the pyrene moiety (T_2) in **IrBP**. This may explain why the TTA upconversion quantum yield is not significantly increased between **IrBB** and **IrBP**. Photographs of the TTA upconversion experiments are shown in Figure 4.20.

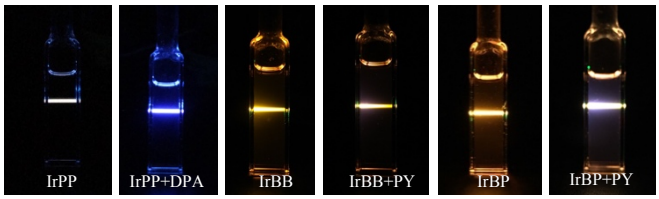

Figure 4.20 *Photographs of the TTA upconversion process with and without the triplet acceptor.*

In order to study the TTET efficiency of each complex, the triplet lifetime quenching Stern Volmer graph was plotted in Figure 4.21. The quenching constant (K_{sv}) was measured for all three complexes and **IrBP** was found to be twice that of **IrBB**. This may contribute to the long-lived triplet excited state of **IrBP**. In **IrPP**, the K_{sv} value is much smaller than the other two compounds, its lowest triplet excited state localised on the pyrene moiety, rather than the BODIPY moiety (^{3}BODIPY*).

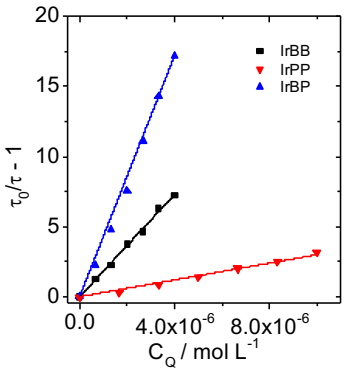

Figure 4.21 *Stern–Volmer plots generated from the triplet excited state lifetime (τ_T) quenching of complexes **IrPP**, **IrBB** and **IrBP** measured with the increasing acceptor concentration in CH_2Cl_2. The lifetimes were measured with the nanosecond time-resolved transient absorption. C [Sensitiser] = 1.0 × 10^{-5} mol/L, 298 K.*

Table 4.4 *Triplet excited state properties of* ***IrPP***, ***IrBB*** *and* ***IrBP***.

	τ_T[a] (μs)	K_{sv}[b] ($10^5 M^{-1}$)	K_q[c] ($10^9 M^{-1}s^{-1}$)	Φ_{UC}[d] (%)	Φ_Δ[e] (%)
IrPP	90	2.99	3.32	8.6[d1]	58.8
IrBB	121	18.2	15.0	4.6[d2]	60.9
IrBP	274	43.0	15.7	5.8[d2]	61.1

[a] Triplet excited state lifetime. [b] Quenching constant. [c] Bimolecular quenching constants. [d] TTA upconversion yield in deaerated CH_2Cl_2 with triplet acceptor DPA[d1] and perylene[d2], with the prompt fluorescence of BDP (Φ_f = 71.2 % in CH_3CN) and 2,6-diiodo-BDP as the standard (Φ_f = 2.7 % in CH_3CN)[122]. [e] Quantum yield of singlet oxygen in CH_2Cl_2, excited at λ 421 nm and $Ru(bpy)_3[2PF_6]$ (Φ_Δ = 57 % in CH_3CN) as standard.

4.5.2 Singlet Oxygen Sensing of IrPP, IrBB and IrBP as Triplet Photosensitisers

IrPP, **IrBB** and **IrBP** were also studied as triplet photosensitisers for singlet oxygen photosensitisation towards their potential application in photodynamic therapy (PDT).

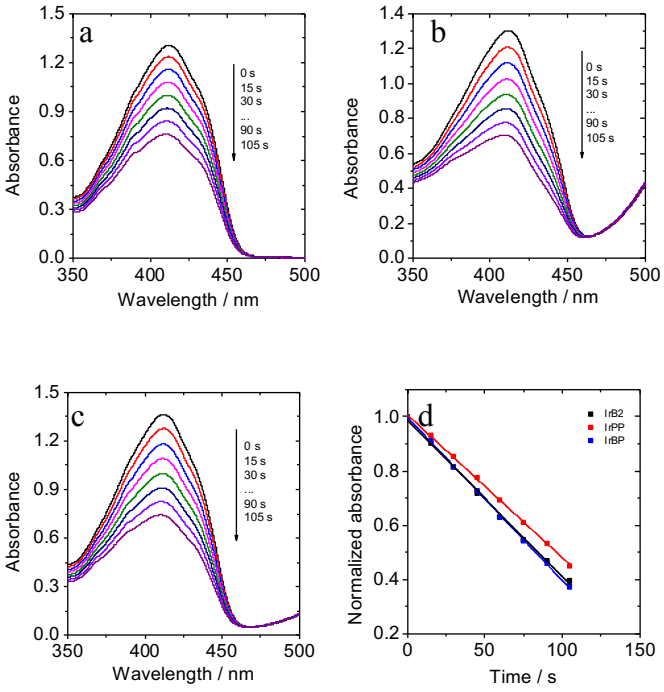

Figure 4.22 *Photosensitisation of* $^1O_2$. *Irradiation time-dependent decrease of absorption at λ 410 nm of DPBF with (a)* ***IrPP***, *(b)* ***IrBB*** *and (c)* ***IrBP*** *as the photosensitiser.* λ_{ex} = *421 nm at 298 K, C = 1.0 × 10^{-5} mol/L in CH_2Cl_2. (d) Comparison of singlet oxygen sensing ability.*

The irradiation time-dependent decrease of each absorption spectra is shown in Figure 4.22. $[Ru(bpy)_3]Cl_2$ was used as the reference standard (Φ_Δ = 57.1 % in CH_3CN), with DPBF chosen as the singlet oxygen scavenger. The mixtures of the respective photosensitiser and singlet oxygen scavenger were excited at the same wavelength, λ 421 nm, in CH_2Cl_2. The absorption spectra were recorded at 15 second intervals, for a total of 105 s. The singlet oxygen quantum yields were determined as 58.8 %, 60.9 %, and 61.1 % respectively, with no sizeable difference seen between the complexes. This means that all three complexes show initial results comparable/better than other iridium compounds.

4.6 Conclusion

The multi-chromophore Ir(III) complex, **IrBP**, was synthesised and characterised. Compared to traditional photosensitisers, the target complex contains two chromophores on separate heteroleptic ligands.

This attribute was found to broaden the complex's absorption wavelength in the visible region. The reference compounds, **IrPP** and **IrBP**, were also successfully synthesised and fully characterised by mass spectrometry and complete NMR studies. For **IrBP**, two absorption bands at λ 388 nm and 540 nm are observed. As **IrBP** contains both a pyrene-containing ligand, and BODIPY-containing ligand, two triplet excited states were generated simultaneously, according to the nanosecond time-resolved transient difference absorption spectrum studies. Both were assigned as ligand centred (ligand-localised) triplet excited states. Moreover, the BODIPY ligand centred triplet excited energy level is lower than it of the pyrene ligand centred. Therefore, TTET is believed to exist between these two triplet energy states. This is postulated as one of the reasons why the τ_T value of **IrBP** is 274 μs, which is a significantly long-lived triplet excited state lifetime.[19, 25] For **IrBB**, the lowest triplet excited state is also localised on BODIPY moiety, but the τ_T value is only 121 μs.

All the generated novel complexes were used as triplet photosensitisers for TTA upconversion and singlet oxygen photosensitisation studies. The TTA upconversion quantum yields of **IrPP**, **IrBB** and **IrBP** were determined as 8.6 %, 4.6 %, 5.8 %, respectively.

5 Towards Multi-Chromophore Heteroleptic Ir(III) Complexes for TTA Upconversion (II)

5.1 Introduction

Based on the work on novel triplet photosensitisers bearing ligands of multiple chromophores in Chapter 4, analysis of its photophysical processes aided the design of a second multi-chromophores Ir(III) complex. This synthetic design incorporates both a triphenylamine (TPA) moiety, and a pyrene moiety as the two distinct light-harvesting chromophores. Concurrent to a desirable broadening of the absorption wavelength, the two chromophores allow further investigations towards the localisation of the triplet excited state, and the effect of electron donating amine chromophore TPA.

5.2 Synthesis of Cyclometalated Iridium(III) Complexes bearing Pyrene- and TPA-moieties

As discussed in Chapter 4, **L-2** (2-(4'-bromophenyl)pyridine) was prepared using 2-bromopyridine and 4-bromophenylboronic acid *via* a Suzuki cross-coupling reaction. **IrBrBr** was further generated *via* a two-step coordination process, first with the generation of the with μ-chloro-bridged Ir dimer of **L-2**, followed by coordination of a 2,2'-bipyridine (bpy) ligand.

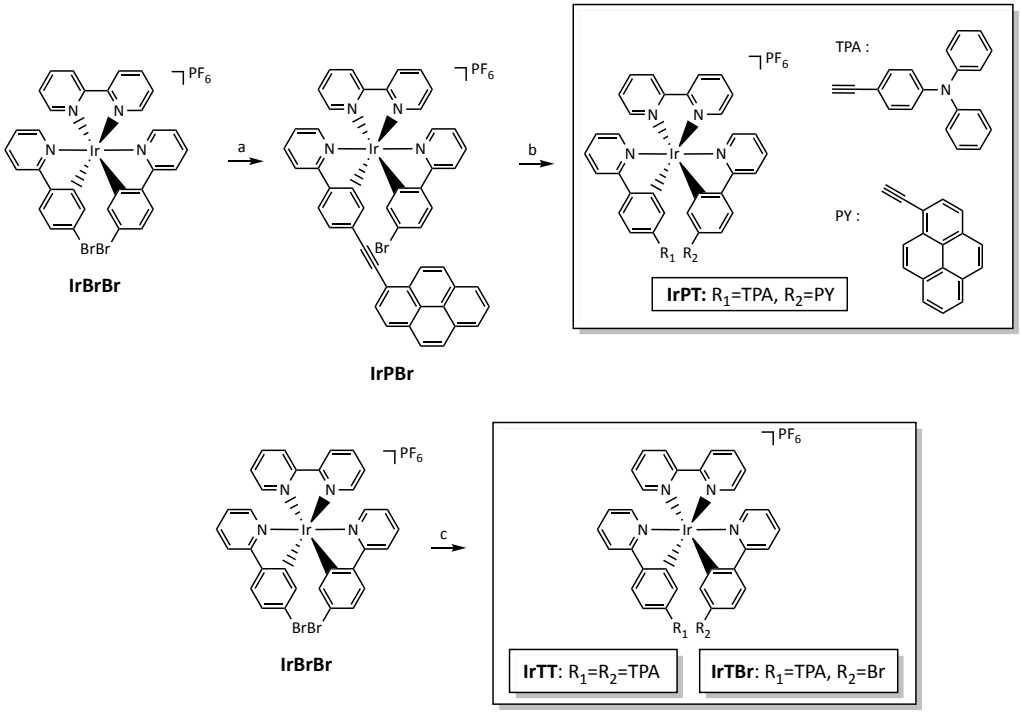

Scheme 5.1 *Synthesis of* ***IrPT****. (a) $(CH_3CH_2)_3N$:CH_3CN (1:1, v/v), $Pd(PPh_3)_2Cl_2$, PPh_3, CuI, 8 h, 60 °C, Ar, yield:* ***IrPBr****, 32 %;* ***IrPP****, 63 %. (b) $(CH_3CH_2)_3N$:CH_3CN (1:1, v/v),*

$Pd(PPh_3)_2Cl_2$, PPh_3, CuI, overnight, 60 °C, Ar, yield: ***IrPT****, 27 %. (c) $(CH_3CH_2)_3N$:CH_3CN (1:1, v/v), $Pd(PPh_3)_4$, overnight, 60 °C Ar, yield:* ***IrTT****, 27 %;* ***IrTBr****, 22 %.*

Upon successful generation of the **IrBrBr** precursor, **IrPBr** was then synthesised *via* a Sonogashira cross-coupling reaction with a single equivalent of 1-ethynylpyrene. The 1-ethynyltriphenylamine precursor was generated through reaction of 4-bromotriphenylaminetriphenylamine and trimethylsilylacetylene (TMSA). The silyl-protecting group of TMSA was readily removed using KCO_3 at room temperature in a mixture solvent system of THF and CH_3OH under an argon atmosphere. In a synthetic preparation similar to that of **IrBP** in Chapter 4, **IrPT** was successfully synthesised *via* a second Sonogashira cross-coupling reaction in a moderate yield (27 %).

In a synthetic modification of the procedure used in the synthesis of **IrPP**, $Pd(PPh_3)_4$ was chosen as a preferred catalyst in the synthesis of **IrTT**. In initial attempts to generate **IrTT**, $Pd(PPh_3)_2Cl_2$, PPh_3, and CuI, were selected as the catalyst and co-catalysts of choice. However, despite using an excess of the 1-ethynyltriphenylamine precursor, following the reaction work up, the product was found to be mainly that of **IrTBr**. One postulated reason for the apparent inability of the second Sonogashira cross-coupling to take place, is that these reaction conditions may facilitate the generation of the homocoupled 1-ethynyltriphenylamine precursor. This product would therefore not be available for subsequent reaction, preventing the formation of the desired complex **IrTT**. The presence of the Cu(I) intermediate is blamed here, and this side reaction is seen in numerous Sonogashira cross-coupling reactions in the literature. In subsequent attempts, the use of the $Pd(PPh_3)_4$ catalyst allowed collecting of much higher yields of the desired complex **IrTT**, despite some **IrTBr** being found further to the reaction work up.

5.3 Structural Characterisation of IrPT and IrTT

5.3.1 Crystallographic Analysis of IrTT

Crystals of **IrTT** suitable for single crystal X-ray diffraction studies were collected *via* the slow evaporation of a solution of acetone-D_6, and recovered further to their growth in a narrow NMR analysis tube. A specimen of $C_{79.50}H_{50}D_{15}F_6IrN_6O_{2.50}P$, approximate dimensions 0.060 mm × 0.100 mm × 0.230 mm, was used for the X-ray crystallographic analysis. The X-ray intensity data were measured at 100(2)K on a Bruker Apex DUO

with an Oxford Cobra low temperature device using a MiTeGen micromount by Dr. Brendan Twamley in Trinity College Dublin. Bruker APEX software was used to correct for Lorentz and polarization effects.

A total of 959 frames were collected. The total exposure time was 4.79 hours. The integration of the data using a triclinic unit cell yielded a total of 118141 reflections to a maximum θ angle of 28.34° (0.75 Å resolution), of which 16968 were independent (average redundancy 6.963, completeness = 99.8 %, R_{int} = 5.62 %, R_{sig} = 3.98 %) and 14605 (86.07 %) were greater than $2\sigma(F^2)$. The final cell constants of a = 11.8682(6) Å, b = 17.7343(9) Å, c = 19.1476(10) Å, α = 117.1614(10)°, β = 95.7005(13)°, γ = 102.6460(12)°, volume = 3405.3(3)Å^3, are based upon the refinement of the XYZ-centroids of reflections above 20 σ(I). Data were corrected for absorption effects using the Multi-Scan method (SADABS). The ratio of minimum to maximum apparent transmission was 0.818. The calculated minimum and maximum transmission coefficients (based on crystal size) are 0.6101 and 0.7457.

The structure was solved with the XT structure solution program using Intrinsic Phasing and refined with the XL refinement package using Least Squares minimisation with Olex2, using the space group P $\overline{1}$, with Z = 2 for the formula unit, $C_{79.50}H_{50}D_{15}F_6IrN_6O_{2.50}P$. (Figure 5.1) The final anisotropic full-matrix least-squares refinement on F^2 with 970 variables converged at R1 = 2.70 %, for the observed data and wR2 = 5.67 % for all data. The goodness-of-fit was 1.015. The largest peak in the final difference electron density synthesis was 0.522 e^-/Å^3 and the largest hole was -0.879 e^-/Å^3 with an RMS deviation of 0.088 e^-/Å^3. On the basis of the final model, the calculated density was 1.460 g/cm^3 and F(000), 1500 e^-. The complete data refinement was also carried out by Dr. Brendan Twamley in Trinity College Dublin.

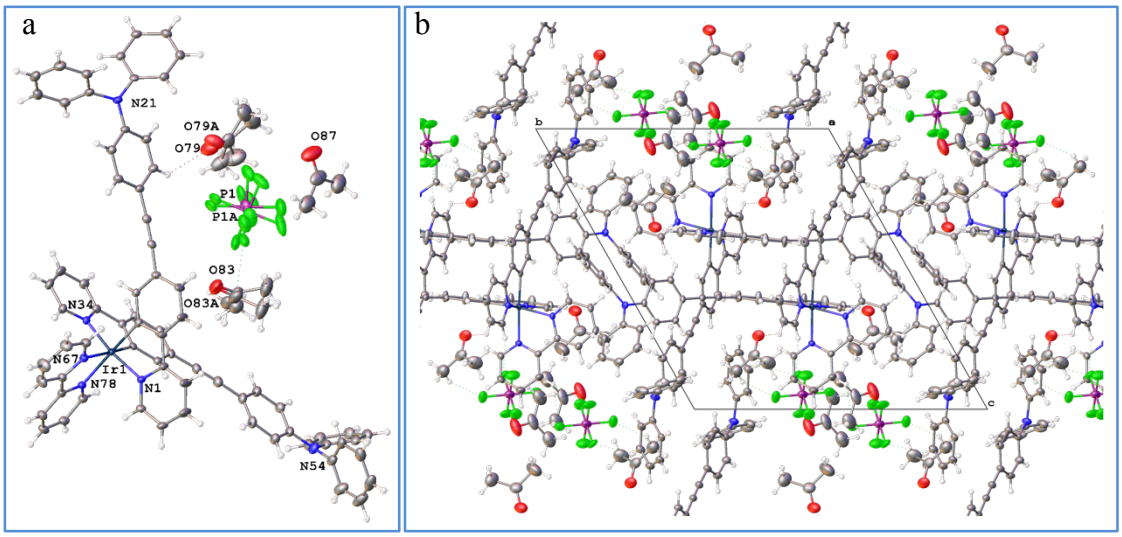

Figure 5.1 *(a) Asymmetric unit of* ***IrTT*** *with partial atom labelling for clarity. Atomic displacement shown at 50 % probability. (b) Packing diagram of the major disordered moiety of* ***IrTT*** *viewed normal to the a-axis. Atomic displacement shown at 50 % probability.*

The PF_6 anion is disordered over two locations (57:43 % occupancy), and modelled with constraints (EADP) using a rigid group. The solvent acetone-D_6, is located in three positions in the ASU. One is half occupied over the inversion centre and the other two were modelled in two positions (O79:O79a, 60:40; O83:O83a 76:24 % occupancy) with restraints (DIFX, SADI, SIMU), constraints (EADP) and a rigid group.

5.3.2 Structural Characterisation of IrPT and IrTT

The isolated **IrPT**, **IrTT** and the novel intermediate complex **IrTBr**, were characterised by a range of multinuclear NMR techniques (^{1}H NMR, ^{13}C NMR, 2D-NMR).

Figure 5.2 shows the ^{1}H spectrum of **IrPT**. Fortunately, the spectrum is found to be well-resolved, allowing the proton signals to be clearly integrated and studied. The typical signals of the pyrene moiety, and the TPA moiety, are visible in the signal regions of δ 8.50-8.00 ppm (blue region ●), and δ 7.40-6.80 ppm (red region ●) respectively. The remainder of the proton signals in the downfield region are assigned to either the 2-phenylpyridine or 2,2'-bipyridine ligands coordinated to the Ir(III) centre.

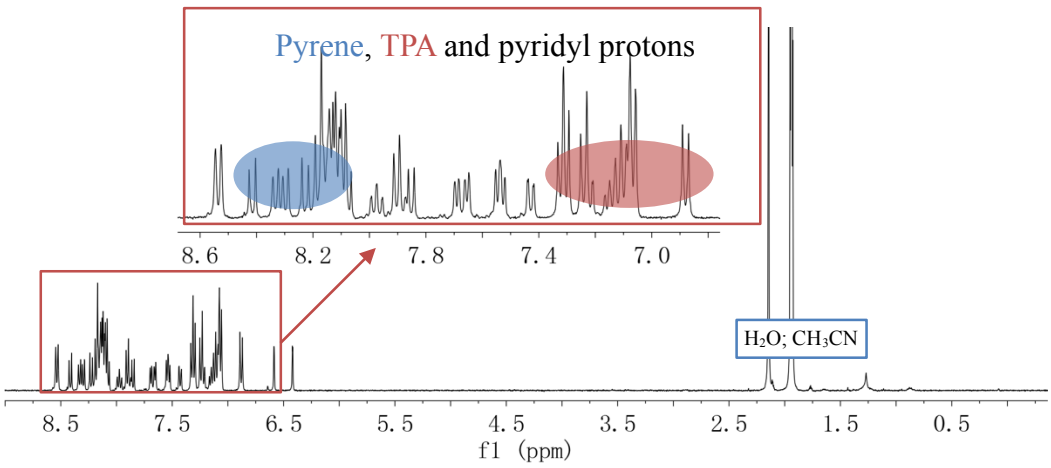

Figure 5.2 *^{1}H NMR spectrum of* ***IrPT*** *(400 MHz, CD_3CN, 20 ℃).*

IrPT consists of fourteen spin systems: one three-spin and three two-spin systems relating to the pyrene moiety; two two-spin and two five-spin systems relating to the TPA moiety; and two pyridyl four-spin systems and two phenyl three-spin systems assigned to 2-phenylpyridine moiety and two pyridyl four-spin systems assigned to bipyridine. The protons of the 2-phenylpyridine ligand appear as four spin systems as excepted. In the ^{1}H-^{1}H COSY spectrum (Figure 5.4), the two three-spin systems in the shielded region blue boxes (▫) belong to the phenyl ring of 2-phenylpyridine.

Analysis of the HSQC spectrum (Figure 5.5), demonstrates the typical large shift of those carbon atoms adjacent to the coordinated N-atoms of the complex in the ^{13}C NMR spectrum. The corresponding proton signals to these shifted carbon signals are marked in purple box (▫). The four pyridyl four-spin systems are easily assigned through use of the same ^{1}H-^{1}H COSY spectrum, and are denoted *via* orange boxes (▫).

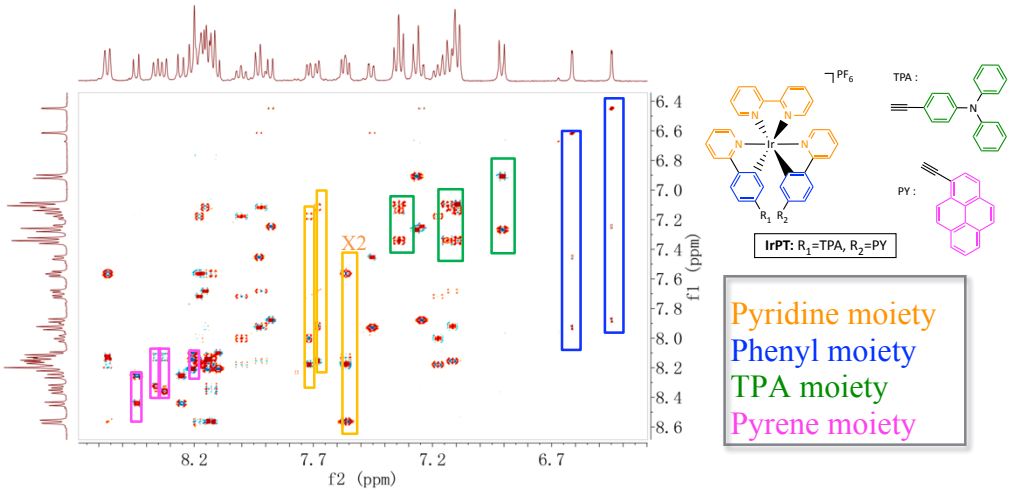

Figure 5.3 *The ^{1}H-^{1}H COSY spectrum analysis of* ***IrPT*** *(400 MHz, CD_3CN, 20 ℃).*

All of the pyrene protons appear at the region δ 8.50-8.00 ppm as previously mentioned, and are found as four groups as expected (▫). The spin systems on the TPA moiety are also easily found green boxes (▫).

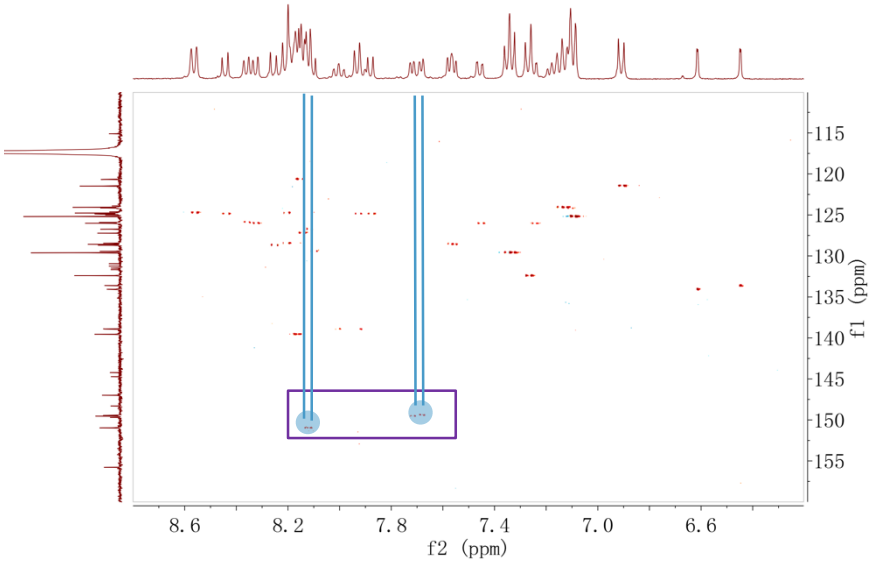

Figure 5.4 *The HSQC spectrum analysis of* ***IrPT*** *(400 MHz, CD_3CN, 20 ℃).*

The ^{13}C NMR spectrum of **IrPT** is presented in Figure 5.6. The four acetylene carbons appear in the typical region of δ 96.61-89.73 ppm. Further to successful characterisation to the heteronuclear NMR studies, analysis of **IrPT** was carried out *via* high resolution mass spectrometry. A MALDI-TOF mass spectrometry technique determined **IrPT** as a value of 1148.3291, corresponding to the $[C_{70}H_{45}N_5Ir]^+$ ion. This correlates well to the calculated value ($[C_{70}H_{45}N_5Ir]^+$ *m/z* = 1148.3304).

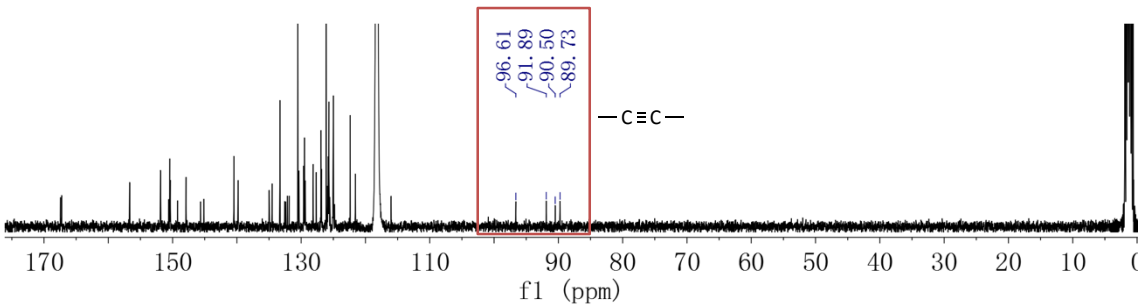

Figure 5.5 *^{13}C NMR spectrum of* ***IrPT*** *(100 MHz, CD_3CN, 20 ℃).*

The symmetrical structure of **IrTT** dramatically simplified the analysis of the ^{1}H and ^{13}C spectra collected. Of note here, is that both the two TPA ligands as a whole are in the same environment and result in a symmetric structure of the whole molecule, but also each TAP moiety itself is symmetric. Therefore, in the ^{13}C NMR spectrum, only 26 peaks

are visible, rather than the 35 carbon signals expected if only the whole structure was symmetric (Figure 5.6).

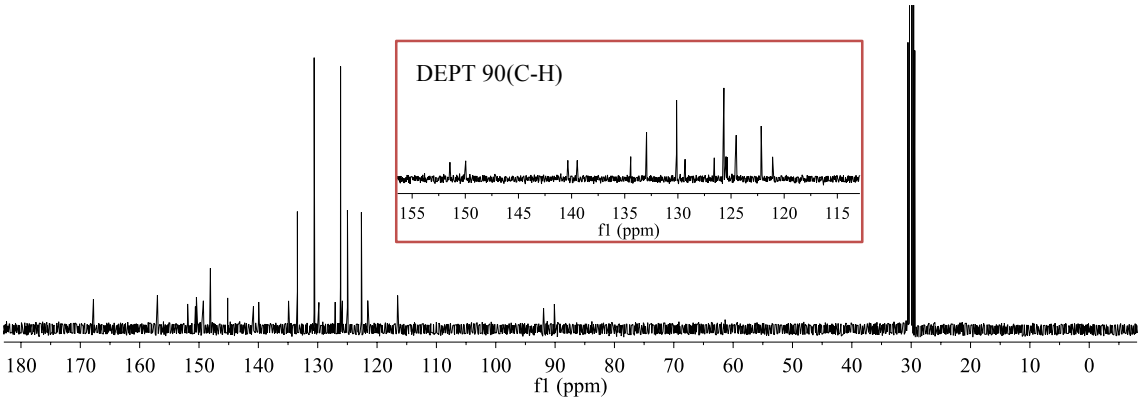

Figure 5.6 *^{13}C NMR spectrum of* ***IrTT*** *(100 MHz, $(CD_3)_2CO$, 20 °C).*

5.4 Photophysical Studies

In order to effectively present the photophysical properties of the multi-chromophore ligand complexes, a detailed comparison between **IrTT**, **IrPP**, and **IrPT** is given in this section.

5.4.1 Steady State Studies

A comparison of the UV-vis spectra of **IrTT**, **IrPP**, and **IrPT** is presented in Figure 5.7. The following nomenclature is used to distinguish the respective ligands; L – pyrene-based ligand, L' – TPA-based ligand, L'' – bpy ligand.

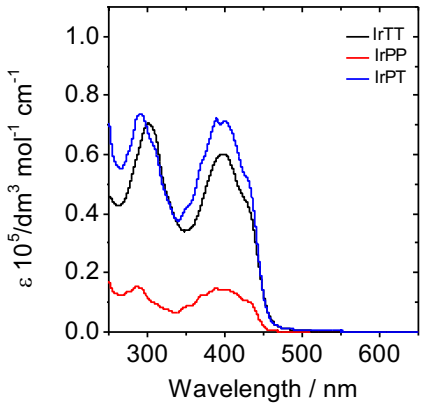

Figure 5.7 *Absorption spectra of* ***IrTT, IrPP*** *and* ***IrPT****. $C = 1 \times 10^{-5}$ mol/L in CH_2Cl_2, 298 K.*

Study of the absorption profile of **IrTT** reveals a peak at λ 300 nm (ε 70,500 dm^3 $mol^{-1}cm^{-1}$). This high intensity peak is assigned to the absorption of TPA moieties, likely an ^{1}IL'CT (intraligand charge transfer) transition from the TPA moiety to the coordinated ppy component of the ligand. This would agree with similar appended TPA moieties in other transition metal complexes.[20] A ^{1}MLCT (metal to ligand charge transfer) absorption band from the mixed ppy-Ir centre occupied molecular orbital to the bpy ligand is also likely to occur at lower energies, and may explain the tail into the visible region.

Analysis of the absorption spectrum of **IrPT** reveals two main absorption bands at λ 290 nm (ε 73,500 dm^3 $mol^{-1}cm^{-1}$), and 398 nm (ε 71,200 dm^3 $mol^{-1}cm^{-1}$). These are assigned to the absorption of TPA moiety and pyrene moiety respectively. Again, a ^{1}MLCT (metal-ligand to ligand charge transfer) absorption band from the mixed ppy-Ir centre occupied molecular orbital to the bpy ligand is also likely to occur at lower energies. The absorption profile of **IrPT** is superimposable to the sum of absorption of **IrTT** and **IrPP**. No obvious electronic interaction between the two chromophore-containing ligands is seen in their ground states.

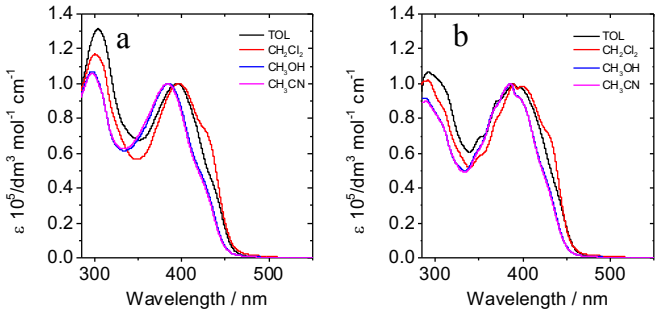

Figure 5.8 *Normalised absorption spectra of (a)**IrTT** and (b)**IrPT** in different solvents. TOL = toluene. C = 1.0 × 10^{-5} mol/L, 298 K.*

The absorption profiles of each complex were also collected in solvents of different polarities. The solvents chosen were toluene, methylene chloride, CH_3OH and acetonitrile. However, as shown in Figure 5.8, the overlapped spectra showed minimal solvatochromic effects. This indicates that the polarity of solvent has little effect on the ground state energies of the generated complexes.

The emission properties of these complexes were studied under different atmospheres, and in different temperatures. For **IrTT**, under a nitrogen atmosphere, an emission band is seen at λ 562 nm when excited at λ_{ex} 400 nm (Figure 5.9, Figure 5.10). This featureless

band is only partly quenched when excited in an air saturated solution (Figure 5.9a). This simple test is a common indicator of phosphorescent character. The phosphorescence quantum yield however was calculated as 0.14, revealing a relatively low emissive efficiency. This implies that the absorption of this complex cannot be efficiently utilised to generate its triplet emissive band. The phosphorescence lifetime of **IrTT** was determined as 0.2 μs, which is a short and conventional lifetime for Ir(III) complexes of this type. However, analysis of **IrPT** in the two atmospheres shows a dramatic air-sensitive emission centred at λ 667 nm (Figure 5.9c). The excited state lifetime of this band is 95 μs in the nitrogen atmosphere.

Table 5.1 *Photophysical properties of* ***IrTT***, ***IrPP*** *and* ***IrPT***.

	λ_{abs} [a] (nm)	ε [b] (10^5 dm^3 mol^{-1} cm^{-1})	λ_{em} [c] (nm)	Φ_P [d] (%)	τ_P [e] (298 K/77 K) (μs)	τ_T [f] (μs) (N_2/Air)
IrTT	300/396	0.705,0.603	562/603	0.14	0.2/37	0.2/0.1
IrPP	399	0.143	667/727	0.22	96/105	90/0.4
IrPT	290/398	0.735,0.712	667/726	0.22	95/168	75/0.4

[a] Results of complexes in a methylene chloride solution (1×10^{-5} mol/L), 298 K. [b] Molar absorption coefficient at the absorption maxima. [c] Main emission peak at 298 K in N_2. [d] Quantum yield phosphorescence in N_2, with 2,6-diiodo-BODIPY as a standard (Φ_f = 2.7 % in CH_3CN). [e] Phosphorescence lifetime, at 298 K and 77 K in N_2. [f] Triplet-state lifetime, λ_{ex} = 355 nm, in N_2.

When compared to the respective atmosphere emission profiles of the two complexes, **IrPT** shows similar emissive properties to **IrPP**. Therefore, the triplet excited state of **IrPT** is tentatively assigned to be of ^{3}IL character. Specifically, the triplet excited state may be localised on the pyrene moiety in **IrPT**. To confirm this assumption, low temperature emission studies were carried out for the two complexes (Figure 5.10).

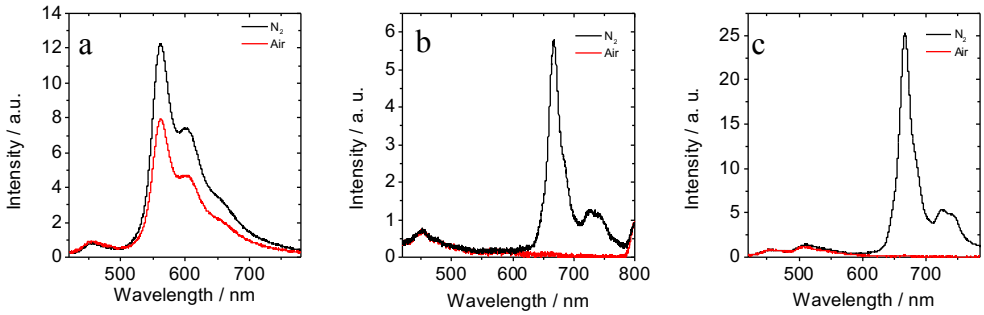

Figure 5.9 *Emission spectra of (a)* ***IrTT***, *(b)* ***IrPP*** *and (c)* ***IrPT*** *in CH_2Cl_2 under a nitrogen, and an air atmosphere. λ_{ex} = 400 nm, C = 1 × 10^{-5} mol/L, 298 K.*

In Figure 5.10a, for **IrTT**, the emission band at 77 K has a similar profile to that collected at 298 K but with increased fine structure. A thermally-induced anti-Stokes shift of the emission peak is observed at λ 562 nm, calculated as a relatively large value of $\Delta E_s = 290$ cm^{-1}. According to literature sources of Ir(III) complexes of this kind,[93] **$Ir(ppy)_2(bpy)[PF_6]$** demonstrates an expected ^{3}MLCT-type emission at λ 590 nm, with a large calculated thermally-induced anti-Stokes shift of ΔE_s = 2100 cm^{-1}. Large thermally-induced anti-Stokes shifts are typical of charge transfer character, and do not typically occur for ligand-centred type emissive states.[123] Corroborating these literature-based assertions with the experimental results collected for **IrTT**, the phosphorescence-type emission is characterised to be mainly of ^{3}IL'CT character originating from the triarylamine TPA moiety to the coordinated ppy ligand. As discussed, some perturbation from the metal is expected, and there is therefore some ^{3}MLCT /^{3}IL'CT mixing. For **IrPT**, the thermally-induced anti-Stokes shift is calculated as only $\Delta E_s = 91$ cm^{-1} (at λ 668 nm). The lack of charge transfer character, revealed through the very small anti-Stokes shifts, characterises the emissive state as a pyrene-based ^{3}IL state for **IrPT**. Confirmation of the location of the triplet excited state is important for potential applications, and as such, transient difference absorption measurements were also collected and studied.

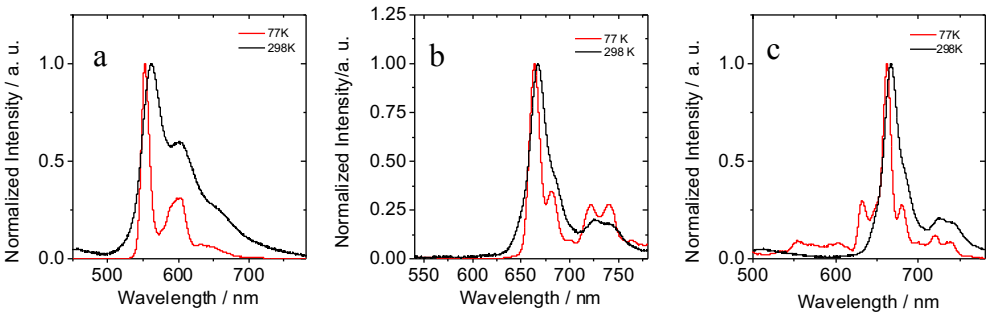

Figure 5.10 *Normalised emission spectra of (a)**IrTT**, (b)**IrPP** and (c)**IrPT** in CH_3CH_2OH:CH_3OH (4:1, v/v) under nitrogen at 77 K (red line,) and room temperature (black line). λ_{ex} = 400 nm, C = 1 × 10^{-5} mol/L.*

5.4.2 Transient State Studies

5.4.2.1 Nanosecond Time-resolved Transient Difference Absorption of IrTT and IrPT

Upon the excitation at λ_{ex} 355 nm, an intense bleaching peak of **IrTT** is found λ 406 nm in Figure 5.11a. It shows a shoulder peak at λ 334 nm. This confirms the triplet excited

state is a mixture ^{3}MLCT and ^{3}IL'CT. The triplet excited lifetime was determined as 0.2 μs, corresponding to its phosphorescence lifetime. For **IrPT**, the significant bleaching peak at λ 390 nm was observed, and correlated to the depletion of the ground state of pyrene moiety (Figure 5.11c). The transient difference absorption spectrum of **IrPT** corresponds well to its steady state absorption spectrum and indicates that the triplet excited state mainly localised on the pyrene-moiety ligand. The triplet excited state lifetime was determined as 75 μs (Figure 5.11f). It is worth noting that the nanosecond time-resolved transient difference absorption spectrum of **IrPT** is very similar to that of **IrPP**. In short, both have a similar triplet excited state feature. This further confirms that the triplet excited state is localised on the pyrene-moiety ligand on **IrPT**.

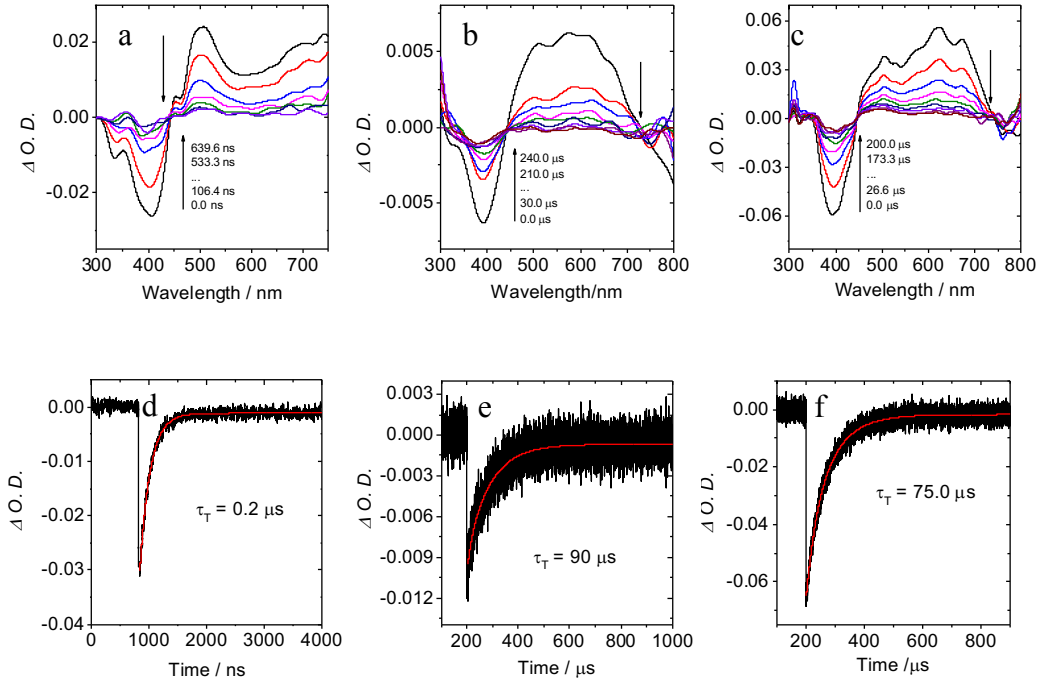

Figure 5.11 *Nanosecond time-scaled transient difference absorption spectra of (a)* ***IrTT****, (b)* ***IrPP*** *and (c)* ***IrPT*** *plus an excitation at λ_{ex} = 355 nm and their decay trace (d)(e)(f). C = 1 × 10^{-5} mol/L, in CH_2Cl_2, 298 K.*

As discussed in Chapter 4, for **IrBP**, the existence of two different functional chromophores results in two different bleaching peaks in the nanosecond time-resolved transient difference spectrum. The first is generated by pyrene moiety, with the other generated by the BODIPY moiety. However, for **IrPT**, only one bleaching peak is observed, with a similar triplet excited lifetime to **IrPP**. In conclusion to this point, it can be concluded that the TPA moiety does not substantially contribute to the triplet excited

state of **IrPT**. This may due to the TPA-based triplet excited state being too high to be reached in **IrPT**, as the triplet excited state is only located on the lowest possible triplet excited state of the complex. This is also explain why the triplet excited state lifetime of **IrPT** is not prolonged from **IrPP**.

The determination of the photophysical properties of the triplet excited state in this work is challenging, as no literature examples exist for complexes of this kind with linked chromophores to the phenyl ring of 2-phenylpyridine. A series of Ir(III) complexes using the N^N ligand, 1,10-phenanthroline, have been previously published by the Draper group. Here, TPA and pyrene moieties were attached to the 3,8-positions of 1,10-phenanthroline.[20] The complex bearing both a TPA and a pyrene moiety, **Ir-PPT** (Figure 1.12), shows a similar triplet excited state character. The triplet excited state is also located on pyrene moiety. However, its triplet excited state lifetime was found to be only 53 μs. In this work, the excited state lifetimes of **IrPT** and **IrPP** were determined as 75 μs, and 90 μs respectively. This confirms that synthetic access to the linked position of the 2-phenylpyridine ligand offers opportunities to prolong the triplet excited state lifetime. This is the highlight of this chapter, and as such, DFT calculations were also undertaken to unambiguously confirm the location of the triplet excited state, and are now presented.

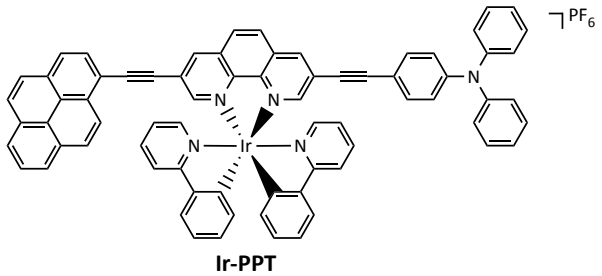

Ir-PPT

Figure 5.12 *Structure of reference complex* ***Ir-PPT****.*[20]

5.4.3 Density Functional Theory (DFT) Calculations

Density Functional Theory (DFT) calculations were carried out to corroborate the experimentally results, with the assignment of the location of the triplet excited state. In **IrTT** (Figure 5.13a), the triplet excited state is mainly located on TPA moiety, and the Ir(III) metal centre. However, for **IrPT** and **IrPP**, the triplet excited state is mainly localised to the pyrene moiety only. This confirms the previous discussed points that for these two complexes, the pyrene moiety dictates the emissive state properties. This phenomena is also illustrated by the short triplet excited state lifetime of **IrTT**.

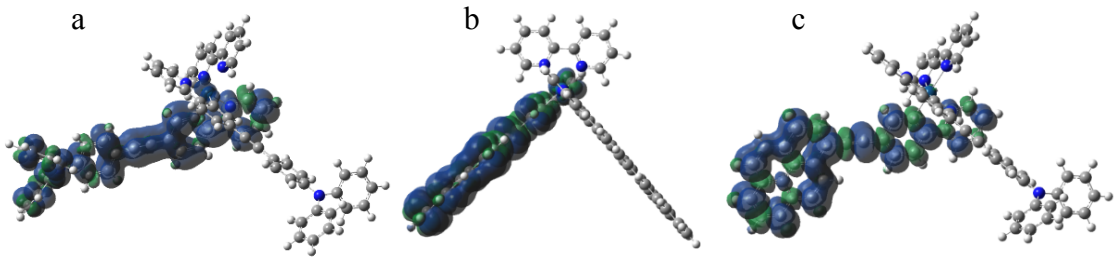

Figure 5.13 *Isosurface of spin density of (a)* ***IrTT****, (b)* ***IrPP*** *and (c)* ***IrPT*** *at the optimised triplet-state geometries. Methylene chloride was used as the solvent for the calculations. Calculations were performed at TDDFT/B3LYP/GENECP/LANL2DZ with Gaussian 09.*

The UV-vis absorption wavelengths, and triplet excited states of these complexes were calculated with a time-dependent DFT (TDDFT) method. For **IrPT**, as shown in Table 5.2, the singlet excited states were λ 467 nm, 460 nm and 342 nm, and mainly contributed by pyrene-localised IL and TPA-based ML'CT. This is found to be closed to our experimental results. For the triplet excited states, the lowest triplet excited state is located at λ 692 nm (1.79 eV), originating from the pyrene-moiety. This is very close to the observed phosphorescence-type emission at room temperature at λ 668 nm (1.86 eV) and 726 nm (1.71 eV) for **IrPT**.

Table 5.2 *Electronic Excitation Energies (eV) and corresponding Oscillator Strength (f), main configurations and CI coefficients of the Low-lying Electronic Excited States of the complex* ***IrPT*** *calculated by TDDDFT/B3LYP/GENECP/LANL2DZ, CH_2Cl_2 as the solvent (PCM model) based on the optimised Ground State Geometries.*

	Electronic Transition	TD-DFT/B3LYP/GEN				
		Energy [a]	*f* [b]	Composition [c]	CI [d]	character
Singlet	$S_0 \rightarrow S_5$	2.6536 eV 467 nm	1.1610	H-2-L	0.2497	ML"CT; LL"CT
				H-1-L+1	0.2331	IL, MLCT
				H-L+2	0.5969	ML'CT
	$S_0 \rightarrow S_6$	2.6978 eV 460 nm	0.9879	H-1-L+1	0.6382	IL, MLCT
				H-L+2	0.2745	L'MCT
	$S_0 \rightarrow S_{25}$	3.6284 eV 342 nm	0.3450	H-5-L+1	0.1080	IL, MLCT
				H-3-L+2	0.6208	ML'CT
				H-L+9	0.1673	IL'
Triplet		1.7918 eV	0.0000[f]	H-1-L+1	0.6080	IL, MLCT

	692 nm		H-1-L+2	0.1174	LL'CT
$S_0 \rightarrow T_1$			H-1-L+3	0.1162	LL"CT
			H-1-L+4	0.2428	IL, LL"CT
$S_0 \rightarrow T_2$	2.2460 eV 552 nm	0.0000[f]	H-2-L	0.1026	MLCT
			H-L	0.6904	L'L"CT

[a] Only the selected low-lying excited states are presented. [b] Oscillator strengths. [c] Only the main configurations are presented. [d] The CI coefficients are in absolute values. [e] L stands for pyrene localised ligand, L' stands for TPA localised ligand and L" stands for bipyridine localised ligand. [f] No spin-orbital coupling effect was considered, thus the *f* values are zero.

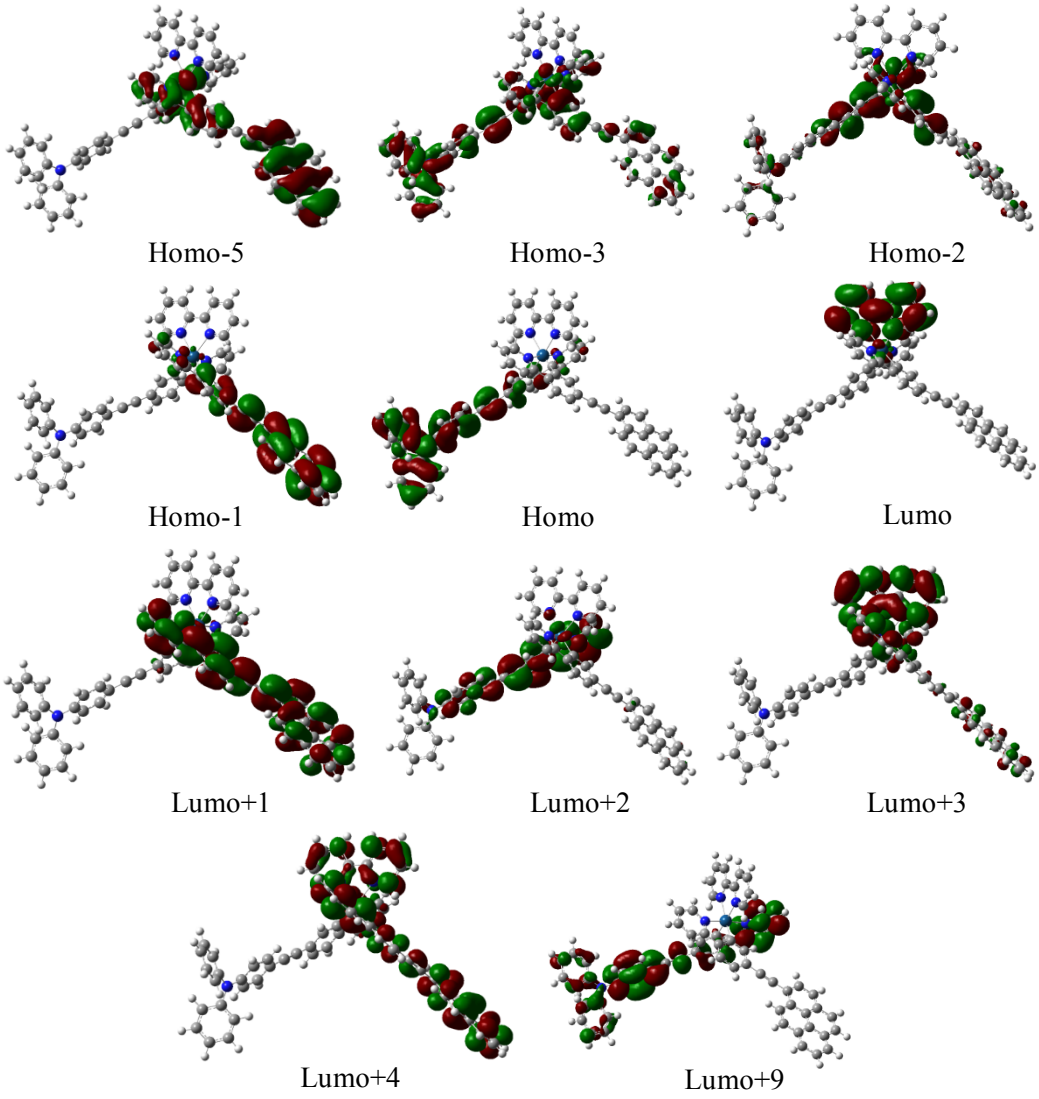

Figure 5.14 *Electron density maps of the frontier molecular orbital of the complex* ***IrPT****, based on ground state optimised geometry from the TDDFT calculations at the TDDFT/B3LYP/GENECP/LANL2DZ level with Gaussian 09W.*

Table 5.3 *Electronic Excitation Energies (eV) and corresponding Oscillator Strength (f), main configurations and CI coefficients of the Low-lying Electronic Excited States of the complex* ***IrTT*** *calculated by TDDDFT/B3LYP/GENECP/LANL2DZ, CH_2Cl_2 as the solvent (PCM model) based on the optimised Ground State Geometries.*

	Electronic Transition	TD-DFT/B3LYP/GEN				
		Energy [a]	*f* [b]	Composition [c]	CI [d]	character
Singlet	$S_0 \rightarrow S_4$	2.6110 eV 475 nm	0.8009	H-2-L	0.4071	ML"CT, L'L"CT
				H-1-L+2	0.1318	L'MCT, IL'CT
				H-L+1	0.5419	L'MCT, IL'CT
	$S_0 \rightarrow S_7$	2.7245 eV 455 nm	0.4307	H-1-L+2	0.6674	L'MCT, IL'CT
				H-L+1	0.1626	L'MCT, IL'CT
				H-L+2	0.1334	L'MCT, IL'CT
	$S_0 \rightarrow S_{24}$	3.6163 eV 343 nm	0.3978	H-4-L+1	0.1319	L'MCT, IL'CT
				H-3-L+2	0.6479	L'MCT, IL'CT
				H-L+8	0.1161	IL'CT
Triplet	$S_0 \rightarrow T_1$	2.1171 eV 586 nm	0.0000[f]	H-3-L+2	0.1843	L'MCT, IL'CT
				H-2-L+1	0.1782	MC
				H-1-L+2	0.3634	L'MCT, IL'CT
				H-L+1	0.4551	L'MCT, IL'CT
	$S_0 \rightarrow T_4$	2.2460 eV 553 nm	0.0000[f]	H-2-L	0.1327	ML"CT
				H-L	0.6861	L'L"CT, L'MCT

[a] Only the selected low-lying excited states are presented. [b] Oscillator strengths. [c] Only the main configurations are presented. [d] The CI coefficients are in absolute values. [e] L stands for pyrene localised ligand, L' stands for TPA localised ligand and L" stands for bipyridine localised ligand. [f] No spin-orbital coupling effect was considered, thus the *f* values are zero.

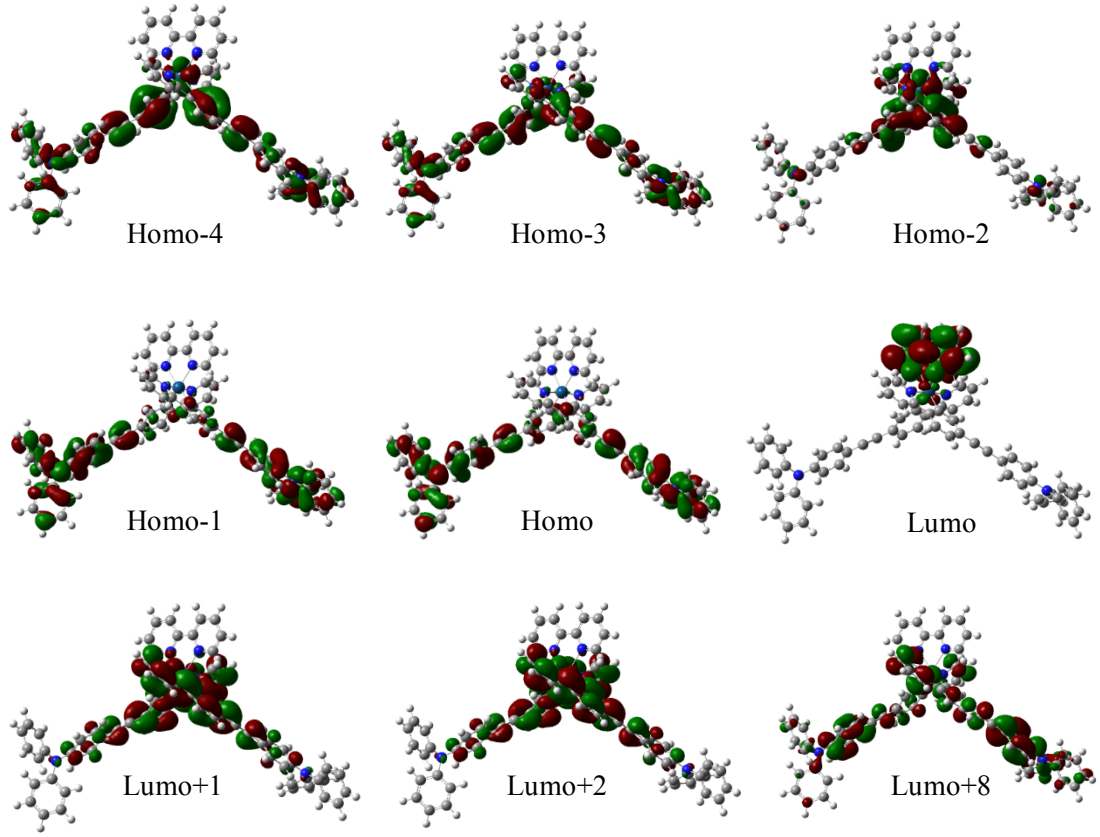

Figure 5.15 *Electron density maps of the frontier molecular orbital of the complex* ***IrTT****, based on ground state optimised geometry from the TDDFT calculations at the TDDFT/B3LYP/GENECP/LANL2DZ level with Gaussian 09W.*

5.5 Triplet Photosensitisation Studies for TTA Upconversion and Potential Photodynamic Therapy

5.5.1 TTA Upconversion Studies of IrTT and IrPT as Triplet Photosensitisers

To explore their triplet photosensitisation ability, TTA upconversion (TTA UC) studies were carried out for the generated complexes. Upon excitation at λ_{ex} 473 nm, **IrTT** showed a weak phosphorescence at λ 562 nm under a nitrogen atmosphere (Figure 5.16a).

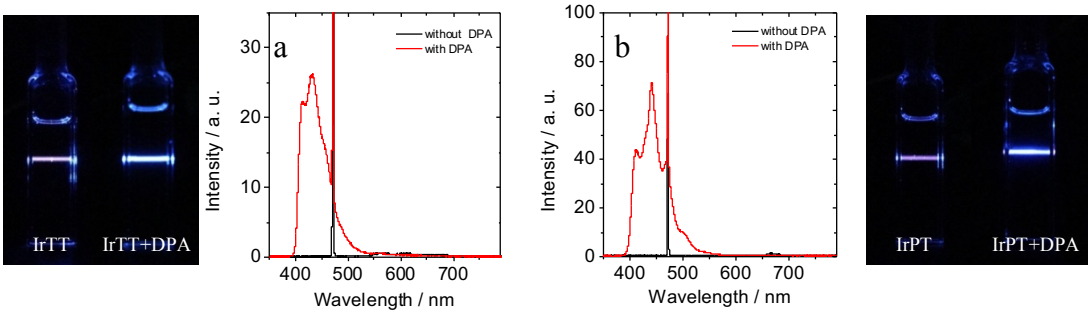

Figure 5.16 *Upconversion with* ***IrTT*** *and* ***IrPT*** *as triplet photosensitisers in CH_2Cl_2, 298 K. (a) Photograph of the TTA upconversion process (with and without acceptors) with* ***IrTT****, and the emission spectra with* ***DPA*** *added (C[****IrTT****] = 1.0 × 10^{-5} mol/L , C[****DPA****] = 7.7 × 10^{-4} mol/L) (b) Photograph of the TTA upconversion process (with and without acceptors) with* ***IrPT****, and the emission spectra with* ***DPA*** *added (C[****IrPT****] = 1.0 × 10^{-5} mol/L , C[****DPA****] = 1.67 × 10^{-3} mol/L). Excited with laser, λ_{ex} = 473 nm, 5.0 mW.*

Upon the addition of triplet acceptor, **DPA**, a new emissive band at λ 433 nm was observed. This observed fluorescence from the **DPA** triplet acceptor confirms the successful TTA upconversion process for this complex. However, the TTA upconversion quantum yield was found to be low (10.9 %). For **IrPT**, the same excitation wavelength and triplet acceptor were chosen. After the addition of **DPA**, upon excitation at λ 473 nm, the delayed fluorescence of **DPA** was observed. The determined TTA upconversion quantum yield was collected as 36.0 %. This is also a significant improvement over **IrPP**,

whose TTA upconversion quantum yield was also collected (Φ_{UC} = 8.6 %). This may due to the absorption coefficient of **IrPP** at λ 473 nm being too small (Figure 5.7).

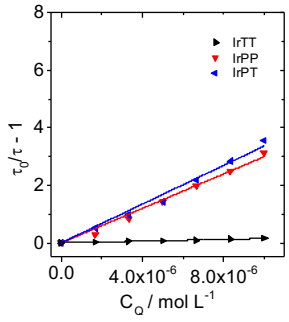

Figure 5.17 *Stern–Volmer plots generated from the triplet excited state lifetime (τ_T) quenching of complexes **IrTT**, **IrPP**, and **IrPT**, measured with the increasing acceptor concentration in CH_2Cl_2. The lifetimes were measured with the nanosecond time-resolved transient difference absorption. C [Sensitiser] = 1.0 × 10^{-5} mol/L, 298 K.*

The triplet-triplet energy transfer (TTET) efficiency was also measured with the plotted triplet lifetime quenching Stern-Volmer graph (Figure 5.17). The calculated quenching constant of **IrPP** is similar to that of **IrPT**. This is reasonable for their similar triplet excited state lifetimes. However, for **IrTT**, the triplet lifetime was too short to be detected accurately with the nanosecond time-resolved transient difference absorption equipment.

Table 5.4 *Triplet excited state properties of **IrTT**, **IrPP** and **IrPT**.*

	τ_T[a] (μs)	K_{sv}[b] (10^5 M^{-1})	K_q[c] (10^9 $M^{-1}s^{-1}$)	Φ_{UC}[d] (%)	Φ_Δ[e] (%)
IrTT	0.2	--[f]	--[f]	10.9	18.5
IrPP	90	2.99	3.32	8.6	58.8
IrPT	75	3.36	4.48	36.0	50.8

[a] Triplet excited state lifetime. [b] Quenching constant. [c] Bimolecular quenching constants. [d] TTA upconversion yield in deaerated CH_2Cl_2 with triplet acceptor DPA, with the prompt fluorescence of BDP as the standard (Φ_f = 71.2 % in CH_3CN)[122]. [e] Quantum yield of singlet oxygen in CH_2Cl_2, excited at λ 421 nm and $Ru(bpy)_3[2PF_6]$ (Φ_Δ = 57 % in CH_3CN) as standard. [f] The lifetime changing was too small to be detected with nanosecond resolved equipment.

5.5.2 Singlet Oxygen Sensing of IrTT, IrPT as Triplet Photosensitisers

IrTT and **IrPT** were also studied as triplet photosensitisers for singlet oxygen photosensitisation for their potential application in photodynamic therapy (PDT) *via* their irradiation time-dependent decrease of absorption spectra (Figure 5.18). $[Ru(bpy)_3]Cl_2$

was used as the reference standard (Φ_Δ = 57.1 % in CH_3CN), with DPBF used as the singlet oxygen scavenger. The mixtures of the respective photosensitiser and singlet oxygen scavengers were exposed to the same excitation wavelength (λ 421 nm) in CH_2Cl_2. The absorption spectra were recorded at 15 second intervals, for a total of 105 s.

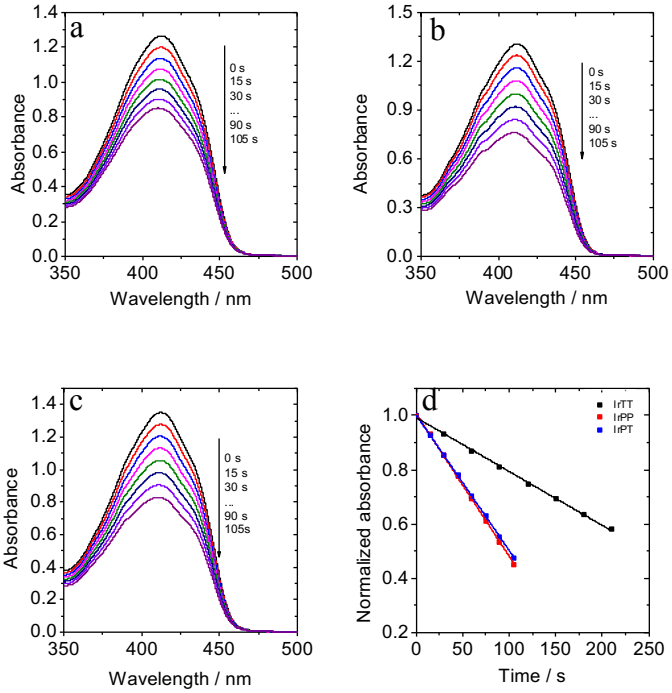

Figure 5.18 *Photosensitisation of $^1O_2$. Irradiation time-dependent decrease of absorption at λ 410 nm of DPBF with (a)* ***IrTT****, (b)* ***IrPP*** *and (c)* ***IrPT*** *as the photosensitiser. λ_{ex} = 421 nm at 298 K, C = 1.0 × 10^{-5} mol/L in CH_2Cl_2. (d) Comparison of singlet oxygen sensing ability.*

Since the excitation wavelength was kept constant, the accurate comparison of the singlet oxygen quantum yields could be performed (Figure 5.18d). The singlet oxygen quantum yield for **IrTT** is found to be only 18.5 %, whereas the singlet oxygen quantum yields of **IrPP** and **IrPT** were determined as 58.8 % and 50.8 % respectively.

5.6 Conclusion

The multi-chromophore heteroleptic Ir(III) complex, **IrPT**, and the reference complexes, **IrTT** and **IrPP**, were synthesised successfully. Compared to conventional photosensitisers, two different chromophores with the complex structure can enhance and broaden the absorption wavelength. For **IrTT**, the triplet excited state is localised on both

the TPA-ligand and the metal centre, and thus, the triplet excited lifetime is very short and determined as 0.2 μs. For **IrPP** and **IrPT**, the introduction of a pyrene-moiety generates a pyrene-localised 3IL triplet excited state, and their triplet excited state lifetimes are determined as 90 μs and 75 μs respectively. The highlight of this study has proven that synthetic access to a novel position on the phenyl ring of the 2-phenylpyridine ligand allows the creation of prolonged triplet excited state lifetimes. All of the generated novel complexes were used as triplet photosensitisers towards TTA upconversion, and singlet oxygen photosensitisation studies. The TTA upconversion quantum yields of **IrTT** and **IrPT** were determined as 10.9 % and 36.0 % respectively. These results offer further insight into the potential improvements of this kind of complex, through the use of multi-chromophore d^6 complexes, and the novel linked position. These studies will inform practical and industrial applications of triplet photosensitisers for future TTA-UC technologies and operations.

6 Novel Application of Ru(II) Triplet Photosensitisers towards Photo-Polymerisation

6.1 Introduction

Based on the work of novel Ir(III) triplet photosensitisers bearing ligands of multiple chromophores in Chapters 4 and 5, Ru(II) complexes were designed that incorporated triphenylamine (TPA) moieties, pyrene moieties, or BODIPY moieties as the light-harvesting chromophores. Concurrent to the desirable broadening of the absorption wavelength, these chromophores would allow further investigations towards the localisation of the triplet excited state; a feature which can be exploited towards novel applications such as photo-polymerisation. With triplet photosensitisers, the photo-polymerisation is able to be excited by the visible light, rather than the traditional UV light. Moreover, the cost of ruthenium complexes is much lower than iridium complexes.

6.2 Synthesis of Polyimine Ru(II) Complexes Bearing Two Chromophore-type Ligands

6.2.1 Synthesis of RuBrBr

Cis-Ru(Br-bpy)$_2$Cl$_2$ was prepared by a two-step reaction *via* a Ru(II) polymer, Dichloro(1,5-cyclooctadiene)ruthenium(II) ([Ru(II)(cod)Cl$_2$]$_n$). [Ru(II)(cod)Cl$_2$]$_n$ was synthesised from commercially available RuCl$_3$.xH$_2$O and 1,5-cyclooctadiene (Scheme 6.1).[124] The mixture was added to CH$_3$CH$_2$OH under a nitrogen atmosphere, and further to refluxing for 24 h, a red participate was generated and collected. The crude [Ru(II)(cod)Cl$_2$]$_n$ was obtained *via* filtration, and subsequently washed with cold CH$_3$CH$_2$OH twice.

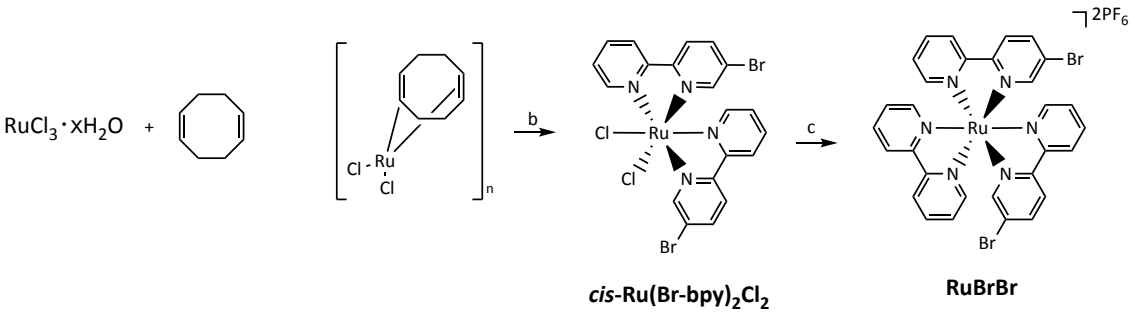

Scheme 6.1 *Synthesis of* ***RuBrBr****. (a) CH$_3$CH$_2$OH, nitrogen, reflux, 24 h, yield: 98 %. (b) 1,2-dichlorobenzene, argon, 180 ^{o}C, 2 h, yield: 96 %. (c)* ***L-1****, CH$_3$CH$_2$OH:H$_2$O (3:1, v/v), argon, 85 ^{o}C, 4 h, yield: 31 %.*

Cis-Ru(Br-bpy)$_2$Cl$_2$ was synthesised using 4-bromo-2,2'-bipyridine, **L-1**, and [Ru(II)(cod)Cl$_2$]$_n$ (Scheme 6.1).[125] The mixture was heated to 180 ^oC in 1,2-dichlorobenzene for 2 h under an argon atmosphere. After cooling to room temperature, diethyl ether was slowly added to the reaction mixture. Addition of the diethyl ether precipitated a black-purple solid which was isolated by filtration. This was then washed with a large excess of diethyl ether. Analysis of the solid revealed the generation of a crude sample of ***cis*-Ru(Br-bpy)$_2$Cl$_2$**.

RuBrBr was successfully generated *via* the standard di-imine coordination reaction of refluxing ***cis*-Ru(Br-bpy)$_2$Cl$_2$** and **L1** in a mixture of CH_3OH and water. The addition of a saturated solution of KPF_6 precipitated **RuBrBr** from the cooled reaction mixture. This was purified by silica-based column chromatography using a mixed mobile phase of acetonitrile (CH_3CN), water, and a saturated solution of KNO_3. Further to concentration of the product fractions, the compound was treated with a second amount of a saturated solution of KPF_6, precipitating **RuBrBr** as a red solid.

6.2.2 Synthesis of RuPP

The final compound **RuPP** (Scheme 6.2) was synthesised *via* a Sonogashira cross-coupling reaction in a dry mixed solvent system of triethylamine (TEA) and CH_3CN with 1-ethynylpyrene, under an argon atmosphere. The ratio of reactants is 1:1 of molar weight. Further to purification with silica-based column chromatography, and treatment with a saturated solution of KPF_6, a pure sample of **RuPP** was obtained. The incomplete reaction product **RuPBr** was also obtained.

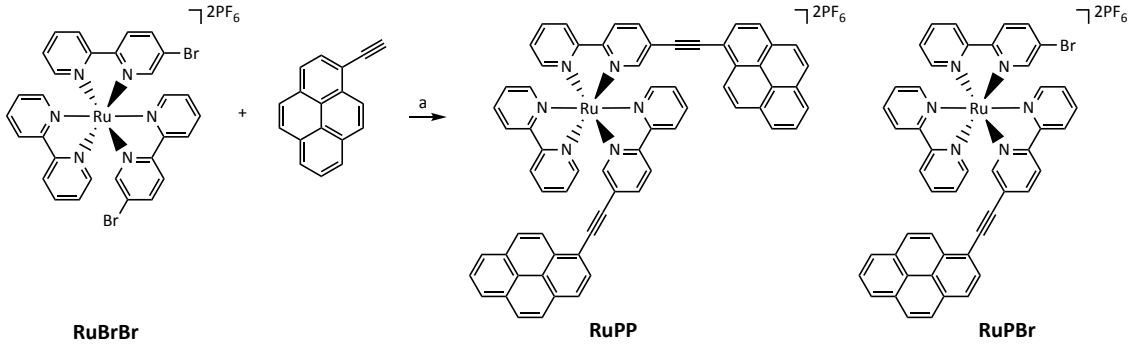

Scheme 6.2 *Synthesis of* ***RuPP****. (a) TEA:CH_3CN (1:1, v/v), Pd(PPh$_3$)$_2$Cl$_2$, PPh$_3$, CuI, overnight, 80 °C, Ar, yield: 35 % (**RuPP**); 33 % (**RuPBr**).*

However, this product exists as two isomers which could not be separated despite exhaustive chromatography methods. This issue is not seen in the corresponding Ir(III)

complex due to the preference nature of its coordination sphere (as discussed in Chapter 4). **RuPP** is also an asymmetric complex. This will be confirmed by NMR spectroscopy and X-ray single crystal analysis in the following section. Due to the extreme difficulty of the purification of **RuPBr**, the synthesis of Ruthenium-derived multi-chromophore bearing triplet photosensitisers was not considered further as part of this body of work.

6.2.3 Synthesis of RuTT

The complex **RuTT** was synthesised in a similar fashion to **RuPP**, but with 1-ethynyltriphenylamine (TPA) as the chromophore-based reactant (Scheme 6.3).

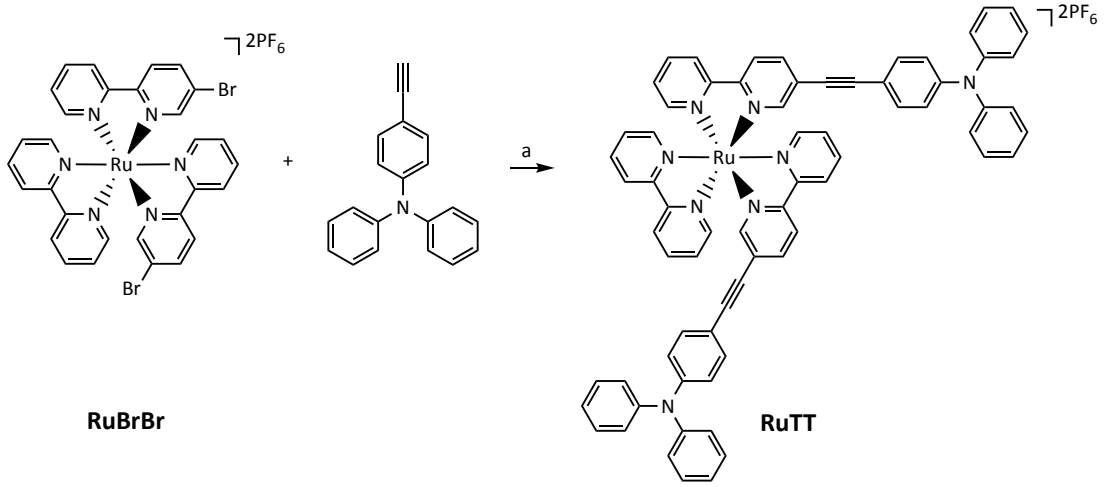

Scheme 6.3 *Structure of* ***RuTT****. (a) TEA:MeCN (1:1, v/v), $Pd(PPh_3)_2Cl_2$, PPh_3, CuI, overnight, 80 °C, Ar, yield: 19 %.*

6.3 Structural Characterisation of RuPP and RuTT

6.3.1 Crystallographic Analysis of RuPP

Crystals suitable for single crystal X-ray diffraction studies of **RuPP** were collected *via* the slow evaporation of a deuterated acetonitrile solution. The structure was solved and refined by Dr. Brendan Twamley in Trinity College Dublin. A specimen of $C_{66}H_{40}F_{12}N_6P_2Ru$, approximate dimensions 0.070 mm × 0.210 mm × 0.230 mm, was used for the X-ray crystallographic analysis. The X-ray intensity data were measured at 100(2)K using an Oxford Cryosystems low temperature device using a MiTeGen micromount. Bruker APEX software was used to correct for Lorentz and polarisation effects.

The structure was solved using the Bruker APEX Software Package and refined with XL in Olex2, using the space group $P\bar{1}$, with Z = 2 for the formula unit, $C_{66}H_{40}F_{12}N_6P_2Ru$. The final anisotropic full-matrix least-squares refinement on F^2 with 784 variables converged at R1 = 3.40 %, for the observed data and wR2 = 7.53 % for all data. The goodness-of-fit was 1.030. The largest peak in the final difference electron density map was 0.581 $e^-/Å^3$ and the largest hole was -0.701 $e^-/Å^3$ with an RMS deviation of 0.068 $e^-/Å^3$. On the basis of the final model, the calculated density was 1.597 g/cm^3 and F(000) was 1320 e^-.

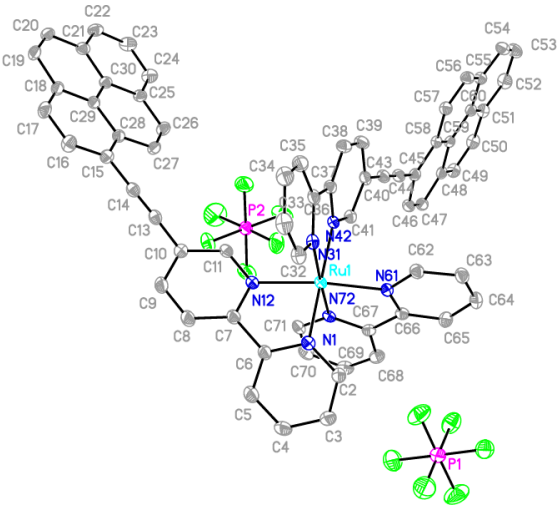

Figure 6.1 *Asymmetric unit of* ***RuPP*** *with atomic displacement parameters shown at 50 % probability. Hydrogen atoms omitted for clarity.*

The most significant difference to compound **IrPP** in Chapter 4 are the π-π stacking interactions in **RuPP**'s single crystal structure (Figure 6.2).

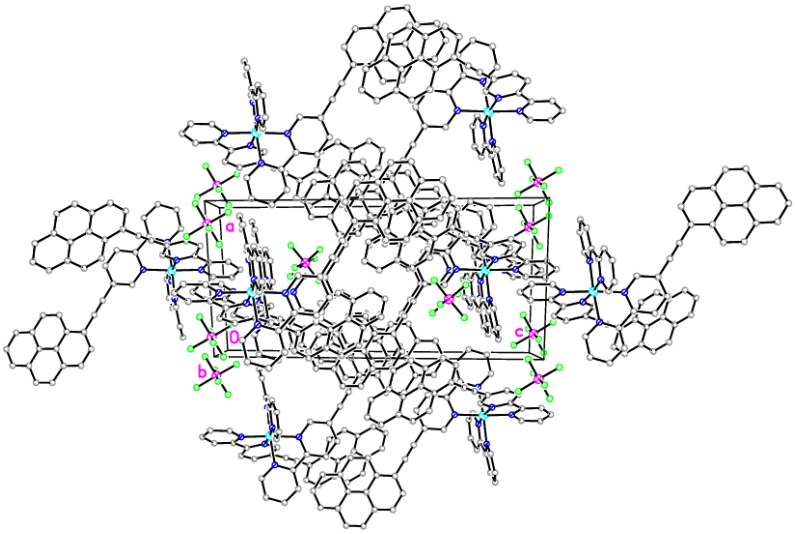

Figure 6.2 *Packing diagram of* ***RuPP*** *viewed down to the a-axis. Hydrogen atoms omitted for clarity.*

6.3.2 Structural Characterisation of RuPP and RuTT *via* NMR Studies and Mass Spectrometry

The isolated **RuPP** and **RuTT** complexes were characterised by a range of multinuclear NMR techniques (^{1}H NMR, ^{13}C NMR, 2D-NMR) and high resolution mass spectrometry.

As previously discussed, **RuPP** has an asymmetric structure. This is confirmed by the NMR spectra. Figure 6.3 shows the ^{1}H spectrum of **RuPP**. As it is well resolved, the proton signals can be clearly integrated to 40. All the proton signals correspond to aromatic C-H type signals, and are located and identified in the downfield region (δ 7.45–8.68 ppm) of the spectrum as expected.

RuPP has two three-spin, and four four-spin pyridyl systems. The pyridyl-ring carbons were distinguished using a HSQC (Heteronuclear Single Quantum Coherence) spectrum in Figure 6.5 (purple box). Those carbon atoms adjacent or close to the coordinated N-atoms, have carbon signals in the expected region of δ 150-155 ppm (*via* the ^{13}C spectrum). Observable in the ^{1}H-^{1}H COSY (COrrelation SpectroscopY) spectrum in Figure 6.4, the pyridyl spin systems are also identifiable, and are highlighted by inset orange boxes.

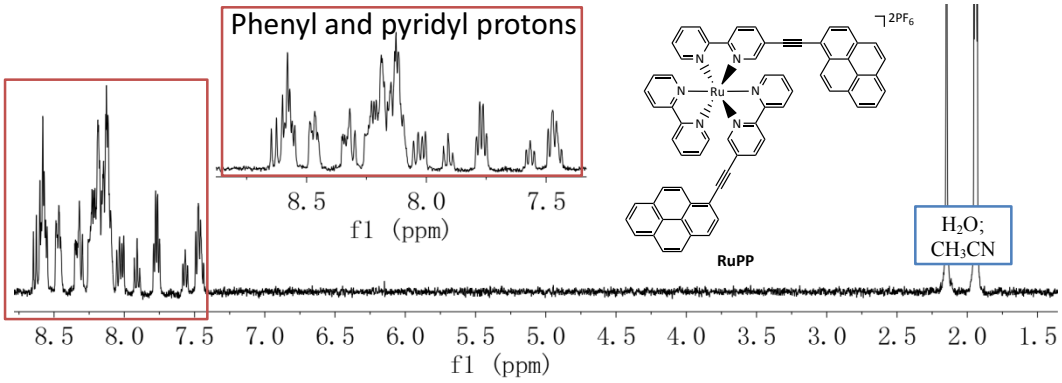

Figure 6.3 *^{1}H NMR spectrum of* ***RuPP*** *(600 MHz, CD_3CN, 20 °C).*

In the ^{13}C NMR spectrum (Figure 6.6), four carbon signals attributed to the two acetylene bonds were found at δ 91.02, 91.06, 96.70, and 96.81 ppm. The four signals of the acetylene carbons further corroborate the structure, as only two signals would be observed in a symmetric system.

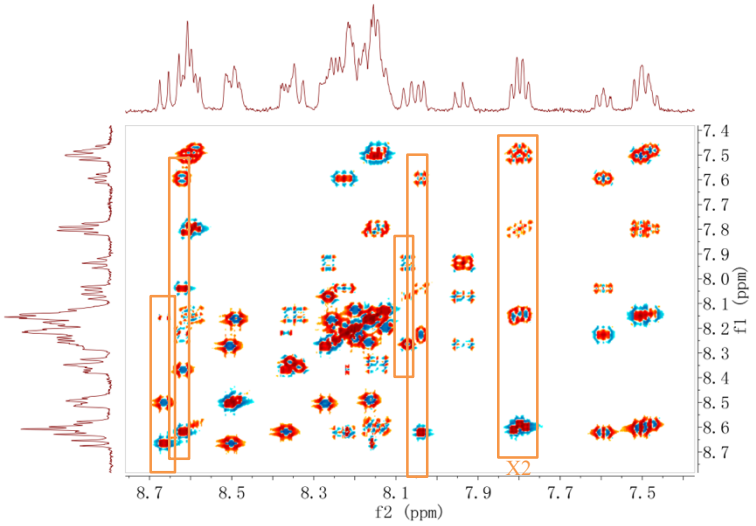

Figure 6.4 *The ^{1}H-^{1}H COSY analysis of* ***RuPP*** *(600 MHz, CD_3CN, 20 ℃).*

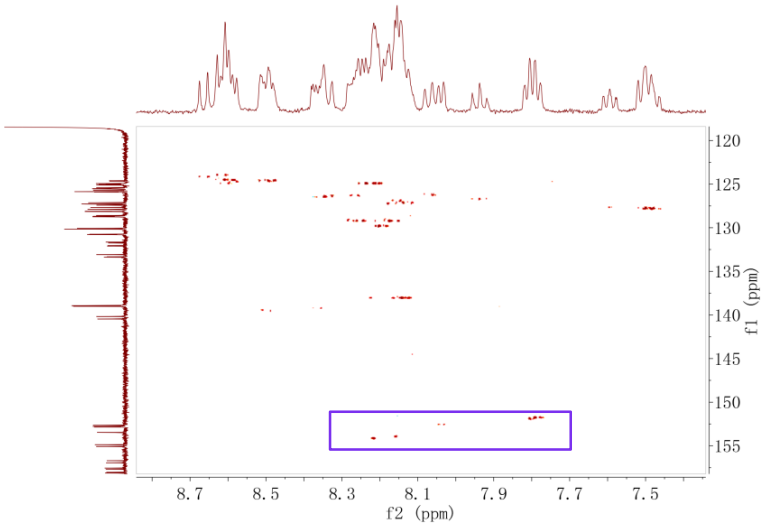

Figure 6.5 *The HSQC spectrum of* ***RuPP*** *(600 MHz, CD_3CN, 20 ℃).*

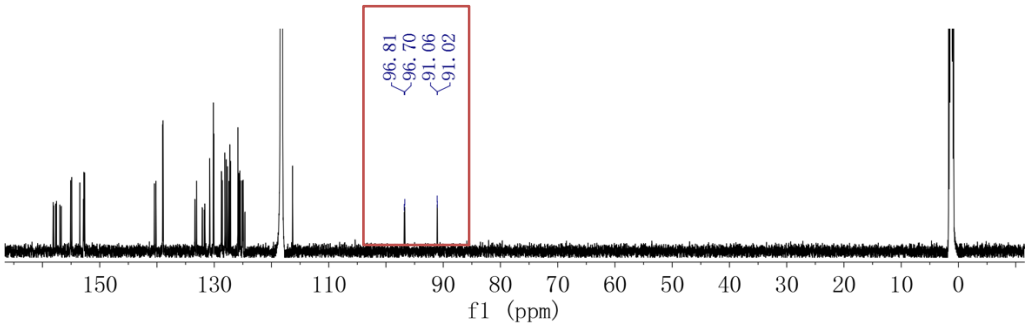

Figure 6.6 *^{13}C NMR spectrum of* ***RuPP*** *(150 MHz, CD_3CN, 20 ℃).*

6.4 Photophysical Studies

6.4.1 Steady State Properties of RuPP and RuTT

The UV-vis spectra of **RuPP** and **RuTT** are presented in Figure 6.7a. **RuPP** shows two absorption bands at λ 288 nm and 422 nm. They are designated as the π-π* transition of 2,2'-dipyridine, and pyrene moiety respectively. The band which starts at λ 450 nm and tails off at λ 550 nm is dominated by a metal to ligand charge transfer (^{1}MLCT) transitions For **RuTT**, there is a broad peak at λ 304 nm, which is assigned to the π-π* transition of 2,2'-dipyridine, and the TPA moiety. Due to the electron donating ability of TPA, this absorption undoubtedly contains some intraligand charge transfer (^{1}ILCT) character, as observed for a number of similar systems in the literature. The peak at λ 429 nm is assigned to TPA based ligand π-π transitions, and a small contribution from a ^{1}MLCT transition.

The absorption profiles of both complexes were measured in four solvents of different polarity; toluene, methylene chloride, CH_3OH, and CH_3CN. For both complexes, a blue shift is observed with the increasing polarity (Figure 6.7b; Figure 6.7c). This indicates that the ground state is affected by the polarity of solvent.

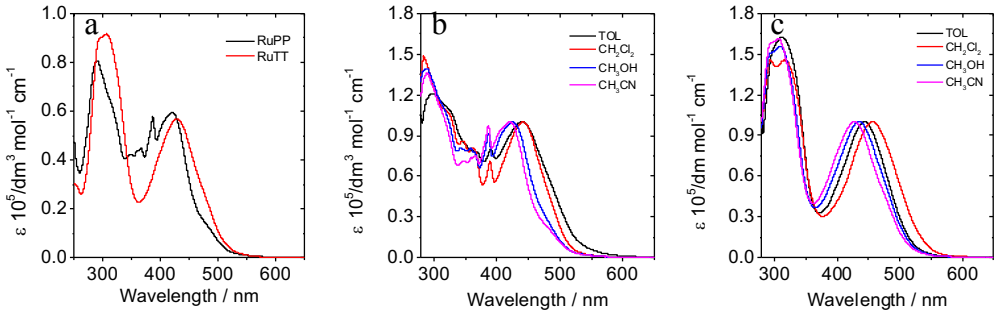

Figure 6.7 *(a) Absorption spectra of* ***RuPP*** *and* ***RuTT****. C = 1 × 10^{-5} mol/L in CH_3CN, 298 K. (b)(c) Normalised absorption spectra of (b)* ***RuPP*** *and (c)* ***RuTT*** *in solvents of different polarity, TOL = toluene. C = 1.0 × 10^{-5} mol/L, 298 K.*

The emission properties of both complexes were studied in CH_3CN, with the emission profiles of the generated complexes recorded under varying atmospheres and temperatures (Figure 6.8). For **RuPP**, two emission bands at λ 679 and 748 nm were observed when measured under N_2. These bands were completely quenched in an aerated solution. Under N_2, luminescence measurements demonstrated a long microsecond scale excited state lifetime (94.0 μs). This result implies that the luminescence of **RuPP** has a

strong phosphorescence character, and is tentatively assigned as heavy pyrene-localised intraligand triplet excited state character (^{3}IL*). For **RuTT**, a structureless emission band was observed at λ 659 nm under N_2. In an aerated solution, the emission band suffered some quenching, but retained some luminescent character. The excited state lifetime of this band was determined as 1.3 μs under a N_2, which is a characteristic of the short lifetimes of similar ruthenium polyimine complexes.[123]

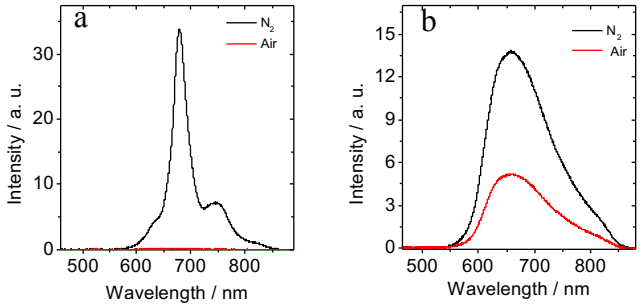

Figure 6.8 *Emission spectra of (a)* ***RuPP*** *and (b)* ***RuTT*** *in CH_3CN under nitrogen and air atmospheres. λ_{ex} = 450 nm, C = 1 × 10^{-5} mol/L, 298 K.*

Low temperature emission measurements were also collected for **RuPP** and **RuTT**. In Figure 6.9a, for **RuPP**, the emission band at 77 K has a similar profile to that collected at 298 K, but with reduced broadness. The profile displays similar vibronic progression to the room temperature spectrum. A thermally-induced anti-Stokes shift of the emission peak is observed at λ 668 nm, and is relatively large ΔE_s = 265 cm^{-1}.

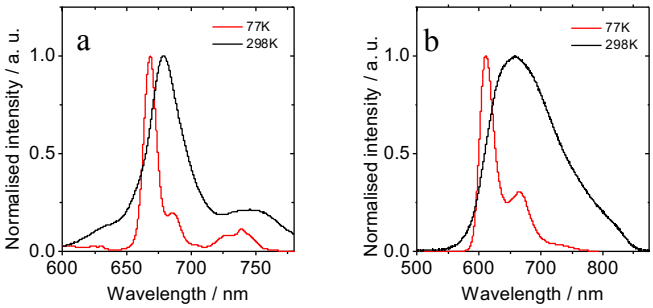

Figure 6.9 *Normalised emission spectra of (a)* ***RuPP*** *and (b)* ***RuTT*** *in a mixed solvent system of CH_3CH_2OH:CH_3OH (4:1, v/v) under nitrogen at 77 K (red line), and room temperature (black line). λ_{ex} = 403 nm, C = 1 × 10^{-5} mol/L.*

This result suggests the emissive character is mainly ^{3}IL* in character, with some contribution from ^{3}MLCT*. For **RuTT**, characteristic charge transfer emission behaviour is observed, exhibiting broad structureless emissions at room temperature, with a

dramatic sharpening of the emission band, and a much large anti-Stokes shift (ΔE_s = 1172 cm^{-1}) seen at 77K.

6.4.2 Transient State Properties of RuPP and RuTT

Nanosecond laser flash photolysis experiments were undertaken to confirm the ^{3}IL emission assignment in **RuPP** (Figure 6.10a). The bleaching peak was observed sharply at λ 400 nm. The lifetime was detected as 90.8 μs which closely matches the room temperature emissive lifetime. For **RuTT**, a bleaching peak at 410 nm was observed (Figure 6.10b). This observation, coupled with the low temperature measurements allows some confidence in the assignment of the excited state of **RuTT** as ILCT in nature.

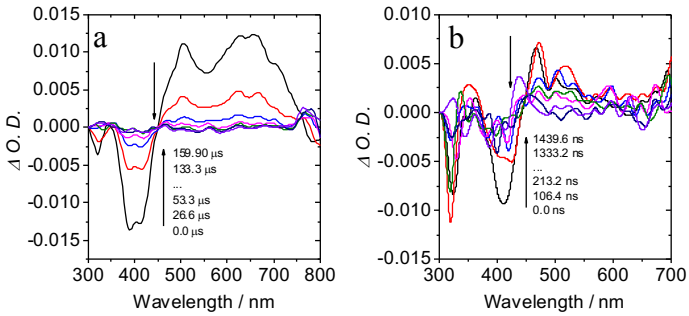

Figure 6.10 *Nanosecond time-scaled transient difference absorption spectra of (a)* ***RuPP*** *and (b)* ***RuTT*** *plus an excitation at λ_{ex} = 355 nm. C = 1 × 10^{-5} mol/L, in CH_3CN, 298 K.*

6.5 Triplet Photosensitisation Studies towards TTA Upconversion

Upon excitation at λ_{ex} 473 nm, **RuPP** showed a weak phosphorescence at λ 679 nm under a nitrogen atmosphere (Figure 6.11a). Upon the addition of triplet acceptor, **DPA**, a new emissive band at λ 430 nm was observed. This observed fluorescence from the **DPA** triplet acceptor confirms a successful TTA upconversion process for this complex. The TTA upconversion quantum yield was found to be high (Φ_{UC} = 27.2 %). For **RuTT**, the same excitation wavelength and triplet acceptor were chosen. After the addition of **DPA**, upon excitation at λ 473 nm, the delayed fluorescence of **DPA** was observed. The determined TTA upconversion quantum yield was determined to be 17.0 %. However, in the TTA system of **RuTT** with **DPA**, the ratio of triplet photosensitiser to acceptor is low. This means that the triplet energy transfer process is not efficient.

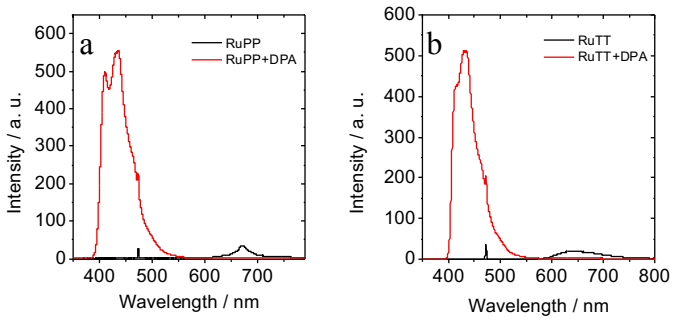

Figure 6.11 *Upconversion with* ***RuPP*** *and* ***RuTT*** *as triplet photosensitisers in CH_3CN, 298 K. (a) The emission spectra of* ***RuPP*** *with and without* ***DPA*** *added (C[**RuPP**] = 1.0 × 10^{-5} mol/L, C[**DPA**] = 8 × 10^{-3} mol/L). (b) The emission spectra of* ***RuPP*** *with and without* ***DPA*** *added (C[**RuPP**] = 1.0 × 10^{-5} mol/L, C[**DPA**] = 2.33 × 10^{-3} mol/L). Excited with laser, λ_{ex} = 473 nm, 70.8 mW/cm^{-2}.*

6.6 Novel Application of TTA Upconversion (TTA-UC) in Photoinitiated Polymerisation with RuPP

6.6.1 Background

Photoinitiated polymerisation is one of the most widely used polymerisation techniques. Here, monomer units undergo polymerisation initiated by reactive species, such as radicals, cations or anions that can be generated by the photon-irradiation of a selected photoinitiator (PI). Highly cross-linked polymers can be readily prepared by photoinitiated polymerisation of multifunctional monomers at room temperature. This technology is called UV curing.[126] In UV curing, the PIs are efficiently activated through excitation wavelengths in the range of the UV or near UV region, and require high energy irradiation sources. The primary advantage of the light-cure processing of adhesives is the speed of the cure, which is usually less than 5 seconds. However, there are several drawbacks of this process. i) in order to allow the adhesive to be exposed to the irradiation source, at least one side of the substrate must be transparent to the irradiation source, ii) the absorption of most commercial PIs is in the UV light range and many of the materials can also be effected by the UV light.

To address these problems, a TTA-UC system is proposed to be applied to photoinitiated polymerisation. As illustrated in Scheme 1. 3 in Chapter 1, TTA-UC consists of two parts, the triplet photosensitiser (PS), and the triplet acceptor. When a mixed solution is

irradiated by a relatively long wavelength external terrestrial light source, a shorter emission is generated *via* the TTA-UC mechanism. Therefore, through the combination of the TTA-UC process, and traditional photoinitiated polymerisation, the TTA-UC system will act as an embedded secondary light source in the adhesive matrix, and improve the light-curing of the adhesive. This is particularly useful for the adhesion of UV-opaque plastic and glass substrates. This process is presented clearly in Scheme 6.3.

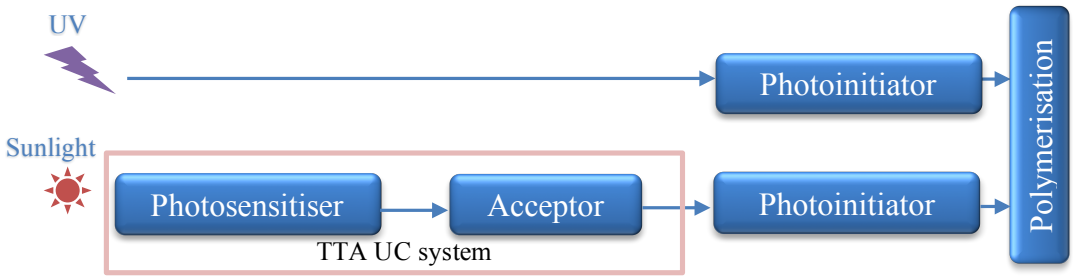

Scheme 6.4 *Processes of polymerisation with and without TTA Upconversion system. UV-ultraviolet light.*

Rare-earth metal-based upconversion has been applied to deep photoinitiated polymerisation *via* nanoparticles in 2016.[127] However, as discussed in the Chapter 1. TTA-UC shows better properties than the rare-earth metal-based upconversion. The process typically generates higher upconversion quantum yields, requiring a non-coherent low excitation power density light source (including a solar light source), and with a tuned absorption.

This work was carried out through a Technology Innovation Development Award programme (15TIDA2952), through an industrial collaboration with the Draper Research Group based in Trinity College Dublin.

6.6.2 Results and Discussion

In Figure 6.12, some traditional commercial available PIs are presented. All of the compounds show absorption in the UV and near UV region. Taking the emissive band of the upconverted fluorescence of **DPA** into account, **Irgacure 814** and **TPO-L** are difficult to be excited due to their weak absorption in the region over λ 375 nm. Therefore, **TPO** was chosen as the PI for the initial investigation. **RuPP** and **DPA** were selected as the desired triplet photosensitiser and triplet acceptor for the attempt of photoinitiated polymerisation due to their high upconversion yield of 27.2 %. Ethenylbenzene (Styrene)

was chosen as the desired monomer unit due to its facile polymerisation (and ease of polymerisation detection).

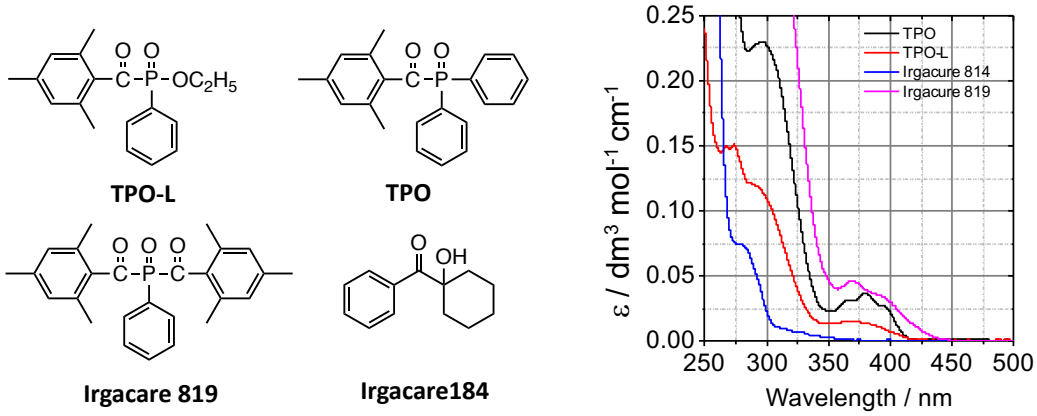

Figure 6.12 *Structures of the traditional photoinitiators:* ***TPO-L****;* ***TPO****;* ***Irgacare 819*** *and* ***184****; The absorption spectra of photoinitiators. C = 1 × 10^{-4} mol/L in CH_3Cl, 298 K.*

The process of the experiment is illustrated by Scheme 6.5. Upon the excitation at λ 473 nm, **RuPP** is excited and the triplet excited state of **RuPP** (^{3}**RuPP***) is generated. The triplet energy transfers from ^{3}**RuPP*** to the triplet acceptor, **DPA**, *via* a Triplet-Triplet Energy Transfer (TTET) process. Then collision between two excited triplet acceptors (^{3}**DPA***) occur, resulting in the delayed fluorescence of **DPA** *via* a Triplet-Triplet Annihilation (TTA) process. This upconverted fluorescence works the irradiation wavelength(s) added for photoinitiated polymerisation. After the **TPO** is excited, yielding the reactive species, the styrene is polymerised.

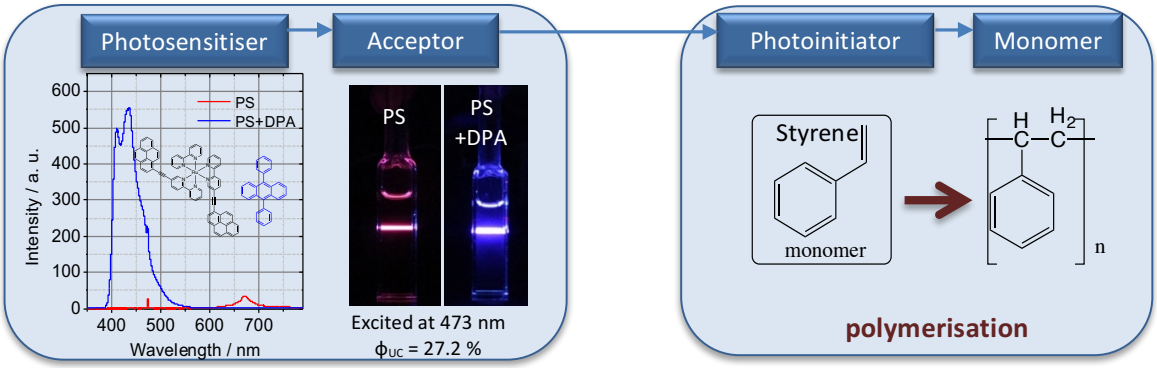

Scheme 6.5 *Process of applying TTA-UC to photoinitiated polymerisation. PS-photosensitiser,* ***RuPP****; λ_{ex} = 473 nm.*

To explore whether the TTA-UC system is directly responsible for the photoinitiated polymerisation, control experiments were carried out. (Table 6.1) Sample 1 fulfils the criteria for a full system, and has all the necessary components including the photosensitiser, the acceptor, the photoinitiator, and the monomer. Sample 2 does not contain the photosensitiser. Both samples were also measured with fixed parameters (concentration of PS and acceptor; light power; solvent/monomer ratio). The experimental conditions of each reaction are listed in Table 6.2.

Table 6.1 *Components of control experiments.*

	Component	Sample 1	Sample 2
TTA Upconversion	Photosensitiser	✓	--
	Acceptor	✓	✓
Polymerisation	Photoinitiator	✓	✓
	Monomer	✓	✓

Table 6.2 *Experiments with fixed conditions.*

Component	Name	Group 1		Group 2		Group 3		Group 4	
		Sample 1	Sample 2	Sample 1	Sample 2	Sample 1	Sample 2	Sample 1	Sample 2
Photosensitiser	RuPP (mol / L)	1×10^{-5}	--	2×10^{-5}	--	1×10^{-5}	--	1×10^{-5}	--
Acceptor	DPA (mol / L)	8×10^{-5}		16×10^{-5}		8×10^{-5}		8×10^{-5}	
Light Source	Power (mW)	5		5		10		5	
Monomer	Styrene (mL)	1		1		1		2	
Solvent	CH_2Cl_2 (mL)	2		2		2		1	
Photoinitiator	TPO (w%)	1%							

The two samples in Group 1, the conditions are similar with the photosensitisation experiments in the earlier sections. The concentration of **RuPP** is 1×10^{-5} mol/L, with the concentration of **DPA** as 8×10^{-5} mol/L. The power density of the light source is 70.8 mW/cm^2. Methylene chloride, styrene, **RuPP**, and **DPA** were added sequentially to Sample 1. The only difference between Sample 1 and Sample 2 is the addition of **RuPP**. The two sample mixtures were bubbled with nitrogen for 15 min. On maintaining a

nitrogen atmosphere, the solution of **TPO** was added, and the both samples were irradiated at λ 473 nm for 40 minutes (Figure 6.13).

Figure 6.13 *Group 1; Sample 1 was irradiated by an external light source at λ 473 nm under a nitrogen atmosphere.*

Further to irradiation, the mixture was added to 15 mL of CH_3CH_2OH at room temperature in air. This step can help polystyrene precipitate from the solvent mixture, allowing determination of polymerisation. In Figure 6.14, Sample 1 is yellow-like due to the colour of the **RuPP** photosensitiser. On comparing of Sample 1 and Sample 2, a white cloudy product has been generated in Sample 1 only. Further to leaving Sample 1 overnight, a white solid precipitate was observed. This confirms that polymerisation has occurred in the presence of the TTA-UC system. At the same time, since the PI cannot be excited at λ 473 without the TTA-UC system, no white solid was observed in Sample 2. In conclusion, these results indicate that it is possible to apply TTA-UC in photoinitiated polymerisation, to red shift the appropriate irradiation wavelength.

Figure 6.14 *Photographs of Group 1 samples mixed with CH_3CH_2OH. (Left set: mixture after irradiation; Right set: mixture after irradiation and left overnight.)*

The fixed parameter (Table 6.2) experiments were also carried out. Reaction conditions of Group 2, 3 and 4 are presented in Table 6.2. These all showed a positive result with Sample 1, and a negative result with Sample 2. To further corroborate the results, a Gel Permeation Chromatography (GPC) technique needs to be carried out to detect the molar

weight of product. This will reveal the extent to where polymerisation has occurred, and if so, the length of the polymer chain generated. This work is continuing.

6.7 Conclusion

The di-chromophore polyimine Ru(II) complexes, **RuPP** and **RuTT**, were synthesised successfully. Compared to conventional photosensitisers, two chromophores within the complex structure can enhance absorption in the visible region. For **RuTT**, the triplet excited state is localised on both the TPA-ligand and the metal centre, and thus, the triplet excited lifetime is very short and determined as 1.3 μs. For **RuPP**, the introduction of a pyrene-moiety generates a pyrene-localised ^{3}IL triplet excited state, and the triplet excited state lifetime is determined as 90.8 μs. Its triplet excited state is mainly attributed to an ^{3}IL excited state, with a small contribution from a ^{3}MLCT excited state. Both generated complexes were used as triplet photosensitisers towards TTA upconversion. The TTA upconversion quantum yields of **RuPP** and **RuTT** were determined as 27.2 % and 17.0 % respectively. A novel application of TTA-UC was explored with **RuPP** as the triplet photosensitiser, and **DPA** as the triplet acceptor towards photoinitiated polymerisation. This work demonstrates the use of a transition metal-based photosensitiser, which absorbs efficiently in the visible region, and which shows a high TTA-UC quantum yield. This emission is of a higher energy light (λ 382-550 nm), and acts as a secondary photon source to initiate the photo-polymerisation process. These studies will inform practical and industrial applications of triplet photosensitisers for future TTA-UC technologies and operations.

6.8 Future work

Based on the exploration in this project, triplet photosensitisers with broaden absorption in the visible and near IR region, long triplet excited state lifetimes, high TTA upconversion quantum yield and efficient singlet oxygen sensitisation have been successfully synthesised. However, due to the requirements of TTA upconversion systems on the energy donor (photosensitiser) and energy acceptor, the design of novel triplet energy acceptor is also important for improving the TTA upconversion quantum yield. Moreover, it would be meaningful to investigate the energy-pooling of excited

triplet donor and acceptor's process (Equation 1.1e, Chapter 1). This study would further help to predict triplet excited states and design novel TTA upconversion systems in the future.

Another concern about TTA upconversion nowadays is that this system is sensitive to oxygen and works in an organic solvent based environment. Even though there are several works on TTA upconversion in air and in solid state, it still has a lot of limitations to overcome. For example, most of the air-blocked TTA upconversion systems are based on polymer or nanoparticles[17, 128-130], as even though it has an advantage over application in devices, the solid state limits the collisions between molecules.[131] Consequently it decreases the triplet-triplet energy transfer and triplet-triplet annihilation rate consequently. Thus, the exploration of solid state upconversion with high TTA upconversion quantum yield is a potential orientation of this area.

Water solubility is also very important for biological applications, such as photodynamic therapy and bioimaging. However, most of the reported TTA-based upconversion systems have been fabricated in organic solution which limits their application in bioimaging.[132] Therefore, the next generation of triplet photosensitisers for biological applications should be water soluble, have low toxicity and even high targeting ability on the tumour.

Moreover, commercialisation mainly depends on the cost of the material. Most of the currently available triplet photosensitisers for TTA upconversion are generated from precious metal centres, like Ir(III), Ru(II), Pd(II), Pt(II) and Au(I). Thus, novel triplet photosensitiser with cheaper metal centres (such as Cu(II)) or non-metal materials will be important for applications in the future.

7 Experimental

7.1 Experimental Details

General information: Unless otherwise indicated, all reactions which are sensitive to air were carried out with a purged inert atmosphere of either nitrogen or argon using standard Schlenk, a two- or three- necked round bottom flask and vacuum line techniques. Solvents (Methylene dichloride, Diethyl ether, Tetrahydrofuran, N,N-Diisopropylethylamine) were dried using a solvent purification system (Innovation Technology Inc.) and distilled under a nitrogen atmosphere (Triethylamine) if mentioned as dry solvent in the procedure. Triethylamine was dried over sodium and *m*-xylene was dried over sodium. Starting materials 2-bromopyridine, n-BuLi, trimethyltin chloride, 2,4-dimethylpyrrole, benzoyl chloride, 2,5-dibromopyridine, sodium hydroxide, magnesium sulfate, potassium hexafluorophosphate, bromine, N-iodosuccinimide, ethyltrimethylsilane, pyrene, CuI, PPh_3, $Pd(PPh_3)_4$ and standard solvents were used without further purification. $RuCl_3 \cdot xH_2O$ were purchased from Sigma Aldrich and $IrCl_3 \cdot H_2O$ were purchased from Alfa Aesar. Flash chromatography was performed using silica gel (Sigma Aldrich) as the stationary phase. The known compounds were synthesized according to the literature procedures.

Mass spectroscopy: Electrospray mass spectra were recorded on a Micromass-LCT spectrometer. Electron impact mass spectra were measured on a Waters corp. GCT Premier electron impact mass spectrometer. MALDI-TOF mass spectra were recorded on a Waters MALDI-Q-TOF Premier spectrometer using an α-cyano-4-hydroxy cinnamic acid matrix. Accurate mass spectra were referenced against Leucine enkephalin (555.6 g mol^{-1}) or [Glue1]-Fibrinopeptide B (1570.6 g mol^{-1}) and reported to within 5 ppm. The solvents for dissolution are acetone, acetonitrile and methanol.

NMR Spectroscopy: Nuclear magnetic resonance spectra (NMR) were recorded in deuterated chloroform, methylene chloride, acetone, acetonitrile, dimethyl sulfoxide on a (i) Bruker Avance DPX-400 MHz spectrometer (operating at 400.13 MHz for ^{1}H, 100.6 MHz for ^{13}C), (ii) Bruker AV-400 MHz spectrometer (operating at 400.13 MHz for ^{1}H, 100.6 MHz for ^{13}C, 128.4 MHz for ^{11}B, 376.6 MHz for ^{19}F) or (iii) Bruker AV-600 MHz spectrometer (operating at 600.13 MHz for ^{1}H, 150.6 MHz for ^{13}C). ^{13}C spectra were proton decoupled. Chemical shifts (δ) are reported in ppm and coupling constants (*J*) in Hertz.

IR spectroscopy: IR spectra were recorded on a PerkinElmer Sectrum 100 FTIR spectrometer fitted with a Universal ATR accessory in a solid form.

Cyclic voltammetry (CV): Data were collected from CHI610D (Shanghai Huachen) in a nitrogen atmosphere.

Photophysical Measurements: Most photophysical measurements were carried out with solutions contained in 1×1 cm^2 quartz cuvettes in HPLC grade solvents, except the low temperature emission measurements which were carried out in quartz tubes. All the measurements were carried out at least three times to maximise accuracy. Average values were calculated and presented in the thesis. UV-visible absorption spectra were recorded on a Shimadzu UV-2450 spectrophotometer. Emission spectra were obtained on a RF5301 spectrofluorometer (Shimadzu). Excitation spectra were got from a FS5 spectrofluorometer (Edinburgh Photonics). The phosphorescence lifetime was measured on OB920 and FLS 920 (Edinburgh Photonics) which was equipped with 405 nm, 445 nm, 473 nm picosecond lasers (series: EPL) and a microsecond Xe lamp (μF920H). The nanosecond time-resolved difference transient absorption spectra were detected by laser flash photolysis spectrometer (LP920, Edinburgh Instruments) and recorded on a Tektronix TDS 3012B oscilloscope. The laser source used is a nanosecond pulsed Q-Switched Nd:YAG laser coupled to an OPO (Optical Parametric Oscillator) to create tunability over a wide range of wavelengths. A gated intensified CCD is used to capture the whole spectrum in the presence and absence of the pump laser pulse. The lifetime values (by monitoring the decay trace of the transients) were obtained with the LP920 software. The emission spectra at low temperature (77 K) were measured with a quartz tube in a Dewar filled with liquid nitrogen or FLS920 spectrofluorometer (Edinburgh Instruments) in a glassed solvent system. Time-resolved emission spectra were recorded on OB 920 (Edinburgh Instruments). Luminescence quantum yields of the complexes were measured with different standard as reference (depending on their absorption and emission properties). The femtosecond time-resolved difference transient absorption spectra were measured by optical femtosecond pump-probe spectroscopy. The output of a mode-locked Ti-sapphire amplified laser system (Spitfire Ace, Spectra-Physics) with wavelength 800 nm, pulse-width 35 fs, repetition rate 1 kHz, average power 4 W was split into two beams (10:1). The strong radiation was converted into UV-VIS-IR in the range of 240-2400 nm by use of Optical Parametric Amplifier (TOPAS, Light Conversion) and used as a pump beam. The weaker beam after passing a variable delay

line (up to 6 ns) was focused in a 3 mm thickness rotated CaF_2 plate to produce a white light continuum (WLC), which was used as a probe beam. Home-built pump-probe setup was used for obtaining transient absorption spectra and kinetics. The entire setup was controlled by a PC with the help of LabView software (National Instruments). All femtosecond measurements were performed at room temperature under aerated conditions.

TTA Upconversion: Diode-pumped solid-state lasers (589 nm and 473 nm, continuous wave, CW) was used for the upconversion measurements. For the upconversion experiments, the mixed solution of the photosensitisers and triplet acceptor (DPA or perylene) was degassed in the solution for at least 15 min with N_2, and the gas flow was kept constant during the measurement. The solution was excited with the laser. Then the upconverted fluorescence was recorded with a spectrofluorometer. The upconversion quantum yields were determined with the prompt fluorescence of reference compound as the standard using the following equation:

$$\Phi_{UC} = 2 \times \Phi_{std} \times \left(\frac{1 - 10^{-A_{std}}}{1 - 10^{-A_{sam}}} \right) \times \frac{I_{sam}}{I_{std}} \times (\frac{\eta_{sam}}{\eta_{std}})^2$$

The subscripts "sam" and "std" refer to the photosensitiser and the reference compound (standard), respectively. Φ, A, I, and η represent the quantum yield, absorbance, integrated photoluminescence intensity, and the refractive index of the solvents used for the standard and the samples, respectively. The equation is multiplied by a factor of 2 in order to make the maximum quantum yield to be unity.

Crystal Characterisations: Crystal and structural experimental data are summarized in the Annex. The single-crystal analysis was performed by Dr. Brendan Twamley in Trinity College with a Bruker SMART APEX CCD diffractometer using graphite monochromated Mo-Kα (λ = 0.71073 Å) radiation at the temperatures given in tables. Data reduction was performed using SAINT. Intensities were corrected for Lorentz and polarization effects and for absorption by SADABS. Space groups were determined from systematic absences and checked for higher symmetry. The structures were solved by direct methods using SHELX-97. All non-hydrogen atoms were refined with anisotropic displacement parameters. Hydrogen atoms were included in calculated positions with isotropic displacement parameters 1.3 times the isotropic equivalent of their carrier

carbons. Absolute structure determinations were based on the Flack parameter. The functions minimised were $\Sigma w(F_o^2 - F_c^2)$, with $w = [\sigma^2(F_o^2) + (aP)2 + Bp]^{-1}$, where $P = [\max(F_o^2) + 2\,F_c^2]/3$. In all cases, final syntheses showed no significant residual electron density in chemically sensible positions.

7.2 Synthesis Details

Synthesis of **RuBRu**:

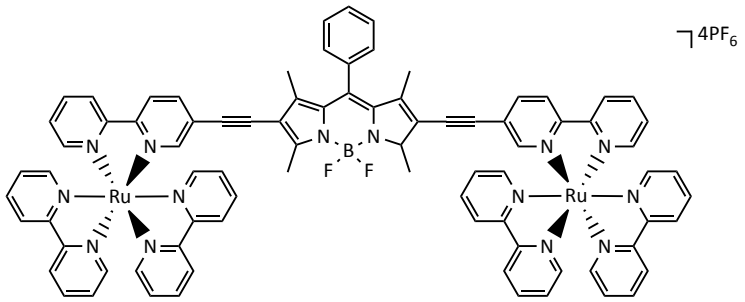

RuBRu

Under an argon atmosphere, 2,6-diethynyl-1,3,5,7-tetramethyl-8-phenyl-4,4-difluoroboradiazaindacene (15 mg, 0.040mmol), [Ruthenium(II)(2,2'-bipyridine)$_2$(5-bromo-2,2'-bipyridine)]$(PF_6)_2$ (76 mg, 0.081 mmol), $[Pd(PPh_3)_2Cl_2]$ (1.4 mg, 0.002 mmol), PPh_3 (1.0 mg, 0.004 mmol) and CuI (0.4 mg, 0.002 mmol) were added in 5 mL of a dry solvent mixture ($(i\text{-}Pr)_2NH$: CH_3CN: Benzene =1: 2: 2). After stirring, the mixture was heated at 60 °C for 2.5 h. The solvent was removed under reduced pressure, and then the solid was dissolved in the minimum of acetonitrile. A saturated aqueous solution of potassium hexafluorophosphate was added dropwise to the mixture to give crude product as a black-red solid. After the mixture was filtered, the crude product was purified by column chromatography on silica gel (CH_3CN/H_2O/sat. KNO_3, 100:9: 1, v/v/v) and treated with a saturated aqueous solution of potassium hexafluorophosphate again. Red precipitate was collected *via* filtration; the solid was washed with water and diethyl ether. Yield: 23.3 mg, 27.9 %.

^{1}H NMR (400 MHz, CD_3CN, 298 K, δ in ppm) δ 8.53-8.46 (m, 12H), 8.10-8.00 (m, 12H), 7.83 (d, 2H, *J*=5.5 Hz), 7.75-7.71 (m, 8H), 7.66-7.62 (m, 5H), 7.43-7.38 (m, 12H), 2.56 (s, 6H), 1.44 (s, 6H).

^{13}C NMR (150 MHz, CD_3CN, 298 K, δ in ppm) δ 158.80, 156.78, 156.72, 156.68, 156.22, 155.32, 152.42, 151.68, 151.64, 151.51, 151.39, 145.67, 144.24, 138.76, 138.00,

137.97, 137.87, 137.84, 133.27, 131.32, 129.76, 129.53, 127.74, 127.66, 127.59, 124.57, 124.41, 124.26, 123.95, 123.84, 114.44, 91.51, 89.39, 13.06, 12.90.

^{11}B NMR (128 MHz, $CDCl_3$, 298 K, δ in ppm) δ 0.45 (t, B, J_{BF} = 31.5 Hz).

^{19}F NMR (376 MHz, $CDCl_3$, 298 K, δ in ppm) δ -145.59 (q, 2F, J_{FB} = 31.4 Hz).

IR (ν_{max} /cm^{-1}) 3607(w), 3096(w), 2930(w), 2205, 1662(s), 1539(s), 1366(s), 1322(s), 1267(s), 1188(s).

MALDI-TOF-MS: calc. for ($[C_{83}H_{63}N_{14}F_{20}P_3Ru_2]^+$) *m/z* = 1943.2434, found *m/z* = 1943.2465.

Synthesis of **IrBIr**:

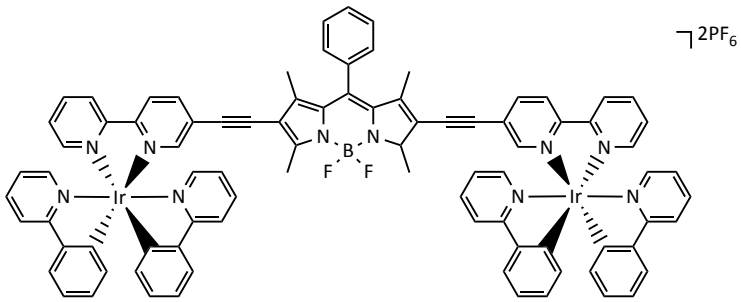

IrBIr

Under an argon atmosphere, 2,6-diethynyl-1,3,5,7-tetramethyl-8-phenyl-4,4-difluoroboradiazaindacene (15 mg, 0.040mmol), [Iridium(III)(2-phenylpyridine)$_2$(5-bromo-2,2'-bipyridine)](PF_6) (70 mg, 0.081 mmol), [Pd(PPh_3)$_2$$Cl_2$] (1.4 mg, 0.014 mmol), PPh_3 (1.0 mg, 0.031 mmol) and CuI (0.4 mg, 0.026 mmol) were added in 6 mL of a dry solvent mixture ((i-Pr)$_2$NH: CH_3CN =1: 1). After stirring, the mixture was heated at 60 °C for overnight. The solvent was removed under reduced pressure, and then the solid was dissolved with a minimum of acetonitrile. A saturated aqueous solution of potassium hexafluorophosphate was added dropwise to the mixture to give crude product as a black-purple solid. After the mixture was filtered, the crude product was purified by column chromatography on silica gel (CH_3CN/H_2O/sat. KNO_3, 150:9: 1, v/v/v) and treated with a saturated aqueous solution of potassium hexafluorophosphate again. Dark-red precipitate was collected with filtration and the solid was washed with water and diethyl ether. Yield: 10.2 mg, 12.9 %.

^{1}H NMR (400 MHz, $CDCl_3$, 298 K, δ in ppm) δ 8.52-8.48 (m, 4H), 8.14-8.00 (m, 11H), 7.90-7.81 (m, 10H), 7.75-7.71 (m, 8H), 7.70-7.64 (m, 6H), 7.54-7.53 (m,2H), 7.38-7.39 (m, 2H), 7.07-6.93 (m, 12H), 6.30 (d, 4H, J = 7.4 Hz), 2.56 (s, 6H), 1.43 (s, 6H).

^{13}C NMR (100 MHz, $CDCl_3$, 298 K, δ in ppm) δ 166.82, 166.80, 158.43, 154.68, 153.83, 151.64, 150.31, 149.60, 149.30, 149.00, 148.87, 145.47, 143.64, 143.55, 139.42, 138.89, 138.19, 138.14, 132.97, 131.10, 131.03, 129.93, 129.36, 129.12, 128.05, 127.25, 125.43, 124.49, 124.45, 124.06, 123.17, 123.03, 122.21, 122.16, 119.53, 119.41, 91.33, 88.68, 77.84, 77.51, 77.19, 12.47, 12.30.

^{11}B NMR (128 MHz, $CDCl_3$, 298 K, δ in ppm) δ 0.45 (t, B, J_{BF} = 30.9 Hz).

^{19}F NMR (376 MHz, $CDCl_3$, 298 K, δ in ppm) δ -145.59 (q, 2F, J_{FB} = 31.5 Hz).

IR (ν_{max} /cm^{-1}) 3607(w), 3096(w), 2930(w), 2205, 1658(s), 1520(s), 1366(s), 1478(s), 1387(s), 1189(s).

MALDI-TOF-MS: calc. for ($[C_{87}H_{63}N_{10}F_8PIr_2]^+$) *m/z* = 1827.4199, found *m/z* = 1827.4265.

Synthesis of **RuC**:

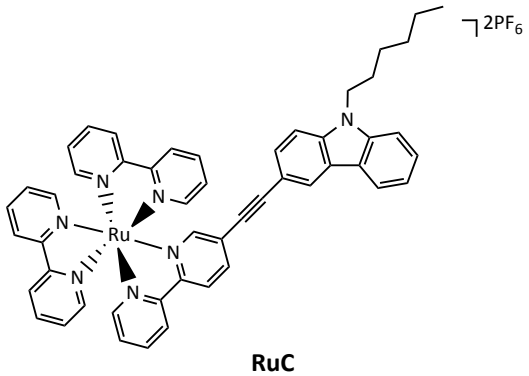

RuC

Under an argon atmosphere, [Ruthenium(II)(2,2'-bipyridine)$_2$(5-bromo-2,2'-bipyridine)]$(PF_6)_2$ (0.340 g, 0.426 mmol), $Pd(PPh_3)_2Cl_2$ (15.0 mg; 0.021 mmol), PPh_3 (11.0 mg; 0.0426 mmol) and CuI (8.0 mg, 0.0426 mmol) were added to a three neck round bottom flask. The solution of 3-Ethynyl-9-hexyl-9H-carbazole (0.117g; 0.4262mmol) in 30mL mixture solvent ($(CH_3CH_2)_3N$:CH_3CN, 1:1, v/v) was transferred into the round bottom flask *via* a long needle. The mixture was refluxed at 90°C overnight under stirring. After cooling to room temperature, the solvent was removed under reduced pressure. The

crude product was purified by column chromatography on silica gel (CH_3CN/H_2O/sat. KNO_3, 200:9:1, v/v/v) and treated with a saturated aqueous solution of KPF_6. The red precipitate was collected *via* filtration and washed with diethyl ether. Yield: 117 mg, 24 %.

^{1}H NMR (400 MHz, CD_3CN, 298 K, δ in ppm) δ 8.58-8.52 (m, 6H), 8.28 (s, H), 8.19-8.07 (m, 7H), 7.79-7.88 (m, 2H), 7.80 (d, H, J = 5.6 Hz), 7.76-7.72 (m, 3H), 7.60-7.55 (m, 4H), 7.49-7.41 (m, 5H), 7.30 (t, H, J = 7.9 Hz), 4.36 (t, 2H, J = 7.2 Hz), 1.85-1.78 (m, 2H), 1.28-1.25 (m, 6H), 0.82 (t, 3H, 6.9 Hz).

^{13}C NMR (100 MHz, CD_3CN, 298 K, δ in ppm) δ 157.90, 157.87, 157.84, 157.78, 154.45, 156.11, 153.72, 152.87, 152.67, 152.62, 152.61, 152.46, 141.80, 141.71, 140.14, 138.82, 138.77, 138.67, 130.05, 128.56, 128.51, 128.50, 128.46, 128.41, 127.52, 125.47, 125.38, 125.30, 125.27, 125.15, 124.76, 123.58, 122.76, 121.36, 120.61, 111.73, 110.62, 110.54, 99.59, 83.52, 43.69, 32.07, 29.39, 27.27, 23.11, 14.10.

MALDI-TOF-MS: calc. for ($[C_{50}H_{43}N_5Ru]^{2+}$) *m/z* = 843.2623, found *m/z* = 843.2664.

Synthesis of **IrC**:

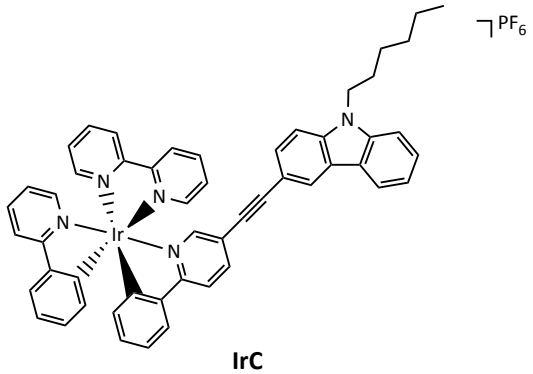

IrC

Under an argon atmosphere, [Iridium(I)(2-phenylpyridine)$_2$(5-bromo-2,2'-bipyridine)](PF_6) (0.340g; 0.3861mmol), $Pd(PPh_3)_2Cl_2$ (13.5 mg, 0.019 mmol), PPh_3 (10.0 mg, 0.039 mmol) and CuI (7.5 mg; 0.039 mmol) were added to a three neck round bottom flask. A solution of 3-Ethynyl-9-hexyl-9H-carbazole (0.135 g, 0.490 mmol) in 30mL mixture solvent ($(CH_3CH_2)_3N$:CH_3CN, 1:1, v/v) was transferred into the round bottom flask *via* a long needle. The mixture was refluxed at 90°C overnight under stirring. After cooling to room temperature, the solvent was removed under reduced pressure. The crude product was purified by column chromatography on silica gel (CH_3CN/H_2O/sat. KNO_3, 200:9:1, v/v/v) and treated with a saturated aqueous solution of KPF_6. The orange

precipitate was collected *via* filtration and washed with diethyl ether. Yield: 215.0 mg, 52 %.

^{1}H NMR (400 MHz, CD_3CN, 298 K, δ in ppm) δ 8.52-8.49 (m, 2H), 8.23-8.20 (m, 2H), 8.12-8.06 (m, 4H), 8.03 (d, H, J =1.8 Hz), 7.98 (d, H, J =5.3 Hz), 7.88-7.80 (m, 4H), 7.74 (d, H, J =5.6 Hz), 7.62 (d, H, J =5.7 Hz), 7.57-7.47 (m, 5H), 7.29-7.25 (m, H), 7.11-7.04 (m, 4H), 6.99-6.91 (m, 2H), 6.33 (d, H, J =7.4 Hz), 6.27 (d, H, J =7.4 Hz), 4.36 (t, 2H, J =7.2 Hz), 1.84-1.80 (m, 2H), 1.31-1.25 (m, 6H), 0.83 (t, 3H, J =7.2 Hz).

^{13}C NMR (100 MHz, CD_3CN, 298 K, δ in ppm) δ 168.28, 168.18, 156.20, 154.94, 152.69, 151.62, 150.98, 150.73, 150.41, 150.20, 145.04, 144.93, 141.84, 141.76, 141.69, 140.23, 139.54, 139.52, 132.51, 132.35, 131.44, 131.31, 130.11, 129.30, 127.55, 126.22, 125.93, 125.81, 125.79, 125.30, 125.23, 124.50, 124.48, 123.67, 123.64, 123.55, 122.81, 121.45, 120.93, 120.80, 120.64, 111.57, 110.64, 110.57, 99.82, 83.50, 43.73, 32.12, 29.45, 27.33, 23.16, 14.15. (peaks at 207.43 and 30.82 were assigned to acetone)

MALDI-TOF-MS: calc. for ($[C_{52}H_{43}N_5Ir]^+$) *m/z* = 930.3148, found *m/z* = 930.3156.

Synthesis of **RuCRu**:

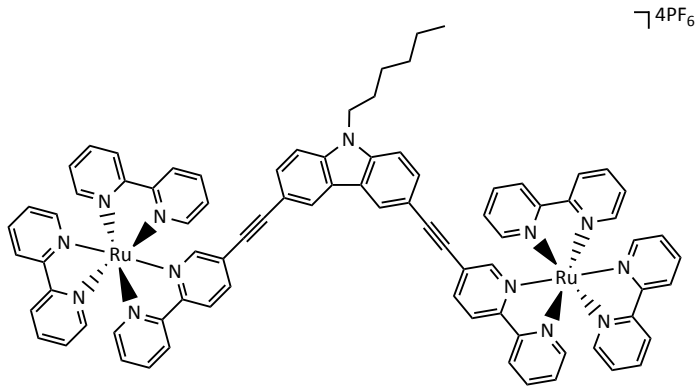

RuCRu

Under an argon atmosphere, 3,6-Diethynyl-9-hexyl-9H-carbazole (28.1 mg, 0.094 mmol), [Ruthenium(II)(2,2’ -dipyridine)$_2$(5-bromo-2,2’-bipyridine)]$(PF_6)_2$ (300.0 mg, 0.320 mmol), $[Pd(PPh_3)_2Cl_2]$ (3.5 mg, 0.005 mmol), PPh_3 (2.7 mg, 0.010 mmol) and CuI (1.9 mg, 0.010 mmol) were added in 20 mL of a dry solvent mixture (CH_3CN: $(CH_3CH_2)_3N$ =1: 1). After stirring, the mixture was heated at 60 °C for overnight. The solvent was removed under reduced pressure, and then the solid was dissolved with a minimum of acetonitrile. A saturated aqueous solution of potassium hexafluorophosphate was added dropwise to the mixture to give crude product as a dark-orange solid. After filtration, the

crude product was purified by column chromatography on silica gel (CH_3CN/H_2O/sat. KNO_3, 100: 9: 1, v/v/v) and treated with a saturated aqueous solution of potassium hexafluorophosphate again. A dark-red precipitate was collected with filtration, and the solid was washed with water and diethyl ether. Yield: 25.2 mg, 13.3 %.

^{1}H NMR (400 MHz, CD_3CN, 298 K, δ in ppm) δ 8.31-8.23 (m, 12H), 8.02 (s, 2H), 7.91 (dd, 2H, J_1 =8.5 Hz, J_2 =1.7 Hz), 7.87-7.78 (m, 10H), 7.61-7.60 (m, 4H), 7.52 (d, 2H, J =5.4 Hz), 7.48-7.47 (m, 4H), 7.45 (d, 2H, J =5.4 Hz), 7.36-7.31 (m, 4H), 7.20-7.13 (m, 10H), 4.12 (t, 2H, J =7.1 Hz), 1.58-1.52 (m, 2H), 1.02-1.00 (m, 6H), 0.57 (t, 3H, J = 6.9 Hz).

^{13}C NMR (100 MHz, CD_3CN, 298 K, δ in ppm) δ 157.92, 157.87, 157.83, 157.45, 156.36, 153.82, 152.90, 152.71, 152.68, 152.50, 142.23, 140.29, 138,83, 138.74, 130.98, 128.56, 128.52, 128.49, 125.48, 125.37, 125.33, 125.30, 125.20, 124.81, 123.06, 112.87, 111.26, 98.96, 83.87, 44.00, 32.06, 29.39, 27.23, 23.12, 14.12.

MALDI-TOF-MS: calc. for ($[C_{82}H_{65}N_{13}F_{18}P_3Ru_2]^+$) *m/z* = 1870.2498, found *m/z* = 1870.2555.

Synthesis of **IrCIr**:

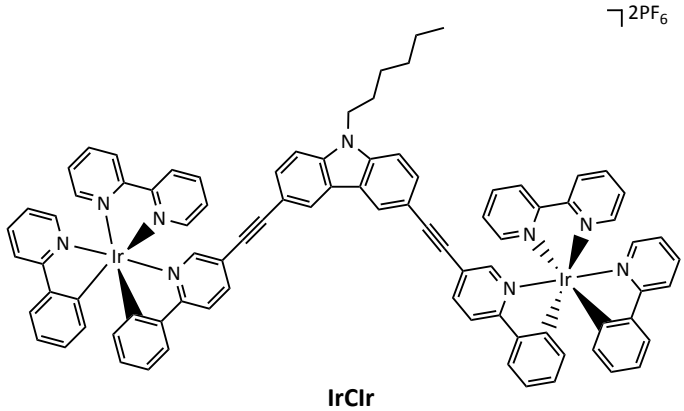

IrCIr

Under an argon atmosphere, 3,6-Diethynyl-9-hexyl-9H-carbazole (27.9 mg, 0.093 mmol), [Iridium(I)(2-phenylpyridine)$_2$(5-bromo-2,2'-bipyridine)](PF_6) (287.4 mg, 0.326 mmol), $Pd(PPh_3)_2Cl_2$ (3.5 mg, 0.005 mmol), PPh_3 (2.7 mg, 0.010 mmol) and CuI (1.9 mg, 0.010 mmol) were added in 20 mL of a dry solvent mixture (DMF: $(CH_3CH_2)_3N$ =1: 1). After stirring, the mixture was heated at 60 °C for 10 h. The solvent was removed under reduced pressure, and then the solid was dissolved with a minimum of acetonitrile. A saturated aqueous solution of potassium hexafluorophosphate was added dropwise to the

mixture to give crude product as an orange solid. After filtration, the crude product was purified by column chromatography on silica gel (CH_3CN/H_2O/sat. KNO_3, 200: 9: 1, v/v/v) and treated with a saturated aqueous solution of potassium hexafluorophosphate again. An orange precipitate was collected with filtration, the solid was washed with water and diethyl ether. Yield: 81.7 mg, 46.3 %.

^{1}H NMR (600 MHz, CD_3CN, 298 K, δ in ppm) δ 8.31-8.29 (m, 4H), 8.02-8.00 (m, 4H), 7.91 (td, 2H, J =7.9 Hz, J = 1.3 Hz), 7.87-7.84 (m, 4H), 7.52-7.51 (m, 2H), 7.40-7.34 (m, 6H), 7.29-7.27 (m, 2H), 6.89-6.87 (m, 2H), 6.84-6.81 (m, 6H), 6.76 (td, 2H, J = 7.4 Hz, J = 1.1 Hz), 6.70 (td, 2H, J = 7.4 Hz, J = 1.2 Hz), 6.13 (d, 2H, J = 7.5 Hz), 6.05 (d, 2H, J = 7.6 Hz), 4.15 (t, 2H, J = 7.0 Hz), 1.62-1.57 (m, 2H), 1.09-1.01 (m, 6H), 0.60 (t, 3H, J = 7.1 Hz).

^{13}C NMR (150 MHz, CD_3CN, 298 K, δ in ppm) δ 168.32, 168.27, 156.23, 155.21, 152.81, 151.71, 151.05, 150.70, 150.44, 150.28, 145.13, 144.98, 142.33, 141.83, 140.31, 139.60, 139.58, 132.60, 132.40, 131.50, 131.37, 131.05, 129.42, 125,97, 125.90, 125.87, 125.53, 125.38, 124.57, 124.50, 123.74, 123.62, 123.13, 120.98, 120.87, 112.75, 111.31, 100.95, 99.23, 83.88, 44.08, 32.11, 29.46, 27.29, 23.17, 14.16. **MALDI-TOF-MS**: calc. for ($[C_{86}H_{65}N_9Ir_2]^+$) m/z = 1609.4622, found m/z = 1609.4680.

Synthesis of **$Ir(ppyBr)_2Cl_2$**:

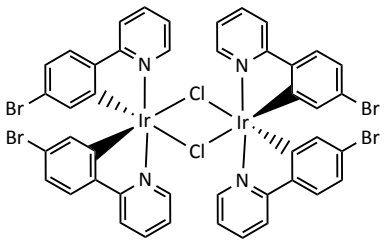

$Ir(ppyBr)_2Cl_2$

Iridium trichloride hydrate (0.300 g, 0.852 mmol) and 2-(4-Bromophenyl)pyridine (0.550 g, 1.704 mmol) were added to a round-bottom flask and dissolved in a mixture of 2-ethoxyethanol (30 mL) and water (10 mL). The mixture was refluxed overnight at 130 ℃. The solution was cooled to room temperature and the yellow participate was collected by filtration. After, the precipitate was washed with diethyl ether. Yield: 485.8 mg, 82.1 %.

^{1}H NMR (400 MHz, $CDCl_3$, 298 K, δ in ppm) δ 9.11 (d, 4H, J = 5.4 Hz), 7.87 (d, 4H, J = 7.8 Hz), 7.80-7.78 (m, 4H), 7.37 (d, 4H, J = 8.3 Hz), 6.97 (dd, 4H, J = 8.3 Hz, J = 1.9 Hz), 6.85-6.81 (m, 4H), 5.95 (d, 4H, J = 1.9 Hz).

Synthesis of $Ir(ppyBr)_2(bpy)[PF_6]$ (**IrBrBr**):

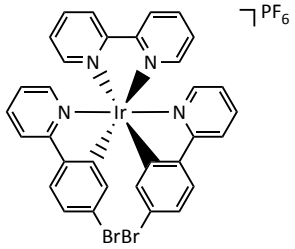

IrBrBr

In a round-bottom flask, a solvent mixture of 15 mL methanol and 15 mL methyl chloride was bubbled with nitrogen for 20 min. Under a nitrogen atmosphere, **$Ir(ppyBr)_2Cl_2$** (485.8 mg, 0.351 mmol) and 2,2'-bipyridine (109.5 mg, 0.702 mmol) were added to the flask. The mixture was heated at 60 ℃ overnight. After the solution cooled to room temperature, the solvent was removed under reduced pressure and a saturated aqueous solution of potassium hexafluorophosphate was added. The crude product appeared as an orange precipitate. The mixture was filtered and washed two times with water and diethyl ether. The crude product was purified by column chromatography on silica gel (CH_3OH/CH_2Cl_2, 1: 10, v/v) to give product as an orange solid. Yield: 650.0 mg, 96.7 %.

^{1}H NMR (400 MHz, CD_3CN, 298 K, δ in ppm) δ 8.55 (d, 2H, J = 8.2 Hz), 8.17 (td, 2H, J_1 = 7.9, J_2 = 1.6 Hz), 8.10 (d, 2H, J = 8.0 Hz), 8.06-8.00 (m, 2H), 7.95-7.88 (m, 2H), 7.77 (d, 2H, J = 8.4 Hz), 7.63-7.58 (m, 2H), 7.58-7.52 (m, 2H), 7.29 (dd, 2H, J_1 = 8.3 Hz, J_2 = 2.0 Hz), 7.14-7.07 (m, 2H), 6.34 (d, 2H, J = 2.0 Hz).

^{13}C NMR (100 MHz, CD_3CN, 298 K, δ in ppm) δ 166.17, 155.70, 152.30, 150.96, 149.41, 143.92, 143.33, 139.69, 139.05, 133.66, 128.58, 126.72, 125.76, 124.81, 124.14, 120.49.

Synthesis of **IrPBr** and **IrPP**:

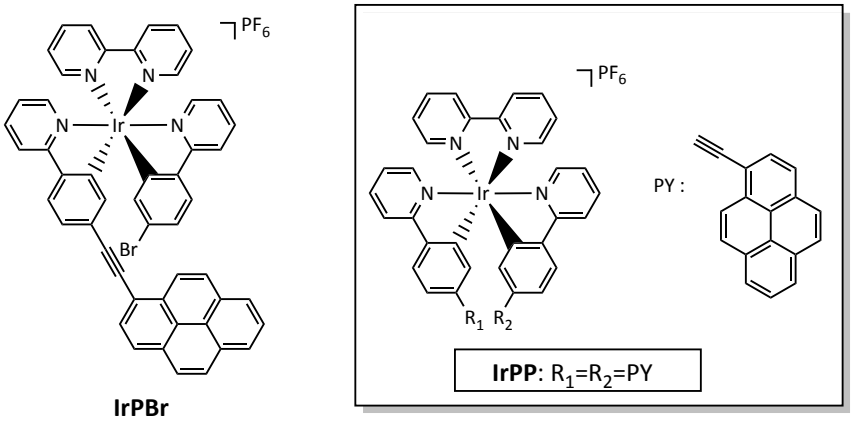

Under an argon atmosphere, 1-ethynylpyrene (350 mg, 0.365 mmol), **IrBrBr** (82.6 mg, 0.365 mmol), $[Pd(PPh_3)_2Cl_2]$ (12.8 mg, 0.018 mmol), PPh_3 (9.8 mg, 0.036 mmol) and CuI (6.9 mg, 0.036 mmol) were added in 5 mL of a dry mixture solvent ($(i\text{-}Pr)_2NH$: CH_3CN=1: 1, v/v). After stirring, the mixture was heated at 80 °C overnight. The solvent was removed under reduced pressure, and then the solid was dissolved with a minimum of acetonitrile. A saturated aqueous solution of potassium hexafluorophosphate was added dropwise to the mixture to give crude product as a dark yellow solid. Recrystallisation was carried out in acetonitrile. **IrPP** was easily participated and filtered. The crude product of **IrPP** was washed with diethyl ether and purified by column chromatography on silica gel (CH_3OH/CH_2Cl_2, 1:100, v/v). The crude product of **IrPBr** was purified by column chromatography on silica gel (CH_3CN/H_2O/sat. KNO_3, 100:9: 1, v/v/v). Both were treated with a saturated aqueous solution of potassium hexafluorophosphate again at the end. The solids were washed with water and diethyl ether. Yield: **IrPBr**, 129.4 mg, 32.1 %; **IrPP**, 140.0 mg, 30.6 %.

IrPBr:

^{1}H NMR (400 MHz, CD_2Cl_2, 298 K, δ in ppm) δ 8.59-8.57 (m, 2H), 8.52 (d, H, J = 8.4 Hz), 8.31-8.27 (m, 2H), 8.24-8.02 (m, 12H), 7.97-7.85 (m, 3H), 7.71 (d, H, J = 8.4 Hz), 7.61-7.49 (m, 5H), 7.32 (dd, H, J_1 = 8.3 Hz, J_2 = 1.9 Hz), 7.17 (t, H, J = 6.7 Hz), 7.11 (t, H, J = 6.6 Hz), 6.66 (d, H, J = 1.1 Hz), 6.48 (d, H, J = 1.8 Hz).

^{13}C NMR (100 MHz, CD_2Cl_2, 298 K, δ in ppm) δ 166.72, 166.69, 155.65, 155.60, 152.07, 150.83, 150.77, 148.73, 148.65, 143.99, 142.68, 139.84, 138.67, 138.63, 134.24, 134.04, 131.84, 131.44, 131.24, 130.97, 129.46, 128.51, 128.38, 128.37, 127.18, 126.56, 126.46, 126.07, 125.82, 125.75, 125.67, 125.40, 125.17, 124.84, 124.59, 124.37, 124.15, 123.95, 123.94, 120.59, 120.44, 117.33, 95.59, 90.21.

MALDI-TOF-MS: calc. for ($[C_{50}H_{31}N_4BrIr]^+$) *m/z* = 959.1362, found *m/z* = 959.1366.

IrPP:

^{1}H NMR (400 MHz, D_6-DMSO, 298 K, δ in ppm) δ 8.92 (d, 2H, *J* = 8.1 Hz), 8.48 (d, 2H, *J* = 8.2 Hz), 8.43 (d, 2H, *J* = 7.6 Hz), 8.39-8.24 (m, 12H), 8.23-8.10 (m, 10H), 8.06 (d, 2H, *J* = 5.1 Hz), 7.83 (d, 2H, *J* = 5.5 Hz), 7.76 (t, 2H, *J* = 6.5 Hz), 7.48 (d, 2H, *J* = 7.9 Hz), 7.37 (t, 2H, *J* = 6.5 Hz), 6.53 (s, 2H).

^{13}C NMR (100 MHz, D_6-DMSO, 298 K, δ in ppm) δ 166.34, 155.85, 150.71, 150.34, 149.98, 145.20, 140.39, 139.68, 134.10, 131.58, 131.53, 131.23, 130.92, 129.87, 129.42, 129.37, 128.97, 127.69, 127.30, 126.62, 126.56, 126.27, 125.78, 125.60, 125.43, 125.23, 124.80, 124.31, 124.11, 123.84, 121.50, 116.86, 96.52, 90.15.

MALDI-TOF-MS: calc. for ($[C_{68}H_{40}N_4Ir]^+$) *m/z* = 1105.2882, found *m/z* = 1105.2891.

Synthesis of **IrBP**:

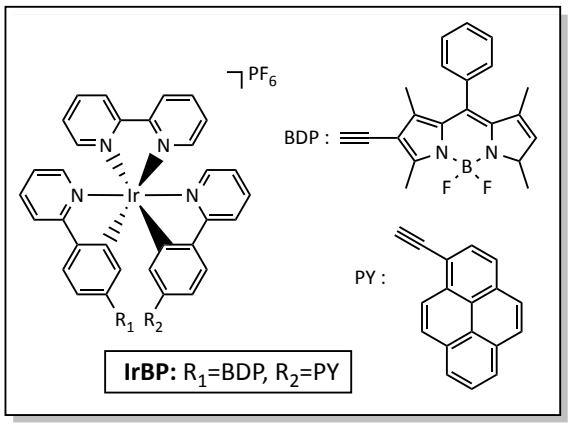

Under an argon atmosphere, 2-ethynyl-1,3,5,7-tetramethyl-8-phenyl-4,4-difluoroboradiazaindacene (33 mg, 0.095 mmol), **IrPBr** (70 mg, 0.063 mmol), $[Pd(PPh_3)_2Cl_2]$ (2 mg, 0.003 mmol), PPh_3 (2 mg, 0.006 mmol) and CuI (1 mg, 0.006 mmol) were added in 5 mL of a dry solvent mixture ($(CH_3CH_2)_3NH$: CH_3CN = 1: 1, v/v). After stirring, the mixture was heated at 80 °C overnight. The solvent was removed under reduced pressure, and then the solid was dissolved with a minimum of acetonitrile. A saturated aqueous solution of potassium hexafluorophosphate was added dropwise to the mixture to give crude product as a dark red solid. The mixture was filtered and washed twice with water and diethyl ether. The crude product was purified by column

chromatography on silica gel (CH_3OH/CH_2Cl_2, 1: 200, v/v; (CH_3CN/H_2O/sat. KNO_3, 300: 9: 1, v/v/v) to give product as a solid. Yield: 15.0 mg, 17.8 %.

^{1}H NMR (400 MHz, CD_3CN, 298 K, δ in ppm) δ 8.55-8.53 (m, 2H), 8.40 (d, H, J = 9.1 Hz), 8.33-8.28 (m, 2H), 8.22-8.04 (m, 12H), 7.96-7.92 (m, H), 7.78-7.87 (m, 3H), 7.70 (d, H, J = 5.9 Hz), 7.64 (d, H, J = 5.3 Hz), 7.54-7.52 (m, 5H), 7.41-7.38 (m, H), 7.32-7.29 (m, 2H), 7.14-7.11 (m, 2H), 7.07-7.03 (m, H), 6.59 (d, H, J = 1.5 Hz), 6.31 (d, H, J = 1.5 Hz), 6.18 (s, H), 2.52 (s, 3H), 2.49 (s, H), 1.39 (s, 3H), 1.36 (s, 3H).

^{13}C NMR (100 MHz, CD_3CN, 298 K, δ in ppm) δ 167.38, 167.29, 159.54, 156.68, 156.67, 156.23, 151.90, 151.78, 150.57, 150.45, 150.38, 146.70, 145.62, 145.06, 143.63, 142.93, 140.45, 139.76, 139.68, 135.05, 134.94, 134.51, 134.00, 133.48, 132.54, 132.35, 132.12, 131.84, 130.31, 130.20, 130.16, 129.57, 129.48, 129.46, 129.33, 128.80, 128.11, 127.62, 126.89, 126.81, 126.31, 125.85, 125.80, 125.74, 125.66, 125.55, 125.03, 124.97, 124.95, 124.78, 123.48, 121.55, 121.48, 115.21, 115.23, 97.42, 96.63, 90.51, 84.29, 14.92, 14.70, 13.57, 13.24.

^{11}B NMR (128 MHz, $CDCl_3$, 298 K, δ in ppm) δ 0.58 (t, B, J_{BF} = 30.6 Hz).

^{19}F NMR (376 MHz, CD_3CN, 298 K, δ in ppm) δ -145.69 (q, 2F, J_{FB} = 27.7 Hz).

MALDI-TOF-MS: calc. for ($[C_{71}H_{49}BN_6F_2Ir]^+$) *m/z* = 1227.3709, found *m/z* = 1227.3765.

Synthesis of **IrPT**:

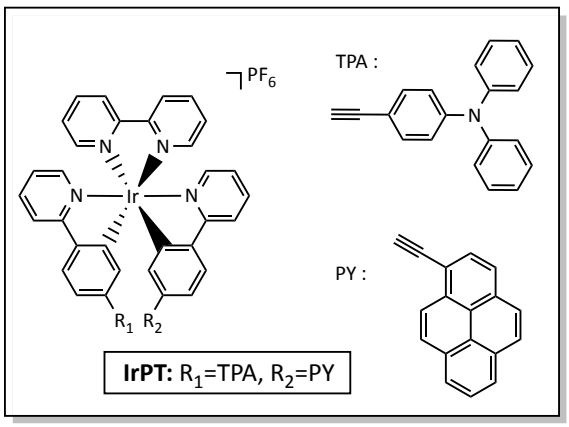

Under an argon atmosphere, **IrPBr** (50 mg, 0.045 mmol), 1-ethynyltriphenylamine (20 mg, 0.074 mmol), $[Pd(PPh_3)_2Cl_2]$ (2 mg, 0.003 mmol), PPh_3 (2 mg, 0.006 mmol) and CuI (1 mg, 0.006 mmol) were added in 20 mL of a dry solvent mixture ($(CH_3CH_2)_3NH$:

CH_3CN = 1: 1, v/v). After stirring, the mixture was heated at 80 °C overnight. The solvent was removed under reduced pressure, and then dissolved the solid with a minimum of acetonitrile. A saturated aqueous solution of potassium hexafluorophosphate was added dropwise to the mixture to give crude product as a dark yellow solid. The mixture was filtered and washed two times with water and diethyl ether. The crude product was purified by column chromatography on silica gel (CH_3OH/CH_2Cl_2, 1: 200, v/v; (CH_3CN/H_2O/sat. KNO_3, 200: 9: 1, v/v/v) to give product as a solid. Yield: 9.4 mg, 16.6 %.

^{1}H NMR (400 MHz, CD_3CN, 298 K, δ in ppm) δ 8.57-8.50 (m, 2H), 8.41 (d, H, J = 9.1 Hz), 8.36-8.27 (m, 2H), 8.23 (d, H, J = 9.2 Hz), 8.20-8.05 (m, 11H), 7.97 (t, H, J = 7.6 Hz), 7.93-7.82 (m, 3H), 7.69 (d, H, J = 5.3 Hz), 7.65 (d, H, J = 5.3 Hz), 7.54-7.51 (m, 2H), 7.43 (d, H, J = 7.9 Hz), 7.35-7.27 (m, 4H), 7.26-7.20 (m, 3H), 7.17-7.04 (m, 8H), 6.91-6.85 (m, 2H), 6.59 (d, H, J = 1.3 Hz), 6.42 (d, H, J = 1.4 Hz).

^{13}C NMR (100 MHz, CD_3CN, 298 K, δ in ppm) δ 167.43, 167.25, 156.68, 151.88, 151.86, 150.60, 150.43, 150.34, 149.22, 147.90, 145.63, 145.14, 140.46, 139.83, 139.80, 134.97, 134.53, 133.31, 132.58, 132.39, 132.14, 131.86, 130.52, 130.34, 129.60, 129.49, 129.36, 128.13, 127.65, 126.92, 126.83, 126.10, 125.91, 125.83, 125.78, 125.68, 125.54, 125.06, 124.98, 124.80, 122.38, 121.58, 121.55, 116.01, 96.61, 91.89, 90.50, 89.73.

MALDI-TOF-MS: calc. for ($[C_{70}H_{45}N_5Ir]^+$) m/z = 1148.3304, found m/z = 1148.3267.

Synthesis of **IrTT**:

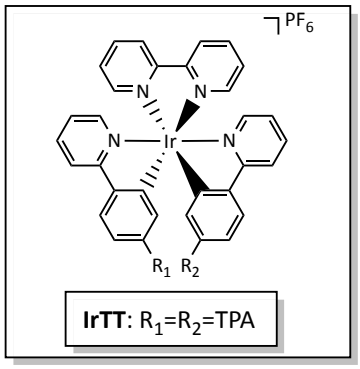

Under a nitrogen atmosphere, 1-ethynyltriphenylamine (85 mg, 0.317 mmol), **IrBrBr** (100 mg, 0.090 mmol), and $Pd(PPh_3)_4$ (13 mg, 0.011 mmol) were added in 20 mL of a dry solvent mixture (($CH_3CH_2)_3NH$: CH_3CN = 1: 1, v/v). After stirring, the mixture was

heated at 80 °C overnight. The solvent was removed under reduced pressure, and then the solid was dissolved with a minimum of acetonitrile. A saturated aqueous solution of potassium hexafluorophosphate was added dropwise to the mixture to give crude product as a dark yellow solid. The mixture was filtered and washed twice with water and diethyl ether. The crude product was purified by column chromatography on silica gel (CH_3OH/CH_2Cl_2, 1: 200, v/v; (CH_3CN/H_2O/sat. KNO_3, 200: 9: 1, v/v/v) to give product as a solid. Yield: 30.6 mg, 26.0 %.

^{1}H NMR (400 MHz, D_6-Acetone, 298 K, δ in ppm) δ 8.86 (d, 2H, J = 8.2 Hz), 8.34-8.27 (m, 4H), 8.20 (d, 2H, J = 5.5 Hz), 7.98 (t, 2H, J = 7.5 Hz), 7.93 (d, 2H, J = 8.1 Hz), 7.87 (d, 2H, J = 6.0 Hz), 7.74 (t, 2H, J = 6.0 Hz), 7.35-7.32 (m, 8H), 7.28-7.25 (m, 4H), 7.22-7.18 (m, 4H), 7.13-7.08 (m, 12H), 6.93-6.90 (m, 4H), 6.48 (d, 2H, J = 1.5 Hz).

^{13}C NMR (100 MHz, D_6-Acetone, 298 K, δ in ppm) δ 167.79, 157.00, 151.92, 150.61, 150.43, 149.27, 148.08, 145.17, 140.83, 139.94, 134.91, 133.42, 133.42, 130.60, 129.80, 126.17, 126.15, 125.94, 125.84, 125.08, 124.99, 122.64, 121.57, 116.54, 91.94, 90.12.

MALDI-TOF-MS: calc. for ($[C_{72}H_{50}N_6Ir]^+$) m/z = 1191.3726, found m/z = 1191.3729.

Synthesis of **IrBB**:

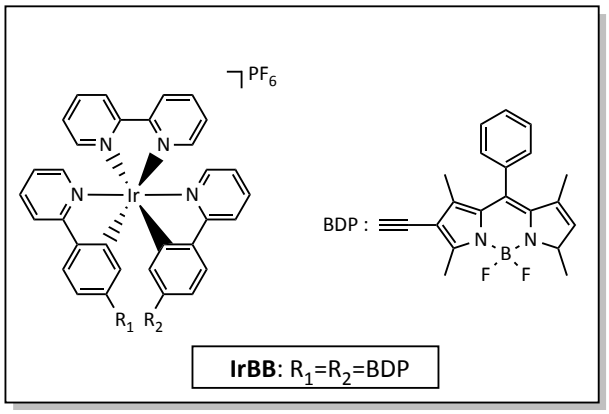

Under a nitrogen atmosphere, 2-ethynyl-1,3,5,7-tetramethyl-8-phenyl-4,4-difluoroboradiazaindacene (123 mg, 0.355 mmol), **IrBrBr** (112 mg, 0.101 mmol), and $Pd(PPh_3)_4$ (15 mg, 0.013 mmol) were added in 30 mL of a dry solvent mixture ($(CH_3CH_2)_3NH$: CH_3CN = 1: 1, v/v). After stirring, the mixture was heated at 80 °C for overnight. The solvent was removed under reduced pressure, and then the solid was dissolved with a minimum of acetonitrile. A saturated aqueous solution of potassium

hexafluorophosphate was added dropwise to the mixture to give crude product as a dark red solid. The mixture was filtered and washed twice with water and diethyl ether. The crude product was purified by column chromatography on silica gel (CH_3OH/CH_2Cl_2, 1: 100, v/v) to give product as a solid. Yield: 15.2 mg, 10.1 %.

^{1}H NMR (400 MHz, CD_2Cl_2, 298 K, δ in ppm) δ 8.02 (d, 2H, J = 5.3 Hz), 7.93 (d, 2H, J = 8.3 Hz), 7.77-7.68 (m, 4H), 7.53-7.45 (m, 14H), 7.29-7.27 (m, 4H), 7.17 (dd, 2H, J_1 = 8.1 Hz, J_2 = 1.3 Hz), 6.98 (t, 2H, J = 6.9 Hz), 6.33 (s, 2H), 6.08 (s, 2H), 2.53 (s, 3H), 2.51 (s, 3H), 1.40 (s, 3H), 1.39 (s, 3H).

^{13}C NMR (100 MHz, CD_2Cl_2, 298 K, δ in ppm) δ 167.64, 166.88, 158.19, 155.91, 155.89, 150.54, 149.15, 148.70, 145.41, 145.39, 143.45, 142.31, 142.21, 139.94, 138.17, 136.46, 134.45, 133.81, 132.66, 130.90, 130.10, 129.30, 129.18, 128.27, 128.24, 127.87, 125.95, 125.62, 124.66, 124.62, 123.52, 122.30, 120.33, 114.57, 96.43, 83.92, 14.54, 14.33, 13.13, 12.80.

MALDI-TOF-MS: calc. for ($[C_{74}H_{58}B_2F_4N_8Ir]^+$) *m/z* = 1349.4536, found *m/z* = 1349.4591.

Synthesis of **RuPP** and **RuPBr**:

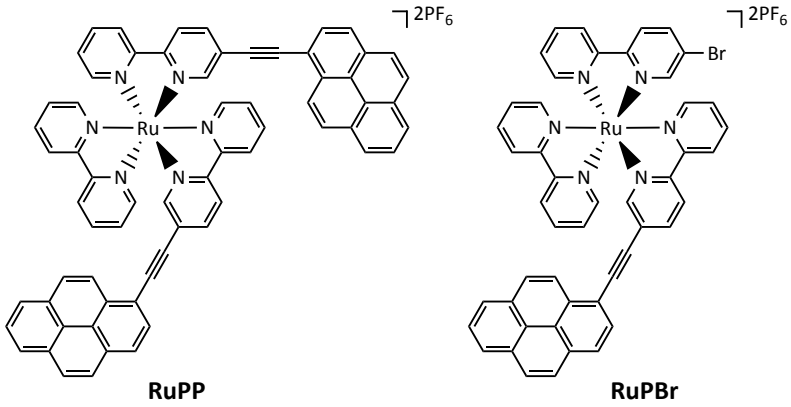

RuPP **RuPBr**

Under an argon atmosphere, 1-ethynylpyrene (63.7 mg, 0.282 mmol), **RuBrBr** (286.5 mg, 0.282 mmol), $[Pd(PPh_3)_2Cl_2]$ (9.8 mg, 0.014 mmol), PPh_3 (7.6 mg, 0.028 mmol) and CuI (5.4 mg, 0.028 mmol) were added in 20 mL of a dry solvent mixture ($(CH_3CH_2)_3NH$: CH_3CN = 1: 1, v/v). After stirring, the mixture was heated at 80 °C overnight. The solvent was removed under reduced pressure, and thenthe solid was dissolved with a minimum of acetonitrile. A saturated aqueous solution of potassium hexafluorophosphate was added dropwise to the mixture to give crude product as an orange solid. The mixture was

filtered and washed two times with water and diethyl ether. The crude product was purified by column chromatography on silica gel (CH_3CN/H_2O/sat. KNO_3, 100: 9: 1, v/v/v) to give product as a solid. Yield: **RuPP**, 119.2 mg, 32.3 %; **RuPBr** isomers, 100.0 mg, 30.5 %.

RuPP:

^{1}H NMR (400 MHz, CD_3CN, 298 K, δ in ppm) δ 8.66 (d, H, J = 8.5 Hz), 8.64-8.56 (m, 5H), 8.53-8.43 (m, 3H), 8.40-8.30 (m, 3H), 8.29-8.09 (m, 18H), 8.08-8.00 (m, 2H), 7.98-7.88 (m, H), 7.85-7.76 (m, 3H), 7.76-7.56 (m, H), 7.55-7.45 (m, 3H).

^{13}C NMR (150 MHz, CD_3CN, 298 K, δ in ppm) δ 158.13, 158.04, 157.69, 157.55, 156.95, 156.70, 156.09, 154.88, 153.47, 152.84, 152.78, 152.64, 140.46, 140.18, 139.01, 138.93, 133.38, 133.33, 133.08, 132.11, 132.04, 131.75, 131.66, 130.79, 130.75, 130.15, 130.08, 128.76, 128.74, 128.70, 128.61, 128.14, 128.11, 127.89, 127.68, 127.42, 127.30, 127.28, 127.14, 125.91, 125.86, 125.70, 125.56, 125.53, 125.50, 125.41, 125.12, 125.05, 125.00, 124.98, 124.94, 124.66, 124.61, 116.31, 96.81, 96.70, 91.06, 91.02.

MALDI-TOF-MS: calc. for ($[C_{66}H_{40}N_6Ru]^+$) m/z = 1018.2358, found m/z = 1018.2358.

RuPBr:

MALDI-TOF-MS: calc. for ($[C_{48}H_{31}N_6BrRu]^+$) m/z = 872.0837, found m/z = 872.0847.

Synthesis of **RuTT**:

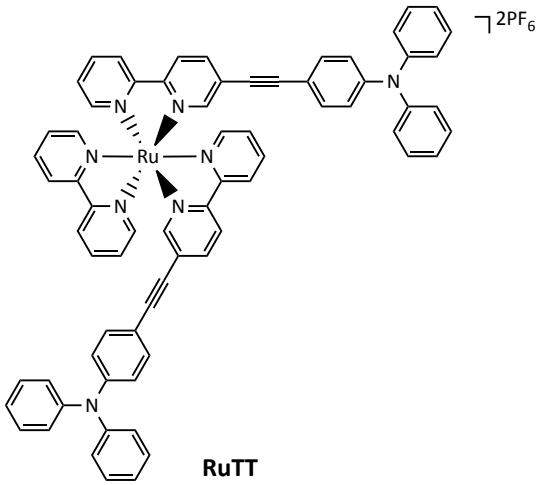

RuTT

Under an argon atmosphere, 1-ethynylpyrene (40.0 mg, 0.149 mmol), **RuBrBr** (110.0 mg, 0.108 mmol), $[Pd(PPh_3)_2Cl_2]$ (5.0 mg, 0.007 mmol), PPh_3 (4.0 mg, 0.015 mmol) and

CuI (2.8 mg, 0.016 mmol) were added in 20 mL of a dry solvent mixture ($(CH_3CH_2)_3NH$: CH_3CN = 1: 1, v/v). After stirring, the mixture was heated at 80 °C overnight. The solvent was removed under reduced pressure, and then the solid was dissolved with a minimum of acetonitrile. A saturated aqueous solution of potassium hexafluorophosphate was added dropwise to the mixture to give crude product as an orange solid. The mixture was filtered and washed two times with water and diethyl ether. The crude product was purified by column chromatography on silica gel (CH_3CN/H_2O/sat. KNO_3, 100: 9: 1, v/v/v) to give product as a solid. Yield: 40.1 mg, 19.3 %.

^{1}H NMR (400 MHz, CD_3CN, 298 K, δ in ppm) δ 8.58-8.47 (m, 6H), 8.16-8.04 (m, 6H), 7.94 (d, H, J = 1.4 Hz), 7.87-7.86 (m, H), 7.83 (d, H, J = 1.4 Hz), 7.74-7.68 (m, 3H), 7.48-7.28 (m, 16H), 7.23-7.06 (m, 12H), 6.96-6.89 (m, 4H).

^{13}C NMR (100 MHz, CD_3CN, 298 K, δ in ppm) δ 157.00(2), 156.89, 156.61, 156.59, 155.30(2), 155.22, 153.30(2), 153.09(2), 152.11(2), 151.80, 151.66, 151.61, 149.40, 146.64(2), 139.37(2), 139.33, 138.00(2), 137.89, 132.82(4), 129.74(8), 127.68, 127.61, 127.58, 125.66(8), 124.68(2), 124.60(2), 124.54(2), 124.44, 124.38, 123.95, 123.85, 120.64(2), 120.62(2), 112.87, 112.82, 97.49, 97.44, 83.53, 83.50.

MALDI-TOF-MS: calc. for ($[C_{70}H_{50}N_8Ru]^+$) m/z = 1104.3202, found m/z = 1104.3232.

8 Reference

1. P. Tertzakian, *A Thousand Barrels a Second*, McGraw-Hill, 2007.
2. Biomass Energy Center, Accessed January 14, 2015.
3. J. Zhang and K. R. Smith, *Environmental Health Perspectives*, 2007, 115, 848-855.
4. HOW SOLAR CELLS WORK - SOLAR CELL OVERVIEW, Accessed January 15, 2015.
5. H. Tributsch, *Photochemistry and Photobiology*, 1972, 16, 261-269.
6. WCubed Commercial Services, *WCubed Commercial Services*, Malibu CA.
7. J. R. Lakowicz, *Principles of Fluorescence Spectroscopy*, Kluwer Academic/Plenum Publishers, New York, 1999.
8. Q. Zhang and X. Liu, *Small*, 2012, 8, 3711-3713.
9. J. Zhao, S. Ji and H. Guo, *RSC Advances*, 2011, 1, 937-950.
10. C. Reinhard, R. Valiente and H. U. Güdel, *The Journal of Physical Chemistry B*, 2002, 106, 10051-10057.
11. H. C. Parker CA, *Proceedings of the Chemical Society*, 1962, 0 , 373-401.
12. D. V. Kozlov and F. N. Castellano, *Chemical Communications*, 2004, 0, 2860-2861.
13. A. Monguzzi, J. Mezyk, F. Scotognella, R. Tubino and F. Meinardi, *Physical Review B*, 2008, 78, 195112.
14. W. Shockley and H. J. Queisser, *Journal of Applied Physics*, 1961, 32, 510-519.
15. S. Baluschev, T. Miteva, V. Yakutkin, G. Nelles, A. Yasuda and G. Wegner, *Physical Review Letters*, 2006, 97, 143903.
16. Y. Y. Cheng, B. Fuckel, R. W. MacQueen, T. Khoury, R. G. C. R. Clady, T. F. Schulze, N. J. Ekins-Daukes, M. J. Crossley, B. Stannowski, K. Lips and T. W. Schmidt, *Energy & Environmental Science*, 2012, 5, 6953-6959.
17. J. Kim, F. Deng, F. N. Castellano and J. Kim, *Chemistry of Materials*, 2012, 24, 2250-2252.
18. R. P. Wayne, *Principles and Applications of Photochemistry*, Oxford Science Publications, 1988.
19. J. Zhao, W. Wu, J. Sun and S. Guo, *Chemical Society Reviews*, 2013, 42, 5323-5351.
20. Y. Lu, N. McGoldrick, F. Murphy, B. Twamley, X. Cui, C. Delaney, G. M. Ó. Máille, J. Wang, J. Zhao and S. M. Draper, *Chemistry – A European Journal*, 2016, 22, 11349-11356.
21. Y. Y. Cheng, T. Khoury, R. G. C. R. Clady, M. J. Y. Tayebjee, N. J. Ekins-Daukes, M. J. Crossley and T. W. Schmidt, *Physical Chemistry Chemical Physics*, 2010, 12, 66-71.

22. J. Saltiel, G. R. March, W. K. Smothers, S. A. Stout and J. L. Charlton, *Journal of the American Chemical Society*, 1981, 103, 7159-7164.

23. T. N. Singh-Rachford and F. N. Castellano, *Coordination Chemistry Reviews*, 2010, 254, 2560-2573.

24. T. N. Singh-Rachford and F. N. Castellano, *The Journal of Physical Chemistry A*, 2009, 113, 9266-9269.

25. L. Flamigni, A. Barbieri, C. Sabatini, B. Ventura and F. Barigelletti, in *Photochemistry and Photophysics of Coordination Compounds II*, eds. V. Balzani and S. Campagna, Springer Berlin Heidelberg, Berlin, Heidelberg, 2007, pp. 143-203.

26. R. R. Islangulov, D. V. Kozlov and F. N. Castellano, *Chemical Communications*, 2005, 0, 3776-3778.

27. G. J. Wilson, A. Launikonis, W. H. F. Sasse and A. W. H. Mau, *The Journal of Physical Chemistry A*, 1997, 101, 4860-4866.

28. G. J. Wilson, W. H. F. Sasse and A. W. H. Mau, *Chemical Physics Letters*, 1996, 250, 583-588.

29. D. S. Tyson, J. Bialecki and F. N. Castellano, *Chemical Communications*, 2000, 0, 2355-2356.

30. R. Lincoln, L. Kohler, S. Monro, H. Yin, M. Stephenson, R. Zong, A. Chouai, C. Dorsey, R. Hennigar, R. P. Thummel and S. A. McFarland, *Journal of the American Chemical Society*, 2013, 135, 17161-17175.

31. S. Ji, W. Wu, W. Wu, P. Song, K. Han, Z. Wang, S. Liu, H. Guo and J. Zhao, *Journal of Materials Chemistry*, 2010, 20, 1953-1963.

32. J. Zhao, S. Ji, W. Wu, W. Wu, H. Guo, J. Sun, H. Sun, Y. Liu, Q. Li and L. Huang, *RSC Advances*, 2012, 2, 1712-1728.

33. M. Galletta, S. Campagna, M. Quesada, G. Ulrich and R. Ziessel, *Chemical Communications*, 2005, 33, 4222-4224.

34. W. Wu, J. Sun, X. Cui and J. Zhao, *Journal of Materials Chemistry C*, 2013, 1, 4577-4589.

35. I. M. Dixon, J. Collin, J. Sauvage, L. Flamigni, S. Encinas and F. Barigelletti, *Chemical Society Reviews*, 2000, 29, 385-391.

36. W. Zhao and F. N. Castellano, *The Journal of Physical Chemistry A*, 2006, 110, 11440-11445.

37. S. Lamansky, P. Djurovich, D. Murphy, F. Abdel-Razzaq, H.-E. Lee, C. Adachi, P. E. Burrows, S. R. Forrest and M. E. Thompson, *Journal of the American Chemical Society*, 2001, 123, 4304-4312.

38. J. Brooks, Y. Babayan, S. Lamansky, P. I. Djurovich, I. Tsyba, R. Bau and M. E. Thompson, *Inorganic Chemistry*, 2002, 41, 3055-3066.

39. S.-y. Takizawa, C. Pérez-Bolívar, P. Anzenbacher and S. Murata, *European Journal of Inorganic Chemistry*, 2012, 2012, 3975-3979.

40. J. Sun, W. Wu, H. Guo and J. Zhao, *European Journal of Inorganic Chemistry*, 2011, 2011, 3165-3173.

41. S. Ji, H. Guo, W. Wu, W. Wu and J. Zhao, *Angewandte Chemie International Edition*, 2011, 50, 8283-8286.

42. R. R. Islangulov, J. Lott, C. Weder and F. N. Castellano, *Journal of the American Chemical Society*, 2007, 129, 12652-12653.

43. S. Baluschev, V. Yakutkin, G. Wegner, T. Miteva, G. Nelles, A. Yasuda, S. Chernov, S. Aleshchenkov and A. Cheprakov, *Applied Physics Letters*, 2007, 90, 181103.

44. T. N. Singh-Rachford, A. Haefele, R. Ziessel and F. N. Castellano, *Journal of the American Chemical Society*, 2008, 130, 16164-16165.

45. T. N. Singh-Rachford and F. N. Castellano, *The Journal of Physical Chemistry Letters*, 2010, 1, 195-200.

46. S. Amemori, N. Yanai and N. Kimizuka, *Physical Chemistry Chemical Physics*, 2015, 17, 22557-22560.

47. P. Du and R. Eisenberg, *Chemical Science*, 2010, 1, 502-506.

48. H. Guo, S. Ji, W. Wu, W. Wu, J. Shao and J. Zhao, *Analyst*, 2010, 135, 2832-2840.

49. I. E. Pomestchenko, C. R. Luman, M. Hissler, R. Ziessel and F. N. Castellano, *Inorganic Chemistry*, 2003, 42, 1394-1396.

50. F. N. Castellano, I. E. Pomestchenko, E. Shikhova, F. Hua, M. L. Muro and N. Rajapakse, *Coordination Chemistry Reviews*, 2006, 250, 1819-1828.

51. H. Sun, H. Guo, W. Wu, X. Liu and J. Zhao, *Dalton Transactions*, 2011, 40, 7834-7841.

52. W. Wu, J. Zhao, J. Sun, L. Huang and X. Yi, *Journal of Materials Chemistry C*, 2013, 1, 705-716.

53. L. Liu, S. Guo, J. Ma, K. Xu, J. Zhao and T. Zhang, *Chemistry – A European Journal*, 2014, 20, 14282-14295.

54. H. Chen, C. Hung, K. Wang, H. Chen, W. S. Fann, F. Chien, P. Chen, T. J. Chow, C. Hsu and S. Sun, *Chemical Communications*, 2009, 0, 4064-4066.

55. Q. Liu, Y. Li, H. Zhang, B. Chen, C. Tung and L. Wu, *Chemistry – A European Journal*, 2012, 18, 620-627.

56. W. Wu, H. Guo, W. Wu, S. Ji and J. Zhao, *The Journal of Organic Chemistry*, 2011, 76, 7056-7064.

57. N. Adarsh, R. R. Avirah and D. Ramaiah, *Organic Letters*, 2010, 12, 5720-5723.

58. C. Zhang, J. Zhao, S. Wu, Z. Wang, W. Wu, J. Ma, S. Guo and L. Huang, *Journal of the American Chemical Society*, 2013, 135, 10566-10578.

59. S. Guo, W. Wu, H. Guo and J. Zhao, *The Journal of Organic Chemistry*, 2012, 77, 3933-3943.

60. T. N. Singh-Rachford and F. N. Castellano, *The Journal of Physical Chemistry A*, 2009, 113, 5912-5917.

61. D. P. Specht, P. A. Martic and S. Farid, *Tetrahedron*, 1982, 38, 1203-1211.

62. D. Huang, J. Sun, L. Ma, C. Zhang and J. Zhao, *Photochemical & Photobiological Sciences*, 2013, 12, 872-882.

63. Y. Cakmak, S. Kolemen, S. Duman, Y. Dede, Y. Dolen, B. Kilic, Z. Kostereli, L. T. Yildirim, A. L. Dogan, D. Guc and E. U. Akkaya, *Angewandte Chemie International Edition*, 2011, 50, 11937-11941.

64. W. Wu, X. Cui and J. Zhao, *Chemical Communications*, 2013, 49, 9009-9011.

65. Z. Yu, Y. Wu, Q. Peng, C. Sun, J. Chen, J. Yao and H. Fu, *Chemistry – A European Journal*, 2016, 22, 4717-4722.

66. C. S. Foote, in *Electron Transfer I*, ed. J. Mattay, Springer Berlin Heidelberg, Berlin, Heidelberg, 1994, pp. 347-363.

67. Y. Nakamura, M. Taki, S. Tobita, H. Shizuka, H. Yokoi, K. Ishiguro, Y. Sawaki and J. Nishimura, *Journal of the Chemical Society, Perkin Transactions 2*, 1999, 0, 127-130.

68. D. Huang, J. Zhao, W. Wu, X. Yi, P. Yang and J. Ma, *Asian Journal of Organic Chemistry*, 2012, 1, 264-273.

69. K. Moor, J. Kim, S. Snow and J. Kim, *Chemical Communications*, 2013, 49, 10829-10831.

70. L. Salem and C. Rowland, *Angewandte Chemie International Edition in English*, 1972, 11, 92-111.

71. S. Guo, J. Sun, L. Ma, W. You, P. Yang and J. Zhao, *Dyes and Pigments*, 2013, 96, 449-458.

72. Y. Liu and J. Zhao, *Chemical Communications*, 2012, 48, 3751-3753.

73. S. K. Sugunan, C. Greenwald, M. F. Paige and R. P. Steer, *The Journal of Physical Chemistry A*, 2013, 117, 5419-5427.

74. K. Nagarajan, A. R. Mallia, K. Muraleedharan and M. Hariharan, *Chemical Science*, 2017, 8, 1776-1782.

75. M. L. Mueller, X. Yan, J. A. McGuire and L.-S. Li, *Nano Letters*, 2010, 10, 2679-2682.

76. H. Von Tappeiner, *Med Wochenschr*, 1903, 47, 2024.

77. P. Majumdar, R. Nomula and J. Zhao, *Journal of Materials Chemistry C*, 2014, 2, 5982-5997.

78. R. Ziessel, B. D. Allen, D. B. Rewinska and A. Harriman, *Chemistry – A European Journal*, 2009, 15, 7382-7393.

79. W. M. Sharman, J. E. van Lier and C. M. Allen, *Advanced Drug Delivery Reviews*, 2004, 56, 53-76.

80. D. B. Papkovsky and R. I. Dmitriev, *Chemical Society Reviews*, 2013, 42, 8700-8732.

81. S. Campagna, F. Puntoriero, F. Nastasi, G. Bergamini and V. Balzani, *Photochemistry and Photophysics of Coordination Compounds I*, eds. V. Balzani and S. Campagna, Springer Berlin Heidelberg, 2007, vol. 280, ch. 133, pp. 117-214.

82. F. Gärtner, S. Denurra, S. Losse, A. Neubauer, A. Boddien, A. Gopinathan, A. Spannenberg, H. Junge, S. Lochbrunner, M. Blug, S. Hoch, J. Busse, S. Gladiali and M. Beller, *Chemistry – A European Journal*, 2012, 18, 3220-3225.

83. S. Ott, M. Kritikos, B. Åkermark and L. Sun, *Angewandte Chemie International Edition*, 2003, 42, 3285-3288.

84. W. Wang, F. Wang, H. Wang, C.-H. Tung and L. Wu, *Dalton Transactions*, 2012, 41, 2420-2426.

85. R. S. Khnayzer, J. Blumhoff, J. A. Harrington, A. Haefele, F. Deng and F. N. Castellano, *Chemical Communications*, 2012, 48, 209-211.

86. C. Ye, B. Wang, R. Hao, X. Wang, P. Ding, X. Tao, Z. Chen, Z. Liang and Y. Zhou, *Journal of Materials Chemistry C*, 2014, 2, 8507-8514.

87. A. C. Benniston, V. Grosshenny, A. Harriman and R. Ziessel, *Angewandte Chemie International Edition in English*, 1994, 33, 1884-1885.

88. A. Harriman, A. Khatyr and R. Ziessel, *Dalton Transactions*, 2003, 0, 2061-2068.

89. J. Wang, Y. Lu, N. McGoldrick, C. Zhang, W. Yang, J. Zhao and S. M. Draper, *Journal of Materials Chemistry C*, 2016, 4, 6131-6139.

90. A. Loudet and K. Burgess, *Chemical Reviews*, 2007, 107, 4891-4932.

91. C. Brotschi, G. Mathis and C. J. Leumann, *Chemistry – A European Journal*, 2005, 11, 1911-1923.

92. S. Sprouse, K. A. King, P. J. Spellane and R. J. Watts, *Journal of the American Chemical Society*, 1984, 106, 6647-6653.

93. J. Sun, F. Zhong, X. Yi and J. Zhao, *Inorganic Chemistry*, 2013, 52, 6299-6310.

94. N. C. Bell, S. J. Doyle, G. Battistelli, C. L. M. LeGuyader, M. P. Thompson, A. M. Poe, A. Rheingold, C. Moore, M. Montalti, S. Thayumanavan, M. J. Tauber and N. C. Gianneschi, *Langmuir*, 2015, 31, 9707-9717.

95. J. Zhao, K. Xu, W. Yang, Z. Wang and F. Zhong, *Chemical Society Reviews*, 2015, 44, 8904-8939.

96. M. A. L. Marques and E. K. U. Gross, in *A Primer in Density Functional Theory*, eds. C. Fiolhais, F. Nogueira and M. A. L. Marques, Springer Berlin Heidelberg, Berlin, Heidelberg, 2003, pp. 144-184.

97. J. Ma, X. Cui, F. Wang, X. Wu, J. Zhao and X. Li, *The Journal of Organic Chemistry*, 2014, 79, 10855-10866.

98. AccessScience Editors, E. AccessScience, 2014, DOI: 10.1036/1097-8542.BR0826141.

99. F. Pene, E. Courtine, A. Cariou and J.-P. Mira, *Critical Care Medicine*, 2009, 37, S50-S58.

100. Y. Lu, F. Xue, Z. Zhou, M. Shi, Y. Yan, L. Qin, H. Yang and S. Yang, *Chemistry – A European Journal*, 2014, 20, 16242-16247.

101. G. Koopman, C. Reutelingsperger, G. Kuijten, R. Keehnen, S. Pals and M. van Oers, *Blood*, 1994, 84, 1415-1420.

102. A. El-ghayoury, A. Harriman, A. Khatyr and R. Ziessel, *The Journal of Physical Chemistry A*, 2000, 104, 1512-1523.

103. A. Harriman and R. Ziessel, in *Carbon-Rich Compounds*, Wiley-VCH Verlag GmbH & Co. KGaA, 2006, ch2, pp. 26-89.

104. A. Harriman, A. Mayeux, C. Stroh and R. Ziessel, *Dalton Transactions*, 2005, 17, 2925-2932.

105. Bruker APEX v2012.12-0, *Bruker AXS Inc.* , Wisconsin, USA.

106. SADABS(2014) Bruker AXS Inc., Madison, Wisconsin, Sheldrick, *G. M. Univeristy of Gottingen*, USA, Germany.

107. M. G. B. Drew, C. J. Harding, V. McKee, G. G. Morgan and J. Nelson, *Journal of the Chemical Society, Chemical Communications*, 1995, 10, 1035-1038.

108. V. Russell, M. Scudder and I. Dance, *Journal of the Chemical Society, Dalton Transactions*, 2001, 6, 789-799.

109. M. A. Spackman and D. Jayatilaka, *CrystEngComm*, 2009, 11, 19-32.

110. S. Fan, C. Kim, B. Fang, K. Liao, G. Yang, C. Li, J. Kim and J. Ko, *The Journal of Physical Chemistry C*, 2011, 115, 7747-7754.

111. W. R. Browne, R. Hage and J. G. Vos, *Coordination Chemistry Reviews*, 2006, 250, 1653-1668.

112. H. Cheema, A. Islam, R. Younts, B. Gautam, I. Bedja, R. K. Gupta, L. Han, K. Gundogdu and A. El-Shafei, *Physical Chemistry Chemical Physics*, 2014, 16, 27078-27087.

113. H. Nie, W. Yang, R. Zheng, Q. Shi, H. Chen, J. Yao and Y. Zhong, *Inorganic Chemistry*, 2015, 54, 1272-1282.

114. S. R. Salpage, A. Paul, B. Som, T. Banerjee, K. Hanson, M. D. Smith, A. K. Vannucci and L. S. Shimizu, *Dalton Transactions*, 2016, 45, 9601-9607.

115. M. Zhou and J. Roovers, *Macromolecules*, 2001, 34, 244-252.

116. J. B. Flanagan, S. Margel, A. J. Bard and F. C. Anson, *Journal of the American Chemical Society*, 1978, 100, 4248-4253.

117. S. Ladouceur, D. Fortin and E. Zysman-Colman, *Inorganic Chemistry*, 2011, 50, 11514-11526.

118. L. Huang, J. Zhao, S. Guo, C. Zhang and J. Ma, *The Journal of Organic Chemistry*, 2013, 78, 5627-5637.

119. P.L. Burn, V. Christou, S.C. Lo, J.N.G. Pillow, J.M. Lupton, I.D.W.Samuel, *Metal-containing dendrimers*, 2002, WO02066552.

120. R. S. Kathayat and N. S. Finney, *Journal of the American Chemical Society*, 2013, 135, 12612-12614.

121. R. P. Sabatini, T. M. McCormick, T. Lazarides, K. C. Wilson, R. Eisenberg and D. W. McCamant, *The Journal of Physical Chemistry Letters*, 2011, 2, 223-227.

122. L. Huang, X. Cui, B. Therrien and J. Zhao, *Chemistry – A European Journal*, 2013, 19, 17472-17482.

123. C. Goze, D. V. Kozlov, D. S. Tyson, R. Ziessel and F. N. Castellano, *New Journal of Chemistry*, 2003, 27, 1679-1683.

124. T. Doi, H. Nagamiya, M. Kokubo, K. Hirabayashi and T. Takahashi, *Tetrahedron*, 2002, 58, 2957-2963.

125. D. L. Ashford, M. K. Brennaman, R. J. Brown, S. Keinan, J. J. Concepcion, J. M. Papanikolas, J. L. Templeton and T. J. Meyer, *Inorganic Chemistry*, 2015, 54, 460-469.

126. M. Shirai, in *Encyclopedia of Polymeric Nanomaterials*, eds. S. Kobayashi and K. Müllen, Springer Berlin Heidelberg, Berlin, Heidelberg, 2013, pp. 1-7.

127. R. Liu, H. Chen, Z. Li, F. Shi and X. Liu, *Polymer Chemistry*, 2016, 7, 2457-2463.

128. P. Duan, N. Yanai, H. Nagatomi and N. Kimizuka, *Journal of the American Chemical Society*, 2015, 137, 1887-1894.

129. M. Haase, H. Schäfer, *Angewandte Chemie International Edition*, 2011, 50, 5808-5829.

130. Q. Liu, T. Yang, W. Feng and F. Li, *Journal of the American Chemical Society*, 2012, 134, 5390-5397.

131. T. N. Singh-Rachford, J. Lott, C. Weder and F. N. Castellano, *Journal of the American Chemical Society*, 2009, 131, 12007-12014.

132. K. Tanaka, K. Inafuku and Y. Chujo, *Chemical Communications*, 2010, 46, 4378-4380.

Annex

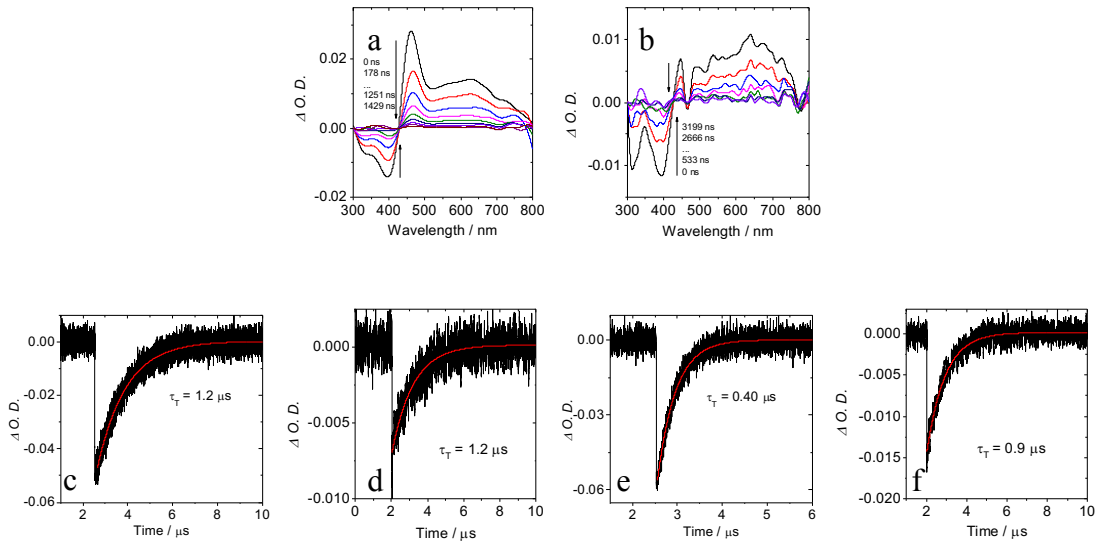

Figure A1 *Nanosecond time-scaled transient different absorption spectra of a)* ***IrCIr*** *and b)* ***IrC*** *in CH_3CN under a nitrogen atmosphere at room temperature. The decay traces of c)* ***RuCRu****, d)* ***RuC****, e)* ***IrCIr*** *and f)* ***IrC*** *at 400 nm. C = 1 × 10^{-5} mol/L.*

Table A1 Oscillator Strength (f), main configurations and CI coefficients of the Low-Electronic Excitation Energies (eV) and corresponding lying Electronic Excited States of the complex **IrCIr** calculated by TDDDFT/B3LYP/GENECP/LANL2DZ, CH_3CN as the solvent (PCM model) based on the optimised Ground State Geometries.

	Electronic Transition	**TDDFT/B3LYP/GEN**				
		Energy [a]	***f*** [b]	**Composition** [c]	**CI** [d]	**Character** [e]
Singlet	$S_0 \rightarrow S_3$	490.25 nm 2.5290 eV	1.3836	H-L	0.6798	ILCT
				H-2-L	0.1204	MLCT/L'LCT
	$S_0 \rightarrow S_6$	455.42 nm 2.7224 eV	0.2569	H-L+1	0.6990	ILCT
	$S_0 \rightarrow S_{10}$	399.81 nm 3.1011 eV	0.3309	H-1-L	0.1359	MLCT/L'LCT
				H-6-L	0.1366	MLCT/L'LCT
				H-5-L+1	0.6095	ILCT
Triplet	$S_0 \rightarrow T_1$	592.10 nm 2.0940 eV	0.0000[f]	H-5-L+1	0.2421	ILCT
				H-13-L	0.1403	ILCT
				H-L	0.5760	ILCT

			H-5-L	0.3189	ILCT/LMCT
$S_0 \rightarrow T_2$	574.91 nm 2.1566 eV	0.0000[f]	H-L+1	0.5161	ILCT
			H-1-L	0.1600	MLCT/L'LCT

[a] Only the selected low-lying excited states are presented. [b] Oscillator strengths. [c] Only the main configurations are presented. [d] The CI coefficients are in absolute values. [e] L stands for carbazole localized ligand; L' stands for the other two 2-phenylpyridine. [f] No spin-orbital coupling effect was considered, thus the *f* values are zero.

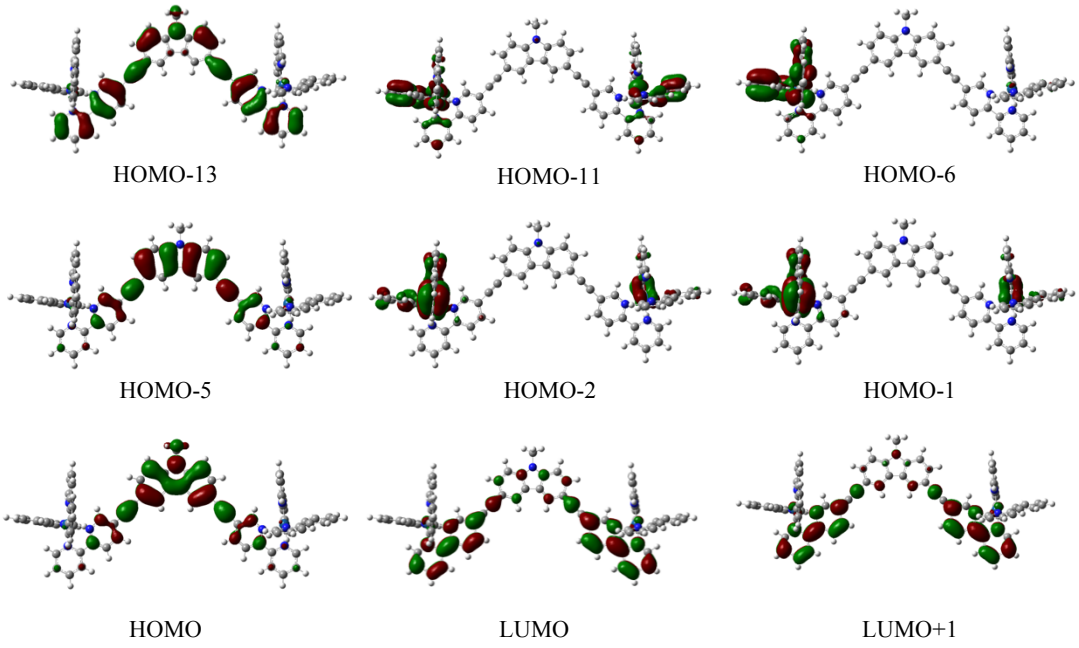

Figure A2 *Electron density maps of the frontier molecular orbitals of the complex* ***IrCIr****, based on ground state optimised geometry by the TDDFT calculations at the TDDFT/B3LYP/GENECP/LANL2DZ level with Gaussian 09W.*

Table A2 Oscillator Strength (f), main configurations and CI coefficients of the Low-Electronic Excitation Energies (eV) and corresponding lying Electronic Excited States of the complex **IrC** calculated by TDDDFT/B3LYP/GENECP/LANL2DZ, CH_3CN as the solvent (PCM model) based on the optimised Ground State Geometries.

	Electronic transition	TDDFT//B3LYP/GEN				
		Energy [a]	*f* [b]	Composition [c]	CI [d]	Character [e]
Singlet	$S_0 \rightarrow S_2$	472.46 nm 2.6242 eV	0.9037	H-L	0.6996	ILCT
HOMO-7	$S_0 \rightarrow S_4$	HOMO-6 394.59 nm 3.1421 eV	0.0618	HOMO-2 H-2-L	0.1281 HOMO-1	ILCT
				H-1-L+1	0.6792	ML'CT
	S_0-S_{15}	334.08nm 3.7112ev	0.4349	H-7-L	0.6074	MLCT/ILCT
	HOMO	LUMO		H-6-L LUMO+1	0.2519	MLCT/L'LCT
Triplet	$S_0 \rightarrow T_1$	589.67 nm 2.1026 eV	0.0000[f]	H-L	0.6173	ILCT
				H-7-L	0.1654	MLCT/ML'CT
				H-6-L	0.1487	MLCT/L'LCT
	$S_0 \rightarrow T_2$	516.52 nm 2.4004 eV	0.0000[f]	H-1-L	0.6998	MLCT/L'LCT

[a] Only the selected low-lying excited states are presented. [b] Oscillator strengths. [c] Only the main configurations are presented. [d] The CI coefficients are in absolute values. [e] L stands for carbazole localized ligand; L' stands for the other two 2-phenylpyridine. [f] No spin-orbital coupling effect was considered, thus the *f* values are zero.

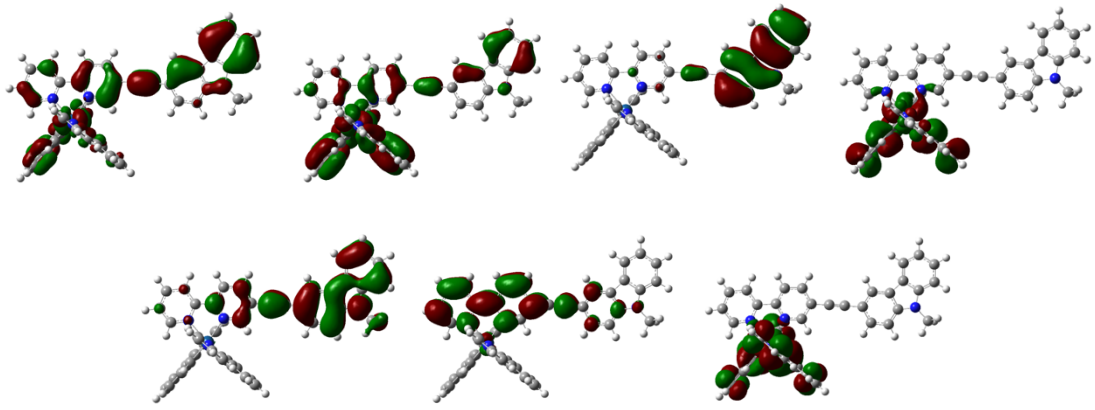

Figure A3 *Electron density maps of the frontier molecular orbitals of the complex* ***IrC****, based on ground state optimised geometry by the TDDFT calculations at the TDDFT/B3LYP/GENECP/LANL2DZ level with Gaussian 09W.*

Crystal data and structure refinement for RuC.

Identification code	RuC
Empirical formula	$C_{50}H_{43}F_{12}N_7P_2Ru$
Formula weight	1132.92
Temperature/K	100(2)
Crystal system	triclinic
Space group	P-1
a/Å	9.9192(3)
b/Å	12.7350(4)
c/Å	19.0381(6)
α/°	86.0585(19)
β/°	80.675(2)
γ/°	83.0251(18)
Volume/Å^3	2352.61(13)
Z	2
ρ_{calc}g/cm^3	1.599
μ/mm^{-1}	4.163
F(000)	1148.0
Crystal size/mm^3	0.18 × 0.04 × 0.02
Radiation	CuKα (λ = 1.54178)
2Θ range for data collection/°	4.71 to 136.894
Index ranges	-11 ≤ h ≤ 11, -15 ≤ k ≤ 15, -22 ≤ l ≤ 22
Reflections collected	38148
Independent reflections	8598 [R_{int} = 0.0686, R_{sigma} = 0.0548]
Data/restraints/parameters	8598/0/650
Goodness-of-fit on F^2	0.994
Final R indexes [I>=2σ (I)]	R_1 = 0.0494, wR_2 = 0.1277
Final R indexes [all data]	R_1 = 0.0640, wR_2 = 0.1380
Largest diff. peak/hole / e Å^{-3}	1.31/-0.35
CCDC no.	1566335

Crystal data and structure refinement for IrBrBr.

Identification code	**IrBrBr**	
Empirical formula	$C_{67}H_{57}Br_4F_{12}Ir_2N_8O_{3.50}P_2$	
Formula weight	2024.18	
Temperature	100 K	
Wavelength	0.71073 Å	
Crystal system	Triclinic	
Space group	$P\bar{1}$	
Unit cell dimensions	a = 13.9309(5) Å	α= 65.3460(10)°.
	b = 16.0734(6) Å	β= 80.6450(10)°.
	c = 17.9023(6) Å	γ = 71.8730(10)°.
Volume	3459.9(2) $Å^3$	
Z	2	
Density (calculated)	1.943 Mg/m^3	
Absorption coefficient	6.284 mm^{-1}	
F(000)	1950	
Crystal size	0.25 x 0.14 x 0.1 mm^3	
Theta range for data collection	2.669 to 28.442°.	
Index ranges	-18≤h≤18, -21≤k≤21, -23≤l≤23	
Reflections collected	80804	
Independent reflections	17416 [R(int) = 0.0433]	
Completeness to theta = 26.000°	99.9 %	
Absorption correction	Semi-empirical from equivalents	
Max. and min. transmission	0.7457 and 0.5648	
Refinement method	Full-matrix least-squares on F^2	
Data / restraints / parameters	17416 / 4 / 909	
Goodness-of-fit on F^2	1.045	
Final R indices [I>2σ(I)]	R1 = 0.0270, wR2 = 0.0471	
R indices (all data)	R1 = 0.0434, wR2 = 0.0510	
Largest diff. peak and hole	1.192 and -2.027 $e.Å^{-3}$	

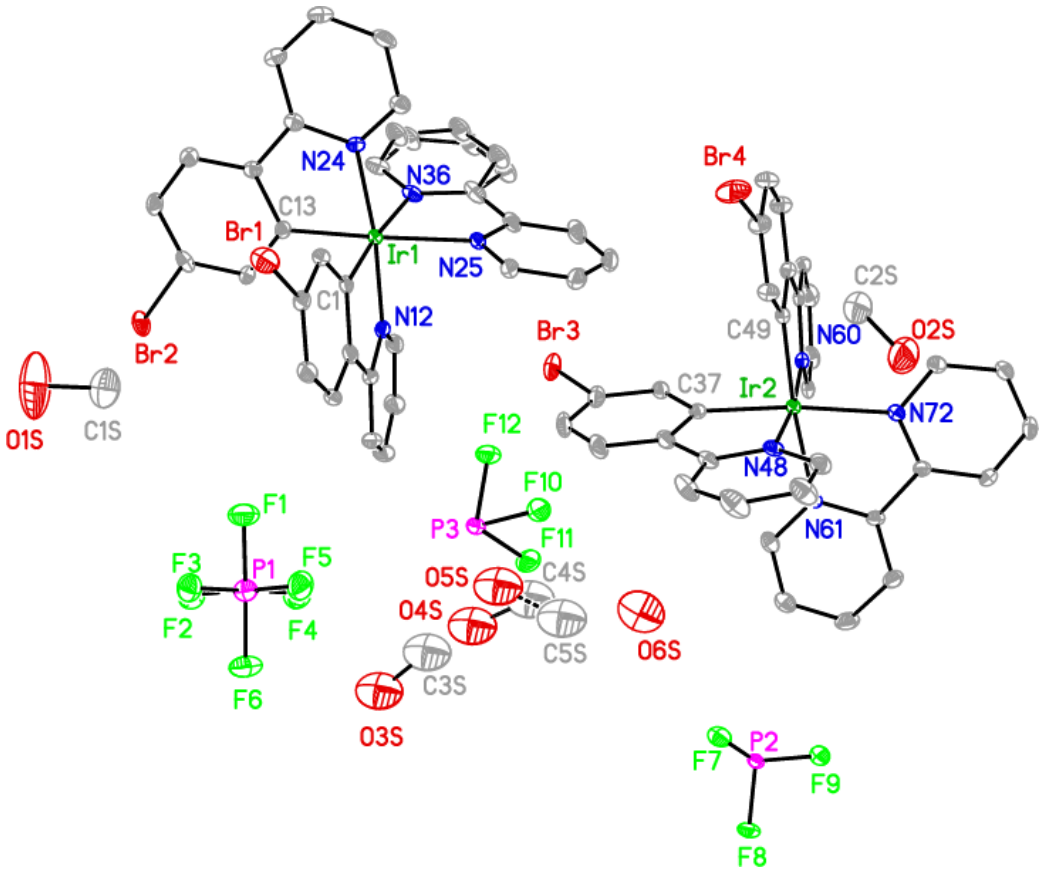

Figure A4 *Asymmetric unit of* ***IrBrBr*** *with atomic displacement parameters shown at 50% probability. Partial atom labelling and hydrogen atoms omitted for clarity.*

Crystal data and structure refinement for IrPP.

Identification code	IrPP	
Empirical formula	$C_{68}H_{40}F_6IrN_4P$	
Formula weight	1250.21	
Temperature	100(2) K	
Wavelength	0.71073 Å	
Crystal system	Monoclinic	
Space group	C2/c	
Unit cell dimensions	a = 66.689(3) Å	α= 90°.
	b = 8.7075(4) Å	β= 93.0296(13)°.
	c = 18.0513(9) Å	γ = 90°.
Volume	10467.6(9) $Å^3$	
Z	8	
Density (calculated)	1.587 Mg/m^3	
Absorption coefficient	2.652 mm^{-1}	
F(000)	4976	
Crystal size	0.26 x 0.11 x 0.04 mm^3	
Theta range for data collection	1.835 to 26.380°.	
Index ranges	$-82\leq h\leq 82$, $-10\leq k\leq 10$, $-22\leq l\leq 22$	
Reflections collected	51238	
Independent reflections	10603 [R(int) = 0.0367]	
Completeness to theta = 25.242°	99.2 %	
Absorption correction	Semi-empirical from equivalents	
Max. and min. transmission	0.0932 and 0.0601	
Refinement method	Full-matrix least-squares on F^2	
Data / restraints / parameters	10603 / 24 / 732	
Goodness-of-fit on F^2	1.053	
Final R indices [I>2σ(I)]	R1 = 0.0610, wR2 = 0.1925	
R indices (all data)	R1 = 0.0704, wR2 = 0.1997	
Largest diff. peak and hole	1.779 and -6.982 $e.Å^{-3}$	

Crystal data and structure refinement for IrTT.

Identification code	IrTT	
Empirical formula	$C_{79.50}H_{50}D_{15}F_6IrN_6O_{2.50}P$	
Formula weight	1496.63	
Temperature	100(2) K	
Wavelength	0.71073 Å	
Crystal system	Triclinic	
Space group	$P\bar{1}$	
Unit cell dimensions	a = 11.8682(6) Å	α= 117.1614(10)°.
	b = 17.7343(9) Å	β= 95.7005(13)°.
	c = 19.1476(10) Å	γ = 102.6460(12)°.
Volume	3405.3(3) $Å^3$	
Z	2	
Density (calculated)	1.460 Mg/m^3	
Absorption coefficient	2.054 mm^{-1}	
F(000)	1500	
Crystal size	0.23 x 0.1 x 0.06 mm^3	
Theta range for data collection	1.304 to 28.341°.	
Index ranges	$-15\leq h\leq 15$, $-23\leq k\leq 23$, $-25\leq l\leq 25$	
Reflections collected	118141	
Independent reflections	16968 [R(int) = 0.0562]	
Completeness to theta = 25.242°	100.0 %	
Absorption correction	Semi-empirical from equivalents	
Max. and min. transmission	0.7457 and 0.6101	
Refinement method	Full-matrix least-squares on F^2	
Data / restraints / parameters	16968 / 141 / 970	
Goodness-of-fit on F^2	1.015	
Final R indices [$I>2\sigma(I)$]	R1 = 0.0270, wR2 = 0.0534	
R indices (all data)	R1 = 0.0392, wR2 = 0.0567	
Largest diff. peak and hole	0.522 and -0.879 $e.Å^{-3}$	

Crystal data and structure refinement for RuPP.

Identification code	tcd578	
Empirical formula	$C_{66}H_{40}F_{12}N_6P_2Ru$	
Formula weight	1308.05	
Temperature	100.03 K	
Wavelength	0.71073 Å	
Crystal system	Triclinic	
Space group	P-1	
Unit cell dimensions	a = 11.8157(4) Å	α= 78.3759(12)°.
	b = 11.8734(4) Å	β= 85.1599(13)°.
	c = 22.5363(8) Å	γ = 61.4321(11)°.
Volume	2719.53(16) $Å^3$	
Z	2	
Density (calculated)	1.597 Mg/m^3	
Absorption coefficient	0.440 mm^{-1}	
F(000)	1320	
Crystal size	0.23 x 0.21 x 0.07 mm^3	
Theta range for data collection	1.845 to 28.465°.	
Index ranges	$-15\leq h\leq 15$, $-15\leq k\leq 15$, $-30\leq l\leq 30$	
Reflections collected	127860	
Independent reflections	13630 [R(int) = 0.0464]	
Completeness to theta = 26.000°	100.0 %	
Absorption correction	Semi-empirical from equivalents	
Max. and min. transmission	0.7457 and 0.6944	
Refinement method	Full-matrix least-squares on F^2	
Data / restraints / parameters	13630 / 0 / 784	
Goodness-of-fit on F^2	1.030	
Final R indices [I>2σ(I)]	R1 = 0.0340, wR2 = 0.0704	
R indices (all data)	R1 = 0.0488, wR2 = 0.0753	
Largest diff. peak and hole	0.581 and -0.701 $e.Å^{-3}$	